JUSTUS-LIEBIG-UNIVERSITÄT GIESSEN

EXPLORATION AND APPLICATION OF HIGH ENTROPY LITHIUM ARGYRODITES AS SOLID ELECTROLYTES FOR ALL-SOLID-STATE BATTERIES

Dem Fachbereich Biologie und Chemie

der Justus-Liebig-Universität Gießen

vorgelegte Dissertation zur Erlangung

des akademischen Grades

Doktor der Naturwissenschaften

− Dr. rer. nat. −

Jing Lin

from Chengdu, China

December 2024

Dekan / Dean	Prof. Dr. Thomas Wilke
1. Gutachter / 1st Reviewer	Prof. Dr. Jürgen Janek (Justus-Liebig-Universität Gießen)
2. Gutachter / 2nd Reviewer	Prof. Dr. Bernd M. Smarsly (Justus-Liebig-Universität Gießen)
Eingereicht / submitted	12.2024
Disputation / disputation	02.2025

Eidesstattliche Erklärung

Die vorliegende Arbeit wurde im Zeitraum von April 2021 bis December 2024 am Battery and Electrochemistry Laboratory (BELLA) des Instituts für Nanotechnologie am Karlsruher Institut für Technologie unter der Betreuung von Prof. Dr. Jürgen Janek erstellt.

Ich erkläre:

Ich habe die vorliegende Dissertation eigenständig und ohne unerlaubte fremde Hilfe angefertigt und mich lediglich der in der Arbeit angegebenen Hilfsmittel bedient. Alle wörtlich oder sinngemäß aus veröffentlichten Schriften entnommenen Textpassagen sowie alle Angaben, die auf mündlichen Auskünften basieren, sind entsprechend gekennzeichnet. Des Weiteren stimme ich einer eventuellen Überprüfung meiner Dissertation durch eine Antiplagiat-Software zu. Bei den von mir durchgeführten und in der Dissertation erwähnten Untersuchungen habe ich mich an die Grundsätze guter wissenschaftlicher Praxis gehalten, wie sie in der „Satzung der Justus-Liebig-Universität Gießen zur Sicherung guter wissenschaftlicher Praxis“ festgelegt sind.

_____

Jing Lin, Karlsruhe, 12.12. 2024

“Use 'entropy' and you can never lose a debate, von Neumann told Shannon, because no one really knows what 'entropy' is."
-- William Poundstone

“Crystals are like people: it is the defects in them that make them interesting.”

-- Sir Charles Frank

Dedicated to my parents, my grandparents and Hang Xu

Abstract

Solid-state batteries (SSBs) are a potentially safe, next-generation energy storage technology. Commercial viability of SSBs relies on the development of solid electrolytes with high ionic conductivity, high (electro)chemical stability, and good processability. A recent innovative approach to modify materials, potentially resulting in improved properties, is the "high-entropy" concept, characterized by $\Delta S_{conf} > 1.5R$ (where ΔS_{conf} and R represent the configurational entropy and ideal gas constant, respectively). However, the beneficial influence of a high configurational entropy on ion diffusion remains largely elusive given the absence of systematic studies. Therefore, this doctoral dissertation aimed to apply the high-entropy concept to solid electrolytes, in particular focusing on lithium argyrodites with the goal to achieve superionic conduction (~10 mS cm^{-1} at room temperature). The scientific objective was to understand the relationship between configurational entropy and charge-transport properties and to evaluate their potential as solid electrolytes for solid-state batteries.

The first part of this thesis mainly focuses on altering configurational entropy via composition of lithium argyrodites by multiple cation and anion substitutions, with the general formula $Li_{6+x}[M_{1a}M_{2b}M_{3c}M_{4d}]S_5I$ (M = P, Si, Ge, and Sb) as well as $Li_{5.5}PS_{4.5}Cl_xBr_{1.5-x}$. Both strategies enabled ionic conductivities of more than 10 mS cm^{-1} at room temperature, owing to increased configurational entropy, *i.e.*, occupational disorder. Then, the second part of this work presents a detailed electrochemical performance evaluation of high-entropy lithium argyrodites and the commercially available lithium argyrodite Li_6PS_5Cl. The outcome shows that solely multi-anion substituted lithium argyrodites possess an enhanced electrochemical stability as compared to the reference solid electrolyte Li_6PS_5Cl and thus lead to an increased solid-state battery performance, especially at high current rates. In contrast, multi-cation substituted lithium argyrodite solid electrolytes suffer from poor oxidative stability and thus might only be applicable as separator layer in all-solid-state batteries. Altogether, our results indicate the possibility of improving ionic conductivity and electrochemical stability in ceramic ion conductors via entropy engineering, *i.e.*, inducing complex substitution, overcoming compositional limitations for the design of advanced electrolytes and opening up new avenues in the field.

Zusammenfassung

Festkörperbatterien (SSBs) sind eine potenziell sichere Energiespeichertechnologie der nächsten Generation. Die kommerzielle Realisierbarkeit von SSBs hängt von der Entwicklung fester Elektrolyte mit hoher Ionenleitfähigkeit, hoher (elektro-)chemischer Stabilität und guter Verarbeitbarkeit ab. Ein neuer, innovativer Ansatz zur Modifizierung von Materialien, der möglicherweise zu verbesserten Eigenschaften führt, ist das „Hochentropie-Konzept“, das durch $\Delta S_{conf} > 1{,}5R$ (wobei ΔS_{conf} und R die Konfigurationsentropie und die allgemeine Gaskonstante darstellen) gekennzeichnet ist. Der positive Einfluss einer hohen Konfigurationsentropie auf die Li-Ionen-Diffusion bleibt jedoch aufgrund des Fehlens systematischer Studien bisher weitgehend unklar. Daher zielt diese Doktorarbeit darauf ab, die Anwendung des Hochentropie-Konzepts auf feste Elektrolyte zu erweitern, insbesondere auf Lithium-Argyrodite, um sie von Lithium-Ionen-Leitern zu Superionenleitern (~10 mS cm^{-1} bei Raumtemperatur) umzuwandeln. Das Ziel war es, den Zusammenhang zwischen Konfigurationsentropie und Ladungstransporteigenschaften zu verstehen und ihr Potenzial als feste Elektrolyte für Festkörperbatterien zu bewerten.

Der erste Teil dieser Arbeit konzentriert sich hauptsächlich auf die Veränderung der Konfigurationsentropie mit der Zusammensetzung von Lithium-Argyroditen durch multiple Kationen- und Anionen-Substitutionen mit der allgemeinen Formel $Li_{6+x}[M_{1a}M_{2b}M_{3c}M_{4d}]S_5I$ (M = P, Si, Ge, and Sb) sowie $Li_{5.5}PS_{4.5}Cl_xBr_{1.5-x}$. Beide Strategien ermöglichen es, die Ionenleitfähigkeit bei Raumtemperatur auf mehr als 10 mS cm^{-1} zu steigern, was auf die Erhöhung des Li^+-Ionen-Gehaltes und/oder Defektdichte zurückzuführen ist. Der zweite Teil dieser Arbeit präsentiert dann eine detaillierte elektrochemische Bewertung von hochentropischen Lithium-Argyroditen mit einer Ionenleitfähigkeit von ~10 mS cm^{-1} und dem kommerziell-erhältlichen Argyrodit Li_6PS_5Cl. Die Ergebnisse zeigen, dass die alleinige Verwendung dieser multisubstituierten Lithium-Argyrodite als Separator-Schicht die Zyklenstabilität verbessern kann. Insbesondere das multianionisch substituierte Lithium-Argyrodit kann sowohl als Katholyt als auch als Separator-Schicht verwendet werden, da es im Vergleich zu multikationisch substituierten Lithium-Argyroditen und Li_6PS_5Cl eine bessere elektrochemische Stabilität mit dem Kathodenmaterial und eine bessere chemische Stabilität mit Li-Metall aufweist. Insgesamt weisen diese Ergebnisse auf die Möglichkeit hin, die Ionenleitfähigkeit in keramischen Ionenleitern durch Entropie-Engineering zu verbessern, kompositorische Einschränkungen für das Design fortschrittlicher Elektrolyte zu überwinden und neue Wege in diesem Bereich zu eröffnen.

List of Abbreviations

SSB	Solid-state battery
CAM	Cathode active material
NPD	Neutron power diffraction
PFG-NMR	Pulsed field gradient-nuclear magnetic resonance
MAS-NMR	Magic angle spinning-nuclear magnetic resonance
EIS	Electrochemical impedance spectroscopy
LE	Liquid electrolyte
SE	Solid electrolyte
HEM	High-entropy material
DOS	Density of states
DFT	Density functional theory
HRTEM	High-resolution transmission electron microscopy
ICP-OES	Inductively coupled plasma-optical emission spectroscopy
LIB	Lithium-ion battery
LGPS	Lithium germanium phosphorus sulfide, $Li_{10}GeP_2S_{12}$
LPSCl	Lithium phosphorus sulfur chloride, Li_6PS_5Cl
LPSBr	Lithium phosphorus sulfur bromide, Li_6PS_5Br
LPSI	Lithium phosphorus sulfur iodine, Li_6PS_5I
NASICON	Sodium (Na) superionic conductor
LLTO	$Li_{3-x}La_{2/3-x}TiO_3$
LLZO	$Li_7La_3Zr_2O_{12}$
LTO	Lithium titanate, $Li_4Ti_5O_{12}$
LSiPSBrO	$Li_{9.54}[Si_{0.6}Ge_{0.4}]_{1.74}P_{1.44}S_{11.1}Br_{0.3}O_{0.6}$
NCM	Lithium nickel cobalt manganese oxide, ($LiNi_{1-x-y}Co_xMn_yO_2$)
NCM851005	$LiNi_{0.85}Co_{0.10}Mn_{0.05}O_2$
SEI	Solid electrolyte interphase
STEM	Scanning transmission electron microscopy
XPS	X-ray photoelectron spectroscopy

XAS	X-ray absorption spectroscopy
XRD	X-ray diffraction
PDF analysis	Pair-distribution function analysis
ESW	Electrochemical stability window
CV	Cyclic voltammetry
GCPL	Galvanostatic cycling with potential limitation
CEI	Cathode electrolyte interphase
HEO	High-entropy oxides
ccp	cubic close packed
fcc	face-centered cubic
LPSX	Li_6PS_5X, with X = Cl, Br, I

Table of Contents

1. Introduction

Due to the high demand for electrochemical energy storage devices with increased energy and power density, SSBs have recently emerged as a possible technology to fulfill such demands.[1–3] Moreover, replacing LEs with SEs has the potential to prevent dendrite formation and mitigate the safety risks of catastrophic fires associated with flammable organic liquid electrolyte-based battery systems.[4] However, challenges related to the use of solid electrolytes persist in several aspects, including ionic conductivity, electrochemical stability, and chemomechanical stability with cathode and anode active materials.[2,5,6] In the recent decade, the ionic conductivity of SEs has been pushed to 20 mS cm^{-1}, reaching values comparable or even exceeding that of liquid electrolytes.[7] Prominent examples include $Li_{10}GeP_2S_{12}$ (LGPS), with an ionic conductivity of ~10 mS cm^{-1} at room temperature, as well as lithium argyrodites.[8–12] However, in the development of superionic conductors, there is still a long way to go. Firstly, is an ionic conductivity of 10 mS cm^{-1} (at room temperature) already high enough to compete with LEs? When considering the microstructure of electrodes, LEs are able to penetrate all open pore volume, and thus enable a much lower tortuosity for Li-ions compared to SEs.[2,6,13] Higher tortuosity results in lower effective ionic conductivity of electrodes in SSBs, compared to LE-based cells. Moreover, for future applications related to high energy density and high-power cells, thick electrodes (over 100 µm) and fast charging are essential. To achieve this, it has been shown that an ionic conductivity of ≥10 mS cm^{-1} is required for SEs.[5,14] Therefore, achieving an effective ionic conductivity of 8-10 mS cm^{-1} requires exploration of superionic conductors capable of surpassing 10 mS cm^{-1}.

Recently, HEMs derived from HEAs with a configurational entropy $\Delta S_{conf} > 1.5R$ (where R refers to the ideal gas constant) have emerged as promising candidates for enhancing material properties.[15,16] This is attributed to the ability to tailor properties via the selection of elemental constituents and their stoichiometry. The high-entropy concept has already been applied to materials in the fields of energy and electronic applications, such as for hydrogen evolution and storage, carbon dioxide conversion, oxygen catalysis, rechargeable batteries and supercapacitors.[17] With more and more improved material properties achieved by applying the high-entropy concept, we attempt to utilize this concept in the field of lithium ion conductors with the goal to increase ionic conductivity of the commercialized SE Li_6PS_5Cl to more than ~10 mS cm^{-1} and evaluating electrochemical properties.

The focus of this doctoral project was the exploration of high-entropy lithium argyrodites through solid-state reactions. The results of studies on the structural properties of the synthesized materials and the Li-ion diffusion characteristics are reported in four publications within this thesis (Publications I, II, III and IV in the results section).[18–20] In particular, Publication III in the results section presents a systematic study on explaining how configurational entropy affects Li-ion diffusion.[21] The final study (Publication V) focused on benchmarking various compositionally complex lithium argyrodite SEs in SSBs.[22] Therein, we have shown that complex anion-substituted high-entropy argyrodite SEs not only outperform in terms of ionic conductivity but also exhibit superior electrochemical stability.

Additionally, the appendix in chapter 6.1.1. (Publication VI) discusses the influence of surface impurities on charge transport in high-entropy materials.[23] Since the topic of this initial investigation deviates somewhat from the main theme of this doctoral thesis, it has not been included in the main text.

2. Fundamentals

This chapter begins with an introduction into ion diffusion in inorganic lithium conductors. It includes a description of the classical "hopping" mechanism, with a focus on the factors that influence lithium diffusion and the requirements for ion conductors to be used as SEs. The chapter then elucidates the concept of high-entropy materials, including the discussion of the effect of entropy on material properties and perspectives on why configurational entropy is able to enhance ion diffusion. Recent advancements in high-entropy lithium conductors are also reviewed. The final section provides a brief introduction to lithium argyrodites, discussing their structural and charge-transport properties, and reviewing their electrochemical performance as SEs in SSBs.

2.1. Inorganic lithium-ion conductor

2.1.1. Ion diffusion mechanism

Inorganic crystals having mobile ions (such as Li^+ or O^{2-}, etc.) whose ionic conductivities lie between ~10^{-7} and 10^{-1} mS cm^{-1} are usually defined as ion conductors, while those achieving values higher than 1 mS cm^{-1} are classified as superionic conductors.[24]

Fundamentally, at finite temperatures, atoms within a crystal usually oscillate around their equilibrium positions. However, these oscillations typically lack the intensity required to overcome the energy barrier for hopping to an adjacent empty site. For ion conductors, a substantial displacement occurs, resulting in a successful diffusion event of the atoms. Typically, an atom hops to an adjacent location (neighboring vacancy or an interstitial site), when overcoming activation energy barriers based on the following defect-mediated ion transport model (illustrated in **Figure 1**) based in defect formation as suggested by Frenkel as well as by Schottky and Wagner.[25–27]

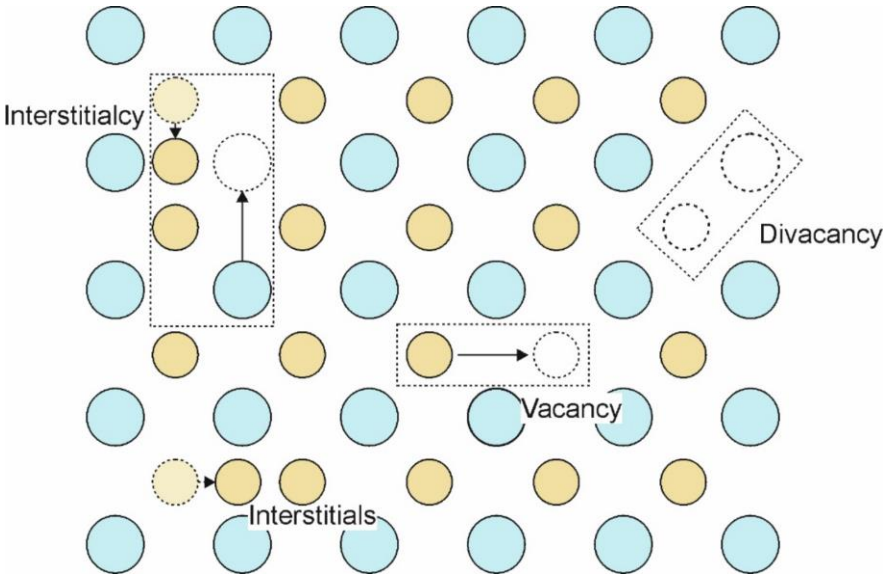

Figure 1: A schematic depiction of the different mechanisms of ion migration, including vacancy (middle), direct interstitial (bottom left), interstitialcy (top left). Framework atoms are represented by blue and yellow circles represent anions (large) and cations (small), respectively. The large and small unfilled circles indicate existing vacancies for anions and

cations. The light blue and light-yellow circles represent the vacancies generated by mobile anions and cations, respectively. Replotted from M. Sotoudeh *et al.*[28]

Typically, the activation energy barriers are considerably greater than the thermal energy $k_{\mathrm{B}}T$. The frequencies of the ion hopping are typically smaller compared to the frequencies of the lattice vibrations, characterized by the Debye frequency (10^{12} to 10^{13} s^{-1}).[29] Specifically, four types of charge-carrier transport mechanisms[30] are summarized based on the defect-mediated ion transport model:

1) Transport by uncorrelated jump processes, *e.g.* in Y^{3+}-doped CeO_2.
2) Highly correlated mechanisms with the rapid transport of ions (multiple ions moving together in a coordinated manner), *e.g.* in Li_3N and $RbBiF_4$.
3) Liquid-like diffusion mechanisms in a highly disordered mobile sublattice, *e.g.* in Ag_2S.
4) Intermediate mechanisms combining both hopping and liquid-like characteristics, *e.g.* in α-AgI.

The uncorrelated jump process describes ion transport in solids derived from liquids under the limitation of dilute mobile ions with uncorrelated and independent hopping. The individual ion hops with no correlation can be described by a random-walk model. The random diffusion coefficient D_{r} can be expressed by the Einstein–Smoluchowski relation:

$$D_{\mathrm{r}} = \frac{\langle R_{\mathrm{m}}^2 \rangle}{b t_{\mathrm{m}}} = \frac{a^2 \omega}{b} \tag{1}$$

where R_{m} is the total displacement of a moving ion in m steps, t_{m} is the duration to complete m steps of ion displacement, a is the hopping distance between two neighboring sites or free path, ω is the number of jumps per unit time to an adjacent site, and b is a geometry factor of 2, 4, or 6 for one-, two-, or three-dimensional diffusion, respectively.[31,32] ω can be described in detail upon the canonical ensemble of statistical mechanics (constant pressure) according to Vineyard's method:

$$G^{migr} = H^{migr} - TS^{migr} \tag{2}$$

$$\omega = \nu_0 \exp\left(-\frac{G^{\mathrm{migr}}}{k_{\mathrm{B}}T}\right) = \nu_0 \exp\left(\frac{S^{\mathrm{migr}}}{k_{\mathrm{B}}}\right) \exp\left(-\frac{H^{\mathrm{migr}}}{k_{\mathrm{B}}T}\right) \tag{3}$$

with ν_0 representing the attempt frequency, commonly referred to as the Debye frequency, which signifies the oscillation frequency occurring near the equilibrium position along the reaction pathway, G^{migr} the Gibbs free energy of atom migration, k_{B} the Boltzmann constant, T the absolute temperature, S^{migr} the entropy of migration, and H^{migr} the activation enthalpy associated with migration.[33]

The ionic conductivity σ is expressed as the relation between mobility μ and charge-carrier density or the ion concentration c, and the charge of the mobile ions q (in the case of lithium, q = e_0):

$$\sigma = cq\mu \tag{4}$$

The charge-carrier density c is related to the defect formation energy H^{form}:

$$c = c_0 \exp\left(-\frac{H^{\mathrm{form}} - TS^{\mathrm{form}}}{k_{\mathrm{B}}T}\right) \quad (5)$$

where c_0 is the maximum concentration of the mobile species. In most cases, the enthalpy change dominates, and entropy term is often neglected. Recently, more and more investigations are focusing on the entropy contribution, which will be discussed in the perspectives section below.

The mobility μ can be correlated to the diffusion coefficient D_σ (macroscopic long-range diffusion) by the Nernst-Einstein equation:

$$\mu k_{\mathrm{B}} T = q D_\sigma \quad (6)$$

with k_{B} being the Boltzmann constant and T the absolute temperature.[26,31]

The relationship between the long-range diffusion coefficient D_σ and random diffusion coefficient D_{r} is described as following through tracer diffusion coefficient D^*:

$$f = \frac{D^*}{D_{\mathrm{r}}} \quad (7)$$

$$H_{\mathrm{R}} = \frac{D^*}{D_\sigma} \quad (8)$$

$$D_\sigma = \frac{f}{H_{\mathrm{R}}} D_{\mathrm{r}} = f_{\mathrm{I}} D_{\mathrm{r}} \quad (9)$$

where f is the correlation factor corresponding to single-ion correlations, H_{R} is the Haven ratio describing the strength of multi-ion correlations, and f_{I} denotes the collective correlation factor measuring the strength of distinct-ion correlation effects.[34]

Combining equations (1-9), the correlation between ion conductivity and activation energy can be described as below, when assuming the 3D isotropic motion and ignoring the contribution of defect formation entropy:

$$\sigma T = \frac{1}{6}\frac{f}{H_{\mathrm{R}}}\frac{c_0 q^2}{k_{\mathrm{B}}}\nu_0 \exp\left(\frac{S^{\mathrm{migr}}}{k_{\mathrm{B}}}\right)\exp\left(-\frac{H^{\mathrm{migr}}}{k_{\mathrm{B}}T}\right)\exp\left(-\frac{H^{\mathrm{form}}}{k_{\mathrm{B}}T}\right) \quad (10)$$

Specifically, equation (10) could be simplified with the definition of activation energy E_{A} to:

$$E_{\mathrm{A}} = H^{\mathrm{migr}} + H^{\mathrm{form}} \quad (11)$$

Then, the ionic conductivity can be described as:

$$\sigma = \frac{\sigma_0}{T}\exp\left(-\frac{E_{\mathrm{A}}}{k_{\mathrm{B}}T}\right) \quad (12)$$

$$\sigma_0 = \frac{1}{6}\frac{f}{H_{\mathrm{R}}}\frac{c_0 q^2}{k_{\mathrm{B}}} a^2 \nu_0 \exp\left(\frac{S^{\mathrm{migr}}}{k_{\mathrm{B}}}\right) \quad (13)$$

where σ_0 is the so-called pre-exponential factor when ignoring S^{form}.

Typically, for ion conductors, a and ν_0 strongly depend on the crystal structure. Moreover, a low activation energy and a high concentration of charge carriers should improve ionic conductivity according to equations (12, 13).

In addition to the aforementioned uncorrelated jump model, conceived from the spirit of the Debye-Hückel-Onsager-Falkenhagen theory, a jump relaxation model incorporating interactions between mobile ions (such as the Coulomb-cage effect) and between mobile and immobile ions (such as periodic lattice potential) will be elucidated below.[35]

In well-crystallized ion conductors, mobile ions experience repulsion from neighboring ions during migration, tending to settle in the local potential minima within the Coulomb cage formed by these ions, also referred to as ion cloud. The interplay between these local Coulomb-cage-effect minima and the long-range periodic lattice potential dictates the overall potential for ion diffusion. When one ion jumps from lattice site A to B, the local potential minimum for each ion is perturbed due to the Coulomb-cage effect, while the periodic lattice potential remains relatively unchanged. This deviation from equilibrium necessitates a structural relaxation process to restore equilibrium. Two competing relaxation processes are conceivable: 1) many-particle route, where the ion's forward movement establishes a new local Coulomb-cage-effect minimum, resulting in a net ionic current; and 2) single-particle route, where the ion may return from B to A, nullifying the ionic current. **Figure 2** illustrates this comparison. Moving forward the mobile ion encounters an energy barrier $\delta_{\mathrm{B}\rightarrow\mathrm{C}}(t)$, whereas moving backward, the barrier $\delta_{\mathrm{B}\rightarrow\mathrm{A}}(t)$ is typically much smaller due to the overall energy landscape. Consequently, correlated ion transport processes often exhibit a preference to backward hopping, explaining the correlation factors $f < 1$ and elucidating the challenge of establishing long-range ion migration. The initial jump relaxation model has been afterwards optimized by assuming that the relaxation rates of both single- and many-particle routes are proportionally related, decaying exponentially over time.[36] This refined model has been proven high accuracy in elucidating ion-transport mechanisms in glassy and disordered crystalline materials.[37,38] However, the Haven ratio, which is currently assumed to be unity in these models, requires further development.

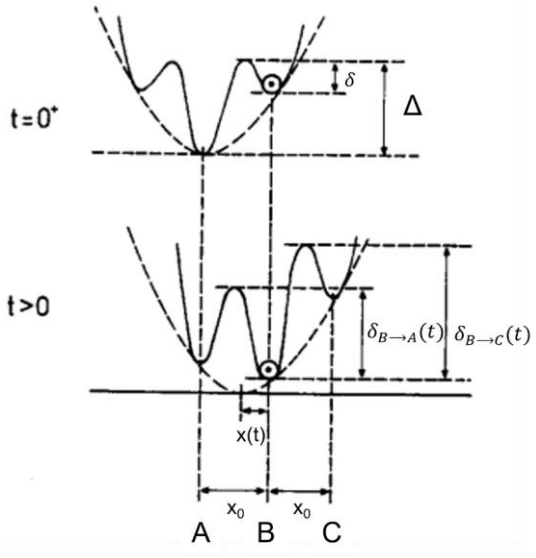

Figure 2: Schematic representation of the jump relaxation model. The evolution of the potential over time after a hop. Adapted from K. Funke *et al.*[39]

In fast ion conductors, the ion diffusion mechanism often involves the simultaneous migration of multiple ions, contrasting the single ion hopping mechanism discussed in the uncorrelated jump process and jump relaxation model. This concerted mechanism, also known as interstitialcy (the combination with interstitial and vacancy), considers the interaction among multiple mobile ions, where they migrate at the same time.[40] Like the jump relaxation model, electrostatic repulsion between migrating and neighboring mobile ions is taken into account. However, unlike the jump relaxation model, where Coulomb interaction raises the energy barrier and impedes long-term diffusion, the concerted migration barrier is lowered by Coulomb interaction among mobile ions. Mobile ions occupying high-energy sites can migrate downhill towards low-energy occupied sites with a low energy barrier, and the corresponding Coulomb interactions between two mobile ions will help reduce the activation energy barrier for a mobile ion occupying a low-energy site to move uphill towards another unoccupied high-energy site (see **Figure 3**).

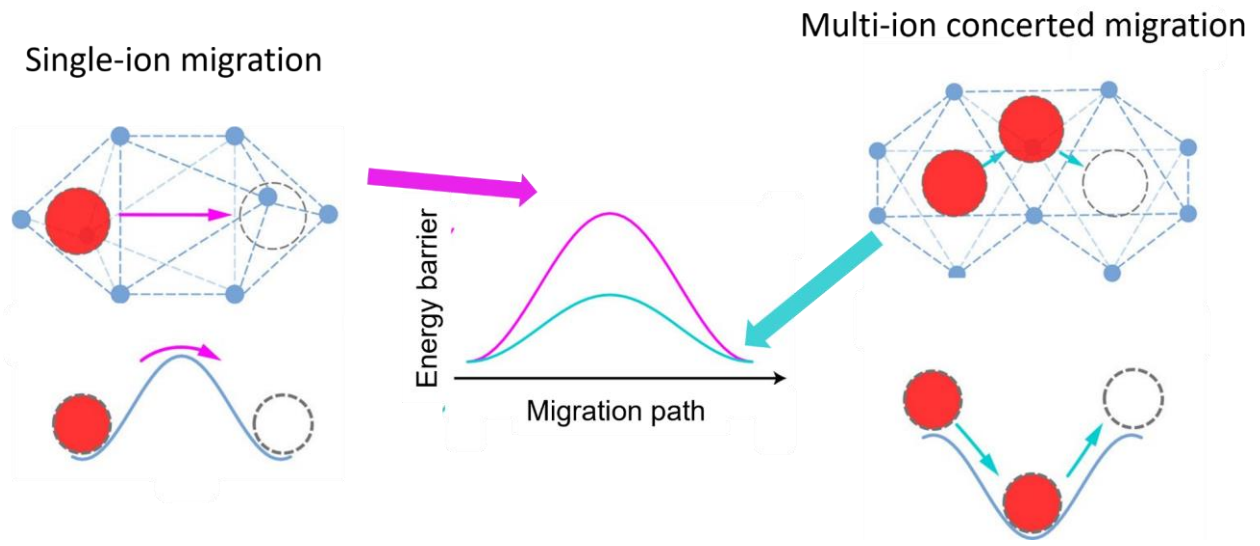

Figure 3: Schematic depiction of single-ion migration (left) and the concerted migration of multiple ions (right). Adapted from X. He *et al.*[40]

The mechanisms mentioned above are based on a general assumption: The anion framework is relatively rigid and translationally immobile during ion migration. The duration of the mobile ion's presence at the local potential minimum between two successive hops is significantly shorter than the relaxation time of the motions of the anion lattice. Consequently, the motion of both the anionic lattice and mobile ions is typically considered to be uncoupled. Recent evidence suggests that the migration of mobile ions is strongly associated with the reorientation of the rotated polyanionic sublattice, described as the paddle-wheel effect.[41,42] Typically, the polyanions $[AB_y]^{n-}$ are formed by covalent A-B bonds, such as $[SO_4]^{2-}$ and $[PO_4]^{3-}$. Specifically, in some oxide ion conductors, anion migration (O^{2-} ions) can also be linked with the rotation of polyanions between neighboring tetrahedral environments, leading to the exchange of oxygen atoms.[41,43] Similar behavior has been observed in Li and Na-ion conductors.[44–46] Although ion migration and anion reorientation are generally observed to occur simultaneously, questions still persist regarding the causal

relationship between them.[47] Also, it still remains uncertain how to distinguish the anion reorientation with the percolation mechanism.[48–50]

Typically, the polarizability of anions also correlates with the ion mobility, especially affecting the activation energy. Large polarizable ions tend to be 'softer', allowing the mobile species to 'squeeze' through their electronic cloud more easily with lower activation energy. The Clausius-Mossotti relation relates the polarizability α to the high-frequency dielectric constant ε_∞ according to:

$$\frac{\varepsilon_\infty - 1}{\varepsilon_\infty + 2} = \frac{4\pi\alpha}{3V_\alpha} \tag{14}$$

where V_α is the unit-cell volume.[51] Such correlation has been found by Wakamura between the activation energy and the high-frequency dielectric constant ε_∞, shown in **Figure 4.**[52] The activation energy E_A decreases as the high-frequency dielectric constant reduces.

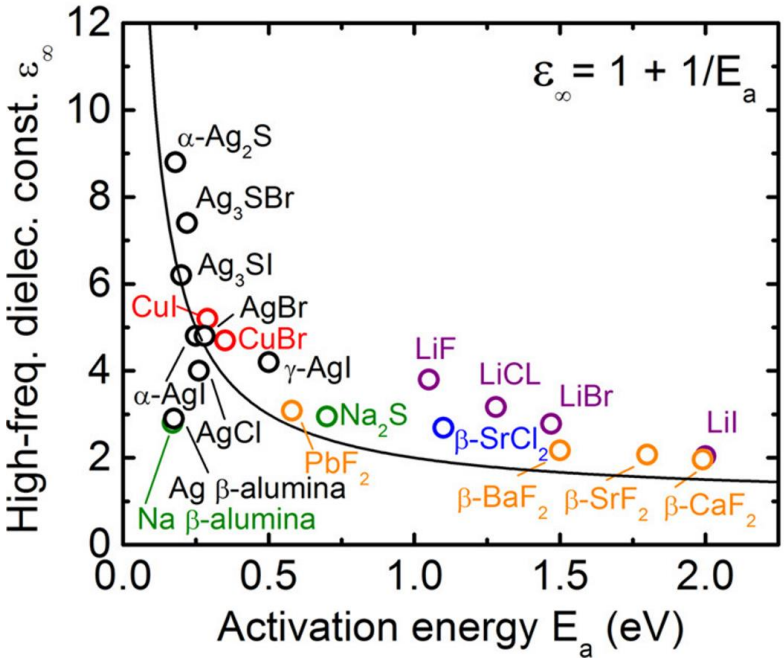

Figure 4: Correlation between activation energy and high-frequency dielectric constant ε_∞. Adapted from J. Bachman *et al.*[53]

In recent years, there has been an increasing number of studies investigating the influence of lattice dynamics on charge carrier transport associated with phonon-ion interactions.[54–57] Phonons, defined as the quantized vibrations of atoms in a solid with harmonic oscillator frequencies and displacement vectors, represent the complex atomic motion and the total kinetic energy of the system. E_A is the thermal excitation energy for ion transport.[57] Considering the thermal atomic vibrations during ion diffusion, E_A should depend on the oscillator frequency and phonon occupation.[56] Focusing on the Li-ion, it has been found that in LISICON-type conductors the lower average vibrational frequency of lithium ions weighted by the phonon DOS derived from DFT calculation is correlated to the lower enthalpy of migration and thus fast ion mobility. It is explained through a flat potential energy

landscape, in which lithium ions can oscillate with larger amplitude. More recently, for argyrodite Li_6PS_5Cl, Ding *et al*. investigated the strong softening of the anharmonic Li-associated low-energy phonons as a function of temperature.[58] The low-energy phonon modes (< 10 meV) are important for facile ion conduction.

Thus, to enhance the ionic conductivity of ion conductors, several insights can be gained from the review of theoretical models for ion diffusion. From a crystallographic perspective, ion migration occurs locally through thermally activated jumps, which must be connected via diffusion pathways to enable long-range diffusion. These pathways should consist of connected channels (via polyhedral connection) with suitable bottleneck sizes, suggesting that well-distributed mobile ions facilitate fast diffusion.[59,60] Specifically, face-sharing polyhedra show broader diffusion pathways, and smaller coordination changes are preferred for superionic conductors. Considering the anionic sublattice, it has been shown that fast ion conductors often exhibit a body-centered cubic anionic substructure, allowing direct Li jumping between neighboring tetrahedral sites, resulting in fast lithium diffusion.[61] According to the defect-mediated theory, another way to increase the ionic conductivity is tailoring the charge-carrier density, namely, balancing concentration of vacancies and interstitials. In addition to the above-mentioned statistic approach, the lattice dynamics referring to vibration, as well as the rotation of the anion sublattice in case of lattices with polyanions or polycations, also plays a significant role in ion diffusion, and higher polarizability anions offer advantages to facilitating fast ion mobility.

It is important to note that the mechanism discussed above primarily addresses bulk transport, while transport occurring along grain boundaries has not been covered. In polycrystalline solids, particularly metals, interdiffusion along grain boundaries, treated as a correlated walk of atoms in a periodic quasi-2D system with multiple jump frequencies, is often faster than in the bulk.[62–64] However, the opposite is observed for inorganic, well-crystallized superionic conductors, where grain boundaries act as bottlenecks that negatively affect ion transport.[65] This ion-blocking effect at grain boundaries has been attributed to grain mismatch, and the underlying mechanism is highly material-dependent.[66–68] On the other hand, grain boundaries (or better summarized as higher-dimensional defects) show positively contribute to ion transport in nanocrystalline or glassy conductors, particularly in materials whose crystalline counterparts exhibit very poor ionic conductivity, such as $LiNbO_3$, Li_2TiO_3, γ-$LiAlO_2$, $LiTaO_3$, and some lithium thiophosphates, where short-range disorder can facilitate ion transport.[69–75] Specifically, in thiophosphates, grain boundaries can also lead to an increased degree of reorientation of PS_4^{3-} polyanions, which could maintain bulk-like coordination even in low-crystallinity regions, thereby enabling more facile diffusion.[67,71,76] In this thesis, we primarily focus on bulk lithium transport. The effect of grain boundaries will be briefly discussed for lithium argyrodites in the sections 2.3.1.

2.1.2. The state of art for solid electrolytes

This section introduces the fundamentals of SSBs, briefly reviewing the major families of SEs and summarizing the key issues faced by these electrolytes in SSB development.

In general, rechargeable LIBs consist of the anode (such as graphite, $LiTi_5O_{12}$, etc.), CAM, such as $LiCoO_2$, spinel-type $LiMn_2O_4$, olivine-type $LiFePO_4$, etc., electrolyte, current collectors, and separator. The anode, cathode, and separator are impregnated by the liquid electrolyte, typically composed of a lithium conductive salt dissolved in organic carbonate-based solvents.[77–79] During the charge and discharge process, Li-ions move between the positive and negative electrodes driven by an electrochemical potential difference. During charge, Li-ions are extracted from the CAM (in this study, the layered transition metal oxide $LiNi_{0.85}Co_{0.10}Mn_{0.05}O_2$ or NCM851005) and migrate through the electrolyte, eventually inserting into the anode material. Meanwhile, an equal number of electrons are released from the cathode to the anode through an external circuit to maintain charge balance. Conversely, during discharge, the process occurs in the opposite direction. The redox reactions for the charging process are described by the following equations (for a specific example):

$$\begin{aligned} &\text{Positive electrode: } LiNi_{0.85}Co_{0.10}Mn_{0.05}O_2 \leftrightarrow Li_{1-x}Ni_{0.85}Co_{0.10}Mn_{0.05}O_2 + xLi^+ + xe^- \\ &\text{Negative eletrode: } Li_4Ti_5O_{12} + xLi^+ + xe^- \leftrightarrow Li_{4+x}Ti_5O_{12} \ (\text{with } x \leq 3) \end{aligned} \quad (15)$$

SSBs, which use SEs in place of LEs and ideally Li metal as anode, can eliminate safety concerns and provide higher energy as well as power densities, as shown in **Figure 5**.[1] Typically, SSBs consist of a thin layer of SE as separator, cathode and anode composites, which are homogeneous mixtures of active material, SE, and electronically conductive additives (e.g. carbon). To further improve the energy density, Li-metal anodes or other high specific capacity materials, such as silicon, are required.[5]

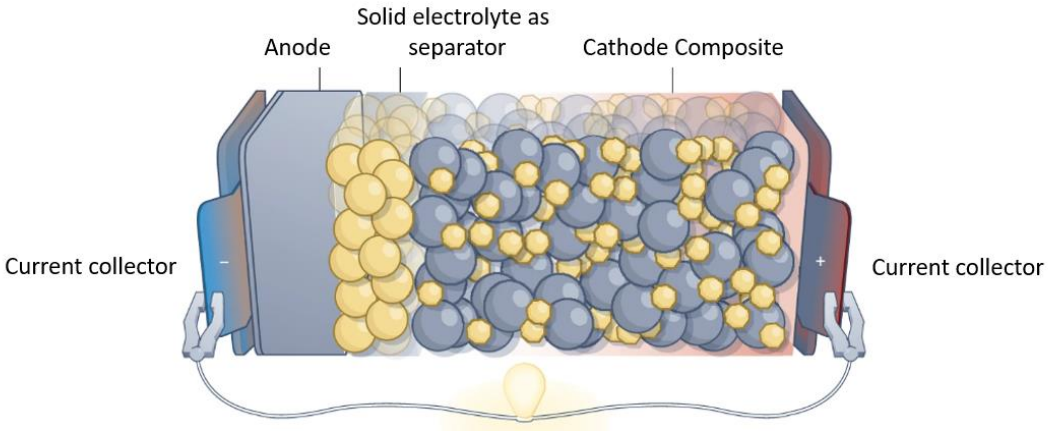

Figure 5: Schematic illustration of the structure of SSBs. Adapted from J. Janek *et al.*[2]

SEs as components in SSBs have been intensively investigated, including a wide variety of materials. A comparison of room-temperature ionic conductivities of different SE families is depicted in **Figure 6**. Among the reported SEs, the sulfide-based ones show superior ionic conductivities. While high ionic conductivity is the key property for SE materials, other factors, such as wide electrochemical stability window, good chemical and electrochemical compatibility with electrode active materials (cathode and anode), high thermal and air/moisture stability, good mechanical properties, simple synthesis, easy integration, environmental friendliness, and low cost, do need to be considered for practical applications

of ion conductors in SSBs (for electric vehicles).[24] Various inorganic SEs have been discovered, including oxide-based SEs, sulfide-based SEs, lithium halides, etc.[80] The properties of these three types of SEs are summarized in **Figure 7** and compared accordingly. In particular, the structural and electrochemical properties of thiophosphate SEs will be discussed in detail in section 2.3.

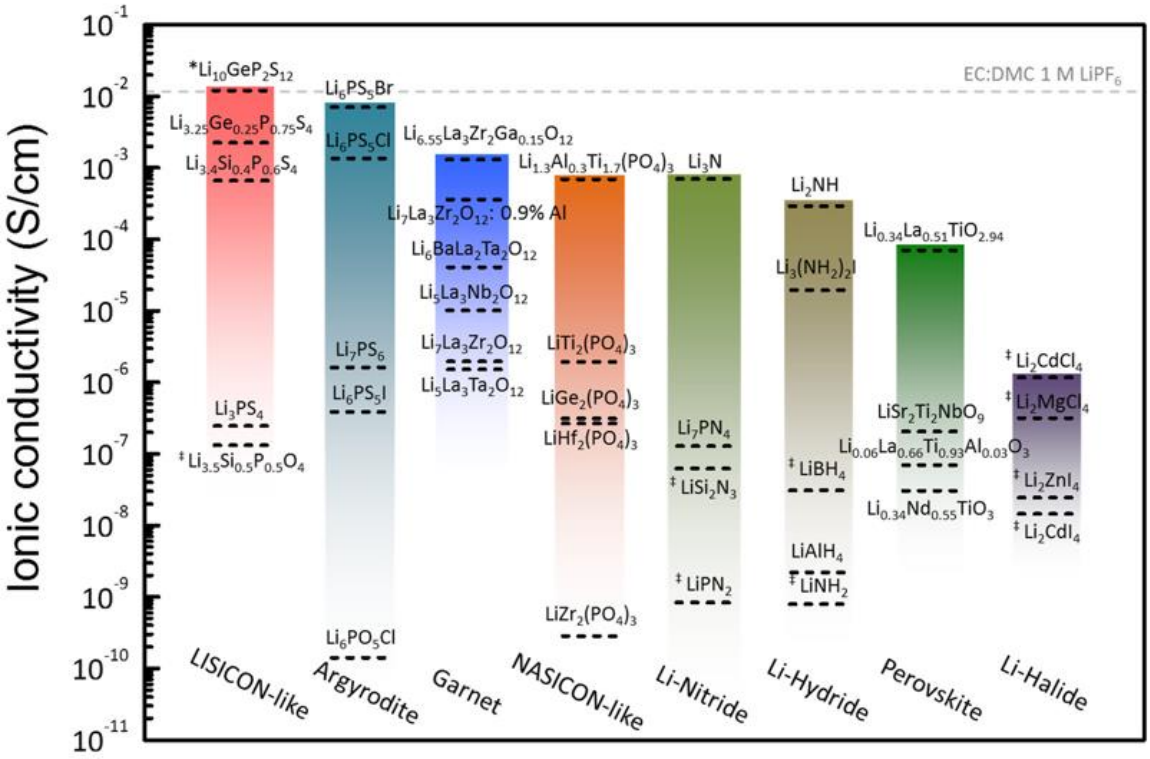

Figure 6: Summary of the reported room-temperature ionic conductivities of different families of SEs. Adapted from J. Bachman *et al.*[53]

Oxide-type lithium SEs often feature robust stability against moisture, high thermal stability, and a wide electrochemical stability window, enabling them to be promising candidates, especially in combination with high-voltage CAMs.[80] However, they face limitations due to their relatively moderate ionic conductivity. The exploration of oxide-type lithium SEs has been developed significantly since the pioneering works on NASICON and LATP in the 1970's and 1990's.[81,82] The notable discoveries are the perovskite-type $Li_{3-x}La_{2/3-x}TiO_3$ (LLTO) in 1993, exhibiting an ionic conductivity ranging from 10^{-2} to 10^{-1} mS cm^{-1} at room temperature, and the garnet-type $Li_7La_3Zr_2O_{12}$ (LLZO) in 2007, with a conductivity of 7×10^{-1} mS cm^{-1} (at 25 °C), later reaching 1 mS cm^{-1} through partial substitution of Zr^{4+} with elements like Al^{3+}, Ga^{3+}, or Ta^{5+} in 2013.[83–85] However, despite the large improvement in ionic conductivities, their high mechanical rigidity is still a challenge for processing and integrating them into SSBs.[86] Therefore sulfide-based SEs would be much more favorable, as they are soft (i.e. low Young's modulus) and can achieve very high ionic conductivities. Starting from the glassy ion conductor Li_2S-P_2S_5-LiI (0.1 mS cm^{-1} at room temperature) in 1981, in 2000, the thio-LiSICON $Li_{4-x}Ge_{1-x}P_xS_4$ ($0 < x < 1$) family has been reported with conductivities of up to 1 mS cm^{-1}.[87,88] In 2011, a new SE, LGPS

was discovered as the first superionic conductor with 12 mS cm^{-1}, which is comparable to that of liquid counterparts (typically around 10 mS cm^{-1}) and has further revitalized the application of SSBs, which previously struggled due to lack of suitable lithium-ion conductors.[8]

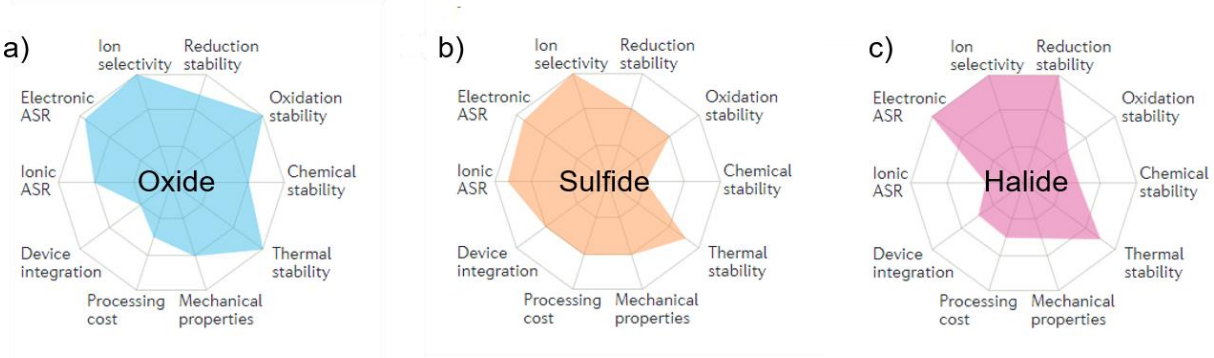

Figure 7: Radar plots of the key performance indicators of oxide-based SEs (a), sulfide-based SEs (b), and lithium halides (c). Adapted from A. Manthiram *et al.*[80]

In 2008, the argyrodite-type SEs (Li_6PS_5X, X = Cl, Br, I) were also developed in parallel and exhibit the highest conductivities so far achieved, exceeding 10 mS cm^{-1}, also offering excellent mechanical ductility.[11,89,90] This allows for straightforward processing and liquid-phase synthesis, facilitating scalability.[5] Moreover, some sulfide SEs can also form a quasi-stable SEI with Li metal and sustain relatively high current density Li stripping/plating. Unfortunately, their (electro)chemical stability window is very narrow (< 2.5 V vs. Li^+/Li), which is not compatible with common high-voltage CAMs, such as $LiCoO_2$ and $LiNi_{1-x-y}Mn_xCo_yO_2$, and thus, protective layers need to be applied to the CAMs as well as anodes to avoid severe (electro)chemical degradation.[80,91] Overall, owing to their high ionic conductivity and quasi-stable SEI formation with Li metal, sulfide SEs remain suitable as the separator layer in SSBs.

Finally, halide-based SEs have recently attracted great attention, as they are oxidatively stable.[92] From the 1930's to 1970's, lithium halides were considered as poor ion conductors (10^{-4}-10^{-3} mS cm^{-1}).[93,94] In 2018, both Li_3YCl_6 and Li_3YBr_6 were discovered by Asano and co-workers, exhibiting excellent room-temperature ionic conductivities of 0.51 and 1.7 mS cm^{-1}, respectively.[95] Since then, the development of new metal-halide SEs, now generally with the formula Li_aMX_b (where M represents a metal cation, such as In, Zr, Y, or Sc, and X a halide), has taken off. For instance, a mixed halide $Li_3YBr_3Cl_3$ and $Li_3GdCl_3Br_3$ exhibited an exceptionally high conductivity of 7.6 and 11 mS cm^{-1}, respectively.[96,97] $Li_2In_{1/3}Sc_{1/3}Cl_4$ revealed an excellent stability with high-voltage CAMs.[98] Notably, they display broader electrochemical stability windows (up to 6.71 V vs. Li^+/Li), better chemical stability toward the CAM, and also high ionic conductivity at room temperature and remarkable deformability.[99,100] However, they still lack in stability toward moisture, anodes, such as Li metal, and suffer from scarce metal constituents.[101] Thus, halide SEs are suited for use at the cathode side rather than as separator layer.

In brief, the discussion above indicates that there is no single SE material capable of simultaneously achieving high ionic conductivity, good chemical and electrochemical compatibility with both cathode and anode materials, mechanical compatibility, air/moisture resistance, and ease of synthesis—all of which are essential for practical applications in SSBs. This observation raises critical questions: Do we have a strategy for designing SEs that meet all these requirements, or should we instead capitalize on the strengths of different SE materials? The former approach leads to the core topic of this thesis—applying the high-entropy concept to lithium argyrodites, investigating the resulting properties and potential applications in SSBs (discussed in section 2.2.).[16] The latter approach, which involves hybrid or sandwich-like cell configuration designs, will be explored in the perspectives section.[102–104]

2.2. High-entropy materials

In this section, the general definition and fundamental thermodynamics of the high-entropy concept will be introduced. Then, this section provides a brief overview of how configurational entropy affects material properties and its applications to energy materials. Ultimately, we will focus on how the high-entropy concept is valuable specifically in the field of SEs.

2.2.1. Configurational entropy and entropy stabilization

The concept of HEMs evolved from the work on HEAs that began in the early 2000's. Initially, HEMs were defined as crystalline, single-phase materials containing more than five elements on a single crystallographic position,[105–107] in which such disorder can be expressed as configurational entropy ΔS_{conf}, with the criterion of being > 1.5*R*.

In statistical physics, the configurational entropy (S_{conf}) of a solid material can be calculated from the Boltzmann's formulation of entropy:

$$S_{\mathrm{conf}} = k_{\mathrm{B}} \ln \Omega \tag{16}$$

where the number of energetically equal microstate Ω refers to the elements occupying the same crystallographic site and k_{B} represents Boltzmann constant and can be expressed as:

$$\Omega = \frac{N!}{\prod_{\mathrm{i}} n_{\mathrm{i}}!} \tag{17}$$

with n_{i} representing the particle number of type i and N the total number $N = \sum_i n_i$. Therefore, the number of microstates Ω here describes the possible distribution of a certain number of atoms from different elements over all sites that can be occupied. Combining equations (16) and (17) and then applying the Stirling's approximation, the configurational entropy representing the statistic ideal mixing in an arbitrary crystal can be calculated as follows:

$$S_{\mathrm{conf}} = k_{\mathrm{B}} \ln \left[\frac{N!}{\prod_{\mathrm{i}} n_{\mathrm{i}}}\right] \approx -R \sum_i x_{\mathrm{i}} \ln x_{\mathrm{i}} \tag{18}$$

where R is the ideal gas constant and x_{i} is the molar fraction of the i-th component. For the individual components of a compound $S_{\mathrm{conf}} = 0$, then ΔS_{conf} is described as for the crystalline compound:[108]

$$\Delta S_{\mathrm{conf}} = -R \sum_{\mathrm{i}} x_{\mathrm{i}} \ln x_{\mathrm{i}} - 0 = -R \sum_{\mathrm{i}} x_{\mathrm{i}} \ln x_{\mathrm{i}} \tag{19}$$

Applied to general HEMs, equation (19) can be specified using the following equation:

$$\Delta S_{\mathrm{conf}} = -R \left[\left(\sum_{\mathrm{i}=1}^{\mathrm{n}} x_{\mathrm{i}} \ln x_{\mathrm{i}} \right)_{\mathrm{cation-site}} + \left(\sum_{\mathrm{j}=1}^{\mathrm{m}} x_{\mathrm{j}} \ln x_{\mathrm{j}} \right)_{\mathrm{anion-site}} \right] \tag{20}$$

where x_i and x_j represent the molar fractions in the cation and anion sites, respectively.

Generally, a material with configurational entropy $\Delta S_{\mathrm{conf}} \geq 1.5R$ ($1.5R$ is defined based on empirical observations from HEAs) is considered as being a HEM.[16] However, the above-mentioned definition does not automatically means entropy stabilization. Entropy stabilization occurs (above a certain temperature) when both the formation enthalpy ΔH_{f} and the formation entropy ΔS_{f} are positive, and when temperature and entropy are large enough to make the Gibbs free energy ΔG_{f} negative, described by the following equation:

$$\Delta G_{\mathrm{f}} = \Delta H_{\mathrm{f}} - T\Delta S_{\mathrm{f}} \qquad (21)$$

Therefore, $T\Delta S_{\mathrm{f}}$ becomes crucial to compensate the enthalpy penalty, making ΔG_{f} negative, thereby governing the phase stability of metastable materials.[109,110]

The term 'entropy stabilization' was first raised in 1968 by Navrotsky and Kleppa when investigating the formation of spinels and pseudobrookite in drop solution calorimetry.[111] For both cases, the configurational entropy of disordered cation distributions overcomes the positive enthalpy of formation. Here, interestingly, the $\Delta S_{\mathrm{conf}} \geq 1.5R$ is not the essential for phase stabilization while lattice vibrations, electronic and magnetic orderings may also contribute significantly.[109,110,112]

It is important to note that the initial state may represent a pre-existing single-phase solid solution, which could consist of several components. However, the stability of the solid solution primarily depends on the type of components and their interactions, rather than on the number of constituents. The relationship between HEAs (in particular, high-entropy oxides) defined through ΔS_{conf} and entropy-stabilized oxides is illustrated in **Figure 8**.[113] The former refers to any systems with $\Delta S_{\mathrm{conf}} > 1.5R$, which is not necessarily entropy stabilized; the later specifically refers to systems stabilized through entropy but are not necessarily stabilized by configurational entropy.

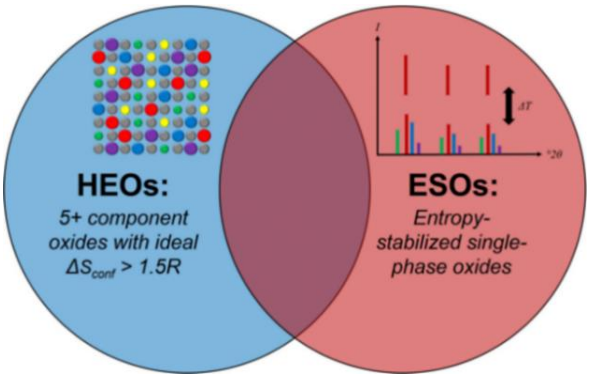

Figure 8: The differences between general high-entropy oxides defined through ΔS_{conf} and entropy-stabilized oxides. Adapted from R. J. Spurling *et al.*[113]

In this thesis, we use the configurational entropy to define the high-entropy lithium argyrodites, and the configurational entropy induced entropy stabilization will be discussed in the perspectives section.

2.2.2. Configurational entropy effect

Configurational entropy effects arising from an increased $\Delta S_{conf,}$ including so-called “cocktail effects”, stabilizing metastable crystal structures and (local) lattice distortions, will be briefly discussed in the following sections.

Derived from nonideal mixing, the “cocktail effect” refers to the superior properties of multicomponent systems compared to the solely individual components, owing to complex interactions induced by compositional complexity. Theoretically, it is attributed to the change of the excess partial free energy $\Delta G_{\mathrm{i,excess}}$, which represents the change of interactions when tailoring the $\Delta S_{conf.}$[114] Therefore, material properties could be engineered by compositional or stoichiometrically changes.

As described in 2.2.1., the entropy stabilization occurs when the ΔH_{f} is positive, which typically indicates metastability. Nevertheless, $T\Delta S_{\mathrm{f}}$ can compensate the enthalpy contribution, enabling the formation of a thermodynamically stable single-phase material through entropy-driven mechanisms. Specifically, for HEMs, ΔS_{conf} is considered to be the major contributor to ΔS_{f}. However, it is important to note that a high ΔS_{conf} does not always guarantee the formation of single-phase HEMs. In reality the ΔH_{f}, T, and most likely kinetics also play important roles in determining the phase stability of HEMs.[114] More interestingly, ΔS_{conf} also can strongly affect the non-configurational contribution of entropy, such as electronic entropy ΔS_{ele}, thereby achieving favorable phase stability. Electronic entropy ΔS_{ele} has always been ignored in individual components due to high delocalization and a very small magnitude of ~1 J/mol at 1000 K (even several orders of magnitudes smaller than ΔS_{vib}). Nevertheless, the excess of ΔS_{ele} is a significant factor in driving the metal-to-insulator transition in high-entropy materials (HEMs) and may contribute to stabilizing the conductive phase.[109]

Lattice distortions caused by large variations in ionic size, valence state, and electronegativity are one of the key characteristics of HEMs. In general, these distortions, particularly at the local level, represent deviations of atom position from the ideal structure and are proportional to the differences in ionic radii, with higher discrepancies yielding larger distortions. The distortion of the lattice directly affects the lattice energy $\Delta U_{\mathrm{lattice}}$ and lattice enthalpy $\Delta H_{\mathrm{lattice}}$, described by the Born-Landé equation. These effects also reduce local symmetry and enhance lattice dynamics, such as increased vibrations and rotations, which in turn influence many properties of HEMs.[115] For example, the large lattice distortions induced by compositional complexity can intensify lattice vibrations, leading to a broader phonon spectrum and an increased ΔS_{vib}. This can result in ultra-low thermal conductivity or superfluid ion diffusion behavior. [54,57,112]

These effects are often coexisting in HEMs and may therefore lead to unprecedented material properties, promising for application in hydrogen evolution and storage, carbon dioxide conversion, oxygen catalysis, rechargeable batteries, and supercapacitors, among others (see **Figure 9**).[16,17]

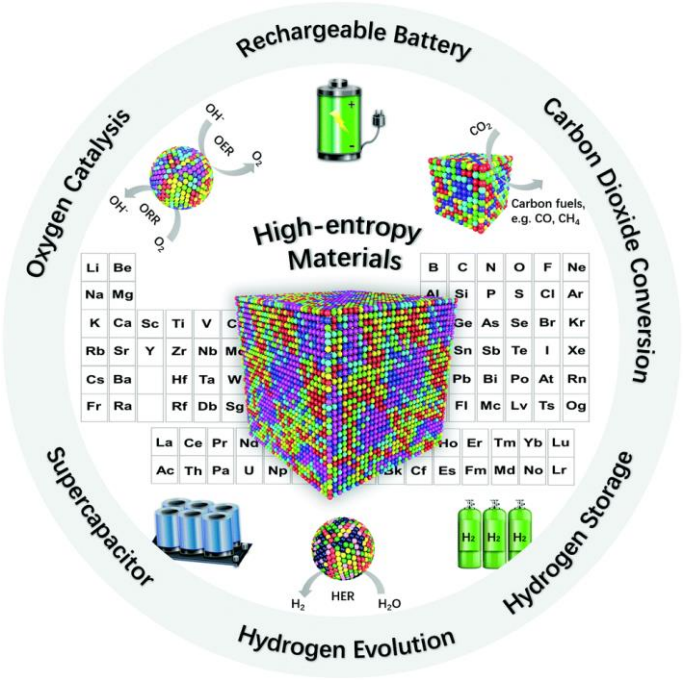

Figure 9: Schematic of high-entropy materials for applications in energy storage and conversion. Adapted from Y. Ma *et al.*[17]

In particular, in the field of rechargeable batteries, rock-salt type high-entropy oxides (HEOs) are the most widely explored class of HEMs and can potentially be utilized as cathode, anode, and electrolyte.[116] In particular, in 2016, Bérardan *et al*. reported HEOs with a rock-salt structure, namely $[Co_{0.2}Mg_{0.2}Cu_{0.2}Ni_{0.2}Zn_{0.2}]_{1-x-y}Ga_xA_yO$ (A = Li, Na, K).[117] These materials exhibit high Li-ion (>1 mS cm^{-1}) and Na-ion conductivity (5×10^{-3} mS cm^{-1}) at room temperature, which has been rationalized by the presence of a large number of oxygen vacancies (charge defaults), providing more percolating channels for Li/Na-ions and therefore an increased ionic conductivity. Additionally, an increased electronic conductivity has been observed, and conflicting reports about charge transport in these materials have been published, suggesting the limitation of using these materials as SEs. However, it is still believed that increasing the configurational entropy, *i.e.* compositional complexity, is able to enhance ionic conductivity. More details will be provided in the following sections.

2.2.3. Benefits of applying the high-entropy concept to solid electrolytes

According to the ion-diffusion mechanism in inorganic conductors (discussed in section 2.1.), to enhance ionic conductivity, a proper crystal structure or substructure should be chosen to enable 3D lithium diffusion pathways with low energy barriers and an increased concentration of mobile ions.[53] A comparison between different parameters (such as atomic weight, melting point, polarizability, boiling point, ionic radius, and spherical volume calculated from ionic radii) as well as compositional complexity with ionic conductivity derived from machine learning is depicted in **Figure 10**.[10] Among the parameters, S_{mix} (same description as ΔS_{conf} mentioned in this thesis) showed a more pronounced correlation with

lithium conductivity and indicates that the high-entropy concept could be utilized in designing advanced superionic conductors due to its ability to simultaneously tailor potentially beneficial parameters (as mentioned in **Figure 10** and discussed in section 2.1.1.) owing to cocktail effects. In addition to the potential for enhancing ionic conductivity, the high-entropy concept is also likely to contribute to improved electrochemical stability, making it a promising approach for the practical application of superionic conductors as SEs in SSBs.

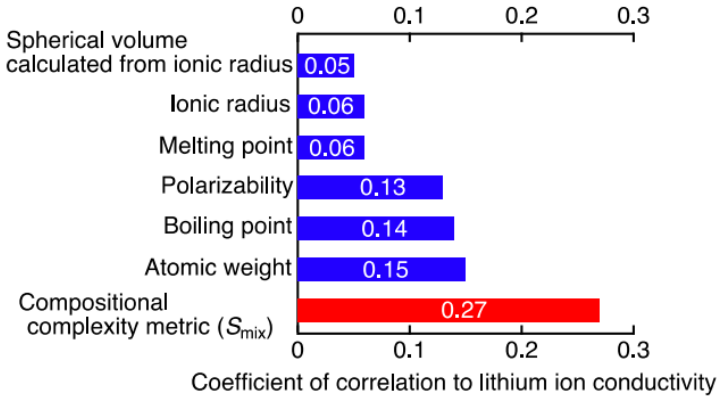

Figure 10: Correlation coefficient between ionic conductivity and compositional complexity for 250 reported oxide lithium-ion conductors. Adapted from Y. Li *et al.*[10]

The potential benefits are explained in detail as follows:

(1) Preference to form highly symmetric structures: High-entropy materials tend to crystallize in high-symmetry structures, such as cubic crystal structures.[118,119] Typically, ions prefer a specific elongation, rotation, or distortion in their local environments, leading to the specific segregation or clustering. Therefore, this leads to breaking of the general structural symmetry.[120] For HEMs, these preferences for certain ions may be in contradiction with the preferences of the other ions, then reflecting no net preference. It results in high symmetry structures for HEMs. Interestingly, most ion conductors are also found to adopt highly symmetric structures. Such crystal structures can lead to well-distributed mobile ions, therefore, allowing for 3D diffusion pathways and therefore facilitating fast ion diffusion.[53]

(2) Lower energy barrier (E_A): It is widely believed that increasing configurational entropy (ΔS_{conf}) will significant lower the energy barrier for ion diffusion owing to introduction of large lattice distortions.[16] This will intensify lattice dynamics and as described in 2.1.1, lattice dynamics can promote fast ion diffusion through phonon-ion interactions or the paddle-wheel effect.[53,57] Moreover, increasing ΔS_{conf} might potentially lower the defect formation energy (H^{form}), thereby further lowering the activation energy E_A (details shown as Equation 11).

(3) High defect concentration: HEMs achieved through substitution with iso- or aliovalent elements are associated with the capability of manipulation defect densities. In HEA research, the vacancy concentration could be increased ten times higher compared to pure metals (based on DFT calculations).[121] Similar results have been observed in HEOs, showing that both cation- and oxygen-vacancy formation energies decrease, due to the large lattice distortion in HEOs.[122] Therefore, tailoring the composition of HEMs makes it a valuable strategy to balance the concentration of charge carrier and vacancies, potentially leading to enhanced ionic conductivity.

(4) Short-range reordering and sublattice redistribution: Complex atomic interaction caused by a large variety in ionic sized and valence stated for individual elements could lead to short-range reordering and sublattice redistribution, establishing new diffusion pathways and therefore possibly facilitating ion migration.[123]

(5) Tuning the (electro)chemical properties: Typically, (electro)chemical stability is related to the chemical composition of SE materials.[19] Given the vast chemical design space of HEMs, through compositional design, the (electro)chemical stability of high-entropy SEs could potentially be improved.[16,124]

Based on the above-mentioned (assumed) advantages, high-entropy solid state electrolytes have been firstly published in 2016 from Bérardan *et al*. for oxide materials with a rock-salt type structure, $[Co_{0.2}Mg_{0.2}Cu_{0.2}Ni_{0.2}Zn_{0.2}]_{1-x-y}Ga_xA_yO$ (A = Li, Na, K). The improved ionic conductivity has been rationalized through a larger number of generated oxygen vacancies, providing more percolating channels for Li-ions.[117] In 2017, Deng *et al.* reported the polyanionic substitution effect on ion transport in LISICON-like Li_4SiO_4 materials (e.g., Li_4SiO_4, $Li_{3.75}Si_{0.75}P_{0.25}O_4$, $Li_{4.25}Si_{0.75}Al_{0.25}O_4$, $Li_4Al_{0.33}Si_{0.33}P_{0.33}O_4$, and $Li_4Al_{1/3}Si_{1/6}Ge_{1/6}P_{1/3}O_4$) and demonstrated the coexistence of various XO_4 polyanions [$(SiO_4)^{4-}$, $(PO_4)^{3-}$, and $(AlO_4)^{5-}$] leads to lower lithium-ion transport barriers.[125] This has been further verified through molecular dynamic simulations and has been described as 'superfluid' ion diffusion phenomenon.[126–129] In 2022, the first systematic investigation into the influence of high entropy on ion transport, specifically in Li-NASICON), Na-NASICON, and Li-garnet structures, has been reported by Zeng *et al.*[130] It has been found that a high entropy leads to orders-of-magnitude higher ionic conductivity and also transformed a non-ion conductor into an ion-conductor when increasing the compositional complexity (see **Figure 11a**). The overlapping distribution of site energies for the alkali ions, due to local distortions caused by entropy, led to a better percolation for the ions, accompanied by a low activation energy (depicted in **Figure 11b**). Chen *et al.* has recently reported that compositional complexity leads to a rearrangement of the local structure, investigated through neutron total scattering and pair distribution function analysis (**Figure 11c**) for $Li_6La_3Zr_{0.5}Hf_{0.5}Ta_{0.5}Nb_{0.5}O_{12}$. It has been shown that the pentavalent ions (e.g. Ta^{5+} and Nb^{5+}) are only surrounded by tetravalent ions, such as Hf^{4+} and Zr^{4+}, as the first-nearest octahedron, and the second-nearest octahedron is occupied by another pentavalent ion.[123] However, there was no significant improvement in ionic conductivity for $Li_6La_3Zr_{0.5}Hf_{0.5}Ta_{0.5}Nb_{0.5}O_{12}$ (~0.33 mS cm^{-1}), compared with $Li_{6.5}La_3Zr_{1.5}Ta_{0.5}O_{12}$ (~0.24 mS cm^{-1}). Thus, it is still an open question if it is possible to increase ionic conductivity of lithium garnets by applying the high-entropy concept.

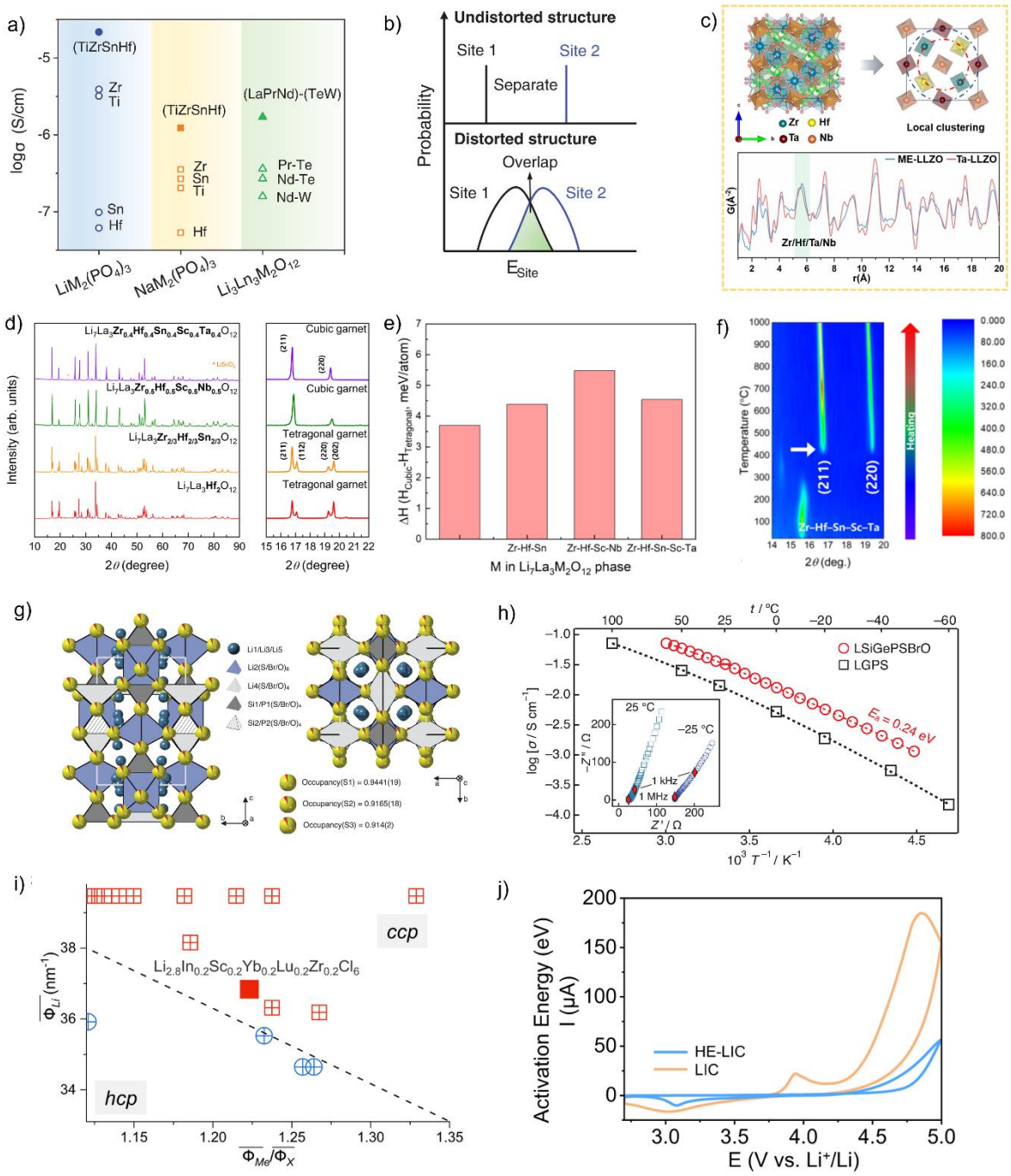

Figure 11: (a) Ionic conductivities of high-entropy conductors and their single-metal counterparts. (b) Schematic illustrating how local distortions create overlapping site energy distributions. (c) Neutron total scattering data for $Li_6La_3Zr_{0.5}Hf_{0.5}Ta_{0.5}Nb_{0.5}O_{12}$ (blue, labeled as ME-LLZO) and $Li_{6.5}La_3Zr_{1.5}Ta_{0.5}O_{12}$ (red, labeled as Ta-LLZO), along with a crystallographic representation of ME-LLZO to show its local clustering supercell. (d) XRD patterns of $Li_7La_3M_2O_{12}$ (M = Zr, Hf, Sn, Sc, Ta, or Nb) with increasing dopants in the Zr site. (e) Calculated formation enthalpy between the cubic and tetragonal phases of $Li_7La_3M_2O_{12}$. (f) Contour plots of *in situ* temperature-dependent XRD measurements conducted on $Li_7La_3Zr_{0.4}Hf_{0.4}Sn_{0.4}Sc_{0.4}Ta_{0.4}O_{12}$. (g) Schematic showing the crystal structure of $Li_{9.54}[Si_{0.6}Ge_{0.4}]_{1.74}P_{1.44}S_{11.1}Br_{0.3}O_{0.6}$ (LSiPSBrO). Arrhenius plots for LSiPSBrO and LGPS are shown in (h). (i) Design of HE layered halide SE guided by the ionic potential method. (j) CV curves of cells. Figures adapted from Y. Zeng *et al.* for (a, b), Y. Chen *et al.* for (c),

S.K. Jung *et al.* for (d-f), Y. Li *et al.* for (g, h), Q. Wang *et al.* for (i), and Z. Song *et al.* for (j).[10,123,124,130–132]

In addition to ionic conductivity, the entropy-driven phase stability has been investigated by Jung *et al.* in 2022 by introducing various dopants on the Zr site in the general composition $Li_7La_3M_2O_{12}$ (M = Zr, Hf, Sn, Sc, Ta or Nb).[131] As displayed in **Figure 11d**, pure cubic phases could be stabilized with the number of dopants on the Zr site equal or above 3. The entropy-driven cubic phase stabilization was verified comparing formation enthalpies of the cubic and tetragonal phase through DFT calculations. As depicted in **Figure 11e,** interestingly, the tetragonal phase is always more stable than the cubic one for all compositions, indicating the cubic phase stabilization in lithium garnets with complex doping is entropy-driven. According to the temperature-dependent XRD measurement (see **Figure 11f**), despite the fact that the high-entropy strategy could lower the cubic phase formation temperature during annealing, the expected cubic-to-tetragonal transition does not occur during cooling, possibly due to sluggish kinetics. But still, the significant improvement in ionic conductivity has not been achieved by applying the high-entropy concept to lithium garnets. In contrast to the garnet structure, ionic conductivity has been improved by an order of magnitude in the Li-perovskite structure (0.2 mS cm^{-1} at room temperature) when applying the high-entropy concept.[133] Then, in 2023, a very high ionic conductivity has been achieved (~30 mS cm^{-1}) at room temperature for lithium thiophosphate LGPS-type materials with the composition $Li_{9.54}[Si_{0.6}Ge_{0.4}]_{1.74}P_{1.44}S_{11.1}Br_{0.3}O_{0.6}$ (LSiPSBrO) through tailoring the anionic sublattice (**Figure 11g, h**).[10] However, the mechanism of configurational entropy boosting ionic conductivity has not been discussed. Another difficulty for high-entropy materials is the compositional design strategy. Recently, Q. Wang *et al.* have reported a guideline to synthesize cubic close-packed (ccp) stacking type high-entropy lithium halides based on the ionic potential, with general formula $Li_{3+m}Me_{1+n}X_6$, where Me represents one or multiple metal elements and X stands for one or multiple halogen elements (**Figure 11i**).[132] Using these principles, $Li_{2.8}In_{0.2}Sc_{0.2}Yb_{0.2}Lu_{0.2}Zr_{0.2}Cl_6$ has been designed and synthesized. However, the ionic conductivity still did not significantly improve, compared to its counterpart Li_3InCl_6. Despite that, high-entropy halides have been found to be electrochemically more stable than low-entropy halides (**Figure 11j**), enabling high current and long-term cycling performance of SSBs.[124]

In general, the research on high-entropy ion conductors is just at its starting point. Regarding materials, until now, only lithium thiophosphates have been reported, exhibiting very high ionic conductivities (detailed information given in **Table S1** in 6.1). Thus, to verify the high-entropy's effect, at least, more high-entropy ion conductors are needed to be explored. In this thesis, we focus on lithium argyrodites to investigate if the high-entropy concept could boost their ionic conductivities. The general structure and electrochemical properties of lithium argyrodites will be shortly discussed in the following section.

2.3. Lithium argyrodites used as solid electrolytes for all-solid-state batteries

Various Li-ion conducting materials, including oxides and sulfides, have been extensively researched. Lithium argyrodites, a notable family of lithium-conducting sulfides, have attracted significant interest due to their high conductivities and straightforward synthesis. This section will first introduce the relationship between structure and charge transport in lithium argyrodites. Subsequently, their electrochemical properties and the challenges for their application as SEs in SSBs will be summarized.

2.3.1. Structure–charge transport relationships

Lithium argyrodites, a prominent group of lithium-conducting sulfides, are characterized by the general formula $Li_{7+x-y}M^{IV}_xM^{V}_{1-x}Ch_{6-y}X_y$ (M^{IV} = Si, Ge, Sn; M^{V} = P, Sb; Ch = O, S, Se; X = Cl, Br, I, BH_4; $0 \le x \le 1$; $0 \le y \le 2$).[47,89,134] Specifically, lithium argyrodites with the formula Li_6PS_5X (X = Cl, Br, I, referred to as LPSX) have attracted considerable interest in the past years.[89] The parent lithium argyrodite Li_7PS_6 crystallizes in an orthorhombic structure (α-Cu_7PSe_6 type, *Pna*2_1) at room temperature and shows a low ionic conductivity (1.6×10^{-3} mS cm^{-1}).[135] At elevated temperature (483 K), it undergoes a phase transition to cubic symmetry (*F*$\bar{4}$3*m*), exhibiting high ionic conductivity (3×10^{-2} mS cm^{-1}). This cubic structure can be stabilized at room temperature by replacement of one S^{2-} with X^- (X = Cl, Br, I) in Li_7PS_6, resulting in Li_6PS_5X (shown in **Figure 12a-c**).[89] The face-centered cubic (fcc) lattice (space group *F*$\bar{4}$3*m*) consists of X^- anions at the 4*a* Wyckoff position. The octahedral vacancies are occupied by P^{5+} on the Wyckoff site 4*b*. S^{2-} are located on two crystallographic positions. Four S^{2-} anions on 16*e* form the $[PS_4]^{3-}$ tetrahedra. The residual "free", non-bonded S^{2-} anions are located on the Wyckoff site 4*d* (tetrahedral interstices of the fcc structure). The free sulfur anions and the halogen anions can exchange with each other, causing anion site disorder X^-(4*a*)/S^{2-}(4*d*) (referring to site inversion), which influences the lithium transport of the LPSX materials (illustrated in **Figure 12a**).[136,137] The anion site-inversion also affects the $[PS_4]^{3-}$ tetrahedra, causing a small rotation of neighboring tetrahedra, thus breaking the local symmetry from cubic to monoclinic (space group *Cm*) within a range of 5 Å.[138]

Typically, lithium ions occupy four types of crystallographic positions within the cubic lithium argyrodites: T5(48*h*), T5a(24*g*), T2(48*h*), and T4(16*e*), as shown in **Figure 12d**.[91] T3(4*c*), which shares four corners with $[PS_4]^{3-}$ tetrahedra, has also been detected in fully ordered (no site-inversion) cubic lithium argyrodite $Li_{6+x}P_{1-x}Si_xO_5Cl$, exhibiting the high-symmetry space group *P*2_13.[139] Based on DFT calculations, three different jumps have been identified to contribute to long-range 3D lithium diffusion, namely 48*h*(T5)–48*h*(T5) doublet jumps (through the nominal 24*g*(T5a) transition site), intra-cage jumps between two adjacent 48*h*(T5) tetrahedra within the same cage, and inter-cage jumps between two 48*h*(T5) positions from different cages, depicted in **Figure 12e, f**.[140] Lithium argyrodites in which the Li^+ ions only occupy the 48*h*(T5) and 24*g*(T5a) Wyckoff sites usually exhibit poor transport properties due to long intercage jump distances, as shown in **Figure 12e**.[141] Nevertheless, these long intercage distances could be significantly shortened via

two routes. Increasing the X^{-}(4*a*)/S^{2-}(4*d*) site inversion (disorder) and introducing additional intermediate Li positions.[12,137,142–145] The former leads to changes in the average anionic charge and elemental distribution on the 4*d* site, surrounded by cage-like Li-ions (T5 and T5a sites). The occupancy and charge of the 4*d* site significantly affects the surrounding lithium distribution, which can be expressed as r_{mean}, the average distance of the surrounding lithium to the center of the cage (4*d*), depicted in **Figure 13**.[137,146] Higher degree of disorder results in a larger $r_{mean,}$ shorter Li-Li jump distance and thus higher ionic conductivity. Moreover, higher site disorder corresponds to lower average anionic charge density on 4*d,* weakening the bonding environment for the lithium within the cage, facilitating ion diffusion. Additional occupancy of T2(48*h*) sites establishes connections between T5 sites within the same Li cage (shown in **Figure 12f**), enabling fast intra-cage motion via T5–T2–T5 pathways, which serve as an intermediate position bridging two T5 sites from different cages, enabling fast intercage jumping via T5–T2–T2–T5 pathways with much shorter distances compared to isolated T5–T5 jumping.[143] Moreover, extra occupancy of the T4 site further promotes long-range diffusion by connecting different Li cages through T5–T4–T5 pathways, as depicted in **Figure 12g**.

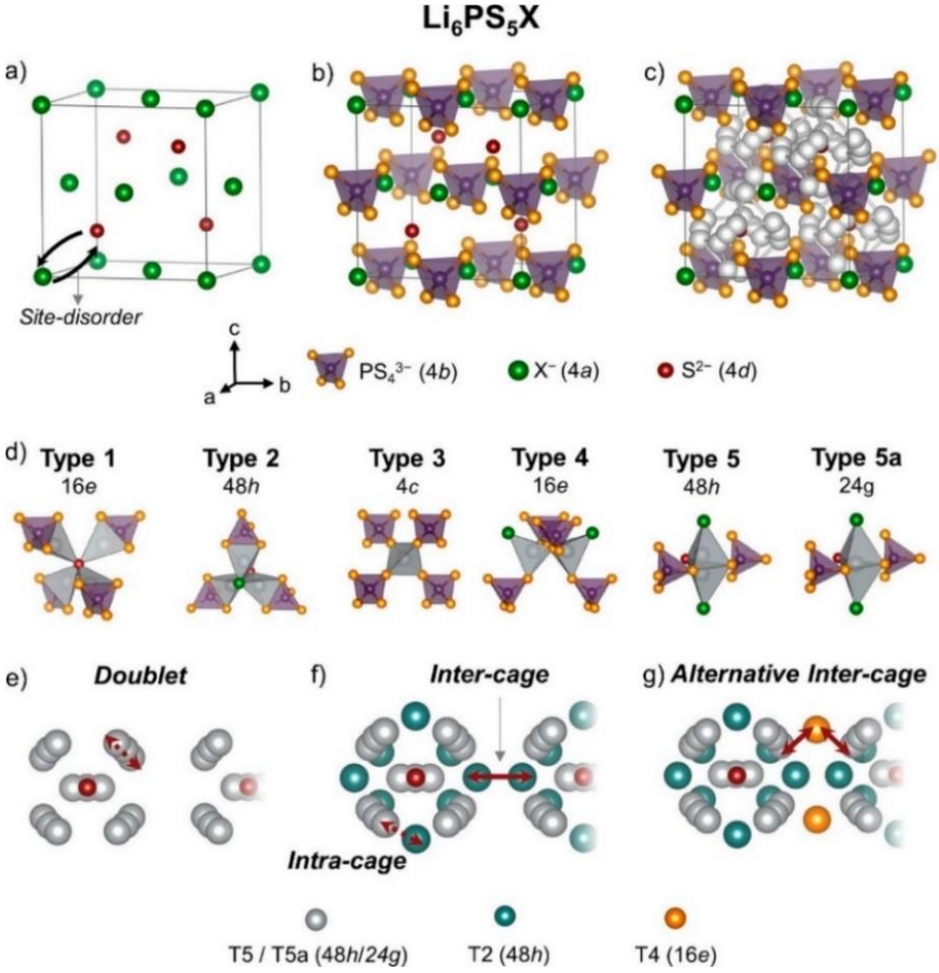

Figure 12: Unit cell of the Li_6PS_5X (X = Cl, Br, I) cubic polymorph. In the ordered configuration: (a-c) X^{-} anions form a face-centered cubic structure, S^{2-} ions occupy half of the tetrahedral voids, PS_4^{3-} units reside in the octahedral interstices (b), and Li^{+} ions create cage-like structures around the free sulfide positions (c). (d) There are five different types

of tetrahedral voids for potential lithium-ion occupations, each with distinct Wyckoff positions. (e, f) Illustration of three different diffusion pathways: Doublet jumping (e), inter-cage jumping (f), and intra-cage jumping. Adapted from L. Zhou *et al.*[91]

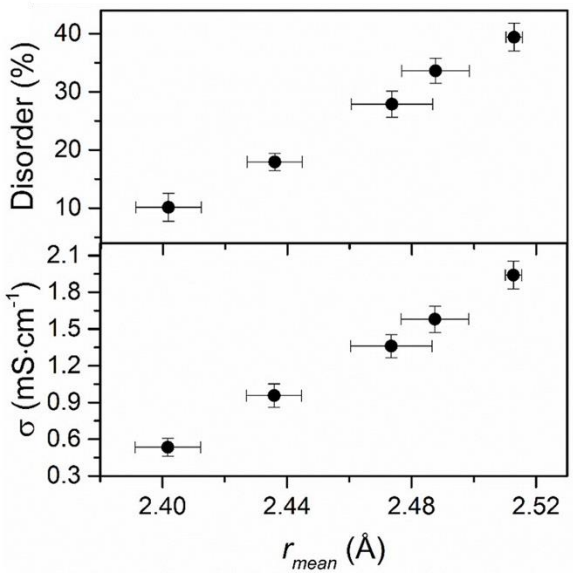

Figure 13: The relationship between ionic conductivity and anion disorder (Br^-/S^{2-}) is linked to the average distance of lithium distribution from the center of the cage (r_{mean}). Adapted from L. Zhou *et al.*[11,91]

Based on these mechanisms, specific strategies for improving the ionic conductivity of lithium argyrodites can be elucidated, and the ionic conductivity of different lithium argyrodites has been summarized in **Table S2** in 6.1. Strong site inversion plays a crucial role in enabling high ionic conductivity. For instance, in Li_6PS_5X (X = Cl, Br, I), significant X^-(4*a*)/S^{2-}(4*d*) site inversion is observed for LPSCl (62.6%) and LPSBr (16.5%), whereas LPSI (0%) exhibits minor disorder due to the larger ionic radius of I^-, hindering exchange with S^{2-}.[136,137] Moreover, this inversion can be significantly increased by aliovalent substitution on the phosphorus site, such as in $Li_{6+x}P_{1-x}Ge_xS_5I$, resulting in improved ionic conductivity (~5 mS cm^{-1}).[12,145] Additionally, the ionic conductivity can be enhanced in aliovalent-substituted lithium argyrodites with the formula $Li_{6+x}M_xSb_{1-x}S_5I$ (M = Si, Ge, Sn), owing to the generation of additional interstitial Li sites, leading to a low activation energy barrier and superionic conductivity through activated, concerted ion migration.[11] Furthermore, direct modification of site inversion can be achieved by replacing the free S^{2-}(4*d*) in LPSCl with Cl^-, resulting in halogen-rich $Li_{5.5}PS_{4.5}Cl_{1.5}$ showing very high ionic conductivity at room temperature, attributed to high vacancy density through anion sublattice engineering.[90] Moreover, the X^-(4*a*)/S^{2-}(4*d*) site inversion can be engineered through different temperature profiles, such as varying the cooling rate and post-annealing treatments, thereby influencing the charge-transport properties, e.g. in LPSBr and $Li_{5.5}PS_{4.5}Cl_{1.5}$.[142,146,147] External pressure does not affect the site inversion, but instead increases internal strain, which in turn enhances Li^+ conductivity.[148]

As discussed in section 2.1.1., similar to other well-crystallized ionic conductors, the grain boundaries in lithium argyrodites with high ionic conductivity, such as LPSCl and LPSBr, are not favorable for Li^+ transport. It has been found that glassy or nanocrystalline LPSCl and LPSBr consistently exhibit lower ionic conductivity compared to their well-crystallized counterparts.[149,150] Specifically, for LPSBr, the relationship between microstructure (site inversion), macrostructure (grain boundaries), and transport properties has been investigated by Sadowski and Albe.[151] Unlike bulk diffusion, low site inversion tends to deteriorate Li^+ transport, although it enhances grain-boundary transport.[151] Alternatively, for LPSI, the introduction of high-dimensional defects through high-energy ball milling has been demonstrated to have potential to boost ion dynamics, leading to a 3-fold increase in ionic conductivities.[69,71,141] It has been revealed that higher-dimensional defects not only facilitate ion diffusion at times but, more importantly, mitigate capacity fading in SSBs and prevent Li dendrite formation, which is typically caused by (chemo)mechanical degradation. This will be discussed in section 2.3.2.[150,152–154]

In addition to crystal structure and defect chemistry, the recent years have shown the influence of dynamic lattice properties on ion diffusion in lithium argyrodites, including lattice softness and phonon-ion coupling.[54,58] The difference between static and dynamic effects is illustrated in **Figure 14**. Typically, the static effect only considers the mobility of the Li^+ ion, with the assumption that the anion framework is relatively rigid and translationally immobile during ion migration, while this is taken into account by the dynamic effect. The studies on Li_6PS_5X (X = Cl, Br, I) have proven that while softer bonds (such as those in Br-based lithium argyrodites) lower the activation barrier, the decreased prefactor simultaneously reduces the ionic conductivity.[136] A similar behavior has been observed in $Li_6PS_{5-x}Se_xI$.[155] Also, regarding the paddle-wheel effect in lithium argyrodites, there is ongoing debate about the existence of PS_4^{3-} unit rotation and whether such rotation could facilitate lithium diffusion.[45,47]

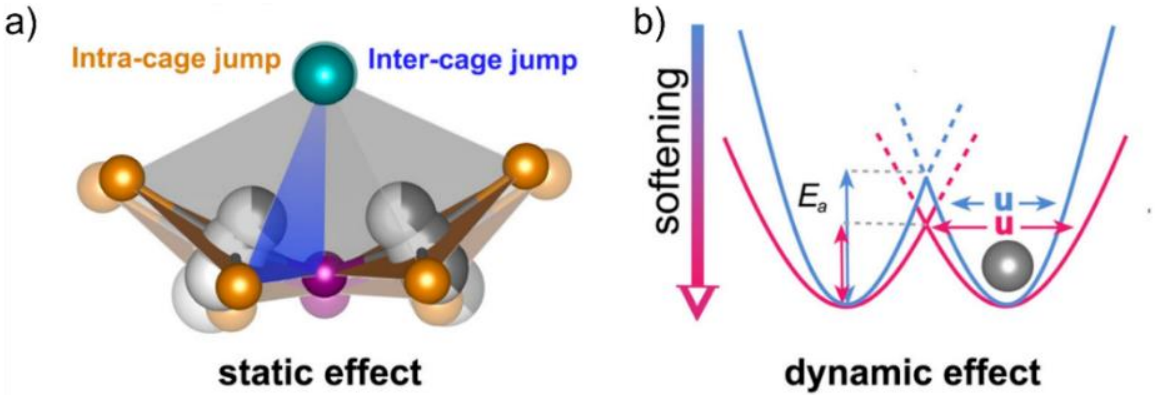

Figure 14: a) Schematic of the diffusion pathways and the influence of wider bottlenecks. b) Schematic illustrating the effect of lattice softening on ionic jumps. Figures (a, b) adapted from R. Schlem *et al.*[155]

2.3.2. Electrochemical and (chemo)mechanical properties in lithium argyrodites enabling all-solid-state batteries

The lithium argyrodite LPSCl is one of the most promising SEs for use in SSBs. Since the crystal structure and the lithium conductivity of LPSX argyrodites have already been presented in subsection 2.3.2, the electrochemical and (chemo)mechanical properties of CAM|SE and SE|Li, in particular for LPSCl, are briefly discussed below.

Like all sulfide SEs, LPSCl has a narrow electrochemical stability window (between 2.0 and 2.6 V vs. Li^+/Li according to theoretical calculations), meaning that it will electrochemically decompose beyond these potentials. Specifically, LPSCl starts to decompose to LiCl and Li_3PS_4, above 2.5 V vs. Li^+/Li, further degrading to P_2S_x and S_x upon 3 V vs. Li^+/Li (see **Figure 15a**).[156] The oxidation process can be simplified by the following reactions:

$$Li_6PS_5Cl \rightarrow LiCl + Li_3PS_4 + S + 2Li^+ + 2e^- \quad (22)$$

$$Li_3PS_4 \rightarrow 0.5P_2S_5 + 1.5S + 3Li^+ + 3e^- \quad (23)$$

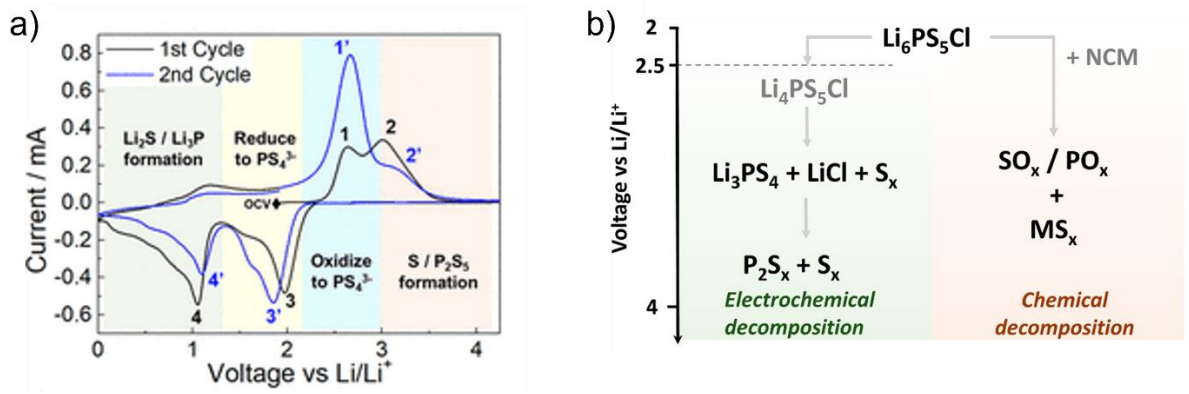

Figure 15: a) Cyclic voltammograms for the initial two cycles of Li_6PS_5Cl. (b) Schematic illustration of the electrochemical and chemical decomposition processes of Li_6PS_5Cl during oxidation. Figures adapted from D. S. Tan *et al* and L. Zhou *et al.*[91,156]

When mixing LPSCl with CAMs as well as conductive additives to form the cathode composite, the electrochemical degradation (oxidation) takes place at all contact interfaces of the SE with electronically conductive materials, including carbon, current collectors (CC), and the CAM itself.[157–159] The low ionic conductivity of the generated products, e.g. Li_2S or LiCl, leads to increasing interfacial resistance, which is detrimental to the cycling stability of SSBs, as depicted in **Figure 15b**.[160] The direct contact between LPSCl and CAMs can also lead to the chemical decomposition of the SE, forming a CEI consisting of SO_x and/or PO_x species and causing continuous capacity fade (**Figure 15b**).[161] As the CAM is the only source of oxygen, the oxygenation of the SE mainly occurs at the SE|CAM interface, and the reduced CAM (specifically the transition metal cations in the CAM) form rocksalt-like phases at the surface. Therefore, the application of a protective surface coating to the CAM is essential to mitigate the electrochemical and chemical decomposition of LPSCl.[162]

LPSCl reduces to sulfur and phosphorus species, like Li_2S and Li_3P [163], at approximately 1.08 V vs. Li^+/Li, as shown in **Figure 16a**, according to:

$$Li_6PS_5Cl + 8Li^+ + 8e^- \rightarrow LiCl + Li_3P + 5Li_2S \quad (24)$$

This reaction has been later investigated by Wagemaker *et al.* They mention that the decomposition process occurs through an intermediate phase $Li_{11}PS_5Cl$, rather than directly to the products.[164] In addition, argyrodites can also react with lithium metal chemically, forming Li_3P, Li_2S, and LiCl as follows (**Figure 16a**):

$$Li_6PS_5Cl + 8Li \rightarrow LiCl + Li_3P + 5Li_2S \quad (25)$$

As the products are predominantly ionically conductive, as confirmed by time-resolved EIS measurements, the resulting interfacial resistance increases during the first few hours of contact before stabilization, indicating the formation of a quasi-stable SEI (**Figure 16b**).[163]

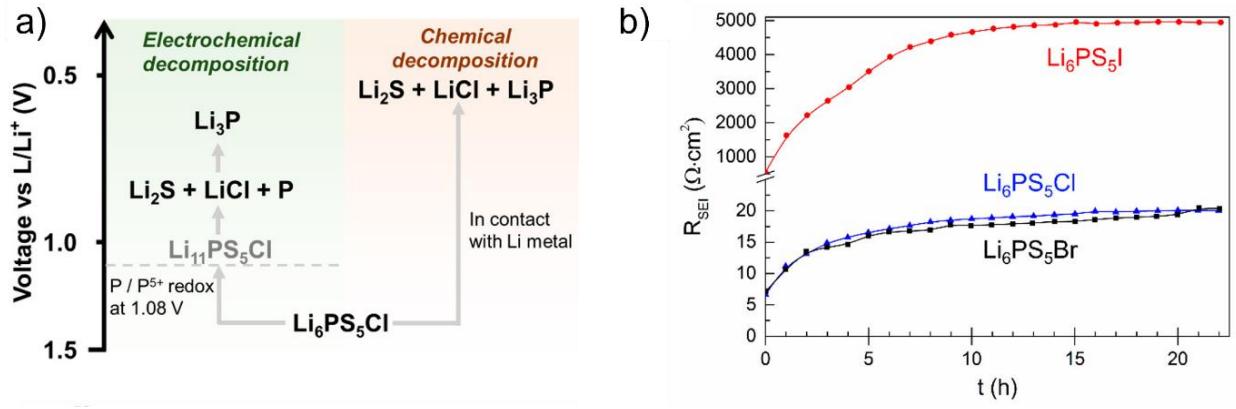

Figure 16: a) Schematic illustration of electrochemical and chemical decomposition for Li_6PS_5Cl during reduction. b) SEI resistance increase for Li_6PS_5Cl, Li_6PS_5Br, and Li_6PS_5I after contact with Li metal. Figures adapted from L. Zhou *et al.* and S. Wenzel *et al.*[91,164]

In addition to the electrochemical properties, the (chemo)mechanical attributes are also critical for SSBs, due to the rigidity of solid-solid contacts. Typically, during charge, a volume shrinkage of Ni-rich NCM can lead to contact loss at the SE|CAM interface, negatively affecting the ionic and electronic percolation pathways and further resulting in poor electrochemical reversibility and severe capacity fading.[152,165]

In summary, lithium argyrodites appear promising due to their high ionic conductivity, potential for cost-efficient production, and compatibility with Li metal and most CAMs when appropriate protection strategies are applied. However, several open questions and challenges still need to be addressed and will be discussed in the next section:

1) Can the high-entropy concept improve the ionic conductivity of lithium argyrodites beyond 10 mS cm^{-1} and further unlock compositional limitations? How does configurational entropy affect lithium diffusion, and is it necessary to apply the high-entropy strategy to lithium argyrodites?

2) How do compositional variations affect the thermodynamic and kinetic stabilities of lithium argyrodites, and how do these factors impact on the long-term cycling stability?

3. Results

Based on the scope of this thesis, which focuses on the exploration and application of high-entropy lithium argyrodites as SEs for SSBs, the results will be presented in the following. Starting from the exploration of new materials (the possible combination shown in **Figure 17**), we applied three approaches:

1) both anion and cation substitutions were combined (i.e. $\Delta S_{conf,cation}$ and $\Delta S_{conf,anion}$) to achieve $\Delta S_{conf} > 1.5R$ to initially verify the synthetic possibility of high-entropy lithium argyrodite (see Publication I).

2) engineering the tetrahedral environment through complex cation substitution at the 4*b* site primarily increasing $\Delta S_{conf,cation}$ (see Publications II and III).

3) tailoring anion site inversion via halogen substitution at the 4*d* and 4*a* sites leading to an increase in $\Delta S_{conf,anion}$ (see Publication IV).

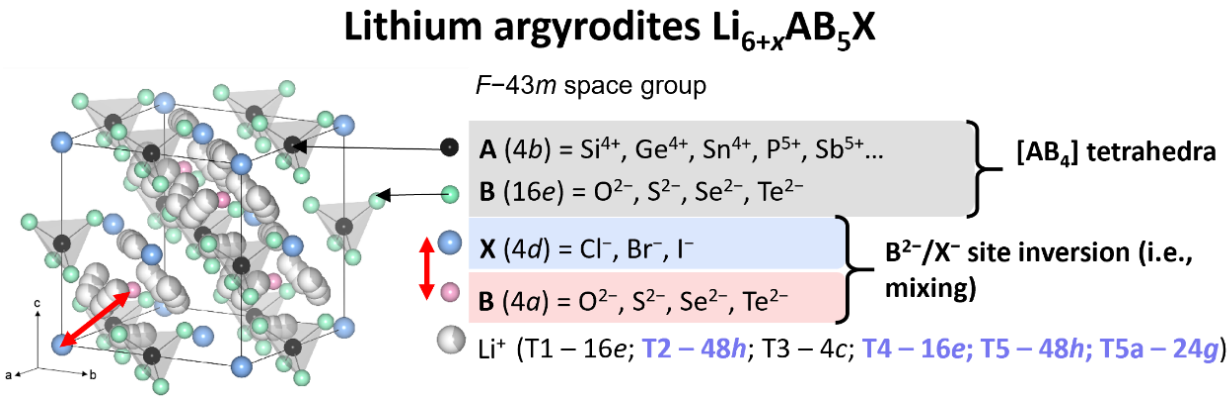

Figure 17: Schematic showing crystal structure of lithium argyrodites with the general formula $Li_{6+x}AB_5X$ and possible elemental selections for the relevant crystallographic positions.

The final study (Publication V) focuses on benchmarking various compositionally complex lithium argyrodites as SEs in SSBs. It was found that complex anion-substituted high-entropy argyrodite SEs exhibit superior electrochemical stability compared to cation-substituted samples. Additionally, the appendix in Chapter 6.1.1. (Publication VI) discusses the impact of surface impurities on the charge transport properties of high-entropy materials.

3.1. Publication I: High-Entropy Polyanionic Lithium Superionic Conductors

Publication I explores high-entropy lithium argyrodites by modifying the compositions derived from Li_6PS_5X (X=Cl, Br, I) through multiple anion and cation substitutions. These high-entropy lithium argyrodites ($Li_6PS_5[Cl_{0.33}Br_{0.33}I_{0.33}]$, $Li_6P[S_{2.5}Se_{2.5}][Cl_{0.33}Br_{0.33}I_{0.33}]$, and $Li_{6.5}[Ge_{0.5}P_{0.5}][S_{2.5}Se_{2.5}][Cl_{0.33}Br_{0.33}I_{0.33}]$) were synthesized by solid-state reaction, involving high-energy milling followed by annealing at temperatures of ≥ 400 °C in vacuum-sealed quartz ampules. The long-range and local structure was examined using complementary SXRD and neutron scattering techniques in combination with ^{31}P MAS NMR spectroscopy revealing an unequal distribution of elements over the respective crystallographic sites. The ion transport was characterized using EIS and ^{7}Li PFG NMR spectroscopy, demonstrating that the compositional disorder marginally affects the room-temperature ionic conductivity (~1 mS cm^{-1}) but instead lowers the activation energy for conduction to 0.22 eV.

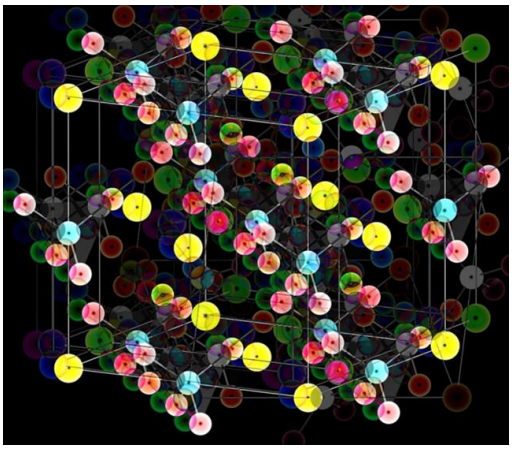

Figure 18: Table of Contents (TOC) of Publication I. Adapted from reference [18].

The experiments were planned and designed by the first author, F. Strauss. F. Strauss developed the synthesis method and analyzed the NPD data. The second author, J. Lin, supported the synthesis and conducted electrochemical experiments and data evaluation. The NPD experiments were carried out at the Spallation Neutron Source (SNS), Oak Ridge National Laboratory (ORNL), and SXRD, as well as total scattering results, were obtained at beamline P02.1, PETRA III, DESY (Hamburg, Germany), with support from Baran. V. M. Duffiet provided support for synchrotron XRD analysis. K. Wang performed the (S)TEM investigation. T. Zinkevich conducted the ^{7}Li PFG-NMR measurements, and analyzed the data together with F. Strauss and J. Lin. S. Indris conducted the MAS NMR spectroscopy experiments and analyzed the data together with discussions involving F. Strauss and J. Lin. A.-L. Hansen analyzed the total scattering XRD. The manuscript was written by F. Strauss and edited by all co-authors.

ACS MATERIALS LETTERS

www.acsmaterialsletters.org

High-Entropy Polyanionic Lithium Superionic Conductors

Florian Strauss,* Jing Lin, Marie Duffiet, Kai Wang, Tatiana Zinkevich, Anna-Lena Hansen, Sylvio Indris, and Torsten Brezesinski*

Cite This: *ACS Materials Lett.* 2022, 4, 418–423

Read Online

ACCESS | Metrics & More | Article Recommendations | Supporting Information

ABSTRACT: **High-entropy ceramics are attracting large interest because of their unique materials properties. Nevertheless, the effect of entropy on the lithium transport remains largely elusive. Here, we report, for the first time, about medium- and high-entropy polyanionic lithium superionic conductors crystallizing in the *F*−43*m* space group and adopting the so-called argyrodite structure. The $Li_6PS_5[Cl_{0.33}Br_{0.33}I_{0.33}]$, $Li_6P[S_{2.5}Se_{2.5}][Cl_{0.33}Br_{0.33}I_{0.33}]$, and $Li_{6.5}[Ge_{0.5}P_{0.5}][S_{2.5}Se_{2.5}]$-$[Cl_{0.33}Br_{0.33}I_{0.33}]$ materials were structurally characterized using complementary synchrotron and neutron scattering techniques in combination with ^{31}P magic-angle spinning (MAS) nuclear magnetic resonance (NMR) spectroscopy. We show that, in contrast to other high-entropy ceramics, an unequal distribution of elements over the respective crystallographic sites occurs in these materials. Using electrochemical impedance spectroscopy (EIS) and ^{7}Li pulsed field gradient (PFG) NMR spectroscopy, we demonstrate that introducing entropy (compositional disorder) marginally affects the room-temperature ionic conductivity (~10^{-3} S cm^{-1}) but instead lowers the activation energy for conduction to 0.22 eV. Our results emphasize the possibility of increasing entropy in polyanionic materials, thereby opening up compositional space for the search of Li-ion conductors with unprecedented properties.**

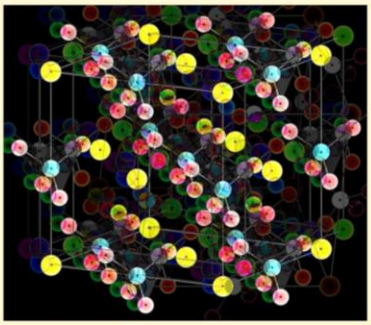

In recent years, high-entropy materials (HEMs) have attracted significant research interest because of their often unexpected and tailorable properties. The high-entropy concept is based on the idea of increasing configurational entropy, ΔS_{config}, in a specific structure type by introducing various elements on a single crystallographic site. Through possible manifold interactions between the incorporated elements, new materials properties arise, or (in some cases) a certain crystal structure can be entropically stabilized.[1−3] Originally, the HEM concept emerged from high-entropy alloys (HEAs)[4,5] and has been extended to high-entropy ceramics (HECs). Both HEAs and HECs can adopt different crystal structures (e.g., rocksalt, perovskite, spinel, etc.), and configurational entropy is usually introduced via cation mixing (in ionic materials).[6−9] However, the high-entropy concept has not yet been applied to polyanionic materials, despite their widespread use as electrode materials and ion conductors. An important feature of polyanionic-based materials is that they may offer a rigid three-dimensional framework, allowing for fast ion diffusion through interstitial space.[10−12] In principle, all ceramic oxide- and sulfide-based Li-ion conductors that are currently receiving interest, due to their potential for implementation as solid electrolytes (SEs) in solid-state batteries (SSBs), possess covalently bonded polyanions as building units, such as $[PO_4]^{3-}$ or $[PS_4]^{3-}$.[13−16] Among them, lithium thiophosphates represent one of the most promising classes of materials because of high ionic conductivity and favorable mechanical properties, ensuring intimate contact with the other battery components.[17−20] Examples are the so-called argyrodites with the general formula Li_6PS_5X (X = Cl, Br, I), having $[PS_4]^{3-}$ tetrahedra along with uncoordinated X^- and S^{2-} anions and offering a structural framework for facile lithium diffusion.[21,22] Argyrodite SEs have been heavily investigated in the past, and indeed high ionic conductivity at room temperature has been achieved by substitution on the phosphorus, chalcogenide, and halide sites.[16,23−25] Thus, materials crystallizing in the argyrodite structure type seem capable of accommodating various elements simultaneously. This possibly allows for achieving a high ΔS_{config} and may provide insights on how configurational entropy alters the Li-ion transport properties. Note that increased lithium and proton conduction in high-entropy rocksalt oxides has been reported;[26,27] however, the effect that ΔS_{config} has on the

Received: December 23, 2021
Accepted: January 21, 2022
Published: January 25, 2022

https://doi.org/10.1021/acsmaterialslett.1c00817
ACS Materials Lett. 2022, 4, 418−423

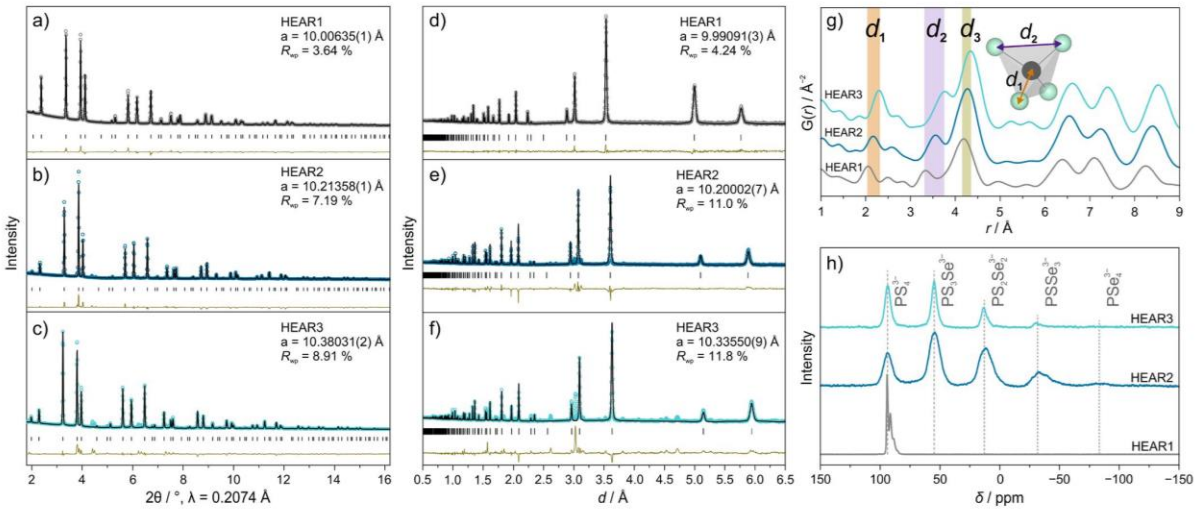

Figure 1. Structural characterization of the high-entropy lithium argyrodites. (a–c) SXRD and (d–f) NPD patterns and corresponding Rietveld refinement plots. The observed, calculated, and difference profiles are shown as colored circles, black lines, and beige lines, respectively. Vertical tick marks indicate the expected Bragg positions. (g) Corresponding PDF curves and (h) ^{31}P MAS NMR spectroscopy results.

charge transport remains unclear, and entropy was introduced by cation mixing only. In contrast, in the present work, we aimed at achieving high entropy primarily via anion mixing in the covalent/ionic host lattice of the argyrodite structure.

After a synthetic survey of possible elements on the P, S, and X sites in Li_6PS_5X (with equimolar stoichiometry), we were able to successfully synthesize polyanionic (and cationic) materials, namely $Li_6PS_5[Cl_{0.33}Br_{0.33}I_{0.33}]$ (HEAR1), $Li_6P[S_{2.5}Se_{2.5}][Cl_{0.33}Br_{0.33}I_{0.33}]$ (HEAR2), and $Li_{6.5}[Ge_{0.5}P_{0.5}][S_{2.5}Se_{2.5}][Cl_{0.33}Br_{0.33}I_{0.33}]$ (HEAR3). First, the halide site, followed by the chalcogenide site, and finally the phosphorus site were substituted to successively alter (increase) the configurational entropy. Assuming equal distribution over the available crystallographic sites, ΔS_{config} values of 1.24R, 2.28R, and 2.98R were calculated for HEAR1, HEAR2, and HEAR3, respectively (see the Supporting Information for details and Table S1). Materials for which $\Delta S_{config} \geq 1.5$ are usually considered high-entropy materials, originated from initial studies on HEAs, thus rendering HEAR2 and HEAR3 HEMs.[4,5] All materials were synthesized by classical solid-state chemistry with a high-energy milling step prior to annealing at temperatures of $\vartheta \geq 400$ °C in vacuum-sealed quartz ampules (see the Supporting Information for details). Initially, the elemental distribution on the nanometer level was probed using scanning transmission electron microscopy (STEM) combined with energy dispersive X-ray spectroscopy (EDS). As shown exemplarily for HEAR3 (see Figure S1), the as-synthesized material consists of micrometer-sized particles, and all elements are uniformly distributed. To reveal the detailed crystal structure, synchrotron X-ray diffraction (SXRD) and time-of-flight neutron powder diffraction (NPD) measurements were conducted on the samples. As is evident from Figure 1a–f, the SXRD and NPD patterns can be indexed within the $F\bar{4}3m$ space group. The a lattice parameter increased linearly from about 10.0 Å for HEAR1 to 10.35 Å for HEAR3 (see Figure S2), thereby confirming the successful incorporation of Se and Ge.

Next, synchrotron X-ray total-scattering data were collected, and pair distribution function (PDF) analysis was conducted. The PDF curves (Figure 1g) show identical local structural features for the different materials. Three contributions can be attributed to the atomic distances around the (polyanionic) tetrahedral environment, $[PS_4]^{3-}$, $[PS_2Se_2]^{3-}$, and $[Ge_{0.5}P_{0.5}S_2Se_2]^{3.5-}$, as indicated in the inset. In particular, d_1 is assigned to the Ge/P–S/Se covalent bond within the tetrahedra and was found to increase from around 2.05 Å for HEAR1 to 2.29 Å for HEAR3. A similar trend was observed for d_2 (S/Se–S/Se) and d_3 (S/Se–S/Se), in agreement with the increase in the a lattice parameter in the order of HEAR1 < HEAR2 < HEAR3. Note that d_2 refers to the S/Se–S/Se distance within the tetrahedra, whereas d_3 denotes the distance to the next-neighboring tetrahedra. The increase in local interatomic distances is consistent with the substitution of S and P with larger Se and Ge, respectively.

To further probe the phosphorus local environment, ^{31}P MAS NMR spectra were collected on the samples (Figure 1h). A narrow signal with some substructure was observed for HEAR1, indicating low local structural disorder. In contrast, four to five broad signals with different intensities were clearly visible for HEAR2 and HEAR3. This suggests a significant increase in local disorder compared to HEAR1. The chemical shift of the peaks can be explained by the different $[PS_{4-x}Se_x]^{3-}$ tetrahedra with x = 0–4. The substructure of the peak at +94 ppm for HEAR1, as well as at −30 ppm for HEAR2, is caused by the different arrangements of neighbors around these tetrahedra. Binominal fitting of the intensities allowed for quantitatively determining the overall number of x in $[PS_{4-x}Se_x]^{3-}$.[21,22] Naturally, for HEAR1, x = 0, as only $[PS_4]^{3-}$ units are present. However, for HEAR2 and HEAR3, x was calculated to equal 1.6 and 0.9, respectively, translating to $[PS_{2.4}Se_{1.6}]^{3-}$ and $[Ge_{0.5}P_{0.5}S_{3.1}Se_{0.9}]^{3.5-}$.

In addition, Raman spectroscopy measurements were conducted on the samples. The respective spectra display bands indicative of the polyanions, $[PS_{4-x}Se_x]^{3-}$ and $[GeS_{4-x}Se_x]^{4-}$ with x = 0–4 (see Figure S3).[28,29] For

https://doi.org/10.1021/acsmaterialslett.1c00817
ACS Materials Lett. 2022, 4, 418–423

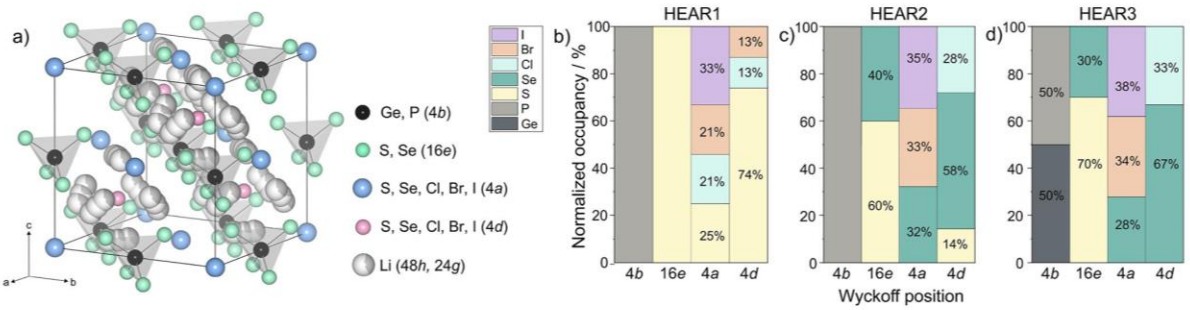

Figure 2. (a) Schematic view of the crystal structure of the high-entropy lithium argyrodites. The different Wyckoff positions and elements are indicated. (b–d) Normalized occupancies of the different crystallographic sites, with the color referring to the elements displayed in the legend.

HEAR1, bands arising from the $[PS_4]^{3-}$ vibrations were clearly visible and centered around 416 and 575 cm^{-1}. These bands can be assigned to symmetric and asymmetric stretching vibrations of the $[PS_4]^{3-}$ tetrahedra, respectively.[29,30] For HEAR2, additional bands, due to the presence of different $[PS_{4-x}Se_x]^{3-}$ species, were present. However, in the case of HEAR3, the identification of single bands correlated with the $[PS_{4-x}Se_x]^{3-}$ and $[GeS_{4-x}Se_x]^{4-}$ tetrahedra is difficult because of strong overlapping. Nevertheless, as a starting point, the local structural information from ^{31}P MAS NMR spectroscopy was considered in the refinements.

HEAR1, HEAR2, and HEAR3 adopt the so-called argyrodite structure (Figure 2a), where anions form a face centered cubic sublattice (Wyckoff positions 4*a* and 4*d*) with chalcogenide anions in half of the tetrahedral voids (Wyckoff position 16*e*) and polyanionic tetrahedra on the octahedral sites (central atom on Wyckoff position 4*b*). The atoms located on the Wyckoff positions 4*a* (halide) and 4*d* (chalcogenide) are known to distribute over both crystallographic sites, which is usually referred to as halide/chalcogenide site inversion. Moreover, the mobile cations (Li) are distributed around the 4*d* site, forming Frank-Kasper-polyhedra with two different Wyckoff positions (48*h* and 24*g*).[21,22] Thus, for the high-entropy argyrodite materials described in this work, the possible site inversion leads to large complexity. Through a combination of diffraction pattern simulation and subsequent Rietveld refinement, the detailed crystal structure could be determined (see the Supporting Information for details). For the least complex material, HEAR1 (Figure 2b), the structure contains $[PS_4]^{3-}$ polyanions along with a rather equal occupation of the S (25%), Cl (21%), Br (21%), and I (33%) on the 4*a* site. We also noticed some halide/chalcogenide mixing, since on the 4*d* site, 13% Br and 13% Cl were found (apart from 74% S). This kind of site inversion (Cl/Br and S) is often observed in lithium argyrodites, whereas I typically does not tend to share occupancy with S because of the large difference in ionic radii.[21,22] For HEAR2 (Figure 2c), additionally, half of the S was substituted with Se. In agreement with the results from the ^{31}P MAS NMR spectroscopy measurements, we found 60% S and 40% Se on the 16*e* site, forming $[PS_{2.4}Se_{1.6}]^{3-}$ tetrahedra. The 4*a* site contained virtually equal amounts of I (35%), Br (33%), and Se (32%). In contrast, Cl (28%) was solely present on the 4*d* site along with Se (58%) and S (14%). In contrast to HEAR1, Cl is pushed to the 4*d* site, with both I and Br remaining on the 4*a* site. Such elemental mixing on the 4*a* and 4*d* Wyckoff positions is most likely the result of mismatch and/or similarities in ionic radii. For HEAR3, a comparable distribution over the different crystallographic sites as for HEAR2 was observed (Figure 2d). The most noticeable difference is that $[Ge_{0.5}P_{0.5}S_{2.8}Se_{1.2}]^{3.5-}$ tetrahedra were present, meaning 70% S and 30% Se on the 16*e* site, in fair agreement with the S/Se ratio determined by ^{31}P MAS NMR spectroscopy. On the 4*a* and 4*d* sites, 38% I/34% Br/28% Se and 33% Cl/67% Se, respectively, were found. Taken together, the refinement of the partial atomic occupancies is in accordance with the targeted stoichiometries, except for HEAR3, where a slight deviation from the original S/Se ratio, $Li_{6.5}[Ge_{0.5}P_{0.5}][S_{2.8}Se_{2.2}][Cl_{0.33}Br_{0.34}I_{0.38}]$, was observed. This might also be the reason for the presence of clear impurity reflections in the SXRD and NPD patterns (Figure 1c,f).

In conclusion, substituting S with Se does not significantly increase the halide/chalcogenide site disorder. However, in this case, selective Cl/Se mixing on the 4*d* Wyckoff position occurs (Figure 2c,d), with the I and Br remaining on the halide 4*a* site. We hypothesize that the unequal mixing over the 4*a* and 4*d* sites, as seen for HEAR2 and HEAR3, is a result of minimizing the lattice distortion by keeping the difference in ionic radii ≤12% (for a specific crystallographic position). As known for argyrodites, altering the anion (and cation) sublattice causes a change in the Li substructure. Usually, Li can be distributed over two different Wyckoff positions, 48*h* and 24*g*. Rietveld refinement analysis of the NPD data showed that Li is mainly located on the 48*h* site (HEAR1, 93%), the fraction of which increased further for HEAR2 (95%) and HEAR3 (100%), see Figure S4a. Moreover, the Li^+–Li^+ jump distances remained virtually unaltered upon changing the anion and cation sublattices (see Figure S4b).

After having examined the crystal structure, the Li-ion conductivity of the as-prepared materials was probed using EIS. EIS measurements were conducted at different temperatures on sintered pellets with deposited gold electrodes. All samples showed a partial semicircle and a capacitive tail, indicating primarily ionic conductivity (see Figure S5). From the measured resistance, the conductivity was determined (Figure 3a). At 25 °C, values of 0.7, 1.3, and 1.1 mS cm^{-1} were calculated for HEAR1, HEAR2, and HEAR3, respectively. The evolution of conductivity with temperature follows an Arrhenius-type behavior with very similar activation energies of 0.29 for HEAR1 and 0.31 eV for both HEAR2 and HEAR3. Consequently, no significant changes in conductivity and activation energy for conduction were observed with increasing compositional disorder. However, because EIS measurements probe the overall sample conductivity (pellet specimen), the

https://doi.org/10.1021/acsmaterialslett.1c00817
ACS Materials Lett. 2022, 4, 418–423

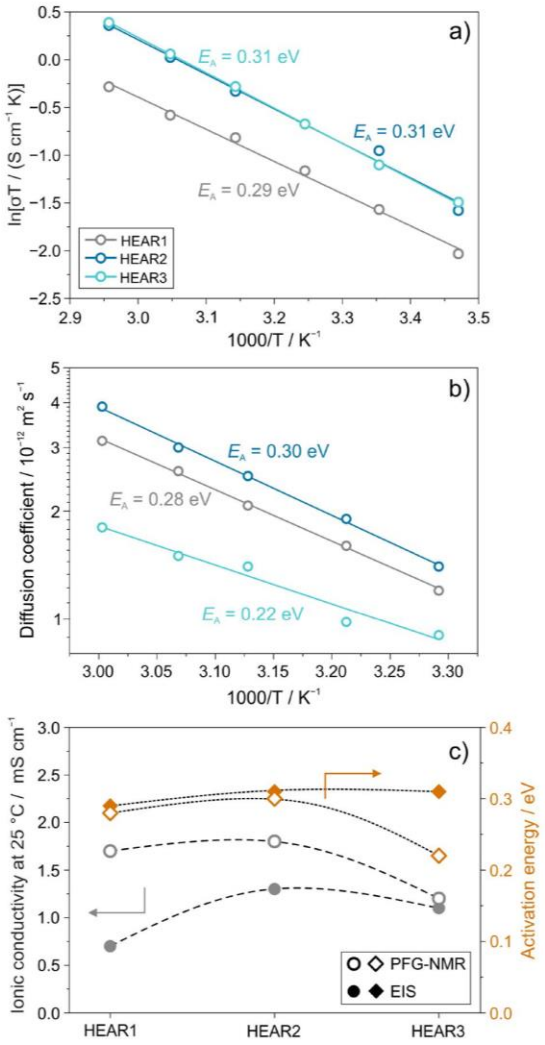

Figure 3. (a) Arrhenius fitting of the ionic conductivity in the temperature range from 15 to 65 °C. (b) Temperature-dependent diffusion coefficient from ^{7}Li PFG NMR spectroscopy. (c) Summary plot of the ionic conductivities at 25 °C and corresponding activation energies determined from EIS and ^{7}Li PFG NMR spectroscopy measurements.

results can be assumed to be affected by grain-boundary effects or crystalline/amorphous impurities.[31,32] For this reason, ^{7}Li PFG NMR spectroscopy measurements were conducted on the materials at different temperatures and at a diffusion time of 100 ms. In so doing, the lithium-diffusion coefficient, D_{Li}, can be determined (Figure 3b), from which the Li-ion conductivity is derived via the Nernst−Einstein equation. For HEAR1, HEAR2, and HEAR3, D_{Li} at 25 °C was found to be $0.99 \cdot 10^{-12}$, $1.13 \cdot 10^{-12}$, and $0.74 \cdot 10^{-12}$ m^2 s^{-1}, respectively, in the range usually observed for superionic conductors.[33,34] From these values, ionic conductivities of 1.7, 1.8, and 1.2 mS cm^{-1}, respectively, were calculated.

The change in D_{Li} also follows an Arrhenius-type behavior, and the activation energies for conduction for HEAR1 (0.28 eV) and HEAR2 (0.30 eV) are very similar to those determined from the EIS measurements. However, for HEAR3, a lower activation energy was calculated compared to EIS (0.22 vs 0.31 eV). An overview of the ionic conductivities and activation energies for the different materials is given in Figure 3c. As is evident, there are two main discrepancies between the EIS and ^{7}Li PFG NMR spectroscopy measurements. First, for HEAR1, the conductivity determined by ^{7}Li PFG NMR spectroscopy is more than twice that from EIS. This is probably due to the presence of crystalline/amorphous side phases, as ^{7}Li PFG NMR spectroscopy probes the bulk material, whereas EIS measures the overall sample conductivity. Second, although the conductivity of HEAR3 from EIS and ^{7}Li PFG NMR spectroscopy is similar, the activation energy for conduction is different. We hypothesize that this difference is also related to the presence of (unknown) impurities, having a more pronounced effect on the EIS data. Similar observations have been made for thiophosphate-based solid electrolytes.[31,32,35]

Taken together, the results indicate that the room-temperature Li-ion conductivity and activation energy (from ^{7}Li PFG NMR spectroscopy) are almost identical for the purely polyanionic high-entropy argyrodite materials, HEAR1 and HEAR2. However, upon additional cation substitution (HEAR3), both the ionic conductivity and activation energy decreased, leading to the lowest value reported for argyrodite-type Li-ion conductors (0.22 eV).[16,24] The activation energy was found to be linearly correlated with the pre-exponential factor of the diffusivity, D_0, known as the Meyer-Neldel rule (see Figure S6).[36,37] This suggests softening of the lattice with increasing configurational entropy,[38,39] which negatively affects the bulk ion transport in the case of HEAR3. Moreover, XRD and NPD revealed similar structural features for all three materials, i.e., a comparable halide/chalcogenide site inversion, ranging from 26 to 33%, and minor changes in the Li substructure.

In summary, we have reported about the successful synthesis of multielement substituted lithium argyrodites with a high ΔS_{config}. This was mainly achieved through anion mixing. Although nominally equal amounts of elemental constituents were used, nonuniform mixing over the respective crystallographic sites was observed, unlike for many other HEMs. Thus, the real ΔS_{config} values can be assumed to be smaller than the calculated ones (see Table S1). The Li-ion conductivity ($\sim 10^{-3}$ S cm^{-1}) was not strongly affected by increasing compositional disorder (configurational entropy). However, low activation energies for conduction ($\leq$0.31 eV) were found. The former is most likely due to close structural similarities between the investigated samples. Nevertheless, increasing the number of elements alters both the configurational entropy and the vibrational entropy (lattice softening), which may have synergistic or antagonistic effects on charge transport.[7,37,40] Distinguishing between these two entropy contributions (and ultimately from structural effects) remains challenging.

Overall, we believe that our study triggers further research into high-entropy ion conductors, potentially allowing for tailoring the electrical and (electro)chemical properties. This is a clear advantage considering the large compositional design space available for exploration.

■ ASSOCIATED CONTENT

Supporting Information

The Supporting Information is available free of charge at https://pubs.acs.org/doi/10.1021/acsmaterialslett.1c00817.

https://doi.org/10.1021/acsmaterialslett.1c00817
ACS Materials Lett. 2022, 4, 418−423

Materials and characterization, calculation of configurational entropy, STEM-EDS images, structural parameters and Li occupancies, Raman and EIS spectra, pre-exponential factor of diffusivity versus activation energy, and LeBail fit for Li_2Se precursor (PDF)

AUTHOR INFORMATION

Corresponding Authors

Florian Strauss − *Battery and Electrochemistry Laboratory, Institute of Nanotechnology, Karlsruhe Institute of Technology (KIT), 76344 Eggenstein-Leopoldshafen, Germany;* orcid.org/0000-0001-5817-6349; Email: florian.strauss@kit.edu

Torsten Brezesinski − *Battery and Electrochemistry Laboratory, Institute of Nanotechnology, Karlsruhe Institute of Technology (KIT), 76344 Eggenstein-Leopoldshafen, Germany;* orcid.org/0000-0002-4336-263X; Email: torsten.brezesinski@kit.edu

Authors

Jing Lin − *Battery and Electrochemistry Laboratory, Institute of Nanotechnology, Karlsruhe Institute of Technology (KIT), 76344 Eggenstein-Leopoldshafen, Germany*

Marie Duffiet − *Battery and Electrochemistry Laboratory, Institute of Nanotechnology, Karlsruhe Institute of Technology (KIT), 76344 Eggenstein-Leopoldshafen, Germany*

Kai Wang − *Institute of Nanotechnology, Karlsruhe Institute of Technology (KIT), 76344 Eggenstein-Leopoldshafen, Germany*

Tatiana Zinkevich − *Helmholtz Institute Ulm (HIU) Electrochemical Energy Storage, 89081 Ulm, Germany; Institute for Applied Materials-Energy Storage Systems, Karlsruhe Institute of Technology (KIT), 76344 Eggenstein-Leopoldshafen, Germany*

Anna-Lena Hansen − *Institute for Applied Materials-Energy Storage Systems, Karlsruhe Institute of Technology (KIT), 76344 Eggenstein-Leopoldshafen, Germany*

Sylvio Indris − *Helmholtz Institute Ulm (HIU) Electrochemical Energy Storage, 89081 Ulm, Germany; Institute for Applied Materials-Energy Storage Systems, Karlsruhe Institute of Technology (KIT), 76344 Eggenstein-Leopoldshafen, Germany;* orcid.org/0000-0002-5100-113X

Complete contact information is available at: https://pubs.acs.org/10.1021/acsmaterialslett.1c00817

Notes

The authors declare no competing financial interest.

ACKNOWLEDGMENTS

F.S. is grateful to the Fonds der Chemischen Industrie for financial support through a Liebig fellowship. J.L. acknowledges the FCI for Ph.D. funding. This work was partially supported by BASF SE. This research used resources at the Spallation Neutron Source (SNS), a DOE Office of Science User Facility operated by the Oak Ridge National Laboratory (ORNL). We acknowledge DESY (Hamburg, Germany), a member of the Helmholtz Association HGF, for the provision of experimental facilities. Parts of this research were carried out at PETRA III, and we would like to thank Volodymyr Baran for assistance in using beamline P02.1.

REFERENCES

(1) Oses, C.; Toher, C.; Curtarolo, S. High-Entropy Ceramics. *Nat. Rev. Mater.* **2020**, *5*, 295−309.

(2) Rost, C. M.; Sachet, E.; Borman, T.; Moballegh, A.; Dickey, E. C.; Hou, D.; Jones, J. L.; Curtarolo, S.; Maria, J.-P. Entropy-Stabilized Oxides. *Nat. Commun.* **2015**, *6*, 8485.

(3) Chen, Y.; Fu, H.; Huang, Y.; Huang, L.; Zheng, X.; Dai, Y.; Huang, Y.; Luo, W. Opportunities for High-Entropy Materials in Rechargeable Batteries. *ACS Mater. Lett.* **2021**, *3*, 160−170.

(4) George, E. P.; Raabe, D.; Ritchie, R. O. High-Entropy Alloys. *Nat. Rev. Mater.* **2019**, *4*, 515−534.

(5) *High-Entropy Alloys*; Gao, M. C., Yeh, J.-W., Liaw, P. K., Zhang, Y., Eds.; Springer International Publishing: Cham, 2016; DOI: 10.1007/978-3-319-27013-5.

(6) Sarkar, A.; Wang, Q.; Schiele, A.; Chellali, M. R.; Bhattacharya, S. S.; Wang, D.; Brezesinski, T.; Hahn, H.; Velasco, L.; Breitung, B. High-Entropy Oxides: Fundamental Aspects and Electrochemical Properties. *Adv. Mater.* **2019**, *31*, 1806236.

(7) Zhang, R.-Z.; Reece, M. J. Review of High Entropy Ceramics: Design, Synthesis, Structure and Properties. *J. Mater. Chem. A* **2019**, *7*, 22148−22162.

(8) Sarkar, A.; Breitung, B.; Hahn, H. High Entropy Oxides: The Role of Entropy, Enthalpy and Synergy. *Scr. Mater.* **2020**, *187*, 43−48.

(9) Ma, Y.; Ma, Y.; Wang, Q.; Schweidler, S.; Botros, M.; Fu, T.; Hahn, H.; Brezesinski, T.; Breitung, B. High-Entropy Energy Materials: Challenges and New Opportunities. *Energy Environ. Sci.* **2021**, *14*, 2883−2905.

(10) Masquelier, C.; Croguennec, L. Polyanionic (Phosphates, Silicates, Sulfates) Frameworks as Electrode Materials for Rechargeable Li (or Na) Batteries. *Chem. Rev.* **2013**, *113*, 6552−6591.

(11) Gong, Z.; Yang, Y. Recent Advances in the Research of Polyanion-Type Cathode Materials for Li-Ion Batteries. *Energy Environ. Sci.* **2011**, *4*, 3223−3242.

(12) Jin, T.; Li, H.; Zhu, K.; Wang, P.-F.; Liu, P.; Jiao, L. Polyanion-Type Cathode Materials for Sodium-Ion Batteries. *Chem. Soc. Rev.* **2020**, *49*, 2342−2377.

(13) Zhang, Z.; Shao, Y.; Lotsch, B.; Hu, Y.-S.; Li, H.; Janek, J.; Nazar, L. F.; Nan, C.-W.; Maier, J.; Armand, M. New Horizons for Inorganic Solid State Ion Conductors. *Energy Environ. Sci.* **2018**, *11*, 1945−1976.

(14) Reddy, M. V.; Julien, C. M.; Mauger, A.; Zaghib, K. Sulfide and Oxide Inorganic Solid Electrolytes for All-Solid-State Li Batteries: A Review. *Nanomaterials* **2020**, *10*, 1606.

(15) Park, K. H.; Bai, Q.; Kim, D. H.; Oh, D. Y.; Zhu, Y.; Mo, Y.; Jung, Y. S. Design Strategies, Practical Considerations, and New Solution Processes of Sulfide Solid Electrolytes for All-Solid-State Batteries. *Adv. Energy Mater.* **2018**, *8*, 1800035.

(16) Bachman, J. C.; Muy, S.; Grimaud, A.; Chang, H.-H.; Pour, N.; Lux, S. F.; Paschos, O.; Maglia, F.; Lupart, S.; Lamp, P.; Giordano, L.; Shao-Horn, Y. Inorganic Solid-State Electrolytes for Lithium Batteries: Mechanisms and Properties Governing Ion Conduction. *Chem. Rev.* **2016**, *116*, 140−162.

(17) Kato, Y.; Hori, S.; Saito, T.; Suzuki, K.; Hirayama, M.; Mitsui, A.; Yonemura, M.; Iba, H.; Kanno, R. High-Power All-Solid-State Batteries Using Sulfide Superionic Conductors. *Nat. Energy* **2016**, *1*, 16030.

(18) Lau, J.; DeBlock, R. H.; Butts, D. M.; Ashby, D. S.; Choi, C. S.; Dunn, B. S. Sulfide Solid Electrolytes for Lithium Battery Applications. *Adv. Energy Mater.* **2018**, *8*, 1800933.

(19) Teo, J. H.; Strauss, F.; Walther, F.; Ma, Y.; Payandeh, S.; Scherer, T.; Bianchini, M.; Janek, J.; Brezesinski, T. The Interplay between (Electro)chemical and (Chemo)mechanical Effects in the Cycling Performance of Thiophosphate-Based Solid-State Batteries. *Mater. Futures* **2022**, *1*, 015102.

(20) Teo, J. H.; Strauss, F.; Tripković, Đ.; Schweidler, S.; Ma, Y.; Bianchini, M.; Janek, J.; Brezesinski, T. Design-of-Experiments-Guided Optimization of Slurry-Cast Cathodes for Solid-State Batteries. *Cell Rep. Phys. Sci.* **2021**, *2*, 100465.

(21) Deiseroth, H.-J.; Kong, S.-T.; Eckert, H.; Vannahme, J.; Reiner, C.; Zaiß, T.; Schlosser, M. Li_6PS_5X: A Class of Crystalline Li-Rich Solids With an Unusually High Li^+ Mobility. *Angew. Chem., Int. Ed.* **2008**, *47*, 755−758.
(22) Kong, S.-T.; Deiseroth, H.-J.; Reiner, C.; Gün, Ö.; Neumann, E.; Ritter, C.; Zahn, D. Lithium Argyrodites with Phosphorus and Arsenic: Order and Disorder of Lithium Atoms, Crystal Chemistry, and Phase Transitions. *Chem.—Eur. J.* **2010**, *16*, 2198−2206.
(23) Yu, C.; Zhao, F.; Luo, J.; Zhang, L.; Sun, X. Recent Development of Lithium Argyrodite Solid-State Electrolytes for Solid-State Batteries: Synthesis, Structure, Stability and Dynamics. *Nano Energy* **2021**, *83*, 105858.
(24) Bai, X.; Duan, Y.; Zhuang, W.; Yang, R.; Wang, J. Research Progress in Li-Argyrodite-Based Solid-State Electrolytes. *J. Mater. Chem. A* **2020**, *8*, 25663−25686.
(25) Zhou, L.; Minafra, N.; Zeier, W. G.; Nazar, L. F. Innovative Approaches to Li-Argyrodite Solid Electrolytes for All-Solid-State Lithium Batteries. *Acc. Chem. Res.* **2021**, *54*, 2717−2728.
(26) Bérardan, D.; Franger, S.; Meena, A. K.; Dragoe, N. Room Temperature Lithium Superionic Conductivity in High Entropy Oxides. *J. Mater. Chem. A* **2016**, *4*, 9536−9541.
(27) Gazda, M.; Miruszewski, T.; Jaworski, D.; Mielewczyk-Gryń, A.; Skubida, W.; Wachowski, S.; Winiarz, P.; Dzierzgowski, K.; Łapiński, M.; Szpunar, I.; Dzik, E. Novel Class of Proton Conducting Materials—High Entropy Oxides. *ACS Mater. Lett.* **2020**, *2*, 1315−1321.
(28) Marple, M. A. T.; Aitken, B. G.; Kim, S.; Sen, S. Observation of a Phonon Softening Effect on Li Ion Conduction in Mixed-Anion Chalcogenide Glasses. *Chem. Mater.* **2018**, *30*, 5896−5903.
(29) Krauskopf, T.; Muy, S.; Culver, S. P.; Ohno, S.; Delaire, O.; Shao-Horn, Y.; Zeier, W. G. Comparing the Descriptors for Investigating the Influence of Lattice Dynamics on Ionic Transport Using the Superionic Conductor $Na_3PS_{4-X}Se_X$. *J. Am. Chem. Soc.* **2018**, *140*, 14464−14473.
(30) Pätzmann, U.; Brockner, W. Schwingungsspektren von Ag_3PS_4 und Cu_3PS_4/Vibrational Spectra of Ag_3PS_4 and Cu_3PS_4. *Z. Naturforsch. A* **1983**, *38*, 27−30.
(31) Harm, S.; Hatz, A.-K.; Moudrakovski, I.; Eger, R.; Kuhn, A.; Hoch, C.; Lotsch, B. V. Lesson Learned from NMR: Characterization and Ionic Conductivity of LGPS-like Li_7SiPS_8. *Chem. Mater.* **2019**, *31*, 1280−1288.
(32) Morales, D. J.; Greenbaum, S. NMR Investigations of Crystalline and Glassy Solid Electrolytes for Lithium Batteries: A Brief Review. *Int. J. Mol. Sci.* **2020**, *21*, 3402.
(33) Kuhn, A.; Duppel, V.; Lotsch, B. V. Tetragonal $Li_{10}GeP_2S_{12}$ and Li_7GePS_8 - Exploring the Li Ion Dynamics in LGPS Li Electrolytes. *Energy Environ. Sci.* **2013**, *6*, 3548−3552.
(34) Adeli, P.; Bazak, J. D.; Park, K. H.; Kochetkov, I.; Huq, A.; Goward, G. R.; Nazar, L. F. Boosting Solid-State Diffusivity and Conductivity in Lithium Superionic Argyrodites by Halide Substitution. *Angew. Chem., Int. Ed.* **2019**, *58*, 8681−8686.
(35) Holzmann, T.; Schoop, L. M.; Ali, M. N.; Moudrakovski, I.; Gregori, G.; Maier, J.; Cava, R. J.; Lotsch, B. V. $Li_{0.6}[Li_{0.2}Sn_{0.8}S_2]$ - a Layered Lithium Superionic Conductor. *Energy Environ. Sci.* **2016**, *9*, 2578−2585.
(36) Gelin, S.; Champagne-Ruel, A.; Mousseau, N. Enthalpy-Entropy Compensation of Atomic Diffusion Originates from Softening of Low Frequency Phonons. *Nat. Commun.* **2020**, *11*, 3977.
(37) Muy, S.; Bachman, J. C.; Giordano, L.; Chang, H.-H.; Abernathy, D. L.; Bansal, D.; Delaire, O.; Hori, S.; Kanno, R.; Maglia, F.; Lupart, S.; Lamp, P.; Shao-Horn, Y. Tuning Mobility and Stability of Lithium Ion Conductors Based on Lattice Dynamics. *Energy Environ. Sci.* **2018**, *11*, 850−859.
(38) Körmann, F.; Ikeda, Y.; Grabowski, B.; Sluiter, M. H. F. Phonon Broadening in High Entropy Alloys. *Npj Comput. Mater.* **2017**, *3*, 36.
(39) Kraft, M. A.; Culver, S. P.; Calderon, M.; Böcher, F.; Krauskopf, T.; Senyshyn, A.; Dietrich, C.; Zevalkink, A.; Janek, J.; Zeier, W. G. Influence of Lattice Polarizability on the Ionic Conductivity in the Lithium Superionic Argyrodites Li_6PS_5X (X = Cl, Br, I). *J. Am. Chem. Soc.* **2017**, *139*, 10909−10918.
(40) Phani Dathar, G. K.; Balachandran, J.; Kent, P. R. C.; Rondinone, A. J.; Ganesh, P. Li-Ion Site Disorder Driven Superionic Conductivity in Solid Electrolytes: A First-Principles Investigation of β-Li_3PS_4. *J. Mater. Chem. A* **2017**, *5*, 1153−1159.

https://doi.org/10.1021/acsmaterialslett.1c00817
ACS Materials Lett. 2022, 4, 418−423

3.2. Publication II: A High-Entropy Multicationic Substituted Lithium Argyrodite Superionic Solid Electrolytes

Publication II presents the study of a novel high-entropy lithium argyrodite ($Li_{6.5}[P_{0.25}Si_{0.25}Ge_{0.25}Sb_{0.25}]S_5I$) through multication substitution on the tetrahedral site (Wyckoff position 4*d*), exhibiting high ionic conductivity (> 10 mS cm^{-1} at 25 °C) and a low activation energy (0.20 eV). The synthetic exploration associated with the influence of surface impurities on charge transport will be discussed in the Appendix (Publication VI). The general and local structure was examined using NPD in combination with ^{31}P MAS NMR spectroscopy, revealing high S^{2-}/I^- anion site disorder (up to ~11%) and lithium redistribution leading to shortened Li-Li intercage jump distances, which facilitates long-range ion diffusion. Finally, the $Li_{6.5}[P_{0.25}Si_{0.25}Ge_{0.25}Sb_{0.25}]S_5I$ SE was also tested in high-loading SSB cells with a Ni-rich layered oxide cathode. Through *ex situ* XPS analysis, it was found that the strong interfacial side reactions during cycling were attributed to changes in chemical environment for specific elements (*e.g.* Si and Sb).

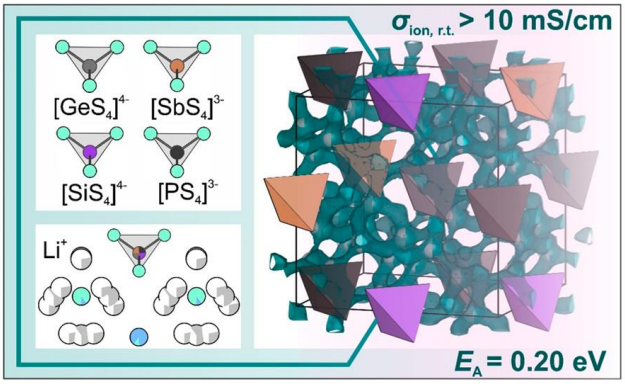

Figure 19: Table of Contents (TOC) of Publication II. Adapted from reference [19].

The experiments were planned and designed by the first author J. Lin under the supervision of J. Janek, T. Brezesinski and F. Strauss. The first author developed, optimized the synthesis method for $Li_{6.5}[P_{0.25}Si_{0.25}Ge_{0.25}Sb_{0.25}]S_5I$ and conducted electrochemical experiments (EIS and GCPL) as well as data analysis. The NPD experiments were carried out at Institute Laue-Langevin (ILL) for beamtime allocation (D2B) under proposal number (5-21-1164) with assistance from C. Ritter. G. Cherkashinin conducted the XPS experiments, analyzed the data and interpreted the results together with J. Lin and F. Strauss. M. Schäfer carried out the ^7Li PFG-NMR measurements and analyzed the data together with J. Lin. G. Melinte performed the (S)TEM investigation. S. Indris conducted the MAS NMR spectroscopy experiments. The first draft was written by J. Lin and further polished by F. Strauss. The final paper was then edited by all co-authors.

ACS MATERIALS LETTERS

www.acsmaterialsletters.org

A High-Entropy Multicationic Substituted Lithium Argyrodite Superionic Solid Electrolyte

Jing Lin, Gennady Cherkashinin, Mareen Schäfer, Georgian Melinte, Sylvio Indris, Aleksandr Kondrakov, Jürgen Janek, Torsten Brezesinski,* and Florian Strauss*

Cite This: *ACS Materials Lett.* 2022, 4, 2187–2194 Read Online

ACCESS | Metrics & More | Article Recommendations | Supporting Information

ABSTRACT: **Bulk-type solid-state batteries (SSBs) constitute a promising next-generation technology for electrochemical energy storage. However, in order for SSBs to become competitive with mature battery technologies, (electro)chemically stable, superionic solid electrolytes are much needed. Multicomponent or high-entropy lithium argyrodites have recently attracted attention for their favorable material characteristics. In the present work, we report on increasing the configurational entropy of the $Li_{6+a}P_{1-x}M_xS_5I$ solid electrolyte system and examine how this affects the structure-conductivity/stability relationships. Using electrochemical impedance spectroscopy and ^7Li pulsed field gradient nuclear magnetic resonance (NMR) spectroscopy, multicationic substitution is demonstrated to result in a very low activation energy for Li diffusion of ~0.2 eV and a high room-temperature ionic conductivity of ~13 mS cm^{-1} (for $Li_{6.5}[P_{0.25}Si_{0.25}Ge_{0.25}Sb_{0.25}]S_5I$). The transport properties are rationalized from a structural perspective by means of complementary neutron powder diffraction and magic-angle spinning NMR spectroscopy measurements. The $Li_{6.5}[P_{0.25}Si_{0.25}Ge_{0.25}Sb_{0.25}]S_5I$ solid electrolyte was also tested in high-loading SSB cells with a Ni-rich layered oxide cathode and found by X-ray photoelectron spectroscopy to suffer from interfacial side reactions during cycling. Overall, the results of this study indicate that optimization of conductivity is equally important to optimization of stability, and compositionally complex lithium argyrodites represent a new playground for a rational design of (potentially advanced) superionic solid electrolytes.**

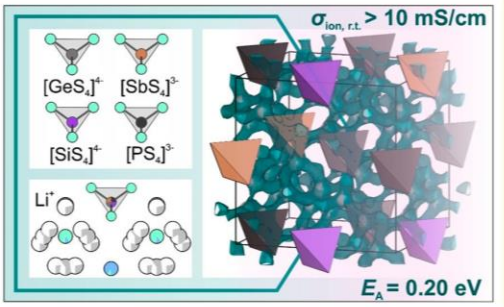

Lithium-ion batteries (LIBs) are one of the most advanced energy-storage technologies at this time.[1,2] The application of solid electrolytes (SEs) instead of conventional liquid electrolytes can potentially lead to significant leaps in cell energy density.[3−6] Among the different classes of inorganic SEs, lithium thiophosphates are considered most promising. This is due in part to their high ionic conductivity ($\sigma_{ion, r.t.} \geq 1$ mS cm^{-1}) and favorable mechanical properties, ensuring intimate contact between the key components in solid-state batteries (SSBs).[7−10] Especially lithium argyrodites with the general formula Li_6PS_5X (X = Cl, Br, I) are attracting much interest as potential high-performance SEs (with $\sigma_{ion, r.t.} \approx 2$ mS cm^{-1} for Li_6PS_5Cl).[11−14] These materials consist of $[PS_4]^{3-}$ structural units and free X^- and S^{2-} ions, offering a framework for fast lithium diffusion.[14,15] The ionic conductivity of lithium argyrodites has been increased by about an order of magnitude via substitution (primarily) on the phosphorus site. This kind of improvement is generally attributed to changes in the Li sublattice, with occupation of "additional" sites[16−19] and/or increased S^{2-}/X^- site inversion, such as in the case of $Li_{6.6}Si_{0.6}Sb_{0.4}S_5I$ (~15 and 24 mS cm^{-1} for cold-pressed and sintered pellets, respectively) and $Li_{6.6}P_{0.4}Ge_{0.6}S_5I$ (~6 and 18 mS cm^{-1} for cold-pressed and sintered pellets, respectively).[16,20−22] Recently, it has been shown that multianionic substituted lithium argyrodites do not possess increased ionic conductivity, although the activation energy for conduction strongly decreased.[23] Multielement (equimolar) substitution,

Received: July 22, 2022
Accepted: October 4, 2022
Published: October 6, 2022

https://doi.org/10.1021/acsmaterialslett.2c00667
ACS Materials Lett. 2022, 4, 2187–2194

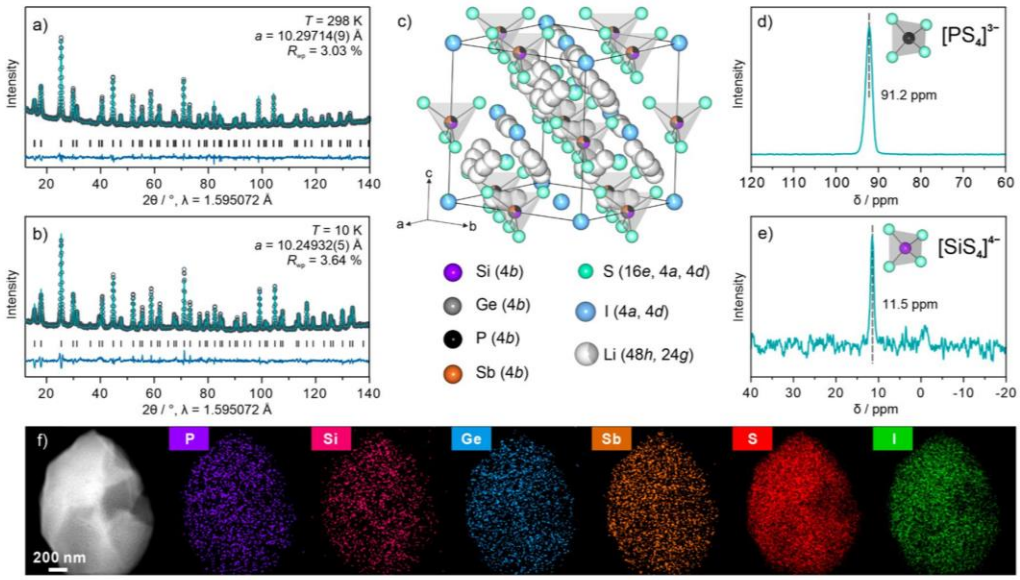

Figure 1. (a–e) Structural characterization of $Li_{6.5}[P_{0.25}Si_{0.25}Ge_{0.25}Sb_{0.25}]S_5I$. NPD patterns collected at (a) T = 298 K and (b) 10 K and corresponding Rietveld refinement plots. The observed, calculated, and difference profiles are shown as gray circles, cyan lines, and blue lines, respectively. Vertical tick marks denote the expected Bragg reflections. (c) Crystal structure with the different elements and Wyckoff positions indicated in the legend. (d) ^{31}P and (e) ^{29}Si MAS NMR spectra. (f) HAADF STEM image and corresponding EDS maps.

specifically having more than five elements sharing a single crystallographic site, refers to so-called high-entropy materials (HEMs) with $\Delta S_{config} \geq 1.5R$.[24] Note that ΔS_{config} represents the configurational entropy and can be calculated as detailed in the Supporting Information. In recent years, the concept of HEMs has been extended from high-entropy alloys to different oxide-, carbide-, and sulfide-based materials.[25−29] HEMs often show new or improved properties over their low-entropy counterparts and have been applied in various fields, for example, as thermoelectric materials or battery electrodes.[30−39] As mentioned above, high configurational entropy in lithium argyrodites, with a ΔS_{config} of up to 2.98R, could so far only be achieved through predominantly anionic mixing.[23] Multi-cationic substitution for increasing the configurational entropy and how this affects the structure−property relationships related to charge transport and electrochemical stability has not yet been explored. In the present work, we report on the synthesis and characterization of a multicationic substituted lithium argyrodite SE.

After screening a variety of cation species for substituting phosphorus in Li_6PS_5I (in an equimolar manner), we successfully synthesized $Li_{6.5}[P_{0.25}Si_{0.25}Ge_{0.25}Sb_{0.25}]S_5I$ by high-energy milling and postannealing at 500 °C in a vacuum-sealed quartz ampule (see Supporting Information for details on the preparation and Table S1 for other compositions targeted in the synthesis). Assuming equal distribution of elements over the different crystallographic sites, ΔS_{config} was calculated to be 2.77R, rendering it a high-entropy material. The respective X-ray diffraction (XRD) pattern showed reflections that could be assigned to a cubic argyrodite structure (Figure S1). The chemical composition was probed using inductively coupled plasma-optical emission spectroscopy (ICP-OES, see Table S2) and found to agree well with the target stoichiometry.

Neutron powder diffraction (NPD) was conducted on the sample at T = 298 and 10 K to gain more insight into the crystal structure. The room-temperature NPD pattern and corresponding Rietveld refinement profile are shown in Figure 1a. The pattern was indexed in the $F\bar{4}3m$ space group, with lattice parameter a = 10.297 14(9) Å, resulting in a cell volume of V = 1091.816(2) Å^3. More detailed structural information is provided in Table S3. For minimizing atomic thermal displacement, NPD was also performed at T = 10 K. As shown in Figure 1b, a similar pattern to that obtained at 298 K was observed. In line with expectations, a Rietveld analysis revealed a smaller lattice parameter (10.249 32(5) Å) and cell volume (1076.677(10) Å^3); see Table S4 for details. Interestingly, unlike Li_6PS_5I, the multicationic substituted argyrodite did not show a polymorphic phase transition at low temperatures.[15] The calculated crystal structure of $Li_{6.5}[P_{0.25}Si_{0.25}Ge_{0.25}Sb_{0.25}]S_5I$ is depicted in Figure 1c. Both the S^{2-} and I^- ions form a face-centered cubic sublattice (Wyckoff positions 4a and 4d). In addition, the S^{2-} ions are situated in half of the tetrahedral voids (Wyckoff position 16e) around the octahedral sites (central atom on Wyckoff position 4b), forming the polyanionic $[P_{0.25}Si_{0.25}Ge_{0.25}Sb_{0.25}S_4]^{3.5-}$ tetrahedra (constituting a combination of $[PS_4]^{3-}$, $[SiS_4]^{4-}$, $[GeS_4]^{4-}$, and $[SbS_4]^{3-}$).

To further corroborate the local tetrahedral environment of P and Si, ^{31}P and ^{29}Si magic-angle spinning (MAS) nuclear magnetic resonance (NMR) spectroscopy measurements were carried out. A distinct peak centered at 91.2 ppm was observed in the ^{31}P MAS NMR spectrum (Figure 1d), indicative of $[PS_4]^{3-}$ and consistent with the ^{31}P chemical shift reported for other lithium thiophosphates.[23,40,41] Compared to Li_6PS_5I, the ^{31}P signal was shifted by ∼5 ppm,[14] which is probably a result of the unique chemical environment. Regarding the ^{29}Si signal, a sharp peak appeared at a chemical shift of 11.5 ppm (Figure 1e), in agreement with the study on LGPS-like Li_7SiPS_8 (with

https://doi.org/10.1021/acsmaterialslett.2c00667
ACS Materials Lett. 2022, 4, 2187−2194

$[SiS_4]^{4-}$ units) by Lotsch and co-workers.[40] Note that the sharp ^{31}P and ^{29}Si MAS NMR signals suggest a relatively low degree of next-neighbor disorder, which was not the case for other types of multicomponent lithium argyrodites.[14,23] In particular, the atoms located on 4*a* (halide) and 4*d* (sulfide) are known to distribute over both crystallographic sites. For $Li_{6.5}[P_{0.25}Si_{0.25}Ge_{0.25}Sb_{0.25}]S_5I$, we observed a S^{2-}/I^- site inversion of 11%, which is relatively high considering the mismatch in ionic radii. Taking into account both the equal distribution of elements on the 4*b* site (tetrahedral environment) and the aforementioned site inversion (Wyckoff positions 4*a* and 4*d*), ΔS_{config} was calculated to be 2.03*R*, rendering $Li_{6.5}[P_{0.25}Si_{0.25}Ge_{0.25}Sb_{0.25}]S_5I$ a true high-entropy material.

Apart from the disorder, detailed information about the Li sublattice was obtained from a Rietveld analysis of the NPD data. The mobile Li atoms are known to form Frank-Kasper polyhedra in the argyrodite structure. They are usually distributed around the 4*d* site over two Wyckoff positions, namely, 48*h* and 24*g*.[14] For $Li_{6.5}[P_{0.25}Si_{0.25}Ge_{0.25}Sb_{0.25}]S_5I$, 38 and 62% were found on 24*g* and 48*h*, respectively, at room temperature (Figure S2). The Li occupancy remained virtually unaltered upon decreasing the temperature to $T = 10$ K. Such a large fraction of Li located on the intermediate/transition 24*g* site caused strong Coulomb repulsion between the two neighboring 48*h* sites,[21] eventually resulting in an enlarged 48*h*-48*h* doublet jump distance of 1.39 Å, compared to 1.25 Å for Li_6PS_5I (Table S5). This in turn led to decreased intercage jump distances of 3.24 Å, favoring facile long-range lithium diffusion.

The particle morphology and elemental distribution were probed using high-angle annular dark-field scanning transmission electron microscopy (HAADF STEM) and energy-dispersive X-ray spectroscopy (EDS). The average primary particle size was found to be larger than 1 μm (Figure 1f), and the EDS maps indicated uniform distribution on the submicrometer level (i.e., accumulation/segregation of individual elements can be ruled out).

To gain information about the oxidation state of the different elements, X-ray photoelectron spectroscopy (XPS) measurements were conducted on the $Li_{6.5}[P_{0.25}Si_{0.25}Ge_{0.25}Sb_{0.25}]S_5I$ sample. For the Sb 3d core-level region, only the $3d_{5/2}$ component is shown in Figure 2a, due to large spin−orbit splitting (~9.3 eV). The Sb $3d_{5/2}$ spectrum was superimposed by the O 1s signal at a binding energy of $E_{bin} \approx 532.5$ eV. The asymmetry of the Sb $3d_{5/2}$ component to low E_{bin} indicated two oxidation states, 529.5 eV for Sb^{3+} and 530.4 eV for Sb^{5+}, confirming the Sb−S chemical environment in the surface region.[42−45] The O 1s peak was asymmetric to high E_{bin}, suggesting the presence of at least two chemical states, at 532.0 and 532.9 eV (Figure 2a). These states can probably be attributed to oxygenated Si, Sb, P, and/or Ge. However, clear assignment is challenging. It should be noted that the formation of Sb−O species, due to oxygen contamination, cannot be fully ruled out. For example, the Sb $3d_{5/2}$ peak of Sb_2O_5 is expected to appear at $E_{bin} > 531$ eV.[42] Fitting of the Sb $3d_{3/2}$ region also revealed two oxidation states, at $E_{bin} = 538.9$ (Sb^{3+}) and 539.8 eV (Sb^{5+}) (Figure S3). Overall, we attribute the Sb^{5+} contribution to Sb in $[SbS_4]^{3-}$, while the Sb^{3+} presumably stems from not fully oxidized surface impurities, despite using excess sulfur in the synthesis. The S 2p detail spectrum is shown in Figure 2b. The E_{bin} of 161.6 eV assumes the presence of sulfide species, in agreement

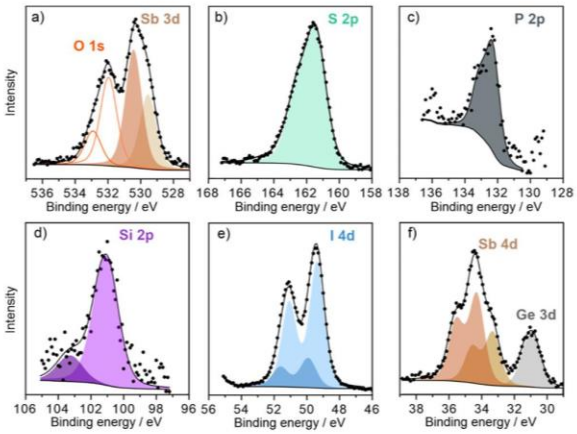

Figure 2. High-resolution (a) Sb $3d_{5/2}$ and O 1s, (b) S 2p, (c) P 2p, (d) Si 2p, (e) I 4d, and (f) Sb 4d and Ge 3d photoelectron spectra collected from $Li_{6.5}[P_{0.25}Si_{0.25}Ge_{0.25}Sb_{0.25}]S_5I$. Black circles and lines represent the experimental data and curve-fitting results, respectively.

with available literature reports on lithium thiophosphates.[46−48] Figure 2c displays the P 2p core-level region. Only a single component was detected at $E_{bin} = 132.4$ eV, which can be assigned to the $[PS_4]^{3-}$ units.[46−48] The binding energy was slightly higher compared with related thiophosphate SEs (~131.9 eV). We assume that the shift in E_{bin} results either from the different chemical environment (compositional disorder) or the formation of partially oxygenated P species. Figure 2d shows the Si 2p detail spectrum. The main feature at $E_{bin} = 101.1$ eV can be assigned to $[SiS_4]^{4-}$, as observed for lithium thiosilicates.[49,50] This finding agrees with the structural characterization results. The binding energy of the minor Si 2p component ($E_{bin} = 103.3$ eV) was slightly higher than that of free SiS_2.[49,50] It probably stems from SiO_x impurities,[51,52] since lithium thiophosphate surfaces are known to be very reactive toward oxygen-containing species. The I 4d region (~2.0 eV spin−orbit splitting) indicated the presence of two chemical states, at 49.3 and 49.9 eV, associated with the I^- species (Figure 2e). The I $3d_{5/2}$ data in Figure S4 corroborate this result.[53,54] We hypothesize that the two chemical states result from the different crystallographic sites, with different local chemical environments, occupied by I^- (Wyckoff positions 4*a* and 4*d*, with ~89 and 11% I^-, respectively). The Ge 3d and Sb 4d regions are shown in Figure 2f. The Sb 4d peaks (~1.3 eV spin−orbit splitting) were situated at slightly higher E_{bin} from the Ge 3d photoemission. Their shape (i.e., two chemical states with $E_{bin} = 33.3$ and 34.3 eV due to Sb^{3+} and Sb^{5+}, respectively, with Sb−S environment) supports the discussion above on the Sb $3d_{5/2}$ spectrum.[42,43] The Ge 3d spectrum revealed a single component at $E_{bin} = 30.9$ eV. The latter binding energy refers to $[GeS_4]^{4-}$ (30.8−30.9 eV)[42,55] and is much lower than that expected for GeO_2 (32.4−32.5 eV).[56,57] Thus, the presence of oxygenated Ge is rather unlikely.

The XPS and structural analysis results collectively provide evidence that the bulk material adopts an argyrodite-type structure. However, we found slight deviations in chemical composition and the state of selected elements in the surface region. Especially antimony seems to exist in mixed oxidation states, and the presence of oxygenated species (most pronounced for SiO_x) was observed, despite the material

https://doi.org/10.1021/acsmaterialslett.2c00667
ACS Materials Lett. 2022, 4, 2187−2194

processing under inert atmosphere conditions. Nevertheless, some undesirable side reactions with trace water/oxygen and/or precursor impurities throughout handling/data collection cannot be ruled out. The results obtained from quantitative XPS analysis are shown in Table S6. Considering the typical error, they agree reasonably well with the theoretical composition.

After characterization of the bulk/surface structure, the Li-ion dynamics were probed using both ^{7}Li pulsed field gradient (PFG) NMR spectroscopy and electrochemical impedance spectroscopy (EIS). ^{7}Li PFG NMR spectroscopy was used to determine the diffusion coefficient D_{Li} in the temperature range of 30−70 °C and the activation energy E_A for Li diffusion (Figure S5). D_{Li} was found to be 7.09×10^{-12} m^2 s^{-1} at ϑ = 30 °C, similar to other thiophosphate superionic conductors with a high Li diffusivity.[58−60] The Arrhenius plot of diffusivity versus T^{-1} is shown in Figure 3a, with E_A = (0.20 ± 0.01) eV determined from the slope. The electrical conductivity was measured by EIS on sintered pellets using ion-blocking indium electrodes. The Nyquist plots of the electrochemical impedance in the temperature range of 15−65 °C only showed a capacitive tail, suggesting high ion mobility (Figure S6). A room-temperature conductivity of 13.2 mS cm^{-1} was calculated from the data. As shown in Figure 3b, the temperature dependence of the conductivity followed an Arrhenius-type behavior, with a similar activation energy E_A = (0.19 ± 0.01) eV to that determined by ^{7}Li PFG NMR spectroscopy. In addition, the ionic conductivity was calculated from the D_{Li} using the Nernst−Einstein equation (Figure 3b). It was found to be slightly lower than that from the EIS measurements (for a given temperature). However, the activation energies were virtually identical. We believe that the differences in conductivity are due to the presence of trace impurities (segregated at the grain boundaries); see previous section on XPS. The electronic conductivity was determined by DC polarization experiments to be 1.52×10^{-7} S cm^{-1} at room temperature (Figure S7), which is 2−3 orders of magnitude higher compared to related Li-ion conductors.[58,61,62] We hypothesize that this is due, in part, to the presence of Sb-based surface impurities showing mixed oxidation states.

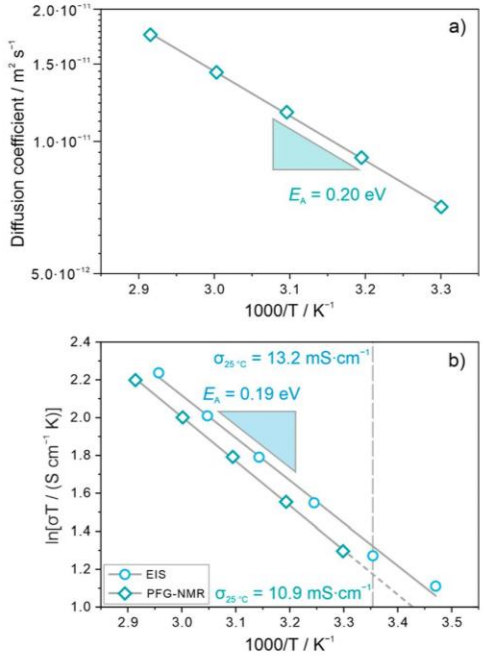

Figure 3. (a) Arrhenius plot of D_{Li} vs T^{-1}. (b) Ionic conductivity determined from EIS and ^{7}Li PFG NMR spectroscopy using the Nernst−Einstein equation. The room-temperature conductivities and activation energies are indicated.

Overall, the multicationic substituted $Li_{6.5}[P_{0.25}Si_{0.25}Ge_{0.25}Sb_{0.25}]S_5I$ was found to exhibit a very high ionic conductivity, with an activation energy for conduction that is among the lowest reported to date for lithium argyrodites (Table S7),[16,20,42] rendering it a promising material for bulk-type SSB applications.

The electrochemical behavior of $Li_{6.5}[P_{0.25}Si_{0.25}Ge_{0.25}Sb_{0.25}]S_5I$ as superionic SE was tested in pellet-stack SSBs with $LiNbO_3$-coated NCM851005 ($LiNi_xCo_yMn_zO_2$, NCM; here, with 85% Ni content) and LTO ($Li_4Ti_5O_{12}$) as cathode and anode, respectively (see Supporting Information for details on the electrode preparation and cell assembly). The charge/discharge cycling was performed between 1.35 and 2.75 V versus $Li_4Ti_5O_{12}/Li_7Ti_5O_{12}$ (approximately 2.9−4.3 V vs Li$^+$/Li) at a rate of C/2 and 25 °C (Figure 4). First-cycle specific charge and discharge capacities of 204 mA h g^{-1} (~2.3 mA h cm^{-2}) and 151 mA h g^{-1} (~1.7 mA h cm^{-2}) were achieved, corresponding to a Coulomb efficiency of 74% (Figure 4a). In the fifth cycle, the SSB cell delivered a specific discharge capacity of 148 mA h g^{-1}, and the Coulomb efficiency increased to 98.4%. Because of the high ionic conductivity of $Li_{6.5}[P_{0.25}Si_{0.25}Ge_{0.25}Sb_{0.25}]S_5I$, the cell was also subjected to rate performance testing from C/2 to 2C. As can be seen from Figure 4b, it was capable of delivering specific discharge capacities of ~118 and 72 mA h g^{-1} at 1C and 2C, respectively. On further cycling at C/2, the reversible capacity decayed to ~100 mA h g^{-1} (~1.1 mA h cm^{-2}) after 200 cycles, while the Coulomb efficiency stabilized close to 100%. Although a surface-protected cathode active material (CAM) was

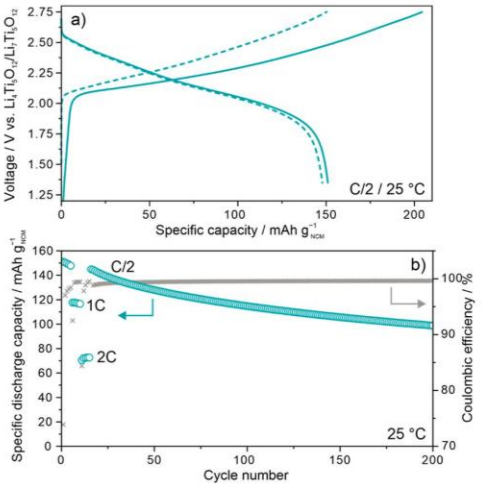

Figure 4. (a) Initial (solid line) and 5th-cycle (dashed line) voltage profiles of an SSB cell at C/2 rate and 25 °C. (b) Capacity retention and Coulomb efficiency over 200 cycles.

https://doi.org/10.1021/acsmaterialslett.2c00667
ACS Materials Lett. 2022, 4, 2187−2194

employed in the present work, especially the first-cycle efficiency was relatively low, indicating that detrimental side reactions (i.e., (electro)chemical SE decomposition) occurred at the CAM|SE and carbon black|SE interfaces. In addition, the fairly linear capacity fading upon long-term cycling points toward continuous SE degradation, meaning the formation of stable interfaces and interphases in this kind of battery system seems unlikely.

Ex situ XPS measurements were conducted on the cathode after cycling to learn more about the SE decomposition. The asymmetry of the Sb $3d_{5/2}$ component (Figure 5a) again

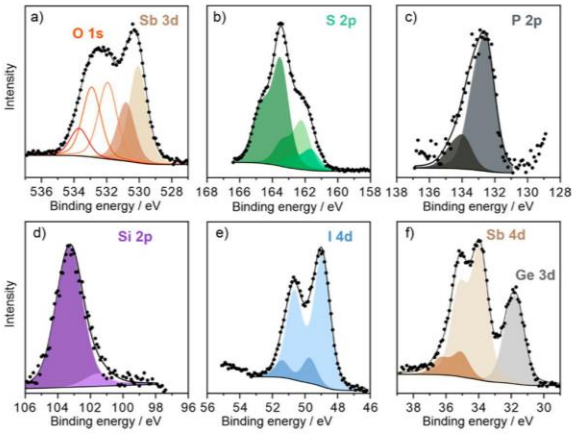

Figure 5. High-resolution (a) Sb $3d_{5/2}$ and O 1s, (b) S 2p, (c) P 2p, (d) Si 2p, (e) I 4d, and (f) Sb 4d and Ge 3d photoelectron spectra of $Li_{6.5}[P_{0.25}Si_{0.25}Ge_{0.25}Sb_{0.25}]S_5I$ after SSB cycling (200 cycles at C/2 rate and 25 °C). Black circles and lines present the experimental data and curve-fitting results, respectively.

indicated two oxidation states, 530.1 eV for Sb^{3+} and 530.8 eV for Sb^{5+}. The latter E_{bin} values are similar to those observed for the pristine material (Figure 2a), but with the major difference that the intensity of the Sb^{3+} component was strongly increased, suggesting Sb^{5+} reduction during electrochemical cycling. The shape of the O 1s core-level region also changed significantly (increase in intensity of the high binding-energy features at 531.9 and 532.9 eV as well as appearance of a new component at 533.7 eV), due to the formation of oxygenated species (Figure 5a). This is also reflected in the increased amount of surface oxygen, as determined by quantitative XPS (Table S6). The S 2p spectrum indicated that the sulfur is strongly involved in the degradation of the SE (Figure 5b). Apart from the component at E_{bin} = 161.6 eV observed for the pristine material (Figure 2b), two new intense features appeared at E_{bin} = 162.2 and 163.5 eV. These components can be attributed to oxidized sulfur species (polysulfides), which usually have a broad binding-energy range depending on the chain length, gradually approaching the E_{bin} of elemental sulfur (163.5 eV).[46,63] The SSB cycling further led to the appearance of an additional peak at E_{bin} = 134.0 eV in the P 2p detail spectrum (Figure 5c), not present in Figure 2c. This component can be assigned to PO_x species (metal phosphates and/or metaphosphates),[46,48,64] the formation of which is commonly observed in thiophosphate-based SSBs upon cycling. The Si 2p spectrum showed an intense peak at 103.3 eV with some minor asymmetry to low E_{bin}, indicating another chemical state at E_{bin} = 101.5 eV (Figure 5d). Both components were also detected prior to cycling (Figure 2d), the difference being that the higher binding-energy peak increased strongly in intensity.[51,52] It is known that Ni-rich NCM CAMs release lattice oxygen during charge because of structural instabilities (including electrochemical oxidation of surface carbonates). The evolved oxygen can undergo follow-up reactions with thiophosphate SEs, thus being responsible, at least to some degree, for the formation of oxygenated decomposition products.[65−68] Note that the NCM851005 CAM was the only oxygen source in the cathode. However, chemical reactions with the protective surface coating cannot be ruled out. Figure 5e shows the I 4d core-level region of the SE after cycling. No major differences to the spectrum shown in Figure 2e were found. The variation in peak intensities (see also I $3d_{5/2}$ data in Figure S4) might be due to slight changes in local structural disorder. The Sb 4d and Ge 3d regions are shown in Figure 5f. The Ge 3d detail spectrum showed a single peak, but it is ∼1 eV higher in binding energy than for the pristine material (31.8 vs 30.9 eV). This is indicative of the presence of partially oxygenated Ge species (the E_{bin} lies between that of materials with $[GeS_4]^{4-}$ structural units and GeO_2). Similar to the pristine SE, the Sb 4d spectrum revealed the presence of Sb^{3+} and Sb^{5+}, with E_{bin} = 33.9 and 35.1 eV, respectively (Figure 5f). The shift toward higher binding energies was accompanied by an increase in intensity of the Sb^{3+} component because of Sb^{5+} reduction upon SSB operation (note that the Sb 3d data in Figure 5a show the same trend).

The XPS results clearly demonstrate that the $Li_{6.5}[P_{0.25}Si_{0.25}Ge_{0.25}Sb_{0.25}]S_5I$ SE in the composite cathode underwent adverse side reactions during cycling. Except for both phosphorus and iodine, all other elemental constituents were involved in the reactions. Especially silicon, sulfur, and antimony seem to be highly susceptible to oxygenation, oxidation, and reduction, respectively. We note that the (electro)chemical reduction of Sb^{5+} to Sb^{3+} might be correlated with the oxidation of S^{2-}, leading to some kind of internal (irreversible) redox process, as also observed for other lithium thiophosphates.[69,70]

In summary, we have successfully synthesized a compositionally complex lithium argyrodite SE by partially substituting phosphorus with other elements in an equimolar manner. The material showed a high ionic conductivity at room temperature (∼13 mS cm^{-1}), along with very low activation energy for conduction (∼0.2 eV), similar to the best-performing lithium argyrodites reported so far (Table S7). The properties arise from distinct structural features induced by the multicationic substitution. High S^{2-}/I^- site inversion was achieved (11%, among the highest values reported in the literature for $Li_{6+a}P_{1-x}M_xS_5I$ materials),[16,21] which has been shown to energetically facilitate intercage jumps and to be beneficial to long-range lithium diffusion.[20,21,58] In addition, multicationic substitution led to a redistribution of Li over the respective 24*g* and 48*h* sites. Specifically, the 24*g* site occupancy was much increased, thereby decreasing the intercage jump distances. A low activation energy seems to be one of the key features of high-entropy Li-ion conductors.[23,71] Taken together, the unique charge-transport characteristics of $Li_{6.5}[P_{0.25}Si_{0.25}Ge_{0.25}Sb_{0.25}]S_5I$ result from a combination of favorable (local) structural changes to the Li sublattice and lattice softening because of the presence of various different elements. The material was also tested as a potential SE for use in bulk-type SSBs with a Ni-rich NCM cathode and LTO

https://doi.org/10.1021/acsmaterialslett.2c00667
ACS Materials Lett. 2022, 4, 2187−2194

anode. However, it was found to be prone to (electro)chemical degradation, even though the CAM employed was protected by a coating of $LiNbO_3$. The latter prevents direct contact with the SE and usually helps to mitigate interfacial stability problems.

The results of this study might pave the way for designing advanced SEs that not only exhibit a high ionic conductivity but are also (electro)chemically stable (essential for practical applications). In particular, we have shown that complex substitution in superionic lithium argyrodites leads to a low activation energy for Li diffusion and further identified specific elemental constituents that negatively affect battery performance. Considering the large compositional space available, multicationic substituted lithium argyrodites can be seen as providing a starting point for tailoring the key properties (by opening up a new playground with infinite possibilities).

■ ASSOCIATED CONTENT

Supporting Information

The Supporting Information is available free of charge at https://pubs.acs.org/doi/10.1021/acsmaterialslett.2c00667.

Experimental section (including details on synthesis, characterization, calculation of configurational entropy, and quantitative XPS analysis), laboratory XRD pattern, structural parameters, Li occupancies, ICP-OES results, additional XPS detail spectra, temperature-dependent diffusion coefficient from ^{7}Li PFG NMR spectroscopy, EIS spectra, and tables showing other compositions targeted in the synthesis, Li−Li jump distances, atomic percentages from quantitative XPS analysis, ionic/electronic conductivities, and activation energies for various lithium argyrodites (PDF)

■ AUTHOR INFORMATION

Corresponding Authors

Torsten Brezesinski − *Battery and Electrochemistry Laboratory, Institute of Nanotechnology, Karlsruhe Institute of Technology, 76344 Eggenstein-Leopoldshafen, Germany;* orcid.org/0000-0002-4336-263X; Email: torsten.brezesinski@kit.edu

Florian Strauss − *Battery and Electrochemistry Laboratory, Institute of Nanotechnology, Karlsruhe Institute of Technology, 76344 Eggenstein-Leopoldshafen, Germany;* orcid.org/0000-0001-5817-6349; Email: florian.strauss@kit.edu

Authors

Jing Lin − *Battery and Electrochemistry Laboratory, Institute of Nanotechnology, Karlsruhe Institute of Technology, 76344 Eggenstein-Leopoldshafen, Germany*

Gennady Cherkashinin − *Institute for Materials Science, Technical University Darmstadt, 64287 Darmstadt, Germany;* orcid.org/0000-0001-8363-6028

Mareen Schäfer − *Institute for Applied Materials−Energy Storage Systems, Karlsruhe Institute of Technology, 76344 Eggenstein-Leopoldshafen, Germany;* orcid.org/0000-0001-6589-2087

Georgian Melinte − *Institute of Nanotechnology, Karlsruhe Institute of Technology, 76344 Eggenstein-Leopoldshafen, Germany*

Sylvio Indris − *Institute for Applied Materials−Energy Storage Systems, Karlsruhe Institute of Technology, 76344 Eggenstein-Leopoldshafen, Germany; Helmholtz Institute Ulm Electrochemical Energy Storage, 89081 Ulm, Germany;* orcid.org/0000-0002-5100-113X

Aleksandr Kondrakov − *Battery and Electrochemistry Laboratory, Institute of Nanotechnology, Karlsruhe Institute of Technology, 76344 Eggenstein-Leopoldshafen, Germany; BASF SE, 67056 Ludwigshafen, Germany;* orcid.org/0000-0003-1465-2854

Jürgen Janek − *Battery and Electrochemistry Laboratory, Institute of Nanotechnology, Karlsruhe Institute of Technology, 76344 Eggenstein-Leopoldshafen, Germany; Institute of Physical Chemistry & Center for Materials Research, Justus-Liebig-University Giessen, 35392 Giessen, Germany;* orcid.org/0000-0002-9221-4756

Complete contact information is available at: https://pubs.acs.org/10.1021/acsmaterialslett.2c00667

Notes

The authors declare no competing financial interest.

■ ACKNOWLEDGMENTS

J.L. acknowledges the Fonds der Chemischen Industrie (FCI) for financial support. F.S. is grateful to the FCI for financial support through a Liebig fellowship. This work was partially supported by BASF SE. The authors thank Dr. C. Ritter for collecting the NPD data and Institute Laue-Langevin (ILL) for beamtime allocation under proposal number (5-21-1164) (DOI: 10.5291/ILL-DATA.5-21-1164). Dr. T. Bergfeldt is acknowledged for conducting the ICP-OES analysis. TEM data were acquired at the Karlsruhe Nano Micro Facility (KNMFi, www.knmf.kit.edu), a Helmholtz research infrastructure at Karlsruhe Institute of Technology (KIT, www.kit.edu).

■ REFERENCES

(1) Myung, S.-T.; Maglia, F.; Park, K.-J.; Yoon, C. S.; Lamp, P.; Kim, S.-J.; Sun, Y.-K. Nickel-Rich Layered Cathode Materials for Automotive Lithium-Ion Batteries: Achievements and Perspectives. *ACS Energy Lett.* **2017**, *2*, 196−223.

(2) Sun, Y.-K. High-Capacity Layered Cathodes for Next-Generation Electric Vehicles. *ACS Energy Lett.* **2019**, *4*, 1042−1044.

(3) Janek, J.; Zeier, W. G. A Solid Future for Battery Development. *Nat. Energy* **2016**, *1*, 16141.

(4) Robinson, A. L.; Janek, J. Solid-State Batteries Enter EV Fray. *MRS Bull.* **2014**, *39*, 1046−1047.

(5) Kato, Y.; Hori, S.; Saito, T.; Suzuki, K.; Hirayama, M.; Mitsui, A.; Yonemura, M.; Iba, H.; Kanno, R. High-Power All-Solid-State Batteries Using Sulfide Superionic Conductors. *Nat. Energy* **2016**, *1*, 16030.

(6) Lee, Y.-G.; Fujiki, S.; Jung, C.; Suzuki, N.; Yashiro, N.; Omoda, R.; Ko, D.-S.; Shiratsuchi, T.; Sugimoto, T.; Ryu, S.; Ku, J. H.; Watanabe, T.; Park, Y.; Aihara, Y.; Im, D.; Han, I. T. High-Energy Long-Cycling All-Solid-State Lithium Metal Batteries Enabled by Silver−Carbon Composite Anodes. *Nat. Energy* **2020**, *5*, 299−308.

(7) Gao, Z.; Sun, H.; Fu, L.; Ye, F.; Zhang, Y.; Luo, W.; Huang, Y. Promises, Challenges, and Recent Progress of Inorganic Solid-State Electrolytes for All-Solid-State Lithium Batteries. *Adv. Mater.* **2018**, *30*, 1705702.

(8) Lau, J.; DeBlock, R. H.; Butts, D. M.; Ashby, D. S.; Choi, C. S.; Dunn, B. S. Sulfide Solid Electrolytes for Lithium Battery Applications. *Adv. Energy Mater.* **2018**, *8*, 1800933.

(9) Reddy, M. V.; Julien, C. M.; Mauger, A.; Zaghib, K. Sulfide and Oxide Inorganic Solid Electrolytes for All-Solid-State Li Batteries: A Review. *Nanomaterials* **2020**, *10*, 1606.

(10) Zhang, Z.; Shao, Y.; Lotsch, B.; Hu, Y.-S.; Li, H.; Janek, J.; Nazar, L. F.; Nan, C.-W.; Maier, J.; Armand, M.; Chen, L. New

Horizons for Inorganic Solid State Ion Conductors. *Energy Environ. Sci.* **2018**, *11*, 1945−1976.
(11) Bai, X.; Duan, Y.; Zhuang, W.; Yang, R.; Wang, J. Research Progress in Li-Argyrodite-Based Solid-State Electrolytes. *J. Mater. Chem. A* **2020**, *8*, 25663−25686.
(12) Yu, C.; Zhao, F.; Luo, J.; Zhang, L.; Sun, X. Recent Development of Lithium Argyrodite Solid-State Electrolytes for Solid-State Batteries: Synthesis, Structure, Stability and Dynamics. *Nano Energy* **2021**, *83*, 105858.
(13) Zhou, L.; Minafra, N.; Zeier, W. G.; Nazar, L. F. Innovative Approaches to Li-Argyrodite Solid Electrolytes for All-Solid-State Lithium Batteries. *Acc. Chem. Res.* **2021**, *54*, 2717−2728.
(14) Deiseroth, H.-J.; Kong, S.-T.; Eckert, H.; Vannahme, J.; Reiner, C.; Zaiß, T.; Schlosser, M. Li_6PS_5X: A Class of Crystalline Li-Rich Solids With an Unusually High Li^+ Mobility. *Angew. Chem., Int. Ed.* **2008**, *47*, 755−758.
(15) Kong, S.-T.; Deiseroth, H.-J.; Reiner, C.; Gün, Ö.; Neumann, E.; Ritter, C.; Zahn, D. Lithium Argyrodites with Phosphorus and Arsenic: Order and Disorder of Lithium Atoms, Crystal Chemistry, and Phase Transitions. *Chem.-Eur. J.* **2010**, *16*, 2198−2206.
(16) Zhou, L.; Assoud, A.; Zhang, Q.; Wu, X.; Nazar, L. F. New Family of Argyrodite Thioantimonate Lithium Superionic Conductors. *J. Am. Chem. Soc.* **2019**, *141*, 19002−19013.
(17) Hogrefe, K.; Minafra, N.; Hanghofer, I.; Banik, A.; Zeier, W. G.; Wilkening, H. M. R. Opening Diffusion Pathways through Site Disorder: The Interplay of Local Structure and Ion Dynamics in the Solid Electrolyte $Li_{6+x}P_{1-x}Ge_xS_5I$ as Probed by Neutron Diffraction and NMR. *J. Am. Chem. Soc.* **2022**, *144*, 1795−1812.
(18) Zhao, E.; He, L.; Zhang, Z.; Doux, J.-M.; Tan, D. H. S.; Wu, E. A.; Deysher, G.; Chen, Y.-T.; Zhao, J.; Wang, F.; Meng, Y. S. New Insights into Li Distribution in the Superionic Argyrodite Li_6PS_5Cl. *Chem. Commun.* **2021**, *57*, 10787−10790.
(19) Minafra, N.; Kraft, M. A.; Bernges, T.; Li, C.; Schlem, R.; Morgan, B. J.; Zeier, W. G. Local Charge Inhomogeneity and Lithium Distribution in the Superionic Argyrodites Li_6PS_5X (X = Cl, Br, I). *Inorg. Chem.* **2020**, *59*, 11009−11019.
(20) Kraft, M. A.; Ohno, S.; Zinkevich, T.; Koerver, R.; Culver, S. P.; Fuchs, T.; Senyshyn, A.; Indris, S.; Morgan, B. J.; Zeier, W. G. Inducing High Ionic Conductivity in the Lithium Superionic Argyrodites $Li_{6+x}P_{1-x}Ge_xS_5I$ for All-Solid-State Batteries. *J. Am. Chem. Soc.* **2018**, *140*, 16330−16339.
(21) Ohno, S.; Helm, B.; Fuchs, T.; Dewald, G.; Kraft, M. A.; Culver, S. P.; Senyshyn, A.; Zeier, W. G. Further Evidence for Energy Landscape Flattening in the Superionic Argyrodites $Li_{6+x}P_{1-x}M_xS_5I$ (M = Si, Ge, Sn). *Chem. Mater.* **2019**, *31*, 4936−4944.
(22) Minafra, N.; Culver, S. P.; Krauskopf, T.; Senyshyn, A.; Zeier, W. G. Effect of Si Substitution on the Structural and Transport Properties of Superionic Li-Argyrodites. *J. Mater. Chem. A* **2018**, *6*, 645−651.
(23) Strauss, F.; Lin, J.; Duffiet, M.; Wang, K.; Zinkevich, T.; Hansen, A.-L.; Indris, S.; Brezesinski, T. High-Entropy Polyanionic Lithium Superionic Conductors. *ACS Mater. Lett.* **2022**, *4*, 418−423.
(24) Behera, A. High Entropy Materials. In *Advanced Materials: An Introduction to Modern Materials Science;* Behera, A., Ed.; Springer International Publishing: Cham, Switzerland, 2022; pp 291−320.
(25) Ma, Y.; Ma, Y.; Wang, Q.; Schweidler, S.; Botros, M.; Fu, T.; Hahn, H.; Brezesinski, T.; Breitung, B. High-Entropy Energy Materials: Challenges and New Opportunities. *Energy Environ. Sci.* **2021**, *14*, 2883−2905.
(26) Sarkar, A.; Breitung, B.; Hahn, H. High Entropy Oxides: The Role of Entropy, Enthalpy and Synergy. *Scr. Mater.* **2020**, *187*, 43−48.
(27) Zhang, R.-Z.; Reece, M. J. Review of High Entropy Ceramics: Design, Synthesis, Structure and Properties. *J. Mater. Chem. A* **2019**, *7*, 22148−22162.
(28) Sarkar, A.; Wang, Q.; Schiele, A.; Chellali, M. R.; Bhattacharya, S. S.; Wang, D.; Brezesinski, T.; Hahn, H.; Velasco, L.; Breitung, B. High-Entropy Oxides: Fundamental Aspects and Electrochemical Properties. *Adv. Mater.* **2019**, *31*, 1806236.
(29) Oses, C.; Toher, C.; Curtarolo, S. High-Entropy Ceramics. *Nat. Rev. Mater.* **2020**, *5*, 295−309.
(30) Lun, Z.; Ouyang, B.; Kwon, D.-H.; Ha, Y.; Foley, E. E.; Huang, T.-Y.; Cai, Z.; Kim, H.; Balasubramanian, M.; Sun, Y.; Huang, J.; Tian, Y.; Kim, H.; McCloskey, B. D.; Yang, W.; Clément, R. J.; Ji, H.; Ceder, G. Cation-Disordered Rocksalt-Type High-Entropy Cathodes for Li-Ion Batteries. *Nat. Mater.* **2021**, *20*, 214−221.
(31) Lin, L.; Wang, K.; Sarkar, A.; Njel, C.; Karkera, G.; Wang, Q.; Azmi, R.; Fichtner, M.; Hahn, H.; Schweidler, S.; Breitung, B. High-Entropy Sulfides as Electrode Materials for Li-Ion Batteries. *Adv. Energy Mater.* **2022**, *12*, 2103090.
(32) Chen, R.; Qiu, P.; Jiang, B.; Hu, P.; Zhang, Y.; Yang, J.; Ren, D.; Shi, X.; Chen, L. Significantly Optimized Thermoelectric Properties in High-Symmetry Cubic Cu_7PSe_6 Compounds *via* Entropy Engineering. *J. Mater. Chem. A* **2018**, *6*, 6493−6502.
(33) Sarkar, A.; Velasco, L.; Wang, D.; Wang, Q.; Talasila, G.; de Biasi, L.; Kübel, C.; Brezesinski, T.; Bhattacharya, S. S.; Hahn, H.; Breitung, B. High Entropy Oxides for Reversible Energy Storage. *Nat. Commun.* **2018**, *9*, 3400.
(34) Zhao, C.; Ding, F.; Lu, Y.; Chen, L.; Hu, Y.-S. High-Entropy Layered Oxide Cathodes for Sodium-Ion Batteries. *Angew. Chem., Int. Ed.* **2020**, *59*, 264−269.
(35) Yang, L.; Chen, C.; Xiong, S.; Zheng, C.; Liu, P.; Ma, Y.; Xu, W.; Tang, Y.; Ong, S. P.; Chen, H. Multiprincipal Component P2-$Na_{0.6}(Ti_{0.2}Mn_{0.2}Co_{0.2}Ni_{0.2}Ru_{0.2})O_2$ as a High-Rate Cathode for Sodium-Ion Batteries. *JACS Au* **2021**, *1*, 98−107.
(36) Fu, F.; Liu, X.; Fu, X.; Chen, H.; Huang, L.; Fan, J.; Le, J.; Wang, Q.; Yang, W.; Ren, Y.; Amine, K.; Sun, S.-G.; Xu, G.-L. Entropy and Crystal-Facet Modulation of P2-Type Layered Cathodes for Long-Lasting Sodium-Based Batteries. *Nat. Commun.* **2022**, *13*, 2826.
(37) Ma, Y.; Hu, Y.; Pramudya, Y.; Diemant, T.; Wang, Q.; Goonetilleke, D.; Tang, Y.; Zhou, B.; Hahn, H.; Wenzel, W.; Fichtner, M.; Ma, Y.; Breitung, B.; Brezesinski, T. Resolving the Role of Configurational Entropy in Improving Cycling Performance of Multicomponent Hexacyanoferrate Cathodes for Sodium-Ion Batteries. *Adv. Funct. Mater.* **2022**, *32*, 2202372.
(38) Ma, Y.; Ma, Y.; Dreyer, S. L.; Wang, Q.; Wang, K.; Goonetilleke, D.; Omar, A.; Mikhailova, D.; Hahn, H.; Breitung, B.; Brezesinski, T. High-Entropy Metal−Organic Frameworks for Highly Reversible Sodium Storage. *Adv. Mater.* **2021**, *33*, 2101342.
(39) Wang, J.; Cui, Y.; Wang, Q.; Wang, K.; Huang, X.; Stenzel, D.; Sarkar, A.; Azmi, R.; Bergfeldt, T.; Bhattacharya, S. S.; Kruk, R.; Hahn, H.; Schweidler, S.; Brezesinski, T.; Breitung, B. Lithium Containing Layered High Entropy Oxide Structures. *Sci. Rep.* **2020**, *10*, 18430.
(40) Harm, S.; Hatz, A.-K.; Moudrakovski, I.; Eger, R.; Kuhn, A.; Hoch, C.; Lotsch, B. V. Lesson Learned from NMR: Characterization and Ionic Conductivity of LGPS-like Li_7SiPS_8. *Chem. Mater.* **2019**, *31*, 1280−1288.
(41) Dietrich, C.; Sadowski, M.; Sicolo, S.; Weber, D. A.; Sedlmaier, S. J.; Weldert, K. S.; Indris, S.; Albe, K.; Janek, J.; Zeier, W. G. Local Structural Investigations, Defect Formation, and Ionic Conductivity of the Lithium Ionic Conductor $Li_4P_2S_6$. *Chem. Mater.* **2016**, *28*, 8764−8773.
(42) Lee, Y.; Jeong, J.; Lee, H. J.; Kim, M.; Han, D.; Kim, H.; Yuk, J. M.; Nam, K.-W.; Chung, K. Y.; Jung, H.-G.; Yu, S. Lithium Argyrodite Sulfide Electrolytes with High Ionic Conductivity and Air Stability for All-Solid-State Li-Ion Batteries. *ACS Energy Lett.* **2022**, *7*, 171−179.
(43) Zakaznova-Herzog, V. P.; Harmer, S. L.; Nesbitt, H. W.; Bancroft, G. M.; Flemming, R.; Pratt, A. R. High Resolution XPS Study of the Large-Band-Gap Semiconductor Stibnite (Sb_2S_3): Structural Contributions and Surface Reconstruction. *Surf. Sci.* **2006**, *600*, 348−356.
(44) Wang, L.; Yang, B.; Xia, Z.; Leng, M.; Zhou, Y.; Xue, D.-J.; Zhong, J.; Gao, L.; Song, H.; Tang, J. Synthesis and Characterization of Hydrazine Solution Processed $Cu_{12}Sb_4S_{13}$ Film. *Sol. Energy Mater. Sol. Cells* **2016**, *144*, 33−39.
(45) Avilez Garcia, R. G.; Meza Avendaño, C. A.; Pal, M.; Paraguay Delgado, F.; Mathews, N. R. Antimony Sulfide (Sb_2S_3) Thin Films by

https://doi.org/10.1021/acsmaterialslett.2c00667
ACS Materials Lett. 2022, 4, 2187−2194

Pulse Electrodeposition: Effect of Thermal Treatment on Structural, Optical and Electrical Properties. *Mater. Sci. Semicond. Process.* **2016**, *44*, 91−100.
(46) Teo, J. H.; Strauss, F.; Walther, F.; Ma, Y.; Payandeh, S.; Scherer, T.; Bianchini, M.; Janek, J.; Brezesinski, T. The Interplay between (Electro)Chemical and (Chemo)Mechanical Effects in the Cycling Performance of Thiophosphate-Based Solid-State Batteries. *Mater. Futures* **2022**, *1*, 015102.
(47) Ma, Y.; Teo, J. H.; Kitsche, D.; Diemant, T.; Strauss, F.; Ma, Y.; Goonetilleke, D.; Janek, J.; Bianchini, M.; Brezesinski, T. Cycling Performance and Limitations of $LiNiO_2$ in Solid-State Batteries. *ACS Energy Lett.* **2021**, *6*, 3020−3028.
(48) Auvergniot, J.; Cassel, A.; Ledeuil, J.-B.; Viallet, V.; Seznec, V.; Dedryvère, R. Interface Stability of Argyrodite Li_6PS_5Cl toward $LiCoO_2$, $LiNi_{1/3}Co_{1/3}Mn_{1/3}O_2$, and $LiMn_2O_4$ in Bulk All-Solid-State Batteries. *Chem. Mater.* **2017**, *29*, 3883−3890.
(49) Liang, J.; Li, X.; Zhao, Y.; Goncharova, L. V.; Li, W.; Adair, K. R.; Banis, M. N.; Hu, Y.; Sham, T.-K.; Huang, H.; Zhang, L.; Zhao, S.; Lu, S.; Li, R.; Sun, X. An Air-Stable and Dendrite-Free Li Anode for Highly Stable All-Solid-State Sulfide-Based Li Batteries. *Adv. Energy Mater.* **2019**, *9*, 1902125.
(50) Foix, D.; Gonbeau, D.; Taillades, G.; Pradel, A.; Ribes, M. The Structure of Ionically Conductive Chalcogenide Glasses: A Combined NMR, XPS and Ab Initio Calculation Study. *Solid State Sci.* **2001**, *3*, 235−243.
(51) Ingo, G. M.; Dirè, S.; Babonneau, F. XPS Studies of SiO_2-TiO_2 Powders Prepared by Sol-Gel Process. *Appl. Surf. Sci.* **1993**, *70*−*71*, 230−234.
(52) Tunc, I.; Suzer, S.; Correa-Duarte, M. A.; Liz-Marzán, L. M. XPS Characterization of Au (Core)/SiO_2 (Shell) Nanoparticles. *J. Phys. Chem. B* **2005**, *109*, 7597−7600.
(53) Kim, S.; Kim, S.-K.; Sun, P.; Oh, N.; Braun, P. V. Reduced Graphene Oxide/LiI Composite Lithium Ion Battery Cathodes. *Nano Lett.* **2017**, *17*, 6893−6899.
(54) Strydom, C. A.; van Staden, J. F.; Strydom, H. J. An XPS Investigation of the Influence of Bromide and Iodide Solutions on the Surface of Silver Chloride Coated Ion-Selective Electrodes. *Electroanalysis* **1991**, *3*, 197−201.
(55) Zhang, W.; Leichtweiß, T.; Culver, S. P.; Koerver, R.; Das, D.; Weber, D. A.; Zeier, W. G.; Janek, J. The Detrimental Effects of Carbon Additives in $Li_{10}GeP_2S_{12}$-Based Solid-State Batteries. *ACS Appl. Mater. Interfaces* **2017**, *9*, 35888−35896.
(56) Zhang, W.; Richter, F. H.; Culver, S. P.; Leichtweiss, T.; Lozano, J. G.; Dietrich, C.; Bruce, P. G.; Zeier, W. G.; Janek, J. Degradation Mechanisms at the $Li_{10}GeP_2S_{12}/LiCoO_2$ Cathode Interface in an All-Solid-State Lithium-Ion Battery. *ACS Appl. Mater. Interfaces.* **2018**, *10*, 22226−22236.
(57) Mori, D.; Oka, H.; Hosoi, T.; Kawai, K.; Morita, M.; Crumlin, E. J.; Liu, Z.; Watanabe, H.; Arima, K. Comparative Study of GeO_2/Ge and SiO_2/Si Structures on Anomalous Charging of Oxide Films upon Water Adsorption Revealed by Ambient-Pressure X-Ray Photoelectron Spectroscopy. *J. Appl. Phys.* **2016**, *120*, 095306.
(58) Adeli, P.; Bazak, J. D.; Park, K. H.; Kochetkov, I.; Huq, A.; Goward, G. R.; Nazar, L. F. Boosting Solid-State Diffusivity and Conductivity in Lithium Superionic Argyrodites by Halide Substitution. *Angew. Chem., Int. Ed.* **2019**, *58*, 8681−8686.
(59) Kuhn, A.; Duppel, V.; Lotsch, B. V. Tetragonal $Li_{10}GeP_2S_{12}$ and Li_7GePS_8 − Exploring the Li Ion Dynamics in LGPS Li Electrolytes. *Energy Environ. Sci.* **2013**, *6*, 3548−3552.
(60) Kuhn, A.; Gerbig, O.; Zhu, C.; Falkenberg, F.; Maier, J.; Lotsch, B. V. A New Ultrafast Superionic Li-Conductor: Ion Dynamics in $Li_{11}Si_2PS_{12}$ and Comparison with Other Tetragonal LGPS-Type Electrolytes. *Phys. Chem. Chem. Phys.* **2014**, *16*, 14669−14674.
(61) Sedlmaier, S. J.; Indris, S.; Dietrich, C.; Yavuz, M.; Dräger, C.; von Seggern, F.; Sommer, H.; Janek, J. Li_4PS_4I: A Li^+ Superionic Conductor Synthesized by a Solvent-Based Soft Chemistry Approach. *Chem. Mater.* **2017**, *29*, 1830−1835.
(62) Strauss, F.; Zinkevich, T.; Indris, S.; Brezesinski, T. Li_7GeS_5Br−An Argyrodite Li-Ion Conductor Prepared by Mechanochemical Synthesis. *Inorg. Chem.* **2020**, *59*, 12954−12959.
(63) Walther, F.; Randau, S.; Schneider, Y.; Sann, J.; Rohnke, M.; Richter, F. H.; Zeier, W. G.; Janek, J. Influence of Carbon Additives on the Decomposition Pathways in Cathodes of Lithium Thiophosphate-Based All-Solid-State Batteries. *Chem. Mater.* **2020**, *32*, 6123−6136.
(64) Walther, F.; Koerver, R.; Fuchs, T.; Ohno, S.; Sann, J.; Rohnke, M.; Zeier, W. G.; Janek, J. Visualization of the Interfacial Decomposition of Composite Cathodes in Argyrodite-Based All-Solid-State Batteries Using Time-of-Flight Secondary-Ion Mass Spectrometry. *Chem. Mater.* **2019**, *31*, 3745−3755.
(65) Bartsch, T.; Strauss, F.; Hatsukade, T.; Schiele, A.; Kim, A.-Y.; Hartmann, P.; Janek, J.; Brezesinski, T. Gas Evolution in All-Solid-State Battery Cells. *ACS Energy Lett.* **2018**, *3*, 2539−2543.
(66) Kim, A.-Y.; Strauss, F.; Bartsch, T.; Teo, J. H.; Hatsukade, T.; Mazilkin, A.; Janek, J.; Hartmann, P.; Brezesinski, T. Stabilizing Effect of a Hybrid Surface Coating on a Ni-Rich NCM Cathode Material in All-Solid-State Batteries. *Chem. Mater.* **2019**, *31*, 9664−9672.
(67) Strauss, F.; Teo, J. H.; Maibach, J.; Kim, A.-Y.; Mazilkin, A.; Janek, J.; Brezesinski, T. Li_2ZrO_3-Coated NCM622 for Application in Inorganic Solid-State Batteries: Role of Surface Carbonates in the Cycling Performance. *ACS Appl. Mater. Interfaces* **2020**, *12*, 57146−57154.
(68) Strauss, F.; Payandeh, S.; Kondrakov, A.; Brezesinski, T. On the Role of Surface Carbonate Species in Determining the Cycling Performance of All-Solid-State Batteries. *Mater. Futures* **2022**, *1*, 023501.
(69) Koerver, R.; Walther, F.; Aygün, I.; Sann, J.; Dietrich, C.; Zeier, W. G.; Janek, J. Redox-Active Cathode Interphases in Solid-State Batteries. *J. Mater. Chem. A* **2017**, *5*, 22750−22760.
(70) Auvergniot, J.; Cassel, A.; Foix, D.; Viallet, V.; Seznec, V.; Dedryvère, R. Redox Activity of Argyrodite Li_6PS_5Cl Electrolyte in All-Solid-State Li-Ion Battery: An XPS Study. *Solid State Ion.* **2017**, *300*, 78−85.
(71) Zhao, G.; Suzuki, K.; Okumura, T.; Takeuchi, T.; Hirayama, M.; Kanno, R. Extending the Frontiers of Lithium-Ion Conducting Oxides: Development of Multicomponent Materials with γ-Li_3PO_4-Type Structures. *Chem. Mater.* **2022**, *34*, 3948−3959.

https://doi.org/10.1021/acsmaterialslett.2c00667
ACS Materials Lett. 2022, 4, 2187−2194

3.3. Publication III: Tuning Lithium-Ion Mobility in Argyrodite Solid Electrolytes via Entropy Engineering

Publication III, a follow-up to Publication II (3.2.), further explores complex substituted lithium argyrodites (Table 1) through varying the stoichiometry of $Li_{6.5}[P_{0.25}Si_{0.25}Ge_{0.25}Sb_{0.25}]S_5I$ (details see Publication II), achieving the highest bulk ionic conductivity around 18 mS cm^{-1} for $Li_{6.66}[P_{0.167}Si_{0.5}Ge_{0.167}Sb_{0.167}]S_5I$. Using powder diffraction techniques (NPD and SXRD), ^{6}Li MAS-NMR and charge transport characterization (EIS and ^{7}Li PFG-NMR), the research revealed no apparent correlation between structural parameters and Li-ion transport properties. Instead, the study found that increasing the Li content (to 6.5 mol per unit cell) is associated with higher ionic conductivity (~10 mS cm^{-1}), while an increase in ΔS_{conf} results in a lower activation energy (~0.20 eV). Moreover, compared with reported lithium argyrodites, an elevated configurational entropy demonstrates the capability of enhancing Li-ion mobility.

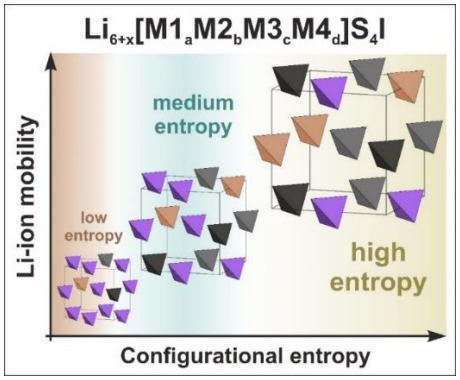

Figure 20: Table of Contents (TOC) of Publication III. Adapted from reference [21].

The experiments were planned and designed by the first author, J. Lin, under the supervision of J. Janek, T. Brezesinski and F. Strauss. The NPD measurements were primarily conducted at the Swiss spallation neutron source (SINQ), Paul Scherrer Institute (PSI) with the proposal number 20051234. Additionally, one NPD measurement was carried out at PEARL neutron source, Delft University of Technology, with the assistance from A. Gautam. J. Lin analyzed the NPD results. The SXRD measurements were performed at beamline P02.1, PETRA III, DESY with the assistance from V. Baran and the data analysis was conducted by J. Lin. J. Lin carried out the EIS experiments and analyzed the data. M. Schaller conducted the ^{7}Li PFG-NMR measurements and analyzed the data together with J. Lin. S. Indris carried out the MAS NMR spectroscopy experiments. The first draft was written by J. Lin. The final paper was then edited by all co-authors.

GDCh Research Article Angewandte International Edition Chemie www.angewandte.org

How to cite: *Angew. Chem. Int. Ed.* **2024**, *63*, e202404874
doi.org/10.1002/anie.202404874

Solid-state Electrolytes

Tuning Ion Mobility in Lithium Argyrodite Solid Electrolytes via Entropy Engineering

Jing Lin, Mareen Schaller, Sylvio Indris, Volodymyr Baran, Ajay Gautam, Jürgen Janek, Aleksandr Kondrakov, Torsten Brezesinski, and Florian Strauss**

Abstract: The development of improved solid electrolytes (SEs) plays a crucial role in the advancement of bulk-type solid-state battery (SSB) technologies. In recent years, multicomponent or high-entropy SEs are gaining increased attention for their advantageous charge-transport and (electro)chemical properties. However, a comprehensive understanding of how configurational entropy affects ionic conductivity is largely lacking. Herein we investigate a series of multication-substituted lithium argyrodites with the general formula $Li_{6+x}[M1_aM2_bM3_cM4_d]S_5I$, with M being P, Si, Ge, and Sb. Structure-property relationships related to ion mobility are probed using a combination of diffraction techniques, solid-state nuclear magnetic resonance spectroscopy, and charge-transport measurements. We present, to the best of our knowledge, the first experimental evidence of a direct correlation between occupational disorder in the cationic host lattice and lithium transport. By controlling the configurational entropy through compositional design, high bulk ionic conductivities up to 18 mS cm^{-1} at room temperature are achieved for optimized lithium argyrodites. Our results indicate the possibility of improving ionic conductivity in ceramic ion conductors via entropy engineering, overcoming compositional limitations for the design of advanced electrolytes and opening up new avenues in the field.

Introduction

With the growing demand for mature electrochemical energy-storage devices, solid-state batteries (SSBs) have emerged as a promising technology due to their high (practical) energy and powder densities and improved safety. Ion conductors with superionic conductivity, good (electro)chemical stability, and easy processability are key enablers for such technology.[1,2] Currently, different material classes such as sulfides, halides, hydrides, and oxides are under investigation, with each of them having advantages and disadvantages.[2,3] Among them, lithium thiophosphates, including $Li_{10}GeP_2S_{12}$, Li_2S–P_2S_5 glasses, and argyrodite Li_6PS_5X (X=Cl, Br, I), have attracted considerable attention owing to high room-temperature ionic conductivities, which are comparable to those of liquid electrolytes, along with mechanical softness.[3,4]

Lithium argyrodites are built up from $[PS_4]^{3-}$ tetrahedral units, free X^- and S^{2-} ions forming a cubic crystal skeleton, and Li^+ being located on different partially occupied crystallographic sites, thereby offering a framework for fast ion diffusion.[5,6] Starting from the initially reported, poorly conducting lithium argyrodite Li_6PS_5I, the conductivity could be significantly improved via substitution on the phosphorus site. For example, high ionic conductivities have been reported for $Li_{6.6}P_{0.4}Ge_{0.6}S_5I$ (5.4 mS cm^{-1}, cold-pressed state) or $Li_{6.7}Si_{0.7}Sb_{0.3}S_5I$ (12.6 mS cm^{-1}, cold-pressed state) and rationalized by facilitated lithium diffusion enabled by increased S^{2-}/I^- site inversion and/or occupation of additional lithium positions and therefore shortened Li–Li intercage jump distances.[7,8] Achieving high ionic conductivity in argyrodites depends on various parameters such as balanc-

[*] J. Lin, J. Janek, A. Kondrakov, T. Brezesinski, F. Strauss
Battery and Electrochemistry Laboratory (BELLA), Institute of Nanotechnology (INT), Karlsruhe Institute of Technology (KIT), Hermann-von-Helmholtz-Platz 1, 76344 Eggenstein-Leopoldshafen, Germany
E-mail: torsten.brezesinski@kit.edu
florian.strauss@kit.edu

M. Schaller, S. Indris
Institute for Applied Materials—Energy Storage Systems (IAM-ESS), Karlsruhe Institute of Technology (KIT), Hermann-von-Helmholtz-Platz 1, 76344 Eggenstein-Leopoldshafen, Germany

V. Baran
Deutsches Elektronen-Synchrotron DESY, Notkestr. 85, 22607 Hamburg, Germany

A. Gautam
Section Storage of Electrochemical Energy, Radiation Science and Technology, Faculty of Applied Sciences, Delft University of Technology, Delft 2629 JB, The Netherlands

J. Janek
Institute of Physical Chemistry & Center for Materials Research (ZfM/LaMa), Justus-Liebig-University Giessen, Heinrich-Buff-Ring 17, 35392 Giessen, Germany

A. Kondrakov
BASF SE, Carl-Bosch-Str. 38, 67056 Ludwigshafen, Germany

GDCh Research Article Angewandte International Edition Chemie

ing the density of charge carriers and vacancies, altering the polyhedral volume, and introducing site disorder.[4] These factors can broaden the lithium diffusion pathways and shorten the jump distances between the cages, thus positively affecting ion diffusion.[9–11] All of these parameters can be tailored in a given (argyrodite) crystal structure via iso- or aliovalent substitution in the host lattice.[4,12]

Deviating from this rather classical strategy, multielement-substituted (high-entropy) solid electrolytes (SEs) have recently attracted much attention. Such materials are capable of overcoming compositional limitations, which in turn may help to accelerate the development of advanced SEs.[13] Aside from that, high-entropy SEs allow for the possibility of a flattened energy landscape for ion transport through strong (local) lattice distortions.[14–16] The term "high entropy" commonly refers to materials with a configurational entropy of $\Delta S_{conf} \geq 1.5R$, with R representing the gas constant, which can be calculated from shared occupancies over similar crystallographic sites.[13,17] In general, systematic control over ΔS_{conf} through compositional variations, i.e. entropy engineering, has rarely been achieved. Furthermore, the solubility of dopants/substituents in materials can potentially be increased to such an extent that the optimum charge-carrier concentration is achieved and/or improved properties emerge.

With regards to compositionally complex SEs, only a few materials have been reported up until now, including garnet, perovskite, Na SuperIonic CONductor (NASICON), halide, argyrodite, and $Li_{10}GeP_2S_{12}$ (LGPS)-type samples.[15,16,18–26] For high-entropy LGPS-type ($Li_{9.54}[Si_{0.6}Ge_{0.4}]_{1.74}P_{1.44}S_{11.1}Br_{0.3}O_{0.6}$) and lithium argyrodite materials (e.g. $Li_{6.5}[P_{0.25}Si_{0.25}Sb_{0.25}Ge_{0.25}]S_5I$ and $Li_{5.5}PS_{4.5}Cl_{0.8}Br_{0.7}$), high ionic conductivities ($>10\ mS\,cm^{-1}$ at room temperature) could be realized in practice.[15,16,21,23] To unlock the potential of high-entropy ion conductors for SSB application, a detailed understanding of the role of configurational entropy on charge transport, as well as on the (electro)chemical and mechanical properties is required. However, direct correlation between the degree of disorder and the ionic conductivity remains elusive because of the challenge in separating configurational entropy from other effects. Nevertheless, Li et al. have recently reported on the relationship between compositional disorder in the anion sublattice and ionic conductivity of $Li_{5.5}PS_{4.5}Cl_xBr_{1.5-x}$ solid solutions.[23] However, the effect of occupational disorder (configurational entropy) induced by multicationic substitution in lithium argyrodites has not been investigated yet.

In the present work, we attempt to disentangle the effect of configurational entropy on ion mobility in $Li_{6+x}[M1_aM2_bM3_cM4_d]S_5I$ (M=P, Si, Ge, and Sb) from other structural parameters. A series of samples were successfully synthesized and their crystal structure examined through synchrotron X-ray diffraction (SXRD), neutron powder diffraction (NPD), and ^{31}P, ^{29}Si, and ^{6}Li magic-angle spinning (MAS) nuclear magnetic resonance (NMR) spectroscopy measurements. The charge-transport properties were probed using complementary electrochemical impedance spectroscopy (EIS) and ^{7}Li pulsed-field gradient (PFG) NMR spectroscopy. It is shown that structural (occupational) disorder strongly increases the Li-ion conductivity and lowers the energy barrier for diffusion.

Results and Discussion

A series of multication-substituted lithium argyrodites were prepared by high-energy ball milling and post-annealing at 500 °C in vacuum-sealed quartz ampules (see Supporting Information for details). The respective samples are referred to as $P_{0.75}$, $P_{0.5}$, $Si_{0.5}$, EQ, $Ge_{0.5}$, $Sb_{0.5}$, and $Sb_{0.75}$ hereafter (Table 1). Other compositions, which have been synthetically explored but did not yield single-phase materials are reported elsewhere.[15] Structural characterization using laboratory XRD revealed reflections consistent with the cubic argyrodite structure, and the patterns showed a gradual shift in the position of the reflections (Figure S1, Supporting Information). The chemical composition of the samples was studied by inductively coupled plasma-optical emission spectroscopy (ICP-OES), confirming the targeted stoichiometries (Table S1, Supporting Information).

To examine the crystal structure, SXRD and NPD measurements were conducted on the different materials. The room-temperature SXRD and NPD patterns for $Li_{6.66}[P_{0.167}Si_{0.5}Ge_{0.167}Sb_{0.167}]S_5I$ ($Si_{0.5}$), as well as the corresponding Rietveld refinement profiles are shown in Figure 1a and b, respectively. The patterns can be indexed in the $F\text{-}43m$ space group, with lattice parameter $a=$ 10.28599(1) Å and 10.2867(3) Å and cell volume $V=$ 1088.274(2) Å^3 and 1088.51(9) Å^3, respectively. Structural parameters from refinements for all samples are given in Tables S2–S14 (Supporting Information). Notably, the lattice parameters derived from SXRD and NPD are in excellent agreement with one another (Figure S2, Supporting Information). As expected, the observed increase in lattice parameter upon substituting Si^{4+}, Ge^{4+}, and Sb^{5+} for P^{5+} is consistent with variations in ionic radii and stoichiometries, thus confirming successful multicationic substitution.[27] The calculated crystal structure for $Si_{0.5}$ is shown in Figure 1c. Both the S^{2-} and I^- ions form a face-centered cubic sublattice (Wyckoff position 4*a*). Additionally, the S^{2-} and I^- ions also occupy half of the tetrahedral voids (Wyckoff position 4*d*). The rest of the S^{2-} ions resides on the Wyckoff position 16*e* around the octahedral sites (central atom on Wyckoff position 4*b*), forming $[P_{0.167}Si_{0.5}Ge_{0.167}Sb_{0.167}S_4]^{3.66-}$ tetrahedra, which can be consid-

Table 1: The multication-substituted argyrodite SEs prepared and characterized in this work.

Label	Nominal composition
$P_{0.75}$	$Li_{6.17}[\mathbf{P_{0.75}}Si_{0.083}Ge_{0.083}Sb_{0.083}]S_5I$
$P_{0.5}$	$Li_{6.33}[\mathbf{P_{0.5}}Si_{0.167}Ge_{0.167}Sb_{0.167}]S_5I$
$Si_{0.5}$	$Li_{6.66}[P_{0.167}\mathbf{Si_{0.5}}Ge_{0.167}Sb_{0.167}]S_5I$
Equimolar (EQ)	$Li_{6.5}[P_{0.25}Sb_{0.25}Si_{0.25}Ge_{0.25}]S_5I$
$Ge_{0.5}$	$Li_{6.66}[P_{0.167}Si_{0.167}\mathbf{Ge_{0.5}}Sb_{0.167}]S_5I$
$Sb_{0.5}$	$Li_{6.33}[P_{0.167}Si_{0.167}Ge_{0.167}\mathbf{Sb_{0.5}}]S_5I$
$Sb_{0.75}$	$Li_{6.17}[P_{0.083}Si_{0.083}Ge_{0.083}\mathbf{Sb_{0.75}}]S_5I$

GDCh Research Article Angewandte International Edition Chemie

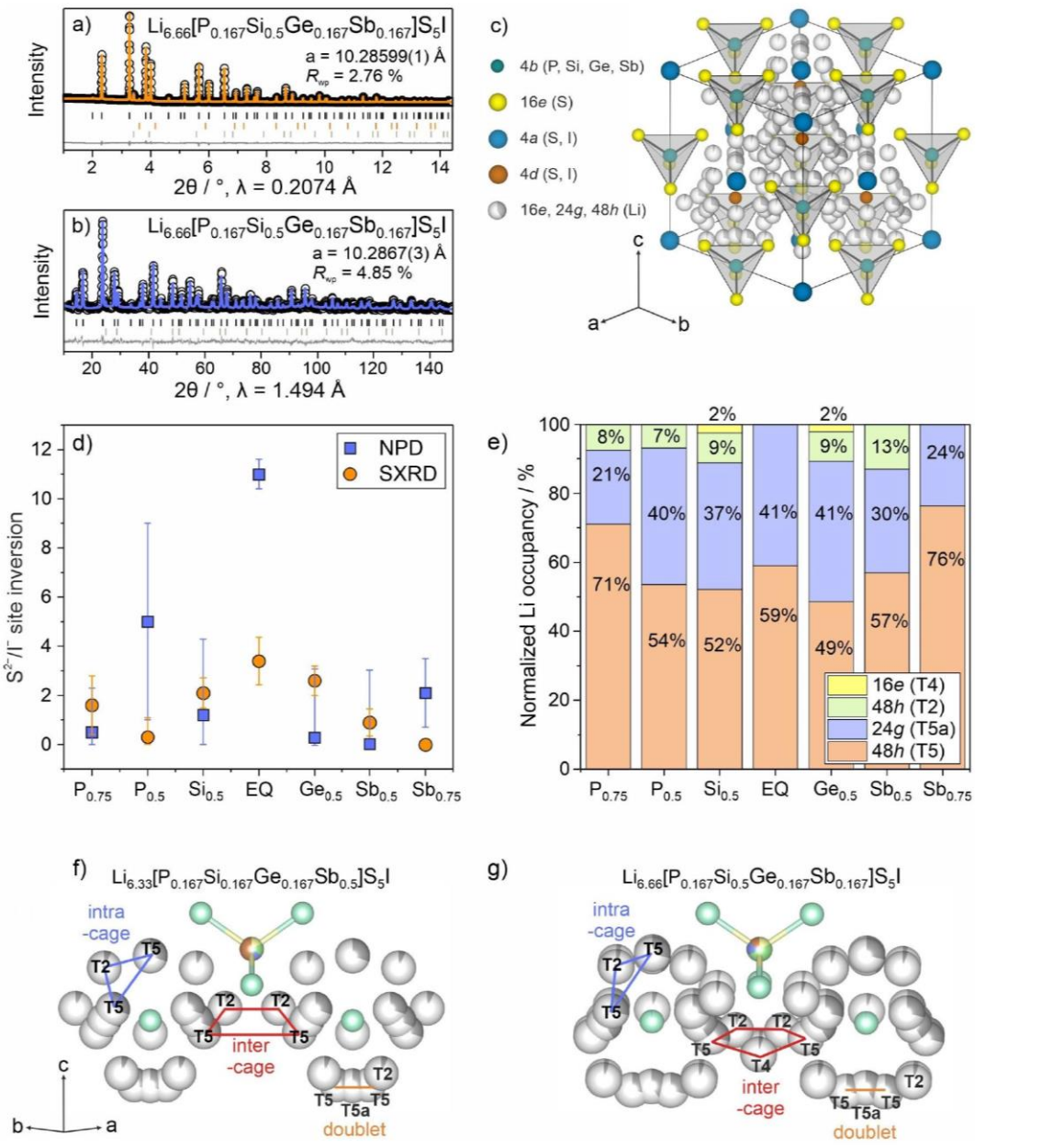

Figure 1. Structural characterization of the multication-substituted argyrodite SEs. (a) SXRD and (b) NPD patterns of $Li_{6.66}[P_{0.167}Si_{0.5}Ge_{0.167}Sb_{0.167}]S_5I$ ($Si_{0.5}$) with corresponding Rietveld refinement profiles. Black circles are the experimental data, orange (SXRD) and blue (NPD) lines the calculated patterns, and gray lines represent the difference profiles. Vertical tick marks denote the position of expected Bragg reflections [black (argyrodite), light gray (LiI), yellow (Li_2S)]. (c) Schematic illustration of the crystal structure for $Si_{0.5}$ with Wyckoff positions and elemental constituents indicated in the legend to the left. (d) Anion site inversion determined by Rietveld analysis of SXRD (orange) and NPD (blue) data. (e) Normalized Li occupancies. (f,g) Schematic illustrations of two neighboring Li cages. The data for EQ in (d) and (e) was taken from the literature.[15,21] If error bars are not visible, the standard deviation is smaller than the data symbol.

ered as a combination of $[PS_4]^{3-}$, $[SiS_4]^{4-}$, $[GeS_4]^{4-}$, and $[SbS_4]^{3-}$. In the argyrodite structure, S^{2-} (4*d*) and I^- (4*a*) are known to mix over the respective Wyckoff positions, referring to anion site inversion (through aliovalent substitution on the phosphorus site).[8,28] Rietveld analysis of the SXRD and NPD data allowed for quantification of the degree of site inversion, as shown in Figure 1d. The differences between the site inversion determined by SXRD and NPD lie in the standard deviation range, except for $Li_{6.5}[P_{0.25}Si_{0.25}Ge_{0.25}Sb_{0.25}]S_5I$ (EQ). Note that site inversion also depends upon the Li substructure (surrounding the 4*d* Wyckoff position) and the tetrahedral environment,[4] and therefore the large discrepancy seen for EQ could be a result of its intrinsic complexity.

Rietveld analysis of NPD data further offered insights into the structural arrangement of the Li sublattice. Figure 1e depicts the normalized Li occupancies over the different crystallographic sites. As can be seen, lithium predominantly occupies type (T) 5 (48*h*) and 5a (24*g*) Wyckoff sites in all samples. However, in the case of $P_{0.75}$, $P_{0.5}$, $Si_{0.5}$, $Ge_{0.5}$, and $Sb_{0.5}$, a fraction of type 2 (48*h*) Wyckoff sites was also occupied. Moreover, for the primarily aliovalent substituted lithium argyrodites, such as $Si_{0.5}$ and $Ge_{0.5}$, additional occupancy was found for type 4 (16*e*) Wyckoff sites, with relatively low occupation values of about (2 ± 0.1) %, see Figure 1e. It is worth noting that for EQ, only two Li positions were identified. This could be associated with the highly distorted tetrahedral environment, where both type 2 and 4 may be considered metastable and thus difficult to detect. In turn, this also leads to the challenge of precisely determining anion disorder, as the Li sublattice and site inversion are closely related, which helps explain the deviation in S^{2-}/I^- between SXRD and NPD, with similar observations made for $Li_{6.5}P_{0.5}Ge_{0.5}S_5I$.[29] To illustrate the diffusion pathways, the Li substructure is shown in Figures 1f,g, and S3 (Supporting Information). Three different jumps were identified for the materials contributing to long-range 3D lithium diffusion, namely 48*h*(T5)-48*h*(T5) doublet jumps [through the nominal 24*g*(T5a) transition site], intracage jumps between two adjacent 48*h*(T5) tetrahedra, and intercage jumps between 48*h*(T5) positions. Lithium argyrodites in which the Li^+ ions only occupy the 48*h*(T5) and 24*g*(T5a) Wyckoff sites usually have poor transport properties, due to long intercage jump distances.[4,29,30] In a previous study, we have demonstrated that EQ possesses a shortened intercage jump distance, thereby facilitating ion mobility.[15] This jump distance is also shorter compared to $Sb_{0.75}$, thus rationalizing the fast diffusion kinetics for EQ. With T2(48*h*) being occupied (Figure 1e), connections between T5 sites within the same Li cage are established, leading to fast intracage motion via T5-T2-T5 pathways (blue lines in Figure 1f,g). More importantly, T2 serves as an "intermediate" position bridging two T5 sites from different cages, enabling intercage jumping via T5-T2-T2-T5 pathways with much shortened distances (red lines in Figure 1f,g). Typically, the T5-T2 and T2-T2 distances are much shorter than that of isolated T5-T5 jumping. Additionally occupied T4 sites further promote long-range diffusion (low energy barrier) by connecting different Li cages through T5-T4-T5 pathways. The Li–Li jump distances for the different samples are given in Table S15 (Supporting Information).

In summary, multicationic substitution in lithium argyrodites strongly affects the Li sublattice and favors ion diffusion through shortened Li–Li jump distances, in some cases by occupation of additional crystallographic sites. However, it should be noted that the appearance of additionally occupied sites (T2 and T4) is presumably also connected, at least to some degree, to the overall Li content.

To investigate the local environment surrounding phosphorus and silicon, ^{31}P and ^{29}Si MAS NMR spectroscopy measurements were performed (Figure 2a,b). All samples exhibit a distinct ^{31}P peak between 90 and 96 ppm

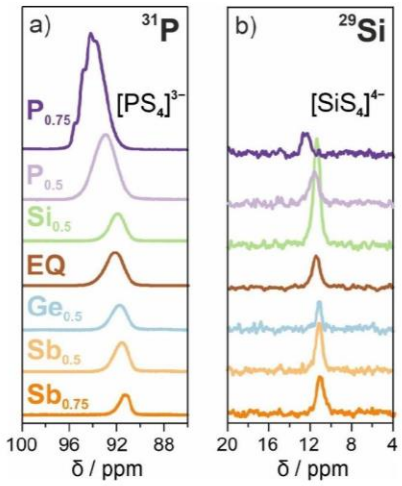

Figure 2. (a) ^{31}P and (b) ^{29}Si MAS NMR spectra collected from the multication-substituted argyrodite SEs. The data for EQ was taken from the literature.[15,21]

characteristic of the $[PS_4]^{3-}$ tetrahedral environment. This is consistent with previous observations on other lithium thiophosphate SEs.[5,14,15,21,23,31,32] The ^{31}P intensity decreased from $P_{0.75}$ to $Sb_{0.75}$, with the peak gradually shifting from 94.05 to 91.3 ppm (Figure S4, Supporting Information). In the case of $P_{0.75}$, the spectrum also revealed several contributions indicated by shoulder peaks at higher ppm values. Multiple contributions in the ^{31}P spectrum are often associated with the S^{2-}/X^- site inversion (X=Cl^-, Br^-, I^-) in lithium argyrodites.[5,14,23,32] However, considering the low degree of S^{2-}/I^- (1.19 % from SXRD and 0.5 % from NPD), the latter can be ruled out for $P_{0.75}$. This suggests that it is potentially determined by other structural distortions, which strongly depend on the local arrangement of neighboring tetrahedral species (i.e. $[SiS_4]^{4-}$, $[GeS_4]^{4-}$, and $[SbS_4]^{3-}$). The ^{29}Si spectra also showed a single contribution at ~11 ppm for all samples, with no obvious trend in peak shift with varying composition. However, both the appearance of a single peak and the chemical shift confirm the $[SiS_4]^{4-}$ tetrahedral environment and corroborate the absence of impurity phases.[15,21,33–35]

Additionally, ^6Li MAS NMR spectra were recorded, revealing a narrow peak located around 1.2 ppm, which is indicative of fast Li motion (Figure S5, Supporting Information).[15,21,23,29,31] Overall, similar spectra with no apparent signs of impurity contributions were obtained for the multication-substituted SEs, confirming the robustness of the argyrodite lattice.

After characterizing the long-range and local structural features of the samples, the charge-transport properties were examined via EIS and ^7Li PFG NMR spectroscopy. EIS measurements were conducted on sintered pellets in the temperature range of 15–65 °C (Figure S6, Supporting Information). Fitting of the spectra revealed room-temperature ionic conductivities ranging from (0.043 ± 0.004) mS cm^{-1} for $P_{0.75}$ to (14.05 ± 1.019) mS cm^{-1} for $Ge_{0.5}$. The fitting results are given in Table S16 (Supporting

Information), indicating that for EQ, $Si_{0.5}$, and $Ge_{0.5}$, ionic conductivities above 12 mS cm^{-1} can be achieved. For $Sb_{0.5}$ and $P_{0.5}$, ionic conductivities of (4.88 ± 0.673) mS cm^{-1} and (1.91 ± 0.016) mS cm^{-1} were determined. The phosphorus-rich ($P_{0.75}$) and antimony-rich ($Sb_{0.75}$) materials showed low ionic conductivities of (0.043 ± 0.004) mS cm^{-1} and (0.760 ± 0.071) mS cm^{-1}. Corresponding activation energies (E_A) were calculated from Arrhenius fitting of the temperature-dependent conductivity (Figure 3a), with the values ranging from (0.19 ± 0.006) eV for EQ (lowest E_A) to (0.37 ± 0.002) eV for $P_{0.75}$ (highest E_A). As evident, lower activation energies were found for the highly conducting samples.

To characterize the transport properties in more detail, ^{7}Li PFG NMR spectroscopy measurements were performed in the temperature range of 30–70 °C. For EQ, $P_{0.75}$, $Sb_{0.5}$, and $Sb_{0.75}$, the spectra depicting echo intensity against gradient strength could be described with a one-component fit. In contrast, for $P_{0.5}$, $Si_{0.5}$, and $Ge_{0.5}$, two contributions were observed (apparent from plotting the natural logarithm of echo intensity against squared gradient strength). The experimental data were fitted with two contributions given by the Kärger equation for slowly exchanging phases (see Supporting Information for details).[36–38] In Figure S7 (Supporting Information), the echo intensity vs. gradient strength and the natural logarithm of echo intensity vs. squared gradient strength are exemplarily shown for $Sb_{0.75}$ and $Si_{0.5}$ to highlight the existence of a second diffusion component. Specifically, logarithmic plotting yields a straight line for a single diffusive motion while exhibiting a curvature if more than one component is present. This has been reported repeatedly for other lithium thiophosphates and is usually attributed to the presence of a secondary (amorphous) phase, which is unlikely here, though.[37,39] Regardless, the diffusion coefficient (D_{Li}) was determined to range from (9.80 ± 0.59) · 10^{-14} m^2 s^{-1} for $P_{0.75}$ to (1.08 ± 0.01) · 10^{-11} m^2 s^{-1} for $Si_{0.5}$ (major contribution). We note that for $P_{0.5}$, $Si_{0.5}$, and $Ge_{0.5}$, the D_{Li} of the minor contribution was on the order of 10^{-12} m^2 s^{-1}.

Arrhenius fitting of the temperature-dependent lithium diffusion coefficients is shown in Figure 3b for all samples. This allowed determining the E_A, which was found to vary from (0.16 ± 0.003) eV for $Sb_{0.5}$ to (0.37 ± 0.014) eV for $P_{0.75}$, in good agreement with the EIS results. As mentioned above, in the case of $P_{0.5}$, $Si_{0.5}$, and $Ge_{0.5}$, a second

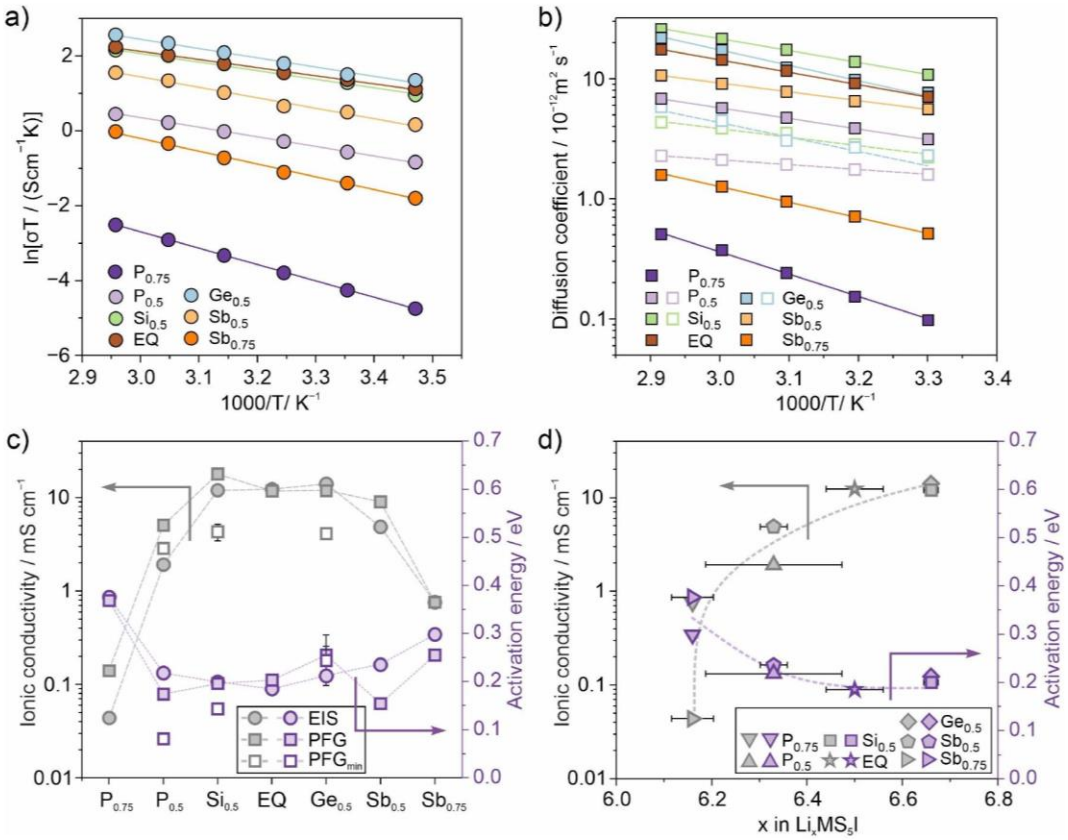

Figure 3. Charge-transport properties of the multication-substituted argyrodite SEs. Arrhenius plots of (a) temperature-dependent conductivities from EIS and (b) lithium diffusion coefficients determined by ^{7}Li PFG NMR spectroscopy. (c) Comparison of room-temperature ionic conductivities (gray) and activation energies (purple) from EIS (circles) and ^{7}Li PFG NMR spectroscopy (squares). (d) Relationship between refined Li content per formula unit and ionic conductivity and activation energy from EIS. The data for EQ was taken from the literature.[15,21] If no error bars are visible, the standard deviation is smaller than the symbol.

GDCh Research Article Angewandte International Edition Chemie

contribution had to be taken into account during fitting of the ^{7}Li PFG NMR data. Their activation energies are given in Table S16 (Supporting Information). Using the Nernst-Einstein equation, the ionic conductivities were calculated from the D_{Li}. Both the activation energies and ionic conductivities determined by EIS and ^{7}Li PFG NMR spectroscopy are shown in Figure 3c. As can be seen, they follow a similar trend for the different samples. In the case of $P_{0.5}$, $Si_{0.5}$, EQ, $Ge_{0.5}$, and $Sb_{0.5}$, room-temperature ionic conductivities above 1 mS cm^{-1} were found. Notably, the ionic conductivity was above 10 mS cm^{-1} for $Si_{0.5}$, $Ge_{0.5}$, and EQ (Table S16, Supporting Information), with the highest bulk conductivity of 17.94 mS cm^{-1} from ^{7}Li PFG NMR spectroscopy for $Si_{0.5}$. Interestingly, the best-conducting samples did not show the lowest E_A. For $Si_{0.5}$, $Ge_{0.5}$, and EQ, activation energies of (0.20 ± 0.002) eV, (0.25 ± 0.018) eV, and (0.20 ± 0.002) eV, respectively, were determined. As discussed previously, in the case of $P_{0.5}$, $Si_{0.5}$, and $Ge_{0.5}$, a second (minor) contribution had to be included to accurately describe the data. Their activation energies and ionic conductivities were lower than those of the major contributions.

Long-range lithium diffusion in argyrodites depends on the intercage jumps and, in particular, on the jump distance and frequency.[4] The Li substructure can be altered by occupying additional T2 and T4 positions, eventually leading to faster T5-T2-T2-T5 and T5-T4-T5 intercage jumps compared to T5-T5 (Figure 1f,g). This in turn may positively impact the D_{Li} and further give rise to two different diffusion components, as seen in the ^{7}Li PFG NMR data. However, some minor contribution from impurity phases cannot be fully excluded, although no signs were found in the diffraction experiments and from the MAS NMR spectroscopy measurements. Nevertheless, EIS and ^{7}Li PFG NMR spectroscopy revealed very high ionic conductivities for some of the samples, particularly for $Si_{0.5}$, $Ge_{0.5}$, and EQ, despite having very different cationic compositions. In the present study, alio- and isovalent substitutions on the phosphorus site were performed successfully, thus the Li content varied to some degree. To assess a possible correlation between Li concentration and charge-transport properties, Figure 3d illustrates the room-temperature ionic conductivity and activation energy as a function of Li content in the multication-substituted argyrodite SEs. At first glance, increased Li content leads to increased ionic conductivity and decreased activation energy. This strategy of "Li-stuffed" ion conductors has been practiced for a long time in the field of garnet-type SEs, but is scarcely discussed for lithium argyrodites.[41] As a matter of fact, it is important to note that the trend of increasing conductivity with increasing Li concentration is valid for most, if not all, highly conducting argyrodite-type solid solutions (e.g. $Li_{6+x}P_{1-x}Ge_xS_5I$ and $Li_{6+x}Sb_{1-x}Si_xS_5I$).[7,29] Higher Li contents typically lead to the appearance of hitherto unoccupied Li sites, accompanied by a decrease in activation energy. A similar trend is apparent for the samples employed here. In particular, the ionic conductivity strongly increased with increasing Li content, from 6.17 mol ($P_{0.75}$ and $Sb_{0.75}$) to 6.33 mol ($P_{0.5}$ and $Sb_{0.5}$) per formula unit. As can be seen from Figure 3d, the ionic conductivity increased further upon increasing the Li content to 6.5 mol (EQ) and then leveled off at 6.66 mol ($Si_{0.5}$ and $Ge_{0.5}$). The activation energy decreased from 0.37 to ~0.20 eV with increasing Li content (up to 6.33 mol) and remained fairly constant for the other samples. However, the ionic conductivity differed significantly among them. Usually, low activation energies and increased ionic conductivity are associated with increased S^{2-}/X^- site inversion and occupation of additional ("intermediate") Li positions in argyrodite SEs. However, this kind of correlation is not valid for the multication-substituted lithium argyrodites discussed here. Nevertheless, it should be noted that the electronic conductivity determined by DC polarization measurements was found to be two to three orders of magnitude higher compared to that of other lithium thiophosphates reported in the literature (Table S17, Supporting Information).[12,42,43]

Taken together, the above analysis did not yield a clear correlation between the structural characteristics and the charge-transport properties. In particular, the observation of very low activation energies (except for $P_{0.75}$ and $Sb_{0.75}$) suggests that occupational disorder (configurational entropy) plays a non-negligible role in these materials. In the present series of lithium argyrodites with the general formula $Li_{6+x}MS_5I$ (M=P, Si, Ge, and Sb), the configurational entropy ΔS_{conf} can be deconvoluted into two contributions (Equations 1 and 2). The first involves $\Delta S_{conf,cation}$, i.e. cation mixing (Wyckoff position 4*b*), and the second $\Delta S_{conf,anion}$, i.e. anion mixing (Wyckoff positions 4*a* and 4*d*), according to:

$$\Delta S_{conf} = \Delta S_{conf,cation} + \Delta S_{conf,anion} \quad (1)$$

and

$$\Delta S_{conf} = -R\left[\left(\sum_{i=1}^{N} x_i \ln x_i\right) + \left(\sum_{k=1}^{N} x_k \ln x_k\right)\right], \quad (2)$$

with x_i and x_k representing the molar fraction of the cation and anion species occupying the 4*b* site and the 4*a* and 4*d* sites, respectively. R and N are the universal gas constant and the number of anions/cations, respectively. In general, the more equally the different species are distributed over the available sites, the higher ΔS_{conf} is, as schematically shown in Figure 4a for the cationic substituents. Overall, this means that the $\Delta S_{conf,cation}$ contribution is greatest when the $[PS_4]^{3-}$, $[SiS_4]^{4-}$, $[GeS_4]^{4-}$, and $[SbS_4]^{3-}$ tetrahedral units are equally distributed across the unit cell, leading to severe (local) structural distortions. Figure 4b shows the calculated ΔS_{conf} for the cation and anion disorder in the different samples. Interestingly, EQ having the highest cation disorder also exhibited the highest anion disorder, leading to $\Delta S_{conf} = -2.08R$. Since there was no apparent connection between the typical structural characteristics of lithium argyrodites and the transport properties, configurational entropy is assumed to play a prominent role. The correlation between ΔS_{conf} and activation energy and ionic conductivity from both EIS and ^{7}Li PFG NMR spectroscopy is depicted

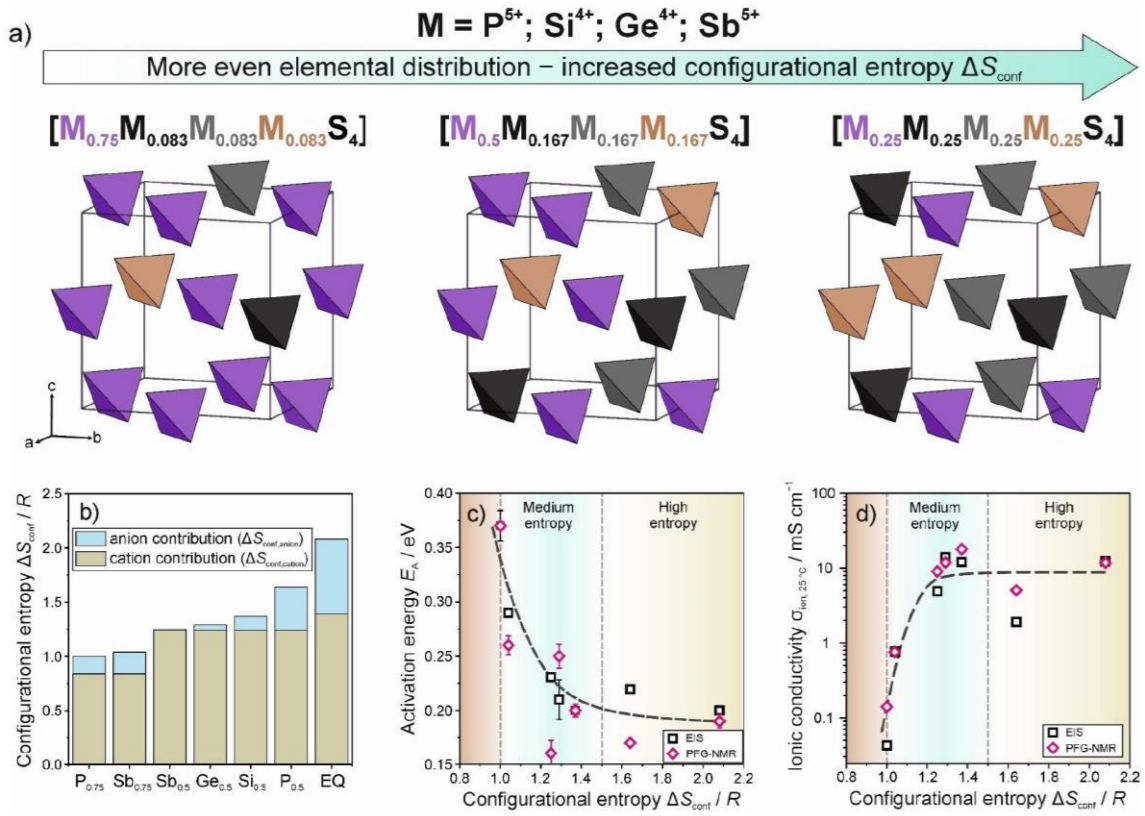

Figure 4. Configurational entropy-property relationships related to lithium diffusion. (a) Schematic representation of the tetrahedra arrangements in the unit cell showing that a more equal distribution leads to increased configurational entropy. (b) Configurational entropy contributions from cation and anion disorder. Correlation between configurational entropy and (c) activation energy and (d) ionic conductivity determined by EIS and ^{7}Li PFG NMR spectroscopy.

in Figure 4c and d, respectively, with the medium- and high-entropy regions being highlighted. As evident from the data, the activation energy decreases with increasing ΔS_{conf}, while the ionic conductivity increases. An increased ΔS_{conf} comes along with an increased vibrational entropy (ΔS_{vib}), which affects the lattice dynamics and distortion. Although it is challenging to unravel the effects of both contributions on mobility, one can assume that ΔS_{vib} positively affects the ion migration via phonon-mediated transport, ultimately leading to a lower energy barrier for diffusion.[23,44–47] In addition, the local structural distortions expressed by ΔS_{conf} lead to atomic displacement disorder, fostering overlapping Li-site energies (broadening) and facilitating long-range diffusion.[20] It should also be noted that aliovalent substitution probably leads to localized defect formation in the Li sublattice, which however has not been considered yet.

In general, ionic conductivity (Equation 3) can be expressed as the product of ion mobility (μ), charge (q), and charge-carrier density (n) according to:[48]

$$\sigma = nq\mu. \tag{3}$$

Because lithium is considered the only mobile charge carrier in the present series of samples, the conductivity solely depends upon the ion mobility and charge-carrier density. Although we have shown that there is a connection between the Li content per formula unit and the conductivity (Figure 3d), no such correlation is apparent with charge-carrier density. The ion mobility can be obtained from the diffusion coefficient (Equation 4), with q being the charge, and k_B and T representing the Boltzmann constant and temperature, respectively.

$$\mu = \frac{qD_{Li}}{k_B T} \tag{4}$$

In general, the diffusion coefficient is a measure of how quickly species (ions) move through the material due to random thermal motion and quantifies the rate at which they are diffusing. The correlation of ionic conductivity with occupational disorder derived from the cation sublattice demonstrates that increasing compositional complexity promotes the Li^+ mobility (Figure S8, Supporting Information). A comparison of lithium mobilities and densities for different argyrodites and LGPS is presented in Figure 5, and individual values are given in Table S18 (Supporting Information).[9] Interestingly, the multication-substituted argyrodite SEs exhibit Li^+ mobilities of $\mu > 10^{-6}$ cm^{2}V^{-1}s^{-1},

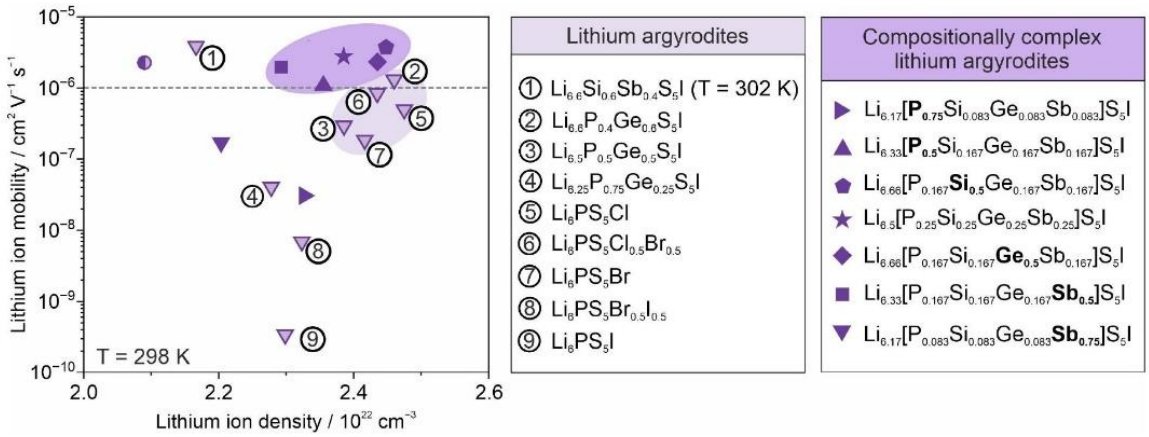

Figure 5. Li^+ mobility versus Li-ion density for different lithium argyrodites and $Li_{10}GeP_2S_{12}$ (denoted by the half-filled circle).[6–8,49,50]

one order of magnitude higher compared to other, more common highly conducting lithium argyrodites. Even the materials having a relatively low ionic conductivity such as $P_{0.5}$ [$(1.91 \pm 0.016)\,mS\,cm^{-1}$] showed high ion mobilities ($1.09 \cdot 10^{-6}\,cm^2\,V^{-1}\,s^{-1}$), similar to that of LGPS ($2.27 \cdot 10^{-6}\,cm^2\,V^{-1}\,s^{-1}$, ~7 $mS\,cm^{-1}$ at room temperature).[49] These results further emphasize that configurational entropy has a beneficial effect on lithium diffusivity.

Conclusions

In summary, we have investigated a series of multication-substituted lithium argyrodites with the general formula $Li_{6+x}[M1_aM2_bM3_cM4_d]S_5I$. All samples were subjected to thorough analysis of the crystal structure and charge-transport properties using a combination of powder diffraction techniques, ^{31}P, ^{29}Si, and ^{6}Li MAS NMR spectroscopy, EIS, and complementary ^{7}Li PFG NMR spectroscopy. We demonstrate that increasing configurational entropy, induced primarily by introducing cation disorder, correlates with decreasing activation energy and increasing ionic conductivity. This translates into room-temperature ionic conductivities above 10 $mS\,cm^{-1}$ for some of the materials, with the highest of 17.9 $mS\,cm^{-1}$ obtained for $Li_{6.66}[P_{0.167}Si_{0.5}Ge_{0.167}Sb_{0.167}]S_5I$. Tailoring the configurational entropy by altering the composition, we present—to the best of our knowledge—the first experimental evidence of a direct correlation between occupational disorder in the cationic host lattice and ion mobility. Overall, the data point toward the possibility of enhancing conductivity in ceramic ion conductors via entropy engineering, potentially also allowing to improve the (electro)chemical stability and mechanical properties.

Acknowledgements

J. L. acknowledges the Fonds der Chemischen Industrie (FCI) for financial support. F. S. is grateful to the Federal Ministry of Education and Research (BMBF) for funding within the project MELLi (03XP0447). This work was partially supported by BASF SE. V. B. acknowledges DESY (Hamburg, Germany), a member of the Helmholtz Association (HGF), for the provision of experimental facilities. Parts of this research were carried out at beamline P02.1, PETRA III. This work is based on experiments performed at the Swiss spallation neutron source SINQ, Paul Scherrer Institute (PSI), Villigen, Switzerland (proposal no. 20051234) and PEARL neutron source, Delft University of Technology. The authors thank Dr. Denis Cheptiakov for assistance during the NPD measurements. Open Access funding enabled and organized by Projekt DEAL.

Conflict of Interest

The authors declare the following competing interest(s): A patent was filed for this work through BASF SE and Karlsruher Institut für Technologie (KIT).

Data Availability Statement

The data that support the findings of this study are available from the corresponding author upon reasonable request.

[1] J. Janek, W. G. Zeier, *Nat. Energy* **2023**, *8*, 230–240.
[2] A. Manthiram, X. Yu, S. Wang, *Nat. Rev. Mater.* **2017**, *2*, 1–16.
[3] Z. Zhang, Y. Shao, B. Lotsch, Y. S. Hu, H. Li, J. Janek, L. F. Nazar, C. W. Nan, J. Maier, M. Armand, L. Chen, *Energy Environ. Sci.* **2018**, *11*, 1945–1976.
[4] L. Zhou, N. Minafra, W. G. Zeier, L. F. Nazar, *Acc. Chem. Res.* **2021**, *54*, 2717–2728.
[5] H. J. Deiseroth, S. T. Kong, H. Eckert, J. Vannahme, C. Reiner, T. Zaiß, M. Schlosser, *Angew. Chem. Int. Ed.* **2008**, *47*, 755–758.
[6] M. A. Kraft, S. P. Culver, M. Calderon, F. Böcher, T. Krauskopf, A. Senyshyn, C. Dietrich, A. Zevalkink, J. Janek, W. G. Zeier, *J. Am. Chem. Soc.* **2017**, *139*, 10909–10918.

[7] L. Zhou, A. Assoud, Q. Zhang, X. Wu, L. F. Nazar, *J. Am. Chem. Soc.* **2019**, *141*, 19002–19013.
[8] M. A. Kraft, S. Ohno, T. Zinkevich, R. Koerver, S. P. Culver, T. Fuchs, A. Senyshyn, S. Indris, B. J. Morgan, W. G. Zeier, *J. Am. Chem. Soc.* **2018**, *140*, 16330–16339.
[9] J. C. Bachman, S. Muy, A. Grimaud, H. H. Chang, N. Pour, S. F. Lux, O. Paschos, F. Maglia, S. Lupart, P. Lamp, L. Giordano, Y. Shao-Horn, *Chem. Rev.* **2016**, *116*, 140–162.
[10] T. Famprikis, P. Canepa, J. A. Dawson, M. S. Islam, C. Masquelier, *Nat. Mater.* **2019**, *18*, 1278–1291.
[11] Y. Wang, W. D. Richards, S. P. Ong, L. J. Miara, J. C. Kim, Y. Mo, G. Ceder, *Nat. Mater.* **2015**, *14*, 1026–1031.
[12] P. Adeli, J. D. Bazak, K. H. Park, I. Kochetkov, A. Huq, G. R. Goward, L. F. Nazar, *Angew. Chem.* **2019**, *131*, 8773–8778.
[13] J. Xu, *Mater. Futures* **2023**, *2*, 047501.
[14] F. Strauss, J. Lin, M. Duffiet, K. Wang, T. Zinkevich, A.-L. Hansen, S. Indris, T. Brezesinski, *ACS Materials Lett.* **2022**, *4*, 418–423.
[15] J. Lin, G. Cherkashinin, M. Schäfer, G. Melinte, S. Indris, A. Kondrakov, J. Janek, T. Brezesinski, F. Strauss, *ACS Materials Lett.* **2022**, *4*, 2187–2194.
[16] Y. Li, S. Song, H. Kim, K. Nomoto, H. Kim, X. Sun, S. Hori, K. Suzuki, N. Matsui, M. Hirayama, T. Mizoguchi, T. Saito, T. Kamiyama, R. Kanno, *Science* **2023**, *381*, 50–53.
[17] Y. Ma, Y. Ma, Q. Wang, S. Schweidler, M. Botros, T. Fu, H. Hahn, T. Brezesinski, B. Breitung, *Energy Environ. Sci.* **2021**, *14*, 2883–2905.
[18] P. Wang, S. Patel, H. Liu, P. H. Chien, X. Feng, L. Gao, B. Chen, J. Liu, Y. Y. Hu, *Adv. Funct. Mater.* **2023**, *33*, 1–11.
[19] S. K. Jung, H. Gwon, H. Kim, G. Yoon, D. Shin, J. Hong, C. Jung, J. S. Kim, *Nat. Commun.* **2022**, *13*, 7638.
[20] Y. Zeng, B. Ouyang, J. Liu, Y. W. Byeon, Z. Cai, L. J. Miara, Y. Wang, G. Ceder, *Science* **2022**, *378*, 1320–1324.
[21] J. Lin, M. Schaller, G. Cherkashinin, S. Indris, J. Du, C. Ritter, A. Kondrakov, J. Janek, T. Brezesinski, F. Strauss, *Small* **2024**, *20*, 2306832.
[22] F. Strauss, J. Lin, A. Kondrakov, T. Brezesinski, *Matter* **2023**, *6*, 1068–1070.
[23] S. Li, J. Lin, M. Schaller, S. Indris, X. Zhang, T. Brezesinski, C.-W. Nan, S. Wang, F. Strauss, *Angew. Chem. Int. Ed.* **2023**, *62*, e202314155.
[24] Q. Wang, Y. Zhou, X. Wang, H. Guo, S. Gong, Z. Yao, F. Wu, J. Wang, S. Ganapathy, X. Bai, B. Li, C. Zhao, J. Janek, M. Wagemaker, *Nat. Commun.* **2024**, *15*, 1050.
[25] Z. Song, T. Wang, H. Yang, W. H. Kan, Y. Chen, Q. Yu, L. Wang, Y. Zhang, Y. Dai, H. Chen, W. Yin, T. Honda, M. Avdeev, H. Xu, J. Ma, Y. Huang, W. Luo, *Nat. Commun.* **2024**, *15*, 1481.
[26] W. Li, Z. Chen, Y. Chen, L. Zhang, G. Liu, L. Yao, *Adv. Funct. Mater.* **2024**, *1–9*, 2312832.
[27] R. D. Shannon, *Acta Crystallogr.* **1976**, *A*, 751–767.
[28] S. Ohno, B. Helm, T. Fuchs, G. Dewald, M. A. Kraft, S. P. Culver, A. Senyshyn, W. G. Zeier, *Chem. Mater.* **2019**, *31*, 4936–4944.
[29] K. Hogrefe, N. Minafra, I. Hanghofer, A. Banik, W. G. Zeier, H. M. R. Wilkening, *J. Am. Chem. Soc.* **2022**, *144*, 1795–1812.
[30] N. Minafra, M. A. Kraft, T. Bernges, C. Li, R. Schlem, B. J. Morgan, W. G. Zeier, S. P. Culver, T. Krauskopf, A. Senyshyn, W. G. Zeier, *Inorg. Chem.* **2020**, *59*, 11009–11019.
[31] R. Schlenker, A. L. Hansen, A. Senyshyn, T. Zinkevich, M. Knapp, T. Hupfer, H. Ehrenberg, S. Indris, *Chem. Mater.* **2020**, *32*, 8420–8430.
[32] I. Hanghofer, M. Brinek, S. L. Eisbacher, B. Bitschnau, M. Volck, V. Hennige, I. Hanzu, D. Rettenwander, H. M. R. Wilkening, *Phys. Chem. Chem. Phys.* **2019**, *21*, 8489–8507.
[33] M. Kaus, H. Stöffler, M. Yavuz, T. Zinkevich, M. Knapp, H. Ehrenberg, S. Indris, *J. Phys. Chem. C* **2017**, *121*, 23370–23376.
[34] F. Hartmann, A. Benkada, S. Indris, M. Poschmann, H. Lühmann, P. Duchstein, D. Zahn, W. Bensch, *Angew. Chem. Int. Ed.* **2022**, *61*, 1–10.
[35] S. Harm, A. K. Hatz, I. Moudrakovski, R. Eger, A. Kuhn, C. Hoch, B. V. Lotsch, *Chem. Mater.* **2019**, *31*, 1280–1288.
[36] D. Wijesekera, T. Stait-Gardner, A. Gupta, J. Chen, G. Zheng, A. M. Torres, W. S. Price, *Concepts Magn. Reson. Part A* **2018**, *47A*, 1–12.
[37] E. P. Ramos, J. D. Bazak, A. Assoud, A. Huq, G. Goward, L. F. Nazar, *ACS Appl. Mater. Interfaces* **2022**, *14*, 56767–56779.
[38] W. S. Price, *Concepts Magn. Reson.* **1998**, *10*, 197–237.
[39] R. Calaminus, S. Harm, D. H. Fabini, L. G. Balzat, A. K. Hatz, V. Duppel, I. Moudrakovski, B. V. Lotsch, *Chem. Mater.* **2022**, *34*, 7666–7677.
[40] P.-H. Chien, B. Ouyang, X. Feng, L. Dong, D. Mitlin, J. Nanda, J. Liu, *Chem. Mater.* **2024**, *36*(1), 382–393.
[41] W. G. Zeier, *Dalton Trans.* **2014**, *43*, 16133–16138.
[42] F. Strauss, J. Lin, L. Karger, D. Weber, T. Brezesinski, *Inorg. Chem.* **2022**, *61*, 5885–5890.
[43] S. J. Sedlmaier, S. Indris, C. Dietrich, M. Yavuz, C. Dräger, F. Von Seggern, H. Sommer, J. Janek, *Chem. Mater.* **2017**, *29*, 1830–1835.
[44] J. Ding, PhD thesis, Duke University **2022**, 1–227.
[45] S. Muy, R. Schlem, Y. Shao-Horn, W. G. Zeier, *Adv. Energy Mater.* **2021**, *11*, 2002787.
[46] S. Muy, J. C. Bachman, L. Giordano, H. H. Chang, D. L. Abernathy, D. Bansal, O. Delaire, S. Hori, R. Kanno, F. Maglia, S. Lupart, P. Lamp, Y. Shao-Horn, *Energy Environ. Sci.* **2018**, *11*, 850–859.
[47] B. Ahammed, E. Ertekin, *Adv. Mater.* **2024**, *6*, 1–15.
[48] M. Sotoudeh, S. Baumgart, M. Dillenz, J. Döhn, K. Forster-Tonigold, K. Helmbrecht, D. Stottmeister, A. Groß, *Adv. Energy Mater.* **2023**, *14*, 2302550.
[49] T. Krauskopf, S. P. Culver, W. G. Zeier, *Chem. Mater.* **2018**, *30*, 1791–1798.
[50] N. Minafra, S. P. Culver, T. Krauskopf, A. Senyshyn, W. G. Zeier, *J. Mater. Chem. A* **2018**, *6*, 645–651.

Manuscript received: March 11, 2024
Accepted manuscript online: May 6, 2024
Version of record online: June 17, 2024

3.4. Publication IV: High-Entropy Lithium Argyrodite Solid Electrolytes Enabling Stable All-Solid-State Batteries

Publication IV discusses the investigation of new high-entropy lithium argyrodites $Li_{5.5}PS_{4.5}Cl_xBr_{1.5-x}$ with a fixed Li content. In these materials, a very high ionic conductivity was achieved for $Li_{5.5}PS_{4.5}Cl_{0.8}Br_{0.7}$ (~9 mS cm^{-1} from EIS and ~22 mS cm^{-1} from ^{7}Li PFG-NMR, $\Delta S_{conf} = 1.98R$) by tuning the anion disorder between sulfur, chlorine and bromine, distributed over two crystallographic sites (4*a* and 4*d*). Through NPD combined with ^{31}P MAS NMR spectroscopy, the occupancy of S^{2-}/Cl^-/Br^- on the anion sublattice was quantitatively analyzed. The Li distribution and jump distances, characterized via NPD, show virtually no differences in these materials, indicating the limitation of classical structure-property explanations. $Li_{5.5}PS_{4.5}Cl_{0.8}Br_{0.7}$ displays the maximum ΔS_{conf} based on the calculation, which also exhibits the highest ionic conductivity, suggesting a direct correlation between ΔS_{conf} and lithium transport properties. Moreover, $Li_{5.5}PS_{4.5}Cl_{0.8}Br_{0.7}$ was used as the solid electrolyte in SSB cells with single-crystal $LiNi_{0.9}Co_{0.06}Mn_{0.04}O_2$ (s-NCM90) as a CAM, showing nearly no capacity decay after 700 cycles.

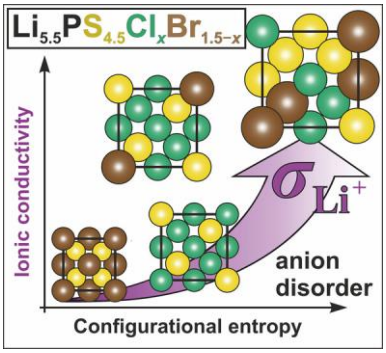

Figure 21: Table of Contents (TOC) of Publication IV. Adapted from reference [20].

Publication IV has a shared first authorship between S. Li and J. Lin. Since the synthesis and electrochemical tests (EIS and GCPL) were carried out by S. Li and S. Wang, J. Lin and F. Strauss were responsible for structural characterization and explaining the structure-property relationships. J. Lin conducted the XRD experiments and analyzed data. The NPD measurements were carried out at the Spallation Neutron Source (SNS), Oak Ridge National Laboratory (ORNL) and at the Swiss spallation neutron source (SINQ), Paul Scherrer Institute (PSI) with the proposal number 20051234. The NPD results were mainly analyzed by F. Strauss and further checked by J. Lin. M. Schäfer conducted the PFG-NMR measurements and analyzed the data together with J. Lin. S. Indris carried out the MAS NMR spectroscopy experiments and analyzed the data. The interpretation was discussed together with J. Lin and F. Strauss. The first draft was mainly written by F. Strauss. J. Lin supported evaluation of the data and writing of the publication. The final paper was then edited by all co-authors.

GDCh Research Articles Angewandte International Edition Chemie www.angewandte.org

How to cite: *Angew. Chem. Int. Ed.* **2023**, *62*, e202314155
doi.org/10.1002/anie.202314155

All-solid-state Batteries

High-Entropy Lithium Argyrodite Solid Electrolytes Enabling Stable All-Solid-State Batteries

Shenghao Li[+], Jing Lin[+], Mareen Schaller, Sylvio Indris, Xin Zhang, Torsten Brezesinski, Ce-Wen Nan, Shuo Wang, and Florian Strauss**

Abstract: Superionic solid electrolytes (SEs) are essential for bulk-type solid-state battery (SSB) applications. Multicomponent SEs are recently attracting attention for their favorable charge-transport properties, however a thorough understanding of how configurational entropy (ΔS_{conf}) affects ionic conductivity is lacking. Here, we successfully synthesized a series of halogen-rich lithium argyrodites with the general formula $Li_{5.5}PS_{4.5}Cl_xBr_{1.5-x}$ ($0 \le x \le 1.5$). Using neutron powder diffraction and ^{31}P magic-angle spinning nuclear magnetic resonance spectroscopy, the $S^{2-}/Cl^-/Br^-$ occupancy on the anion sublattice was quantitatively analyzed. We show that disorder positively affects Li-ion dynamics, leading to a room-temperature ionic conductivity of 22.7 mS cm^{-1} (9.6 mS cm^{-1} in cold-pressed state) for $Li_{5.5}PS_{4.5}Cl_{0.8}Br_{0.7}$ ($\Delta S_{conf} = 1.98R$). To the best of our knowledge, this is the first experimental evidence that configurational entropy of the anion sublattice correlates with ion mobility. Our results indicate the possibility of improving ionic conductivity in ceramic ion conductors by tailoring the degree of compositional complexity. Moreover, the $Li_{5.5}PS_{4.5}Cl_{0.8}Br_{0.7}$ SE allowed for stable cycling of single-crystal $LiNi_{0.9}Co_{0.06}Mn_{0.04}O_2$ (s-NCM90) composite cathodes in SSB cells, emphasizing that dual-substituted lithium argyrodites hold great promise in enabling high-performance electrochemical energy storage.

Introduction

All-inorganic solid-state batteries (SSBs) are regarded as a possibility to boost energy and power density of rechargeable Li batteries. To achieve this, solid electrolyte (SE) materials with a high ionic conductivity, good (electro)chemical stability and some mechanical softness (for processing reasons) are needed.[1–3] And indeed, the ongoing quest for advanced SEs has led to the discovery of ceramic materials, either crystalline or amorphous, that show conductivities exceeding those of liquid (organic) electrolytes.[4,5] These highly conducting materials are solely sulfide based, which in turn is favorable for maintaining good contact with the other electrode constituents, as they are relatively soft.[6–10] However, their (electro)chemical stability window is narrow,[11–14] and therefore an artificial interface is typically required to avoid direct contact with the cathode and/or anode material (to allow for reversible SSB operation).[15–18]

Some highly conducting SEs reported in the literature are, unfortunately, of limited practical relevance, as they contain scarce elements,[19–23] thus the continuing need for further exploration of novel conductors made from more abundant materials. In this regard, lithium argyrodites, originally reported for Li_6PS_5X with X=Cl, Br, I, have emerged as an important class of materials.[24–26] To increase the ionic conductivity in this structure type, the phosphorus, sulfur and halide sites have been substituted with other elements and, in some cases, room-temperature conductivities beyond 10 mS cm^{-1} were achieved.[20,22,27] This increase

[*] S. Li,[+] X. Zhang, S. Wang
Center of Smart Materials and Devices, State Key Laboratory of Advanced Technology for Materials Synthesis and Processing & School of Material Science and Engineering, Wuhan University of Technology
Wuhan 430070 (China)
E-mail: shuowang@whut.edu.cn

J. Lin,[+] T. Brezesinski, F. Strauss
Institute of Nanotechnology, Karlsruhe Institute of Technology (KIT)
Hermann-von-Helmholtz-Platz 1, 76344 Eggenstein-Leopoldshafen (Germany)
E-mail: florian.strauss@kit.edu

M. Schaller, S. Indris
Institute for Applied Materials-Energy Storage Systems (IAM-ESS), Karlsruhe Institute of Technology (KIT)
Hermann-von-Helmholtz-Platz 1, 76344 Eggenstein-Leopoldshafen (Germany)

C.-W. Nan
State Key Laboratory of New Ceramics and Fine Processing, School of Materials Science and Engineering, Tsinghua University
Beijing 100084 (China)

S. Wang
Foshan (Southern China) Institute for New Materials
Foshan 528200 (China)

[+] These authors contributed equally to this work.

in ionic conductivity by about an order of magnitude is usually a result of an altered Li sublattice (presence of additional Li sites, shortened Li^+-Li^+ jump distances, etc.) and an increased S^{2-}/X^- site disorder, both of which leads to facile lithium diffusion. Another approach to boost ionic conductivity in lithium argyrodites is the substitution of sulfur with a halogen (Cl^- or Br^-), leading to an increase in Li vacancies and more pronounced S^{2-}/X^- site disorder. Recently, such halogen-rich, lithium-deficient argyrodites (e.g., $Li_{5.5}PS_{4.5}Cl_{1.5}$) are attracting interest, as they not only possess a high ionic conductivity but also show a better (electro)chemical stability than the parent Li_6PS_5Cl.[28–34] It has also been shown that a second halogen can be introduced, and with that, the conductivity further improves.[35–37] From a structural perspective, it has been recognized that anion disorder induced by halogen mixing and varying the halogen content can have a profound effect on ionic conductivity.[29,35,36,38–41]

Introducing a large anion and/or cation disorder into the host lattice of polyanionic SE materials, referring to high-entropy ion conductors, has been garnering a lot of attention lately, due to potential improvements in conductivity and (electro)chemical stability.[21,42–47] In principle, high-entropy materials (HEMs) refer to materials with a shared occupation of several different elements on a single crystallographic site. This increases the configurational entropy (ΔS_{conf}),[48–50] and can either lead to the emergence of new and/or improved properties or help stabilize metastable phases through the entropy contribution to the Gibbs energy of the multicomponent phase.[51–53] HEMs are usually referred to as having a $\Delta S_{conf} > 1.5R$. In recent years, various HEMs have been synthesized, including oxides, sulfides and carbides, and employed as electrode materials in batteries, catalysts and as dielectric capacitors, among others.[54–56] However, only a few examples of high-entropy Li-ion conductors adopting different structures and being suitable for application in batteries have been reported so far.[21,42,45,46] Regarding lithium argyrodites, recently, a multicationic substituted HEM, $Li_{6.5}[P_{0.25}Si_{0.25}Sb_{0.25}Ge_{0.25}]S_5I$, showing an ionic conductivity of $>10\ mS\,cm^{-1}$ at room temperature, along with a very low activation energy for lithium diffusion of 0.20 eV, has been reported. However, the correlation between the degree of disorder and the ionic conductivity remains unclear.

To shed light on this, we prepared a series of (dual-substituted) halogen-rich lithium argyrodite samples with a total halogen content of 1.5 moles and systematically varied the Cl^- to Br^- ratio in $Li_{5.5}PS_{4.5}Cl_xBr_{1.5-x}$ (with $x = 0$, 0.2, 0.4, 0.6, 0.8, 1.0, 1.2 and 1.5). Their crystal structure was probed using a combination of neutron powder diffraction (NPD) and ^{31}P magic-angle spinning (MAS) nuclear magnetic resonance (NMR) spectroscopy, indicating that a maximum anion-disordered sublattice is achieved with $Li_{5.5}PS_{4.5}Cl_{0.8}Br_{0.7}$. Using complementary electrochemical impedance spectroscopy (EIS) and ^7Li pulsed field gradient (PFG) NMR measurements, it is shown that this particular material also possesses the highest ionic conductivity among all prepared samples. Overall, we demonstrate, to our knowledge for the first time, that there is a direct correlation between ΔS_{conf} and ionic conductivity in this class of ion conductors. Finally, the $Li_{5.5}PS_{4.5}Cl_{0.8}Br_{0.7}$ SE was also tested in pellet-type SSB cells and found to allow for stable cycling over 700 cycles.

Results and Discussion

To understand the impact of halogen substitution on the charge-transport properties, eight samples with varying composition were synthesized. An initial structural assessment using laboratory X-ray diffraction (XRD) revealed their phase purity, with the patterns showing a gradual shift of the reflections to higher 2θ values with increasing bromine content (see Figure S1a and b). Le Bail analysis further indicated that the patterns can be indexed to the $F\bar{4}3m$ space group and showed, as expected, a linear decrease in the a lattice parameter (and therefore unit cell volume) with increasing chlorine content (see Figure S1c), confirming solid-solution behavior over the whole compositional range. This is due to the smaller ionic radius of Cl^- compared to Br^-,[57] as the nominal sulfur, phosphorus and lithium contents remain unchanged. The calculated lattice parameters are given in Table S1. Because XRD is not able to differentiate between chlorine and sulfur, due to very similar X-ray scattering cross sections, and neither provides insight into the Li substructure, high-resolution NPD data were collected at room temperature from selected samples, namely $Li_{5.5}PS_{4.5}Cl_xBr_{1.5-x}$ with $x = 0$, 0.4, 0.8, 1.2 and 1.5. A representative diffraction pattern for $Li_{5.5}PS_{4.5}Cl_{0.8}Br_{0.7}$, along with the corresponding Rietveld plot, is presented in Figure 1a. Note that the lattice parameters derived from XRD and NPD are in good agreement (see Figure S1c). The calculated crystal structure is shown in Figure 1b, with the "free" S^{2-} and halogen ions forming a face-centered cubic anion sublattice (Wyckoff positions 4*a* and 4*d*) and additional S^{2-} ions being located in half of the tetrahedral voids (16*e*) around the octahedral sites (4*b*), thereby forming $[PS_4]^{3-}$ tetrahedra. Moreover, in the argyrodite structure, S^{2-} (4*d*) and halogen anions (4*a*) are known to mix over the respective Wyckoff positions, referring to anion site inversion. Comparable ionic radii of the respective anions (e.g., S^{2-} and Cl^-) or structural distortions usually enable a high level of halogen anions occupying the 4*d* Wyckoff position, i.e., high sulfur/halogen site inversion. As mentioned previously, Rietveld analysis of the NPD data enabled us to quantify the shared $S^{2-}/Cl^-/Br^-$ occupancy on both the 4*a* and 4*d* sites. The results are shown in Figure 1c and d. For $Li_{5.5}PS_{4.5}Br_{1.5}$ ($x = 0$), the 4*a* and 4*d* sites were found to be occupied by 89 % and 61 % bromine, respectively. If the bromine is gradually replaced by chlorine, the overall halogen occupancy on 4*a* decreases (see Figure 1c), while that on the 4*d* site increases (see Figure 1d). This, for instance, leads to a chlorine occupancy of 63 % and 90 % on the 4*a* and 4*d* Wyckoff positions, respectively, for $Li_{5.5}PS_{4.5}Cl_{1.5}$ ($x = 1.5$), in agreement with literature data.[28] Moreover, for the mixed chlorine/bromine-containing samples (i.e., $Li_{5.5}PS_{4.5}Cl_xBr_{1.5-x}$ with $x = 0.4$, 0.8 and 1.2), bromine apparently prefers to be situated on 4*a*, whereas chlorine

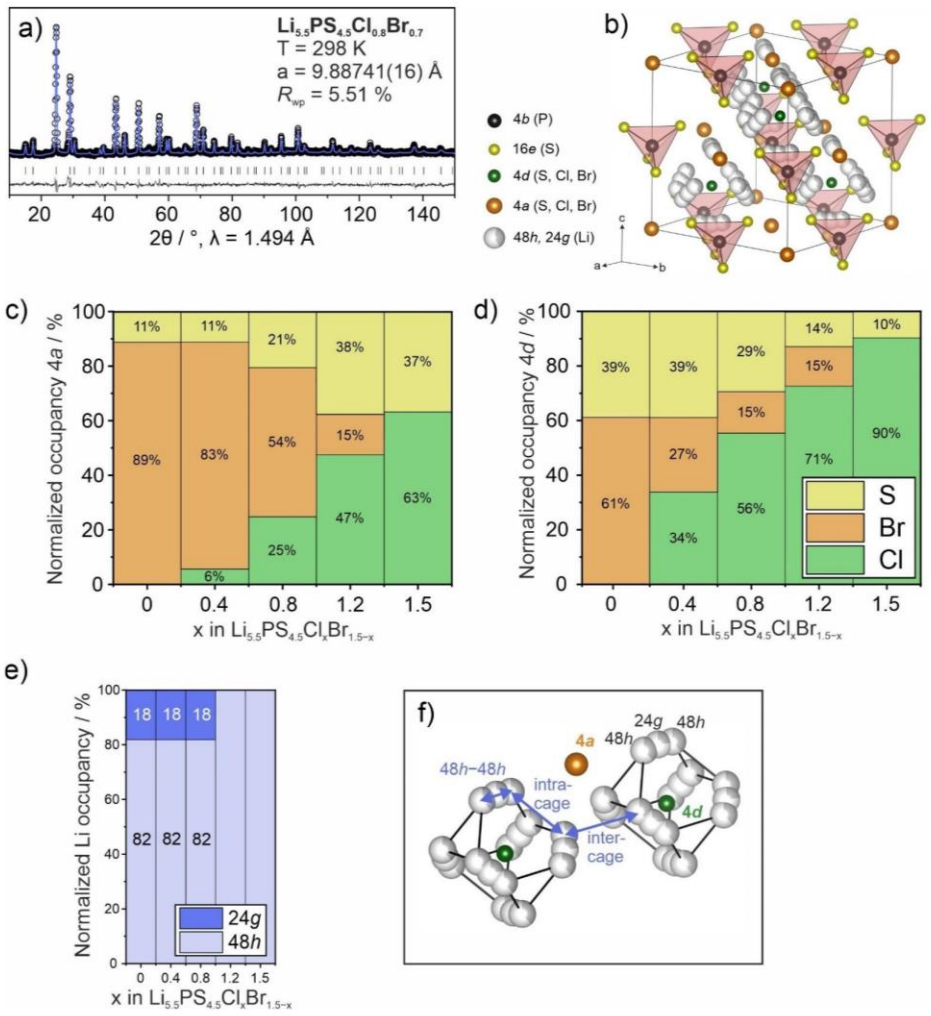

Figure 1. Structural characterization of the halogen-substituted lithium argyrodite solid electrolytes. (a) NPD pattern and corresponding Rietveld analysis for $Li_{5.5}PS_{4.5}Cl_{0.8}Br_{0.7}$ and (b) schematic view of the crystal structure with the different Wyckoff positions and elemental constituents indicated in the legend to the left. Refined structural parameters and compositions are given in Tables S2–S8. The normalized occupancies of the 4*a* and 4*d* Wyckoff positions are depicted in panels (c) and (d). (e) Normalized Li occupancies and (f) two neighboring Li cages with the 4*a* and 4*d* nearest positions being indicated.

predominantly occupies the 4*d* site. This leads to a decrease in average ionic radius with increasing chlorine content (see Figure S2a).

The halogen distribution in the crystal structure also affects the Li sublattice. In particular, two occupied Li positions, namely 48*h* and 24*g*, were identified for $Li_{5.5}PS_{4.5}Cl_xBr_{1.5-x}$ with $x=0$, 0.4 and 0.8, showing a similar distribution with 18% for 24*g* and 82% for 48*h* (see Figure 1e). Interestingly, we found that when the 4*a* and 4*d* Wyckoff positions share a similar average ionic radius (see Figure S2a), only one of the Li positions (48*h*) is occupied. This difference in Li distribution depending on the anion composition is also, at least in part, affected by the average ionic charge. As can be seen from Figure S2b, the average ionic charge on the 4*d* site decreases with increasing chlorine content, eventually leading to a single occupied Li position for $x=1.2$ and 1.5. Thus, depending on the average ionic radius and charge of the shared crystallographic positions, lithium seems to be forced into occupying either only one or two sites (different Coulomb interactions). In the substructure, three different Li^+-Li^+ jump distances are of relevance (see Figure 1f). The 48*h*–48*h* doublet (through the nominal 24*g* transition site) and intracage jumps occur within the Li cages surrounding the halogen/sulfur-mixed 4*d* position. However, the intercage jumps are those that are believed to strongly determine the long-range transport properties, and the neighboring 4*a* position may strongly affect these relatively large Li^+-Li^+ distances.[22,41] However, we find that the different jump distances are similar for the

$Li_{5.5}PS_{4.5}Cl_xBr_{1.5-x}$ samples employed in this work (see Figure 1f and Table S7).

After having revealed distinct differences in the average crystal structure (long-range ordering), the local structure of the samples was probed using ^6Li and ^{31}P MAS NMR spectroscopy. First of all, a gradual shift of the peak intensity maxima in the ^6Li MAS NMR spectra, from 1.23 to 1.0 ppm, with increasing chlorine content is found (see Figure 2a). This can be explained by the withdrawing of electron density from lithium with increasing Cl^- occupancy (decreasing S^{2-} level) on the 4*d* site (located within the Li cages, see Figure 1f). In addition, for $Li_{5.5}PS_{4.5}Cl_xBr_{1.5-x}$ with $x=0$, 0.4 and 0.8, the presence of a distinct shoulder peak of relatively lower intensity is evident at higher chemical shifts. This indicates the presence of two different Li positions, in agreement with the results from NPD analysis (see Figure 1e). It should be noted that the chemical shifts observed for the endmembers $Li_{5.5}PS_{4.5}Cl_{1.5}$ and $Li_{5.5}PS_{4.5}Br_{1.5}$ agree well with those reported in the literature.[28,37] From the ^{31}P MAS NMR measurements, complex spectra showing multiple contributions were obtained. However, they also revealed a gradual shift from higher to lower chemical shift (see Figure 2b). While $Li_{5.5}PS_{4.5}Cl_{1.5}$ shows multiple contributions around 83 ppm, the peaks are centered around 92 ppm for $Li_{5.5}PS_{4.5}Br_{1.5}$. This is in agreement with the ^{31}P MAS NMR shifts seen for Li_6PS_5X (X=Cl or Br).[24] Unlike $Li_{5.5}PS_{4.5}Cl_{1.5}$, for which two major peaks and a broad shoulder at higher chemical shift were detected,

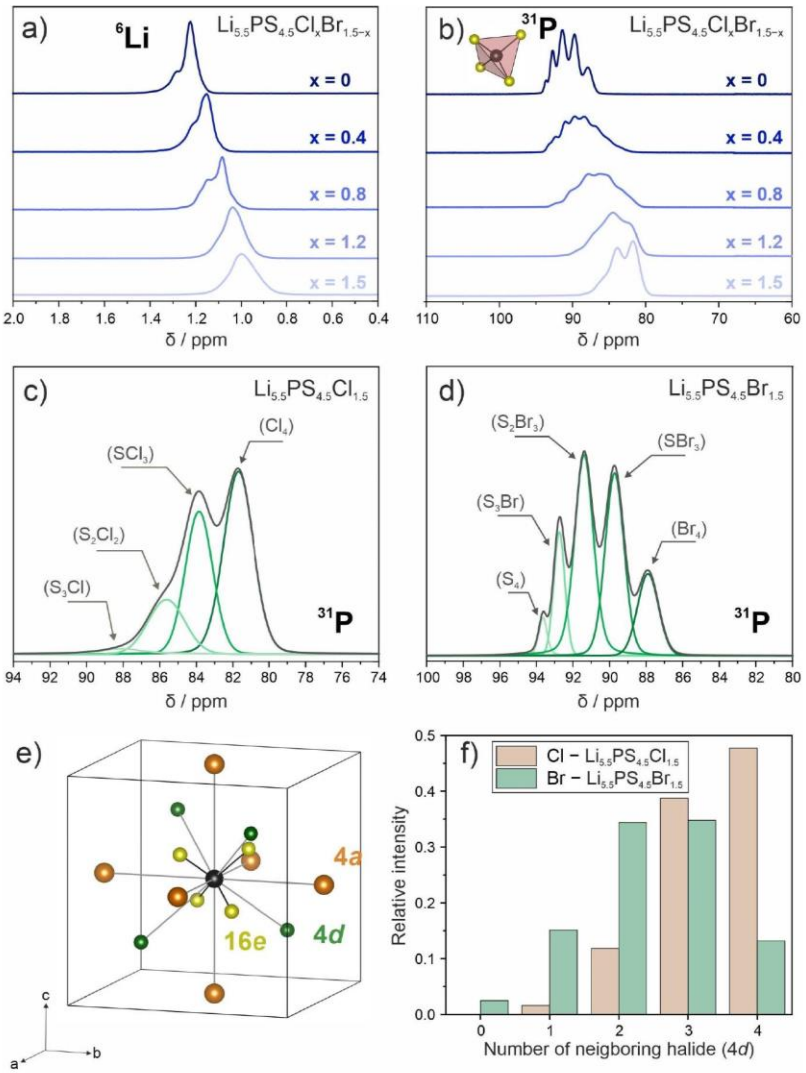

Figure 2. Local structure of the halogen-substituted lithium argyrodite solid electrolytes. (a) ^6Li and (b) ^{31}P MAS NMR spectra. Curve fits to the ^{31}P data for (c) $Li_{5.5}PS_{4.5}Cl_{1.5}$ and (d) $Li_{5.5}PS_{4.5}Br_{1.5}$ showing the different contributions. (e) Nearest neighbors around the $[PS_4]^{3-}$ tetrahedra with phosphorus and sulfur atoms shown in black and yellow, respectively. (f) Calculated probability of specific chemical environments around P from fitting a binomial distribution to the relative intensities in the ^{31}P MAS NMR spectra.

$Li_{5.5}PS_{4.5}Br_{1.5}$ exhibits five peaks of different intensities. For the mixed chlorine/bromine-containing samples, again broad ^{31}P MAS NMR spectra were obtained, with the peak intensities being blurred, indicating a larger degree of disorder. This was to be expected given that three different elements are now sharing the 4*d* site. To reveal the specific chemical environment of the two endmembers, the spectra were curve fitted (see Figure 2c and d). As shown in Figure 2c, the four different contributions for $Li_{5.5}PS_{4.5}Cl_{1.5}$ pertain to the number of nearest neighboring chlorine/sulfur atoms around the $[PS_4]^{3-}$ tetrahedra on the 4*d* Wyckoff position (see Figure 2e). The composition ranges from four chlorine atoms (Cl_4 with highest intensity contribution) to a mixed environment consisting of three sulfur and one chlorine atom (S_3Cl with lowest intensity contribution). A purely sulfur-containing environment (S_4) was not observed for $Li_{5.5}PS_{4.5}Cl_{1.5}$. In contrast, for $Li_{5.5}PS_{4.5}Br_{1.5}$, all possible configurations can be identified (see Figure 2d). Results from quantitative analysis of the different environments, i.e., relative peak intensities, are shown in Figure 2f. Unlike $Li_{5.5}PS_{4.5}Cl_{1.5}$, where a pure chlorine environment is most probable, a mixed S^{2-}/Br^- distribution over the neighboring sites is preferred in the case of $Li_{5.5}PS_{4.5}Br_{1.5}$.

The relative peak intensities observed in the ^{31}P MAS NMR spectra for $Li_{5.5}PS_{4.5}Cl_{1.5}$ and $Li_{5.5}PS_{4.5}Br_{1.5}$ can be well described by a simple binomial distribution:

$$p(n) = \frac{4!}{n! \cdot (4-n)!} \cdot q^n \cdot (1-q)^{4-n} \quad (1)$$

with n being the number of halogen ions on the four neighboring 4*d* sites around the $[PS_4]^{3-}$ tetrahedra and q representing the overall fraction of halogen ions occupying these sites. Fitting such a binomial distribution to the relative intensities (see Figure 2f), $q=0.83$ for $Li_{5.5}PS_{4.5}Cl_{1.5}$ ($x=1.5$) and $q=0.60$ for $Li_{5.5}PS_{4.5}Br_{1.5}$ ($x=0$) were obtained. These values are in excellent agreement with the occupancies determined by NPD (see Figure 2d). A similar analysis for the samples containing both halogen elements is challenging, as assignments of the different contributions to mixed $S^{2-}/Cl^-/Br^-$ environments (15 different possible compositions on the four neighboring 4*d* sites) requires the description by a multinomial distribution.

Next, the charge-transport properties were examined via complementary EIS and ^7Li PFG NMR spectroscopy. EIS measurements were conducted between 10 and 60 °C on cold-pressed pellets for all samples. At 25 °C, only a capacitive tail was visible (see Figure S3), indicating high ionic conductivity. Fitting of the spectra revealed ionic conductivities ranging from 4.2 to 9.6 mS cm^{-1} for $Li_{5.5}PS_{4.5}Br_{1.5}$ (lowest) and $Li_{5.5}PS_{4.5}Cl_{0.8}Br_{0.7}$ (highest), respectively. The corresponding results can be found in Table S9. From Arrhenius fitting of the temperature-dependent conductivity (see Figure 3a), the activation energies (E_A) were calculated to be in the range between 0.30 and 0.34 eV (see Table S9).

The lithium diffusion coefficient (D_{Li}) was probed using ^7Li PFG NMR spectroscopy at temperatures from 29 to 65 °C for the $Li_{5.5}PS_{4.5}Cl_xBr_{1.5-x}$ samples with $x=0$, 0.4, 0.8, 1.2 and 1.5. The echo damping versus gradient field strength is shown in Figure S4 and revealed only a single contribution for all materials. From the measurements, the D_{Li} at 29 °C was determined to be in the range of 1.0–1.4×10^{-11} m^2 s^{-1} (see Figure 3b). These values are among the highest observed for Li-ion conductors[28,58] and suggest an extremely fast mobility, in line with the conductivity deduced from the cold-pressed pellets via EIS. With increasing the temperature to 65 °C, the $Li_{5.5}PS_{4.5}Cl_{0.8}Br_{0.7}$ sample exhibits the strongest increase in D_{Li}, reaching 4.8×10^{-11} m^2 s^{-1}. From Arrhenius fitting of the temperature-dependent D_{Li} data (see Figure 3c), the activation energies were calculated, lying between 0.24 eV for $Li_{5.5}PS_{4.5}Br_{1.5}$ and 0.32 eV for $Li_{5.5}PS_{4.5}Cl_{1.2}Br_{0.3}$. Overall, they are in a similar range as those determined by EIS and about 0.1 eV higher compared to other superionic lithium argyrodites.[20,22,23,37,45] Using the Nernst-Einstein equation, the room-temperature conductivities were calculated from the diffusion coefficients. The obtained values are very high, reaching 22.7 mS cm^{-1} for $Li_{5.5}PS_{4.5}Cl_{0.8}Br_{0.7}$. So far, very few thiophosphate-based Li-ion conductors with a room-temperature conductivity above 20 mS cm^{-1} have been reported, crystallizing either in the argyrodite or LGPS structure type.[21,34,35,59] Finally, the conductivities and activation energies from EIS were compared to those calculated from the ^7Li PFG NMR data (see Table S9). As can be seen from Figure 3d, the ionic conductivities determined by EIS are lower by about 10 mS cm^{-1}, however they exhibit a similar trend with composition. This means that the pure bromine-containing endmember possesses the lowest ionic conductivity among all samples. If chlorine is introduced into the structure, the conductivity increases up to $x=0.8$, thereafter a slight decrease is observed. Note that the gap between the conductivity values from the two techniques is most likely rooted in poor grain boundary contacts, as ^7Li PFG NMR spectroscopy examines the bulk ionic conductivity, whereas EIS probes the overall sample conductivity (cold-pressed pellets). Thus, the measured diffusion coefficient ($\approx 10^{-11}$ m^2 s^{-1} at 29 °C) corresponds to a Li displacement of about 1.3 μm within the diffusion time scale (30 ms).[60] This is much smaller than the average particle size of these solid electrolytes, as observed by scanning electron microscopy (SEM) imaging and elemental mapping (see Figure S5a–e), supporting our assumption that solely bulk ionic conductivity is probed in the ^7Li PFG NMR spectroscopy measurements. Moreover, EIS was conducted on the $Li_{5.5}PS_{4.5}Cl_{0.8}Br_{0.7}$ sample that was hot-pressed into a dense pellet (see Supporting Information for details). The room-temperature ionic conductivity of the sintered pellet was determined to be about 19.8 mS cm^{-1} (see Figure S6), which agrees with the ^7Li PFG NMR results (absence of grain-boundary resistance). Regarding E_A, first a decrease with increasing chlorine content up to $x=0.8$ is observed, followed by a slight increase, reaching the lowest value for the best-conducting sample $Li_{5.5}PS_{4.5}Cl_{0.8}Br_{0.7}$. This is in contrast to the E_A determined by ^7Li PFG NMR spectroscopy, showing a gradual increase with increasing chlorine content. Again, the slightly different trends are due to poor

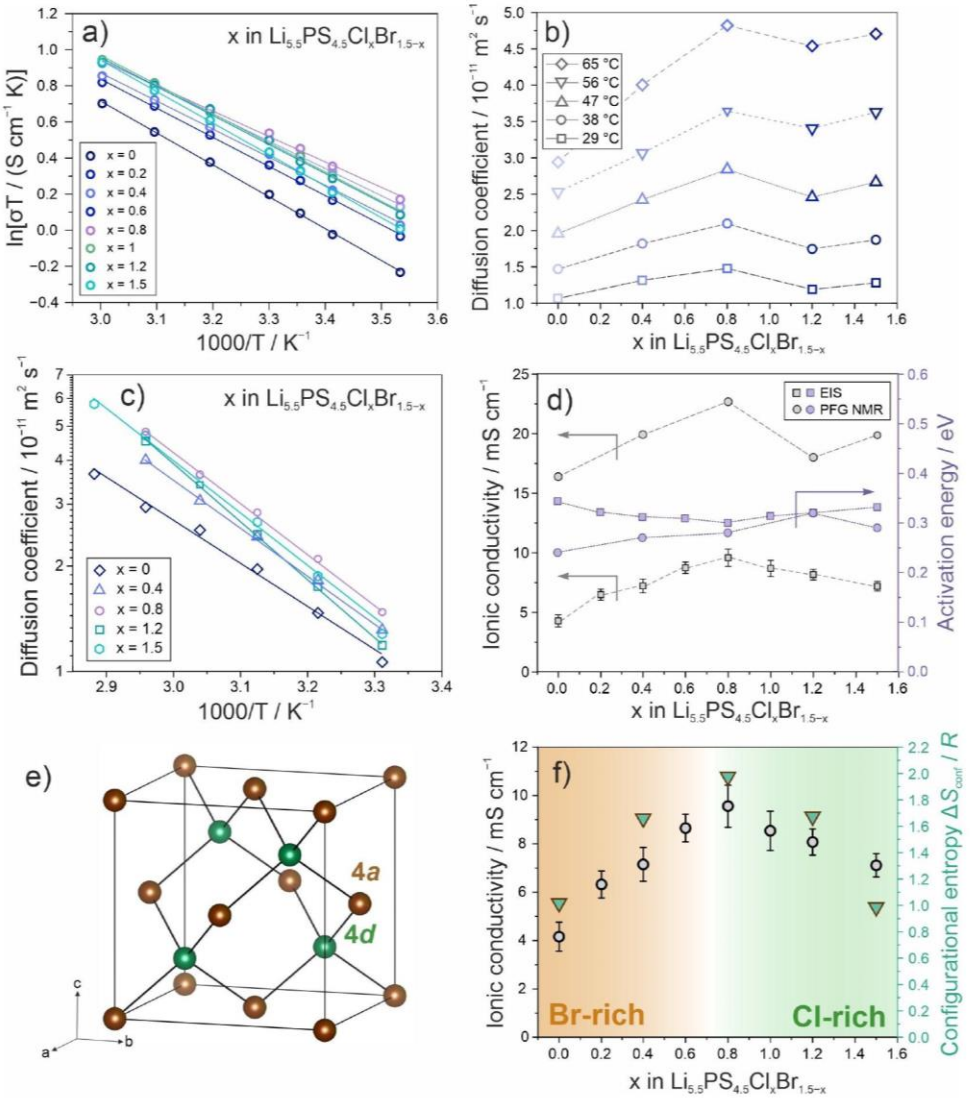

Figure 3. Charge-transport properties of the $Li_{5.5}PS_{4.5}Cl_xBr_{1.5-x}$ samples. (a) Arrhenius plots of conductivity (EIS). (b) Lithium diffusion coefficients at different temperatures and (c) corresponding Arrhenius plots (^{7}Li PFG NMR). (d) Ionic conductivities and activation energies at room temperature determined by EIS and ^{7}Li PFG NMR spectroscopy. (e) Schematic representation of the anion sublattice, including the 4*a* and 4*d* Wyckoff sites. (f) Correlation between configurational entropy calculated from the specific occupancies of the anion sublattice shown in panel (e) and ionic conductivity. If no error bars are visible, the standard deviation is smaller than the symbol.

grain-boundary contacts in the cold-pressed samples used for the EIS measurements.

On the basis of the above data, structure–property relationships can be established. In this regard, it is important to recall that recent reports have shown a possible beneficial effect of structural disorder in the rigid host lattice (framework) on ion diffusion of the mobile species (Li^+, Na^+, H^+).[42-45,61,62] In the case of the $Li_{5.5}PS_{4.5}Cl_xBr_{1.5-x}$ samples, the ΔS_{conf} refers to the number of possibilities for distributing sulfur, chlorine and bromine ions in the zincblende-type anion sublattice (4*a* and 4*d* Wyckoff positions) within the argyrodite structure (see Figure 3e). Usually, a mixing of elements over these two crystallographic sites has been expressed as halogen/sulfur site-inversion or disorder. However, if more than one halogen element is introduced, this descriptor is not accurate anymore. To express the halogen/sulfur disorder more precisely, the ΔS_{conf} presents a much better descriptor, as it also takes into account the partial occupancies of the different elemental constituents (not only mixing over two crystallographic sites). This means that if a high ΔS_{conf} is calculated, the number of anion conformations is large, comparable to the number of conformations a complex organic molecule can adopt. In other words, configurational entropy is a

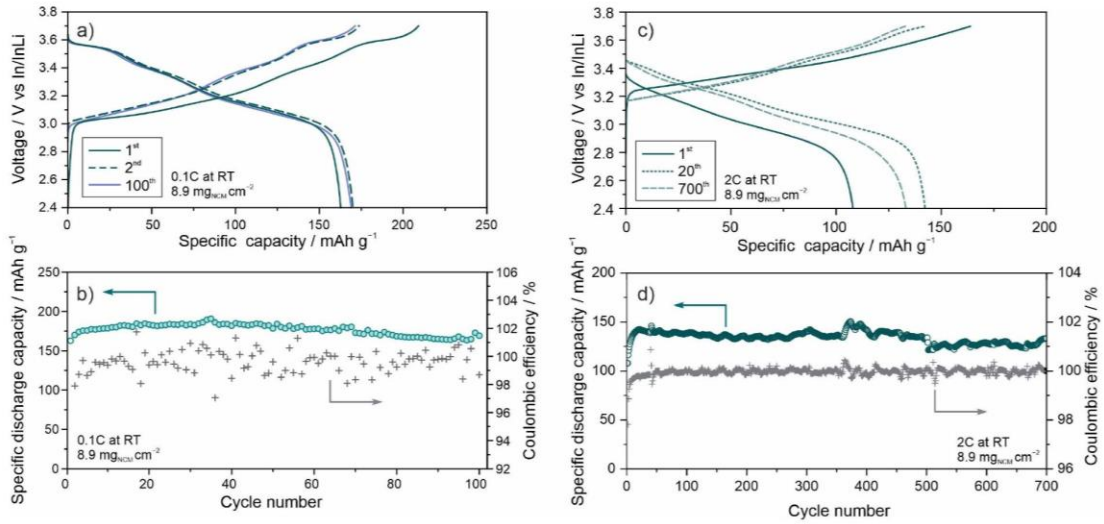

Figure 4. Electrochemical cycling of SSB cells with $Li_{5.5}PS_{4.5}Cl_{0.8}Br_{0.7}$ as SE. (a) Voltage profiles for the 1st, 2nd and 100th cycles at 0.1 C rate and (b) corresponding capacity retention and Coulomb efficiencies. (c) Voltage profiles for the 1st, 20th and 700th cycles at 2 C rate and (d) corresponding capacity retention and Coulomb efficiencies.

measure of anion disorder: The more equally the three anions are distributed over the two available crystallographic sites, the higher the ΔS_{conf} is. This in turn leads to local structural distortions (on the unit cell level, see Figure S2). Therefore, a high ΔS_{conf} of the anion sublattice leads to a statistical uncertainty for lithium diffusion pathways, i.e., broadened (Li-site) energy distributions and facilitated ion motion through the structure. If the ΔS_{conf} is calculated from the specific site occupancies determined by NPD, we find a maximum for the $Li_{5.5}PS_{4.5}Cl_{0.8}Br_{0.7}$ sample, which also exhibits the highest ionic conductivity (see Figure 3f). This result confirms that disorder of the anion sublattice is responsible for increased ionic conductivity. We assume that the structural complexity increases the vibrational entropy (phonon behavior), which is also known to affect ion diffusion through so-called phonon-ion interaction.[63] For example, Ding et al. recently investigated lattice softening in argyrodite Li_6PS_5Cl and found that the low-energy phonon modes (<10 meV) associated with Li are also important for realizing fast ion transport.[64] Taking into account the large disorder of the anion sublattice in $Li_{5.5}PS_{4.5}Cl_{0.8}Br_{0.7}$, phonon effects cannot be ignored and might be responsible, at least to some degree, for the improved Li-ion conductivity.

Finally, the material exhibiting the highest ionic conductivity ($Li_{5.5}PS_{4.5}Cl_{0.8}Br_{0.7}$) was tested as SE in pellet-stack SSB cells using a borate-coated, single-crystalline layered Ni-rich oxide cathode (s-NCM90@Li_3BO_3, 8.9 mg cm^{-2} loading) and an In/InLi anode. First, they were cycled at room temperature and at a rate of 0.1 C. In the initial cycle, specific charge and discharge capacities of 209 and 163 mAh g^{-1} were achieved, corresponding to a Coulomb efficiency (CE) of $\approx$78 % (see Figure 4a). Subsequently, both capacity and CE increased slightly, followed by relatively stable cycling over 100 cycles (see Figure 4b). In the 100th cycle, the cells delivered a specific discharge capacity of 169 mAh g^{-1}. During long-term cycling, the CE fluctuated between 98 and 100 %, suggesting minor detrimental side reactions. To further assess the performance of the $Li_{5.5}PS_{4.5}Cl_{0.8}Br_{0.7}$ SE, the SSB cells were electrochemically tested at a higher C-rate. Specifically, they were subjected to cycling at 2 C. In the initial cycle, specific charge and discharge capacities of 165 and 108 mAh g^{-1} were achieved (see Figure 4c). From the cycling data, the formation of a kinetically stable SE|s-NCM90@Li_3BO_3 interface, preventing further SE degradation, seems likely. After the first cycle, the specific discharge capacity gradually increased, reaching 142 mAh g^{-1} in the 20th cycle. Also, the CE stabilized above 99.5 % after five cycles. Minor capacity decay upon further cycling was observed, with 133 mAh g^{-1} in the 700th cycle (see Figure 4d). The performance assessment of the $Li_{5.5}PS_{4.5}Cl_{0.8}Br_{0.7}$ SE at both low and high C-rate provides evidence that dual-substituted, halogen-rich argyrodite SEs allow for stable SSB operation. We assume that the as-formed cathode interface/decomposition interphase exhibits a low partial electronic conductivity and kinetically prevents further degradation.[65] This is corroborated by the limited reversibility on the first cycle, but high CE observed during long-term cycling.

Conclusion

In summary we have investigated the structure–property relationships in halogen-rich $Li_{5.5}PS_{4.5}Cl_xBr_{1.5-x}$ SE materials for the solid-solution range of $0 \le x \le 1.5$. Using a combination of high-resolution NPD and ^{31}P MAS NMR spectroscopy, we show that a certain anion occupation over the 4*a* and 4*d* Wyckoff sites occurs, which also affects the lithium substructure. Charge-transport characteristics were revealed

by combined temperature-dependent EIS and ^{7}Li PFG NMR spectroscopy measurements. Overall, we demonstrate that an increased $S^{2-}/Cl^{-}/Br^{-}$ disorder, which can be expressed in the form of configurational entropy, leads to very fast Li-ion dynamics. This is reflected in a lithium diffusion coefficient of 1.4×10^{-11} m^{2}s^{-1} (29 °C), as well as in an ionic conductivity of 9.6 mS cm^{-1} in cold-pressed state and a bulk ionic conductivity of 22.7 mS cm^{-1} (25 °C) determined by ^{7}Li PFG NMR spectroscopy. This remarkable achievement is made possible by using inexpensive precursors, making the material suitable for large-scale application. Overall, the results indicate that compositional disorder in the anion sublattice of lithium argyrodites directly facilitates ion diffusion, meaning the conductivity is increasing with increasing configurational entropy. In addition, the sample with the highest conductivity, $Li_{5.5}PS_{4.5}Cl_{0.8}Br_{0.7}$, was tested as SE in SSB cells and found to allow for stable cycling over 700 cycles (with virtually no capacity decay), indicating its suitability for industrial use. Therefore, the concept of increasing ionic conductivity by increasing configurational entropy might pave the way toward the development of advanced SEs, with halogen-rich lithium argyrodites emerging as a promising class of materials.

Acknowledgements

S.W. and C.W.N. acknowledge the Natural Science Foundation of China (grant no. 52388201 and 52302305). S.W. acknowledges the Natural Science Foundation of Hubei Province (grant no. 2022CFB760) and the Guangdong Basic and Applied Basic Research Foundation (grant no. 2021A1515110312). J.L. acknowledges the Fonds der Chemischen Industrie (FCI) for financial support. F.S. is grateful to the Federal Ministry of Education and Research (BMBF) for funding within the project MELLi (03XP0447). This research used resources at the Spallation Neutron Source (SNS), a DOE Office of Science User Facility operated by the Oak Ridge National Laboratory (ORNL). This work is based on experiments performed at the Swiss spallation neutron source SINQ, Paul Scherrer Institute (PSI), Villigen, Switzerland (proposal no. 20051234). The authors thank Xinxin Tan for providing the NCM90 cathode material and Dr. Denis Cheptiakov for assistance in the NPD measurements. Open Access funding enabled and organized by Projekt DEAL.

Conflict of Interest

The authors declare no conflict of interest.

Data Availability Statement

The data that support the findings of this study are available from the corresponding author upon reasonable request.

Keywords: Argyrodite · High-Entropy Materials · Solid Electrolyte · Solid-State Batteries

[1] J. Janek, W. G. Zeier, *Nat. Energy* **2023**, *8*, 230–240.
[2] A. L. Robinson, J. Janek, *MRS Bull.* **2014**, *39*, 1046–1047.
[3] A. Bielefeld, D. A. Weber, J. Janek, *J. Phys. Chem. C* **2019**, *123*, 1626–1634.
[4] J. Lau, R. H. DeBlock, D. M. Butts, D. S. Ashby, C. S. Choi, B. S. Dunn, *Adv. Energy Mater.* **2018**, *8*, 1800933.
[5] Z. Zhang, Y. Shao, B. Lotsch, Y.-S. Hu, H. Li, J. Janek, L. F. Nazar, C.-W. Nan, J. Maier, M. Armand, *Energy Environ. Sci.* **2018**, *11*, 1945–1976.
[6] R. Koerver, W. Zhang, L. de Biasi, S. Schweidler, A. O. Kondrakov, S. Kolling, T. Brezesinski, P. Hartmann, W. G. Zeier, J. Janek, *Energy Environ. Sci.* **2018**, *11*, 2142–2158.
[7] Y. B. Song, H. Kwak, W. Cho, K. S. Kim, Y. S. Jung, K.-H. Park, *Curr. Opin. Solid State Mater. Sci.* **2022**, *26*, 100977.
[8] J. A. Lewis, J. Tippens, F. J. Q. Cortes, M. T. McDowell, *Trends Chem.* **2019**, *1*, 845–857.
[9] J. H. Teo, F. Strauss, F. Walther, Y. Ma, S. Payandeh, T. Scherer, M. Bianchini, J. Janek, T. Brezesinski, *Mater. Futures* **2022**, *1*, 015102.
[10] J. Tippens, J. C. Miers, A. Afshar, J. A. Lewis, F. J. Q. Cortes, H. Qiao, T. S. Marchese, C. V. Di Leo, C. Saldana, M. T. McDowell, *ACS Energy Lett.* **2019**, *4*, 1475–1483.
[11] J. Auvergniot, A. Cassel, J.-B. Ledeuil, V. Viallet, V. Seznec, R. Dedryvère, *Chem. Mater.* **2017**, *29*, 3883–3890.
[12] R. Koerver, I. Aygün, T. Leichtweiß, C. Dietrich, W. Zhang, J. O. Binder, P. Hartmann, W. G. Zeier, J. Janek, *Chem. Mater.* **2017**, *29*, 5574–5582.
[13] J. Auvergniot, A. Cassel, D. Foix, V. Viallet, V. Seznec, R. Dedryvère, *Solid State Ionics* **2017**, *300*, 78–85.
[14] W. D. Richards, L. J. Miara, Y. Wang, J. C. Kim, G. Ceder, *Chem. Mater.* **2016**, *28*, 266–273.
[15] S. P. Culver, R. Koerver, W. G. Zeier, J. Janek, *Adv. Energy Mater.* **2019**, *9*, 1900626.
[16] A.-Y. Kim, F. Strauss, T. Bartsch, J. H. Teo, T. Hatsukade, A. Mazilkin, J. Janek, P. Hartmann, T. Brezesinski, *Chem. Mater.* **2019**, *31*, 9664–9672.
[17] Y. Xiao, L. J. Miara, Y. Wang, G. Ceder, *Joule* **2019**, *3*, 1252–1275.
[18] S. Wang, R. Fang, Y. Li, Y. Liu, C. Xin, F. H. Richter, C.-W. Nan, *J. Materiomics* **2021**, *7*, 209–218.
[19] N. Kamaya, K. Homma, Y. Yamakawa, M. Hirayama, R. Kanno, M. Yonemura, T. Kamiyama, Y. Kato, S. Hama, K. Kawamoto, A. Mitsui, *Nat. Mater.* **2011**, *10*, 682–686.
[20] L. Zhou, A. Assoud, Q. Zhang, X. Wu, L. F. Nazar, *J. Am. Chem. Soc.* **2019**, *141*, 19002–19013.
[21] Y. Li, S. Song, H. Kim, K. Nomoto, H. Kim, X. Sun, S. Hori, K. Suzuki, N. Matsui, M. Hirayama, T. Mizoguchi, T. Saito, T. Kamiyama, R. Kanno, *Science* **2023**, *381*, 50–53.
[22] M. A. Kraft, S. Ohno, T. Zinkevich, R. Koerver, S. P. Culver, T. Fuchs, A. Senyshyn, S. Indris, B. J. Morgan, W. G. Zeier, *J. Am. Chem. Soc.* **2018**, *140*, 16330–16339.
[23] Y. Lee, J. Jeong, H. J. Lee, M. Kim, D. Han, H. Kim, J. M. Yuk, K.-W. Nam, K. Y. Chung, H.-G. Jung, S. Yu, *ACS Energy Lett.* **2022**, *7*, 171–179.
[24] H.-J. Deiseroth, S.-T. Kong, H. Eckert, J. Vannahme, C. Reiner, T. Zaiß, M. Schlosser, *Angew. Chem. Int. Ed.* **2008**, *47*, 755–758.
[25] S.-T. Kong, H.-J. Deiseroth, C. Reiner, Ö. Gün, E. Neumann, C. Ritter, D. Zahn, *Chem. Eur. J.* **2010**, *16*, 2198–2206.
[26] S. Wang, Y. Zhang, X. Zhang, T. Liu, Y.-H. Lin, Y. Shen, L. Li, C.-W. Nan, *ACS Appl. Mater. Interfaces* **2018**, *10*, 42279–42285.

[27] L. Zhou, N. Minafra, W. G. Zeier, L. F. Nazar, *Acc. Chem. Res.* **2021**, *54*, 2717–2728.
[28] P. Adeli, J. D. Bazak, K. H. Park, I. Kochetkov, A. Huq, G. R. Goward, L. F. Nazar, *Angew. Chem. Int. Ed.* **2019**, *58*, 8681–8686.
[29] S. Wang, W. Zhang, X. Chen, D. Das, R. Ruess, A. Gautam, F. Walther, S. Ohno, R. Koerver, Q. Zhang, W. G. Zeier, F. H. Richter, C.-W. Nan, J. Janek, *Adv. Energy Mater.* **2021**, *11*, 2100654.
[30] T.-T. Zuo, F. Walther, J. H. Teo, R. Rueß, Y. Wang, M. Rohnke, D. Schröder, L. F. Nazar, J. Janek, *Angew. Chem. Int. Ed.* **2023**, *62*, e202213228.
[31] L. Peng, C. Yu, S. Cheng, J. Xie, *Batteries & Supercaps* **2023**, *6*, e202200553.
[32] W. D. Jung, J.-S. Kim, S. Choi, S. Kim, M. Jeon, H.-G. Jung, K. Y. Chung, J.-H. Lee, B.-K. Kim, J.-H. Lee, H. Kim, *Nano Lett.* **2020**, *20*, 2303–2309.
[33] D. Gu, H. Kim, B.-K. Kim, J.-H. Lee, S. Park, *CrystEngComm* **2023**, *25*, 4182–4188.
[34] H. Chen, Y. Lu, H. Zhang, Y. Zhou, J. Chen, X. Huang, B. Tian, *Chem. Commun.* **2023**, *59*, 7220–7223.
[35] S. V. Patel, S. Banerjee, H. Liu, P. Wang, P.-H. Chien, X. Feng, J. Liu, S. P. Ong, Y.-Y. Hu, *Chem. Mater.* **2021**, *33*, 1435–1443.
[36] S. Wang, X. Wu, Y. Liang, Y. Xu, S. Guan, K. Wen, X. Miao, Y. Liang, H. He, Y. Lin, Y. Shen, C.-W. Nan, *Front. Chem. Eng.* **2022**, *4*, 883502.
[37] P. Wang, H. Liu, S. Patel, X. Feng, P.-H. Chien, Y. Wang, Y.-Y. Hu, *Chem. Mater.* **2020**, *32*, 3833–3840.
[38] X. Feng, P.-H. Chien, Y. Wang, S. Patel, P. Wang, H. Liu, M. Immediato-Scuotto, Y.-Y. Hu, *Energy Storage Mater.* **2020**, *30*, 67–73.
[39] S. Wang, A. Gautam, X. Wu, S. Li, X. Zhang, H. He, Y. Lin, Y. Shen, C.-W. Nan, *Adv. Energy Sustainability Res.* **2023**, *4*, 2200197.
[40] M. A. Kraft, S. P. Culver, M. Calderon, F. Böcher, T. Krauskopf, A. Senyshyn, C. Dietrich, A. Zevalkink, J. Janek, W. G. Zeier, *J. Am. Chem. Soc.* **2017**, *139*, 10909–10918.
[41] S. Ohno, B. Helm, T. Fuchs, G. Dewald, M. A. Kraft, S. P. Culver, A. Senyshyn, W. G. Zeier, *Chem. Mater.* **2019**, *31*, 4936–4944.
[42] Y. Zeng, B. Ouyang, J. Liu, Y.-W. Byeon, Z. Cai, L. J. Miara, Y. Wang, G. Ceder, *Science* **2022**, *378*, 1320–1324.
[43] F. Strauss, J. Lin, M. Duffiet, K. Wang, T. Zinkevich, A.-L. Hansen, S. Indris, T. Brezesinski, *ACS Mater. Lett.* **2022**, *4*, 418–423.
[44] F. Strauss, J. Lin, A. Kondrakov, T. Brezesinski, *Matter* **2023**, *6*, 1068–1070.
[45] J. Lin, G. Cherkashinin, M. Schäfer, G. Melinte, S. Indris, A. Kondrakov, J. Janek, T. Brezesinski, F. Strauss, *ACS Mater. Lett.* **2022**, *4*, 2187–2194.
[46] S.-K. Jung, H. Gwon, H. Kim, G. Yoon, D. Shin, J. Hong, C. Jung, J.-S. Kim, *Nat. Commun.* **2022**, *13*, 7638.
[47] Y. Chen, T. Wang, H. Chen, W. H. Kan, W. Yin, Z. Song, C. Wang, J. Ma, W. Luo, Y. Huang, *Matter* **2023**, *6*, 1530–1541.
[48] A. Behera, in *Advanced Materials An Introduction to Modern Materials Science* (Ed.: A. Behera), Springer International Publishing, Cham, **2022**, pp. 291–320.
[49] C. Oses, C. Toher, S. Curtarolo, *Nat. Rev. Mater.* **2020**, *5*, 295–309.
[50] R.-Z. Zhang, M. J. Reece, *J. Mater. Chem. A* **2019**, *7*, 22148–22162.
[51] A. Sarkar, B. Breitung, H. Hahn, *Scr. Mater.* **2020**, *187*, 43–48.
[52] C. M. Rost, E. Sachet, T. Borman, A. Moballegh, E. C. Dickey, D. Hou, J. L. Jones, S. Curtarolo, J.-P. Maria, *Nat. Commun.* **2015**, *6*, 8485.
[53] J. Wang, Y. Cui, Q. Wang, K. Wang, X. Huang, D. Stenzel, A. Sarkar, R. Azmi, T. Bergfeldt, S. S. Bhattacharya, R. Kruk, H. Hahn, S. Schweidler, T. Brezesinski, B. Breitung, *Sci. Rep.* **2020**, *10*, 18430.
[54] Y. Ma, Y. Ma, Q. Wang, S. Schweidler, M. Botros, T. Fu, H. Hahn, T. Brezesinski, B. Breitung, *Energy Environ. Sci.* **2021**, *14*, 2883–2905.
[55] A. Sarkar, Q. Wang, A. Schiele, M. R. Chellali, S. S. Bhattacharya, D. Wang, T. Brezesinski, H. Hahn, L. Velasco, B. Breitung, *Adv. Mater.* **2019**, *31*, 1806236.
[56] B. Yang, Y. Zhang, H. Pan, W. Si, Q. Zhang, Z. Shen, Y. Yu, S. Lan, F. Meng, Y. Liu, H. Huang, J. He, L. Gu, S. Zhang, L.-Q. Chen, J. Zhu, C.-W. Nan, Y.-H. Lin, *Nat. Mater.* **2022**, *21*, 1074–1080.
[57] R. D. Shannon, *Acta Crystallogr. Sect. A* **1976**, *32*, 751–767.
[58] A. Kuhn, O. Gerbig, C. Zhu, F. Falkenberg, J. Maier, B. V. Lotsch, *Phys. Chem. Chem. Phys.* **2014**, *16*, 14669–14674.
[59] Y. Kato, S. Hori, T. Saito, K. Suzuki, M. Hirayama, A. Mitsui, M. Yonemura, H. Iba, R. Kanno, *Nat. Energy* **2016**, *1*, 16030.
[60] H. Stöffler, T. Zinkevich, M. Yavuz, A.-L. Hansen, M. Knapp, J. Bednarčík, S. Randau, F. H. Richter, J. Janek, H. Ehrenberg, *J. Phys. Chem. C* **2019**, *123*, 10280–10290.
[61] D. Bérardan, S. Franger, A. K. Meena, N. Dragoe, *J. Mater. Chem. A* **2016**, *4*, 9536–9541.
[62] M. Gazda, T. Miruszewski, D. Jaworski, A. Mielewczyk-Gryń, W. Skubida, S. Wachowski, P. Winiarz, K. Dzierzgowski, M. Łapiński, I. Szpunar, E. Dzik, *ACS Mater. Lett.* **2020**, *2*, 1315–1321.
[63] S. Muy, R. Schlem, Y. Shao-Horn, W. G. Zeier, *Adv. Energy Mater.* **2021**, *11*, 2002787.
[64] J. Ding, PhD thesis, Duke University, **2022**.
[65] A. Banerjee, X. Wang, C. Fang, E. A. Wu, Y. S. Meng, *Chem. Rev.* **2020**, *120*, 6878–6933.

Manuscript received: September 21, 2023
Accepted manuscript online: October 30, 2023
Version of record online: November 13, 2023

3.5. Publication V: Electrochemical Testing and Benchmarking of Compositionally Complex Lithium Argyrodite Electrolytes for All-Solid-State Battery Application

Publication V is a follow-up to Publication III and IV (3.3. & 3.4.), assessing the electrochemical performance of anion/cation-substituted high-entropy lithium argyrodites. These materials demonstrate ionic conductivities of approximately 10 mS/cm at 25 °C, and thus allow for a fair comparison. In addition, the commercially available SE Li_6PS_5Cl was used as reference material. Using different electrochemical characterization techniques, it was revealed that the multication-substituted lithium argyrodites exhibit a narrower electrochemical stability window, and a poorer chemical stability in contact with Li metal in contrast to the anion-substituted high-entropy lithium argyrodite ($Li_{5.5}PS_{4.5}Cl_{0.8}Br_{0.7}$) and Li_6PS_5Cl. At 25 °C and high current rates, both anion and cation substitution make lithium argyrodites superior to the commercialized Li_6PS_5Cl. However, the multication-substituted lithium argyrodites undergoes severe and continuous capacity fading during cycling at 45 °C due to inferior electrochemical stability. To optimize the performance of SSB cells, cation substituted argyrodite SE can solely be used as the separator layer, enhancing the cell cyclability. The best overall performance is achieved with $Li_{5.5}PS_{4.5}Cl_{0.8}Br_{0.7}$, a superionic high-entropy solid electrolyte.

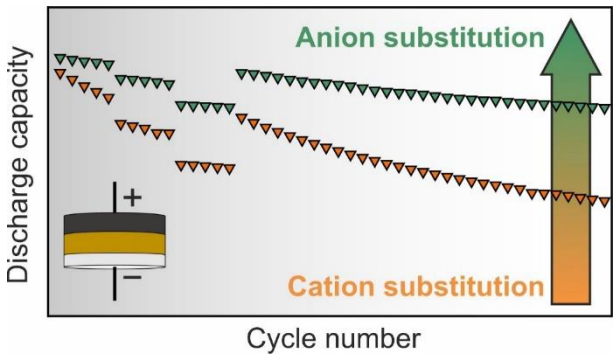

Figure 22: Table of Contents (TOC) of Publication V. Adapted from reference [22].

Publication V has shared first authorship between J. Du and J. Lin. The experiments were planned and designed by J. Lin. under the supervision of T. Brezesinski and F. Strauss. The synthesis of solid electrolytes was primarily done by J. Du, following the optimized procedure developed by J. Lin. J. Du and J. Lin conducted the electrochemical tests together, including CV, time dependent EIS and GCPL tests. The experiments were mainly conducted by J. Du under the supervision of J. Lin. The initial data treatments were performed by J. Du and subsequently reviewed and further checked by J. Lin. R. Zhang conducted the EIS and DRT analysis. The first draft was written by J. Du and J. Lin. The final manuscript was then edited by all co-authors.

Check for updates

Batteries & Supercaps

Research Article
doi.org/10.1002/batt.202400112

Chemistry Europe
European Chemical Societies Publishing

www.batteries-supercaps.org

Electrochemical Testing and Benchmarking of Compositionally Complex Lithium Argyrodite Electrolytes for All-Solid-State Battery Application

Jianxuan Du+,[a] Jing Lin+,[a] Ruizhuo Zhang,[a] Shuo Wang,[b, c] Sylvio Indris,[d] Helmut Ehrenberg,[d] Aleksandr Kondrakov,[a, e] Torsten Brezesinski,*[a] and Florian Strauss*[a]

Ceramic ion conductors play a pivotal role as electrolytes in solid-state batteries (SSBs). Aside from the ionic conductivity, their (electro)chemical stability has a profound effect on the performance. Lithium thiophosphates represent a widely used class of superionic materials, yet they suffer from limited stability and are known to undergo interfacial degradation upon battery cycling. Knowledge of composition-dependent properties is essential to improving upon the stability of thiophosphate solid electrolytes (SEs). In recent years, compositionally complex (multicomponent) and high-entropy lithium argyrodite SEs have been reported, having room-temperature ionic conductivities of $\sigma_{ion} > 10$ mS cm^{-1}. In this work, various multi-cationic and -anionic substituted argyrodite SEs are electrochemically tested via cyclic voltammetry and impedance spectroscopy, as well as under operating conditions in SSB cells with layered Ni-rich oxide cathode and indium-lithium anode. Cation substitution is found to negatively affect the electrochemical stability, while anion substitution (introducing Cl^-/Br^- and increasing halide content) has a beneficial effect on the cyclability, especially at high current rates.

1. Introduction

Bulk-type solid-state batteries (SSBs) are emerging as a promising next-generation electrochemical energy-storage technology. The implementation of inorganic solid electrolytes (SEs) instead of organic liquid electrolytes may possibly help to increase the energy and power density of battery cells and to improve safety.[1,2] For realizing this, highly conducting and (electro)chemically stable SEs are needed, which ideally should also be mechanically flexible to accommodate for volume changes of the active electrode materials during cycling.[3–6]

In search of suitable materials, lithium argyrodites (Li_6PS_5X, with X=Cl, Br, I) have been recognized as one of the most promising classes of SEs. This is due in part to high room-temperature ionic conductivities of $\sigma_{ion} > 1$ mS cm^{-1},[7–10] along with favorable mechanical properties, the latter allowing to effectively establish intimate contact with the active electrode materials and for facile cell assembly (without the need for sintering).[11,12] Moreover, the ion mobility in lithium argyrodites can be altered by iso- or aliovalent substitution on the phosphorus, sulfur, and halide sites or by increasing the halide content, referring to halogen-rich SEs with the general formula $Li_{5.5}PS_{4.5}X_{1.5}$ (X=Cl, Br).[13–18] This has led to the discovery of materials, either cationic or anionic substituted, showing ionic conductivities exceeding 10 mS cm^{-1} at room temperature.[13,14,17,19] However, literature is lacking thorough electrochemical evaluation of highly conducting lithium argyrodites, making rational optimization difficult. This not only pertains to conductivity, but also to stability.

Recently, we have reported on high-entropy lithium argyrodites as a novel class of chemically complex SEs with high ionic conductivities, even in a cold-pressed state.[16,18,20] Despite varying anion and cation compositions, several of these materials exhibit room-temperature ionic conductivities of $\sigma_{ion} \geq 10$ mS cm^{-1}. This now allows to test different SEs of similar ionic conductivity in SSB cells using a layered Ni-rich oxide cathode active material, namely $LiNi_{0.85}Co_{0.10}Mn_{0.05}O_2$ (NCM851005). Specifically, employing $Li_{6.5}[P_{0.25}Si_{0.25}Ge_{0.25}Sb_{0.25}]S_5I$ (equimolar), $Li_{6.67}[P_{0.16}Si_{0.5}Ge_{0.16}Sb_{0.16}]S_5I$ (Si-rich), $Li_{6.67}[P_{0.16}Si_{0.16}Ge_{0.5}Sb_{0.16}]S_5I$ (Ge-rich), $Li_{5.5}PS_{4.5}Cl_{0.8}Br_{0.7}$ (I-free), and Li_6PS_5Cl (LPSCl), we examine the effect that the composition of the superionic SE has on the electrochemical stability and

[a] J. Du,+ J. Lin,+ R. Zhang, Dr. A. Kondrakov, Dr. T. Brezesinski, Dr. F. Strauss
Battery and Electrochemistry Laboratory (BELLA), Institute of Nanotechnology, Karlsruhe Institute of Technology (KIT), Kaiserstr. 12, 76131 Karlsruhe, Germany
E-mail: torsten.brezesinski@kit.edu
florian.strauss@kit.edu

[b] Prof. S. Wang
Center of Smart Materials and Devices, State Key Laboratory of Advanced Technology for Materials Synthesis and Processing, School of Material Science and Engineering, Wuhan University of Technology, Wuhan 430070, China

[c] Prof. S. Wang
Foshan (Southern China) Institute for New Materials, Foshan 528200, China

[d] Dr. S. Indris, Prof. H. Ehrenberg
Institute for Applied Materials-Energy Storage Systems (IAM-ESS), Karlsruhe Institute of Technology (KIT), Kaiserstr. 12, 76131 Karlsruhe, Germany

[e] Dr. A. Kondrakov
BASF SE, Carl-Bosch-Str. 38, 67056 Ludwigshafen, Germany

[+] Contributed equally to this work.

Supporting information for this article is available on the WWW under https://doi.org/10.1002/batt.202400112

Batteries & Supercaps
Research Article
doi.org/10.1002/batt.202400112
Chemistry Europe
European Chemical Societies Publishing

battery performance. Using cyclic voltammetry (CV), time-resolved electrochemical impedance spectroscopy (EIS), and galvanostatic charge-discharge tests, we demonstrate that anion prevails over cation substitution.

2. Results and Discussion

Initially, X-ray diffraction (XRD) measurements were performed to determine the crystal structure and confirm phase purity of the synthesized SEs. Figure 1 shows the respective XRD patterns, along with that collected from the commercially available LPSCl, which served as a benchmark SE, indicating that the materials are single-phase argyrodites. Aside from the presence of Li_2S and/or LiI trace impurities (unreacted precursors), the reflections can be indexed to the *F*-43*m* space group.[7] For the cationic substituted samples, Rietveld refinement of the diffraction data was carried out (see Tables S1–S3, Supporting Information), while Le Bail analysis was performed for the anionic substituted (I-free) material both to determine the lattice parameter and quantify the fraction of crystalline impurities (see Figure S1a–d, Supporting Information). As evident from Table 1, the equimolar, Ge-rich, and Si-rich SEs exhibit a larger lattice parameter than the I-free sample due to the larger ionic radius of iodine compared to chlorine and bromine.[21] Also, the differences observed in the lattice parameter for the equimolar, Ge-rich, and Si-rich SEs align with variations in ionic radii considering the different stoichiometry of the materials. The ionic conductivities determined on cold-pressed pellets at room temperature are given in Table 1. They varied from $\sigma_{ion} \approx 3$ mS cm^{-1} for LPSCl to around 15 mS cm^{-1} for the Ge-rich SE.

The electrochemical stability of the as-prepared materials was investigated by CV measurements conducted on cells with SE/carbon black composite as working electrode, SE as separator layer, and indium-lithium alloy as counter electrode. This configuration allows to assess the electrochemical stability window (ESW) of the different SEs.[22,23] Figure 2a shows the first-cycle CV curves at 0.1 mV s^{-1} and at 45 °C, with the current normalized to the mass of SE in the working electrode. Asymmetric current peaks were observed for all SEs, indicating that (electrochemically driven) side reactions occur, independent of the composition. The potential range of the initial sweep was from open-circuit voltage (OCV) to 3.68 V vs. In/InLi (~4.3 V vs. Li$^+$/Li). For the cationic substituted SEs, a steep increase in specific current was noticed around 2.0 V (~2.62 V vs. Li$^+$/Li). In contrast, for LPSCl and the I-free SE, the current onset was detected at about 2.22 and 2.27 V (~2.84 and 2.89 V vs. Li$^+$/Li), respectively. In general, this can be attributed to sulfide oxidation to polysulfides of different chain lengths [i.e., $nS^{2-} \rightarrow S_n^{2-} + (2n-2)e^-$]. The lower onset potential found for the cationic substituted samples implies a lower anodic stability compared to both the anionic substituted SE and LPSCl. It has been reported that the oxidative decomposition of LPSCl results in the formation of LiCl, P_2S_5, and S (or S_8) according to Equation 1.[24,25]

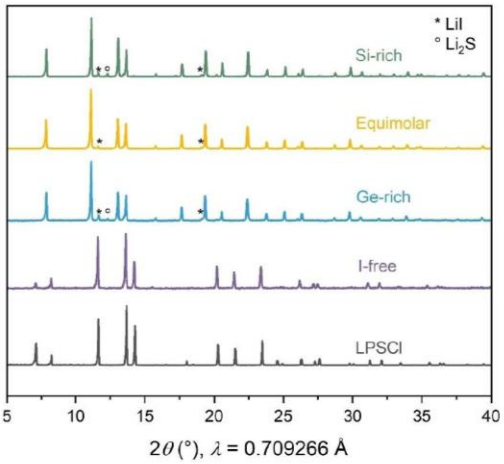

Figure 1. XRD patterns collected from the different SEs. Trace impurities of unreacted precursors are denoted by symbols.

$$Li_6PS_5Cl \rightarrow LiCl + \frac{1}{2}P_2S_5 + \frac{5}{2}S + 5Li^+ + 5e^- \quad (1)$$

However, this equation is simplified as the underlying reaction steps are most likely mechanistically more diverse, possibly involving the formation of a variety of thiophosphates, such as $P_2S_8^{4-}$, $P_2S_7^{4-}$, or $P_2S_6^{2-}$, and lithium polysulfides Li_2S_n (with $n \geq 1$).[26,27] With regard to the multi-element substituted SEs, the electrochemical decomposition reactions become much more complex, also involving semimetal sulfide species.[16] The results indicate that multi-cation substitution on the phosphorus site reduces the onset potential for oxidation

Table 1. Refined lattice parameter of the different SEs and ionic conductivity determined on cold-pressed pellets at room temperature.

Sample	Composition	Lattice parameter *a* (Å)	Ionic conductivity (mS cm^{-1})
Equimolar	$Li_{6.5}[P_{0.25}Si_{0.25}Ge_{0.25}Sb_{0.25}]S_5I$	10.29224(12)	12.3
Si-rich	$Li_{6.67}[P_{0.16}Si_{0.5}Ge_{0.16}Sb_{0.16}]S_5I$	10.28330(9)	12.3
Ge-rich	$Li_{6.67}[P_{0.16}Si_{0.16}Ge_{0.5}Sb_{0.16}]S_5I$	10.32186(13)	14.6
I-free	$Li_{5.5}PS_{4.5}Cl_{0.8}Br_{0.7}$	9.89601(29)	8.8
LPSCl*	Li_6PS_5Cl	9.85485(7)	3.4

*From ref. [22] for lattice parameter and from ref. [9] for ionic conductivity.

Batteries & Supercaps | Research Article
doi.org/10.1002/batt.202400112
Chemistry Europe
European Chemical Societies Publishing

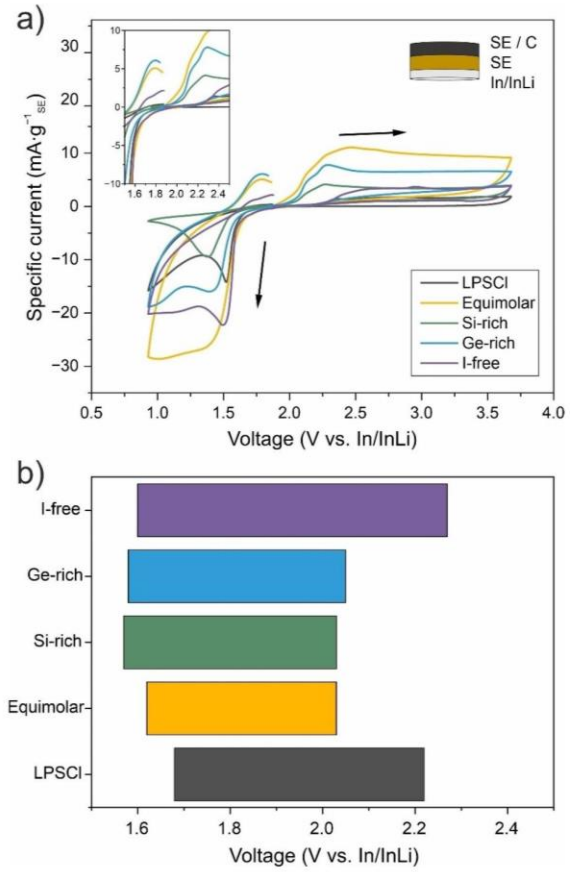

Figure 2. (a) First-cycle CV curves for the different SEs measured at 0.1 mV s^{-1} and 45 °C. The cell configuration used is schematically shown in the inset. (b) The ESWs extracted from the cyclic voltammograms.

by about 250 mV. This implies a lower oxidative stability compared to both the I-free SE and LPSCl, which can be attributed to the lower ionization potential and weaker bonding strength of I^- compared to Br^- and Cl^-, causing a somewhat poorer stability for the cationic substituted samples.[28] However, previous research on $Li_{6+x}P_{1-x}M_xS_5I$ (M=Si^{4+}, Ge^{4+} and $x=0.6$) SEs has shown that the oxidative stability remains virtually unaltered with 60% phosphorus substitution.[29] In contrast, the data presented herein suggest that complex cation substitution has a more profound effect on the stability. However, we cannot rule out that the higher degree of substitution (>75%, see Table 1) is playing a role as well. We hypothesize that the lower oxidative stability of the cationic substituted SEs is closely related to the strength of the M–S bond and the lattice distortion. The former can be simplified expressed as ionic potential φ of M (with φ being the ratio of the electrical charge z to the ionic radius r), with a higher ionic potential indicating a greater bond strength.[30] For phosphorus (4-fold coordination, +5 oxidation state), a higher ionic potential ($\varphi=29.41$ Å^{-1}) was calculated compared to silicon ($\varphi=15.38$ Å^{-1}) and germanium ($\varphi=10.26$ Å^{-1}) (note: an even lower ionic potential can be expected for Sb^{5+}), which helps explain the improved anodic stability of purely phosphorus-containing SEs.

According to the Bell-Evans-Polanyi (B–E–P) principle, which delineates kinetic-thermodynamic relationships, oxidative stability not only correlates with the thermodynamic driving force for oxidizing materials, but also depends on the kinetics.[31,32] We believe that multi-cation substitution reduces the oxidative stability by enhancing the kinetics of the electrochemically-driven decomposition reactions (lower barrier for ion diffusion in the distorted lattice).[33] Specifically, the weakened bonds and softened lattice resulting from the complex substitution may facilitate cation and anion mobility, which is reflected in narrower ESWs. Therefore, unlike previous conclusions, it seems that phosphorus substitution directly affects the electrochemical stability of lithium thiophosphates.[25] Moreover, the anodic current was larger in the second and third cycles for all samples, indicating continuous SE degradation (electrochemical oxidation) during cycling (see Figure S2a–e, Supporting Information).

With regard to the cathodic stability, current flow in the initial sweep was clearly noticed below 1.8 V (~2.42 V vs. Li^+/Li). According to the literature, this can be attributed to phosphorus reduction, as shown in Equation 2 for LPSCl, and/or reduction of polysulfide species formed previously at higher potentials.[26]

$$Li_6PS_5Cl + 8Li^+ + 8e^- \rightarrow LiCl + Li_3P + 5Li_2S \quad (2)$$

Upon further cycling (see Figure S2a–e, Supporting Information), the absolute cathodic current decreased, except for the Si-rich SE where a slight increase was observed. The asymmetry between the reductive and oxidative currents points towards irreversible side reactions, especially for the equimolar, Ge-rich, I-free, and LPSCl SEs. It should be noted though that unravelling the decomposition reactions occurring during cycling is very challenging, since not only the thermodynamic stability of the SEs (and decomposition products), but also the kinetic stability of the formed interfaces/interphases plays a decisive role.[33] Nevertheless, the ESWs of the different materials studied in the present work were extracted from the first-cycle CV curves. As can be seen from Figure 2b, the cationic substituted samples exhibit narrow ESWs ranging from around 1.6 to 2.0 V (~2.22–2.62 V vs. Li^+/Li). For the other SEs, the window is wider, in particular with respect to oxidative stability, where the upper limit is pushed up to 2.27 V (~2.89 V vs. Li^+/Li). Overall, we conclude from the data that altering the composition of thiophosphate SEs affects their anodic and cathodic stability. The ESW decreased in the following order: I-free > LPSCl > Si-rich > Ge-rich > equimolar.

The possibility of using a lithium anode is one of the most promising aspects of SSBs. However, many materials suffer from severe instability when in contact with lithium metal.[34,35] The compatibility of the SEs with lithium was probed at 25 °C using a Li|SE|Li cell configuration. Impedance spectra were recorded directly after assembly and at fixed time intervals up to 24 h without applying external pressure. Figure S3a–e (Supporting Information) shows the respective time-resolved impedance spectra collected from cells containing the different SEs, with all

Batteries & Supercaps | Research Article doi.org/10.1002/batt.202400112 | Chemistry Europe European Chemical Societies Publishing

of them revealing the characteristic shape of mixed conducting interfaces/interphases.[36,37] To quantitatively compare the stability among the SEs tested, the spectra were fitted using suitable equivalent circuits, along with distribution of relaxation times (DRT) analysis.[38,39] For the highly conducting, cationic and anionic substituted SEs, the barely visible bulk response at ultrahigh frequencies (7–1 MHz) was described by a simple resistor R. Several RQ elements (Q = constant phase element) were needed to fit the data (depressed semicircles) from the high- to low-frequency range. Their physical meaning was derived from the specific response times (see Figure S4, Supporting Information).[40,41] In Figure 3a–e, the Nyquist plots of the electrochemical impedance recorded after 0 and 24 h are presented together with the fitting results. Summaries of the calculated parameters are given in Tables S4–S8. R_1 and R_2 can be attributed to the bulk SE and the contact resistance between electrode and current collector, respectively. R_3 and R_4 can be assigned to the interface resistance, comprising various underlying processes, which emphasize the microstructural and chemical complexity of the as-formed interfaces/interphases. For comparison, the total interface resistances (with $R_{total} = R_3 + R_4$) after 0 and 24 h are depicted in Figure 3f. Because of the symmetrical cell configuration, it can be assumed that both sides equally contribute to the total resistance. Therefore, R_{total} was divided by a factor of two to yield resistance values for single Li | SE interfaces. After 24 h, the R_{total} was determined to be 420 Ω for LPSCl, a relatively minor increase compared to the initial value (360 Ω). A clear increase in resistance with time was noticed for the equimolar, Si-rich, and Ge-rich SEs. In these cases, the R_{total} increased from 136 to 372 Ω, 54 to 103 Ω, and 190 to 642 Ω for the equimolar, Si-rich, and Ge-rich SEs, respectively, after 24 h. In contrast, for the I-free SE, a moderate increase in R_{total} by 34 Ω (179 Ω) from the initial value (145 Ω) was observed.

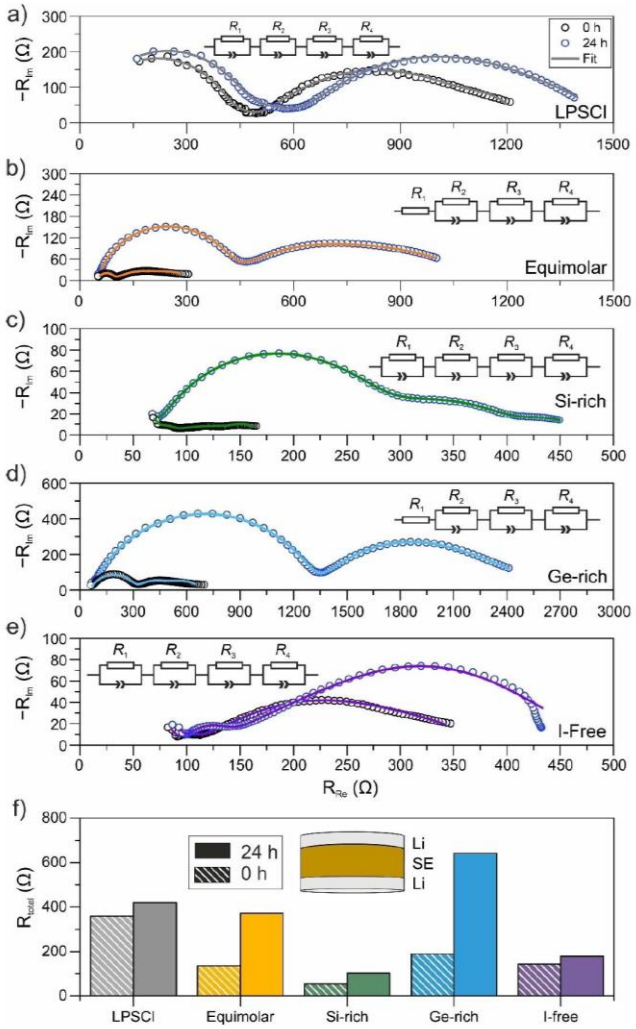

Figure 3. (a–e) Nyquist plots of the electrochemical impedance of symmetrical Li cells using the different SEs after assembly (0 h) and 24 h at 25 °C. Experimental data are shown as empty symbols and curve fits as solid lines. Equivalent circuits used for fitting the data are shown in the insets. (f) Corresponding resistances calculated from the interface and interphase contributions after 0 and 24 h.

Batteries & Supercaps
Research Article
doi.org/10.1002/batt.202400112
Chemistry Europe
European Chemical Societies Publishing

Taken together, the EIS results point towards decreasing stability against lithium metal upon introducing cationic substituents. Moreover, the data indicate that for the cationic substituted SEs, the as-formed interfaces/interphases are kinetically unstable, leading to continuous degradation and impedance growth. By contrast, both LPSCl and the I-free SE exhibit better stability, with the latter material possessing a relatively low areal interface resistance of 141 $\Omega\,cm^2$ after 24 h.

Next, the electrochemical performance of the SEs was examined in pelletized SSBs with $LiNbO_3$-coated NCM851005 as cathode active material and an indium-lithium anode. In these experiments, the SEs were contained in the cathode and further served as the separator. The cells were cycled at 45 °C in a potential window of 2.28–3.68 V vs. In/InLi (~2.9–4.3 V vs. Li^+/Li) applying current rates ranging from C/2 to 2 C. Figure 4a represents the first- and second-cycle voltage profiles at C/2. The initial specific charge/discharge capacities and the Coulomb efficiencies (CEs) of the first two cycles are plotted in Figure 4b and c, respectively. All cells exhibited initial specific charge capacities exceeding 200 $mAh\,g^{-1}$, and they delivered specific discharge capacities of 161 $mAh\,g^{-1}$ (equimolar), 189 $mAh\,g^{-1}$ (Si-rich), 191 $mAh\,g^{-1}$ (Ge-rich), 201 $mAh\,g^{-1}$ (I-free), and 202 $mAh\,g^{-1}$ (LPSCl). This translates to CEs of about 79, 79, 84, 89, and 89%, respectively. As evident from these data, employing the cationic substituted SEs leads to poor first-cycle CEs, whereas the reversibility is much improved for LPSCl and the I-free SE. This result confirms that cation substitution negatively affects the electrochemical stability and agrees well with the trend in ESWs determined from the CV experiments (see Figure 2). Nevertheless, the CEs stabilized above 95% from the second cycle onwards.

Subsequently, the rate performance was tested, followed by long-term cycling at C/2. The corresponding specific discharge capacities and CEs are shown in Figure 5a and b, respectively. Upon increasing the C-rate to 2 C, the LPSCl-containing cell was only capable of delivering 120 $mAh\,g^{-1}$ or less, unlike (especially) the I-fee SE, which allowed for $q_{dis} \geq 160\ mAh\,g^{-1}$. This major difference in rate capability is primarily due to differences in conductivity of the SEs (see Table 1) and the decomposition interphases formed during cycling (leading to impedance buildup). However, the respective cells showed a similar performance during long-term cycling at C/2 and still delivered capacities of ~150 $mAh\,g^{-1}$ after 75 cycles. In contrast, for the cationic substituted SEs, the capacity fading with cycling at C/2 was much more severe, with $q_{dis} \approx 90\ mAh\,g^{-1}$ (equimolar and Ge-rich) and 75 $mAh\,g^{-1}$ (Si-rich) after 75 cycles. Even though the compositionally complex SEs outperformed the LPSCl at high C-rates for the aforementioned reasons, cells using the cationic substituted materials suffered from severe capacity decay due to their lower electrochemical stability, as outlined above. The stability issues are also apparent from the CEs. In the initial cycles (rate performance testing), the CEs approached or even exceeded 99%. However, only for LPSCl and the I-free SE, they remained on average above 99% during extended

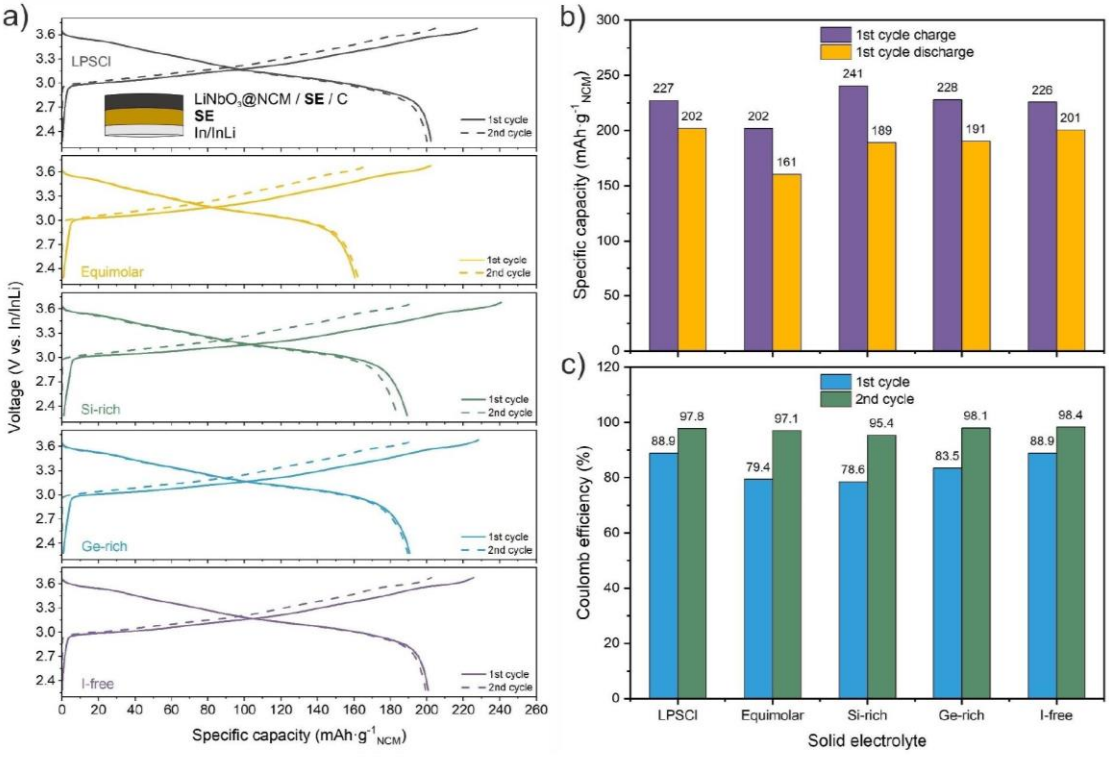

Figure 4. (a) Voltage profiles for the first (solid line) and second (dashed line) cycles of pelletized SSB cells using the different SEs both in the cathode and separator at C/2 rate and 45 °C. (b) Corresponding specific charge/discharge capacities and (c) Coulomb efficiencies.

Batteries & Supercaps
Research Article
doi.org/10.1002/batt.202400112
Chemistry Europe
European Chemical Societies Publishing

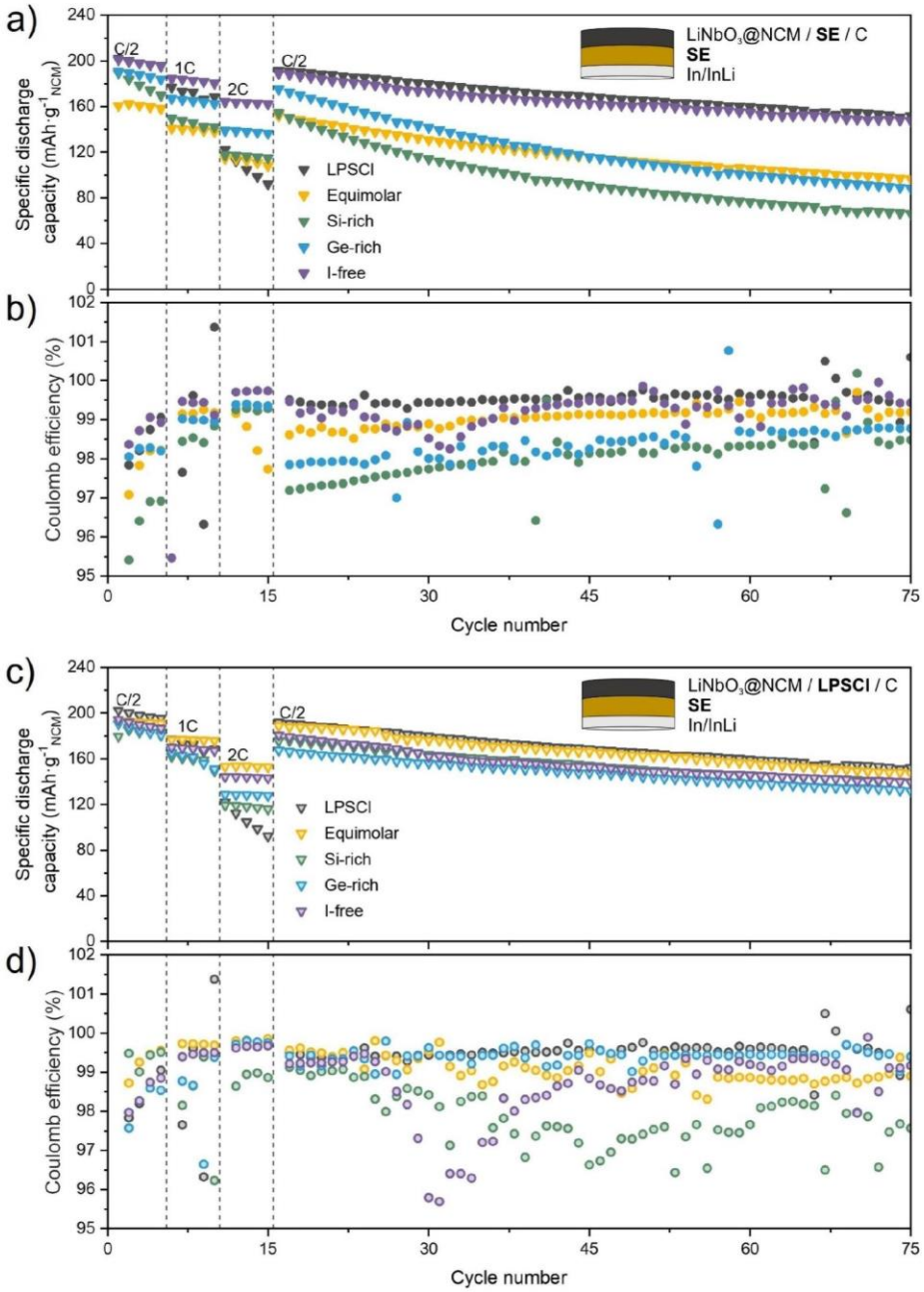

Figure 5. Cycling performance of pelletized SSB cells using the different SEs at 45 °C. (a) Specific discharge capacities at various C-rates and (b) corresponding Coulomb efficiencies. In this configuration [see inset in (a)], the respective SEs were contained in the cathode and served as the separator. (c) Specific discharge capacities at various C-rates and (d) corresponding Coulomb efficiencies achieved with cells using LPSCl in the cathode and the different SEs as the separator [see inset in (c)].

cycling at C/2 rate, corroborating their superiority. It is noteworthy that the trend in electrochemical stability determined from the CV experiments does not directly correlate with the cell cyclability. In fact, it seems that the stability of the decomposition interphases plays an important role too. If the decomposition products formed in the initial cycle(s) are kinetically and/or thermodynamically stable, they would prevent further SE degradation, thus helping to stabilize the cell performance.[42] Yet, the results indicate that the cationic substituted lithium argyrodites in particular do not form stable cathode interfaces and interphases.

Batteries & Supercaps | Research Article
doi.org/10.1002/batt.202400112
Chemistry Europe
European Chemical Societies Publishing

To improve the cycling performance, the ion conductor in the cathode was replaced with LPSCl, and the different SEs were only employed as the separator. As can be seen from Figure 2, LPSCl apparently exhibits the best anodic stability among the materials investigated. Therefore, the degradation related to (irreversible) oxidative SE decomposition should be minimized. The cells were subjected to a similar cycling protocol as described above. At first glance, this strategy appears to be successful, as the specific discharge capacities and the fading behavior were similar for the different cells (see Figure 5c). However, on closer examination, it is found that the cell using LPSCl as SE in the cathode and separator again delivered the lowest capacities at 2 C. This is clearly due to the material's ionic conductivity being lower by a factor of three or more compared to the other SEs. The reduced degradation at the positive electrode side when using LPSCl in the cathode is also evident from the CEs (see Figure 5d). Except for the cell using the Si-rich SE, the CEs stabilized above 98% during cycling at C/2. The fact that the Si-rich SE led to poor reversibility in this SSB configuration points towards continuous side reactions (interphase formation) at the In/InLi | SE interface.

After having tested the SEs in two different SSB configurations at 45 °C, similar electrochemical measurements were conducted at 25 °C. The specific discharge capacities of cells where (i) the respective SEs were contained in the cathode and served as separator at the same time and (ii) LPSCl was employed in the cathode and the different SEs only served as separator are presented in Figure 6a and b, respectively. Because the same cycling protocol was applied to the cells, the capacities were somewhat lower at 25 °C, as expected. At a rate of 2 C, LPSCl was outperformed by all other SEs. Also, if the cationic substituted SEs were employed both in the cathode and separator, the overall degradation was much lower (see Figure 6a) compared to that at 45 °C (see Figure 5a). This is indicative of kinetic instabilities. In addition, it is evident from the data in Figure 6b that the ionic resistance of the separator layer has a profound effect on the cycling performance, which is mitigated to some degree at elevated temperatures.

For better comparison of the specific discharge capacities at the different C-rates and temperatures, they are plotted for the cells where the SEs were contained in the cathode and served as separator in Figure 7a and b. As shown in Figure 7a, the cells using the compositionally complex lithium argyrodites delivered similar capacities at 25 °C, ranging from about 100 mAh g^{-1} at 2 C to 170 mAh g^{-1} at C/2. In contrast, the LPSCl-containing cell showed much lower capacities, with only ~50 and 145 mAh g^{-1} at 2 C and C/2, respectively. However, significant differences were observed for the cells cycled at 45 °C (see Figure 7b). The lowest and highest capacities were found for the equimolar and I-free SEs, with differences of more than 40 mAh g^{-1}, virtually independent of the C-rate. The LPSCl-containing cell revealed the strongest increase in q_{dis}, from ~120 mAh g^{-1} at 2 C to 200 mAh g^{-1} at C/2, among the SEs studied here. This finding can be explained by the higher cell resistance resulting from the lower ionic conductivity of LPSCl compared to the cationic and anionic substituted SEs. In addition to the bulk conductivity, the properties of the interfaces and interphases also play a pivotal role in determining the cell performance. Future studies will be dedicated to better understanding ion and electron transport across the interfaces and its effect on cyclability.

3. Conclusions

In summary, we have investigated the electrochemical stability and performance of a series of novel compositionally complex lithium argyrodite solid electrolytes in bulk-type solid-state batteries and benchmarked them against commercially available Li_6PS_5Cl. The samples tested include cationic and anionic substituted materials, all exhibiting high room-temperature ionic conductivities of $\sigma_{ion} \geq 9\,mS\,cm^{-1}$. Their stability was examined by cyclic voltammetry conducted on carbon-based composite electrodes and by time-resolved electrochemical impedance spectroscopy measurements using symmetrical Li cells. In general, it is found that cation substitution narrows the

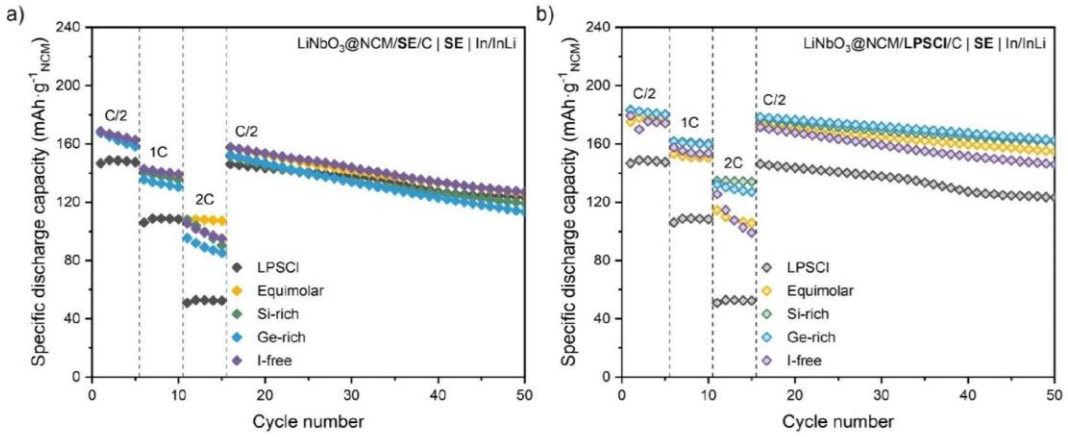

Figure 6. Cycling performance of pelletized SSB cells using the different SEs at 25 °C. (a) The respective SEs were contained in the cathode and served as the separator and (b) LPSCl was employed in the cathode and the different SEs only served as the separator.

Batteries & Supercaps
Research Article
doi.org/10.1002/batt.202400112
Chemistry Europe
European Chemical Societies Publishing

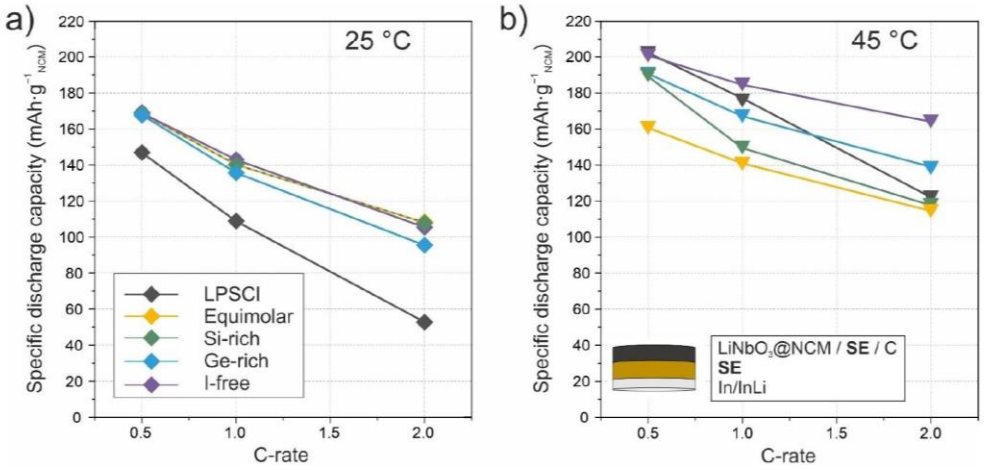

Figure 7. Comparison of specific discharge capacities of pelletized SSB cells using the different SEs (a) at 25 °C and (b) at 45 °C. Data taken from the first cycle of each C-rate. The respective SEs were contained in the cathode and served as the separator.

electrochemical stability window of lithium argyrodite solid electrolytes. To evaluate the ion conductors under realistic (practical) conditions, solid-state battery cells were assembled using a surface-protected, Ni-rich $LiNi_xCo_yMn_zO_2$ (NCM or NMC) as cathode active material. At room temperature and high current rates, the compositionally complex solid electrolytes readily outperform the reference Li_6PS_5Cl. However, the lower stability of the cationic substituted materials leads to accelerated capacity fading upon cycling at elevated temperature. Nevertheless, utilizing these materials only in the separator layer positively affects the cell cyclability. In contrast, the anionic substituted solid electrolyte $Li_{5.5}PS_{4.5}Cl_{0.8}Br_{0.7}$ provides low-resistive interfaces with anode and cathode, leading to the overall best performance, specifically at high current rates. This corroborates recent findings that the I-free, high-entropy solid electrolyte enables stable long-term cycling of all-solid-state batteries.[18] Taken together, we have demonstrated that ionic conductivity is not the only important attribute of inorganic solid electrolytes, and that anion prevails over cation substitution in developing advanced materials for solid-state battery application. We believe that the design parameters described in this work provide a blueprint for future solid electrolytes, with multicomponent materials providing virtually unlimited possibilities.

Experimental Section

Materials Synthesis

Unless specified otherwise, the work was performed under inert argon atmosphere in a glovebox (MBraun, with $[O_2]$ and $[H_2O] <$ 0.1 ppm) or using Schlenk line techniques. All chemicals were used as received, and LPSCl was purchased from NEI Corp. In general, stoichiometric mixtures of Li_2S (99.99%, Sigma-Aldrich), P_2S_5 (99%, Sigma-Aldrich), GeS_2 (99.9%, Goodfellow), SiS_2 (99.99%, Goodfellow), Sb_2S_3 (99.99%, Alfa Aesar), and LiI (99.999%, Sigma-Aldrich) plus 10 wt% excess sulfur (99.99%, Sigma-Aldrich) were loaded into 250 mL zirconia milling jars with 150 g zirconia balls (10 mm diameter). Ampules were pre-dried under dynamic vacuum using a heat gun.

Equimolar ($Li_{6.5}[P_{0.25}Si_{0.25}Ge_{0.25}Sb_{0.25}]S_5I$)

The precursor mixture was milled at 250 rpm for 1 h and then at 450 rpm for 15 h. The recovered powder (~1.2 g) was pelletized at 3 t and vacuum-sealed (10^{-3} bar) in a quartz ampule, followed by annealing at 500 °C for 10 h with heating and cooling rates set to 5 °C min^{-1}.

Si-rich ($Li_{6.67}[P_{0.16}Si_{0.5}Ge_{0.16}Sb_{0.16}]S_5I$) and Ge-rich ($Li_{6.67}[P_{0.16}Si_{0.16}Ge_{0.5}Sb_{0.16}]S_5I$)

The precursor mixture was milled at 250 rpm for 1 h and then at 450 rpm for 40 h, including 10 min rest steps after each 15 min of milling. The recovered powder (~1.2 g) was pelletized at 3 t and vacuum-sealed (10^{-3} bar) in a quartz ampule, followed by annealing at 500 °C for 10 h with heating and cooling rates set to 0.165 and 5 °C min^{-1}, respectively.

I-Free ($Li_{5.5}PS_{4.5}Cl_{0.8}Br_{0.7}$)

The precursor mixture was milled at 250 rpm for 1 h and then at 450 rpm for 15 h. The recovered powder (~1.2 g) was pelletized at 3 t and vacuum-sealed (10^{-3} bar) in a quartz ampule, followed by annealing at 440 °C for 10 h with heating and cooling rates set to 1.5 °C min^{-1}.

Surface Coating of NCM851005 ($LiNi_{0.85}Co_{0.10}Mn_{0.05}O_2$)

The NCM851005 (BASF SE) was first heated for 3 h at 750 °C in oxygen flow of 30 L h^{-1} with heating and cooling rates set to 5 °C min^{-1} to remove surface impurities. To produce a 1.0 wt% $LiNbO_3$ protective coating on the surface of the secondary particles, 410 µL of lithium ethoxide (1.0 M) and 820 µL of niobium ethoxide (0.5 M) in absolute ethanol were added to 5.94 g of NCM851005. The suspension was sonicated for 30 min and then dried in a vacuum overnight. The recovered powder was ground using a mortar and pestle and heated in oxygen for 2 h at 350 °C.[43] XRD

Batteries & Supercaps | Research Article doi.org/10.1002/batt.202400112 | Chemistry Europe European Chemical Societies Publishing

patterns and ATR-IR spectra collected before and after coating are presented in Figure S5 (Supporting Information).

Characterization

Laboratory X-ray Diffraction (XRD)

The samples were flame-sealed in borosilicate capillaries (0.68 mm inner diameter, 0.01 mm wall thickness; Hilgenberg) and subjected to XRD using a Stadi-P diffractometer (STOE) with Mo anode ($\lambda =$ 0.70926 Å) and a MYTHEN 1 K strip detector (DECTRIS). Rietveld and Le Bail analysis of diffraction data was done with the help of FullProf Suite.[44] The Thompson-Cox-Hastings pseudo-Voigt function was used to describe the peak shape after point-by-point background subtraction. Scale factor, peak shape parameters, lattice parameters, and atomic displacement parameters were refined. The zero-shift parameter was treated last.

Attenuated Total Reflection-Infrared (ATR-IR) Spectroscopy

ATR-IR spectroscopy measurements were performed on an ALPHA FT-IR spectrometer (Bruker). All spectra were background corrected using the OPUS software.

Cyclic Voltammetry (CV)

Solid electrolyte and Super C65 carbon black (TIMCAL) were mixed in a 7:3 weight ratio using a planetary mill (Fritsch) at 140 rpm for 30 min using 70 mL zirconia milling jars with 10 zirconia balls (10 mm diameter) and used as working electrode. The carbon black was dried at 300 °C under dynamic vacuum overnight prior to use. The cells were assembled using a customized setup comprising a PEEK sleeve (10 mm diameter) and two stainless steel dies. 100 mg of solid electrolyte was first compressed at 62 MPa to produce the separator. Around 12 mg of working electrode was then evenly distributed on one side of the separator. The stack was compressed at 437 MPa. Finally, an indium foil (9 mm diameter, 125 μm thickness; Thermo Fisher Scientific) and a lithium foil (6 mm diameter, 50 μm thickness; Albemarle Corp.) were freshly punched out and placed on the other side of the separator, with the indium foil facing the solid electrolyte. CV experiments were performed under an external pressure of 81 MPa between 0.93 and 3.68 V vs. In/InLi (~1.55–4.3 V vs. Li^+/Li) at a sweep rate of 0.1 $mV s^{-1}$ and at 45 °C after a resting period at OCV for 30 min using an SP-200 potentiostat (BioLogic). The onset potentials for oxidation and reduction were determined as exemplarily shown for LPSCl in Figure S6 (Supporting Information).

Time-Resolved Electrochemical Impedance Spectroscopy (EIS)

EIS measurements were conducted on symmetrical cells (Li | SE | Li) at 25 °C without additional external pressure. To this end, about 150 mg of solid electrolyte was compressed at 437 MPa. Lithium foils (6 mm diameter, 50 μm thickness) were freshly punched out and placed at both sides of the separator. Impedance data were collected using a VMP-3 potentiostat (BioLogic) over a frequency range from 7 MHz to 100 mHz with an AC voltage amplitude of 20 mV. The first spectrum was measured immediately after cell assembly (0 h). Subsequent spectra were recorded after 2, 4, 6, 10, 16, and 24 h. Evaluation of the EIS data and DRT analysis were performed using the software RelaxIS 3.0.22 (rhd instruments).

Galvanostatic Cycling

For battery performance tests, cathode composites were prepared by mixing the $LiNbO_3$-coated NCM851005, solid electrolyte, and Super C65 in a 69.3:29.7:1 weight ratio using a planetary mill at 140 rpm for 30 min with 70 mL zirconia milling jars containing 10 zirconia balls (10 mm diameter). Cells were assembled in similar manner as described above for the CV testing. The loading was ~10.5 $mg_{NCM} cm^{-2}$.Galvanostatic cycling was performed at 45 °C and under an external pressure of 81 MPa in a potential window of 2.28–3.68 V vs. In/InLi (~2.9–4.3 V vs. Li^+/Li) after resting at OCV for 1 h using a MACCOR battery cycler. The C-rate was varied from C/2 to 2 C, with 1 C = 190 $mA g_{NCM}^{-1}$.

Supporting Information

Supporting Information is available from the Wiley Online Library or from the author.

Acknowledgements

J. L. acknowledges the Fonds der Chemischen Industrie (FCI) for financial support. F. S. is grateful to the Federal Ministry of Education and Research (BMBF) for funding within the project MELLi (03XP0447). This work was partially supported by BASF SE. S. W. acknowledges the Guangdong Basic and Applied Basic Research Foundation (2021A1515110312), the Natural Science Foundation of Hubei Province (2022CFB760), and the Natural Science Foundation of China (52302305). This work contributes to the research performed at CELEST (Center for Electrochemical Energy Storage Ulm-Karlsruhe). Open Access funding enabled and organized by Projekt DEAL.

Conflict of Interests

A patent was filed for some of this work through BASF SE and the Karlsruher Institut für Technologie (KIT).

Data Availability Statement

The data that support the findings of this study are available from the corresponding author upon reasonable request.

Keywords: Configurational entropy · electrochemical testing · interface stability · layered Ni-rich oxide cathode · solid electrolyte

[1] A. L. Robinson, J. Janek, *MRS Bull.* **2014**, *39*, 1046–1047.
[2] J. Janek, W. G. Zeier, *Nat. Energy* **2023**, *8*, 230–240.
[3] P. Minnmann, L. Quillman, S. Burkhardt, F. H. Richter, J. Janek, *J. Electrochem. Soc.* **2021**, *168*, 40537.
[4] Y. Kato, S. Shiotani, K. Morita, K. Suzuki, M. Hirayama, R. Kanno, *J. Phys. Chem. Lett.* **2018**, *9*, 607–613.
[5] Z. Zhang, Y. Shao, B. Lotsch, Y. S. Hu, H. Li, J. Janek, L. F. Nazar, C. W. Nan, J. Maier, M. Armand, L. Chen, *Energy Environ. Sci.* **2018**, *11*, 1945–1976.

Batteries & Supercaps | Research Article doi.org/10.1002/batt.202400112 | Chemistry Europe European Chemical Societies Publishing

[6] P. Minnmann, F. Strauss, A. Bielefeld, R. Ruess, P. Adelhelm, S. Burkhardt, S. L. Dreyer, E. Trevisanello, H. Ehrenberg, T. Brezesinski, F. H. Richter, J. Janek, *Adv. Energy Mater.* **2022**, *12*, 2201425.
[7] H.-J. Deiseroth, S.-T. Kong, H. Eckert, J. Vannahme, C. Reiner, T. Zaiß, M. Schlosser, *Angew. Chem. Int. Ed.* **2008**, *47*, 755–758.
[8] H.-J. Deiseroth, J. Maier, K. Weichert, V. Nickel, S.-T. Kong, C. Reiner, *Z. Anorg. Allg. Chem.* **2011**, *637*, 1287–1294.
[9] R. Schlenker, A.-L. Hansen, A. Senyshyn, T. Zinkevich, M. Knapp, T. Hupfer, H. Ehrenberg, S. Indris, *Chem. Mater.* **2020**, *32*, 8420–8430.
[10] A. Gautam, M. Sadowski, M. Ghidiu, N. Minafra, A. Senyshyn, K. Albe, W. G. Zeier, *Adv. Energy Mater.* **2021**, *11*, 2003369.
[11] J. Lau, R. H. DeBlock, D. M. Butts, D. S. Ashby, C. S. Choi, B. S. Dunn, *Adv. Energy Mater.* **2018**, *8*, 1800933.
[12] J. H. Teo, F. Strauss, F. Walther, Y. Ma, S. Payandeh, T. Scherer, M. Bianchini, J. Janek, T. Brezesinski, *Mater. Futures* **2022**, *1*, 015102.
[13] M. A. Kraft, S. Ohno, T. Zinkevich, R. Koerver, S. P. Culver, T. Fuchs, A. Senyshyn, S. Indris, B. J. Morgan, W. G. Zeier, *J. Am. Chem. Soc.* **2018**, *140*, 16330–16339.
[14] L. Zhou, A. Assoud, Q. Zhang, X. Wu, L. F. Nazar, *J. Am. Chem. Soc.* **2019**, *141*, 19002–19013.
[15] F. Strauss, J. Lin, M. Duffiet, K. Wang, T. Zinkevich, A.-L. Hansen, S. Indris, T. Brezesinski, *ACS Materials Lett.* **2022**, *4*, 418–423.
[16] J. Lin, G. Cherkashinin, M. Schäfer, G. Melinte, S. Indris, A. Kondrakov, J. Janek, T. Brezesinski, F. Strauss, *ACS Materials Lett.* **2022**, *4*, 2187–2194.
[17] P. Adeli, J. D. Bazak, K. H. Park, I. Kochetkov, A. Huq, G. R. Goward, L. F. Nazar, *Angew. Chem. Int. Ed.* **2019**, *58*, 8681–8686.
[18] S. Li, J. Lin, M. Schaller, S. Indris, X. Zhang, T. Brezesinski, C.-W. Nan, S. Wang, F. Strauss, *Angew. Chem. Int. Ed.* **2023**, *62*, e202314155.
[19] S. V. Patel, S. Banerjee, H. Liu, P. Wang, P.-H. Chien, X. Feng, J. Liu, S. P. Ong, Y.-Y. Hu, *Chem. Mater.* **2021**, *33*, 1435–1443.
[20] J. Lin, M. Schaller, G. Cherkashinin, S. Indris, J. Du, C. Ritter, A. Kondrakov, J. Janek, T. Brezesinski, F. Strauss, *Small* **2024**, *20*, 2306832.
[21] R. D. Shannon, *Acta Crystallogr.* **1976**, *32*, 751–767.
[22] G. F. Dewald, S. Ohno, M. A. Kraft, R. Koerver, P. Till, N. M. Vargas-Barbosa, J. Janek, W. G. Zeier, *Chem. Mater.* **2019**, *31*, 8328–8337.
[23] F. Han, Y. Zhu, X. He, Y. Mo, C. Wang, *Adv. Energy Mater.* **2016**, *6*, 1501590.
[24] D. H. S. Tan, E. A. Wu, H. Nguyen, Z. Chen, M. A. T. Marple, J.-M. Doux, X. Wang, H. Yang, A. Banerjee, Y. S. Meng, *ACS Energy Lett.* **2019**, *4*, 2418–2427.
[25] J. Auvergniot, A. Cassel, D. Foix, V. Viallet, V. Seznec, R. Dedryvère, *Solid State Ionics* **2017**, *300*, 78–85.
[26] R. Koerver, F. Walther, I. Aygün, J. Sann, C. Dietrich, W. G. Zeier, J. Janek, *J. Mater. Chem. A* **2017**, *5*, 22750–22760.
[27] S. Wang, M. Tang, Q. Zhang, B. Li, S. Ohno, F. Walther, R. Pan, X. Xu, C. Xin, W. Zhang, L. Li, Y. Shen, F. H. Richter, J. Janek, C.-W. Nan, *Adv. Energy Mater.* **2021**, *11*, 2101370.
[28] T. Famprikis, P. Canepa, J. A. Dawson, M. S. Islam, C. Masquelier, *Nat. Mater.* **2019**, *18*, 1278–1291.
[29] A. Banik, Y. Liu, S. Ohno, Y. Rudel, A. Jiménez-Solano, A. Gloskovskii, N. M. Vargas-Barbosa, Y. Mo, W. G. Zeier, *ACS Appl. Energ. Mater.* **2022**, *5*, 2045–2053.
[30] G. H. Cartledge, *J. Am. Chem. Soc.* **1928**, *50*, 2855–2863.
[31] M. G. Evans, M. Polanyi, *Trans. Faraday Soc.* **1938**, *34*, 11–24.
[32] S. Muy, J. C. Bachman, L. Giordano, H.-H. Chang, D. L. Abernathy, D. Bansal, O. Delaire, S. Hori, R. Kanno, F. Maglia, S. Lupart, P. Lamp, Y. Shao-Horn, *Energy Environ. Sci.* **2018**, *11*, 850–859.
[33] S. Schweidler, M. Botros, F. Strauss, Q. Wang, Y. Ma, L. Velasco, G. C. Marques, A. Sarkar, C. Kübel, H. Hahn, J. Aghassi-Hagmann, T. Brezesinski, B. Breitung, *Nat. Rev. Mater.* **2024**, *9*, 266–281.
[34] T. Krauskopf, F. H. Richter, W. G. Zeier, J. Janek, *Chem. Rev.* **2020**, *120*, 7745–7794.
[35] J. Janek, W. G. Zeier, *Nat. Energy* **2016**, *1*, 16141.
[36] P. Bron, B. Roling, S. Dehnen, *J. Power Sources* **2017**, *352*, 127–134.
[37] L. M. Riegger, R. Schlem, J. Sann, W. G. Zeier, J. Janek, *Angew. Chem. Int. Ed.* **2021**, *60*, 6718–6723.
[38] H. Sumi, H. Shimada, Y. Yamaguchi, T. Yamaguchi, Y. Fujishiro, *Electrochim. Acta* **2020**, *339*, 135913.
[39] N. Tanibata, S. Takimoto, K. Nakano, H. Takeda, M. Nakayama, H. Sumi, *ACS Materials Lett.* **2020**, *2*, 880–886.
[40] Y. Lu, C.-Z. Zhao, J.-Q. Huang, Q. Zhang, *Joule* **2022**, *6*, 1172–1198.
[41] P. S. Sabet, G. Stahl, D. U. Sauer, *J. Power Sources* **2020**, *472*, 228189.
[42] A. Banerjee, X. Wang, C. Fang, E. A. Wu, Y. S. Meng, *Chem. Rev.* **2020**, *120*, 6878–6933.
[43] S. Payandeh, F. Strauss, A. Mazilkin, A. Kondrakov, T. Brezesinski, *Nano Res. Energy* **2022**, *1*, 9120016.
[44] J. Rodríguez-Carvajal, *Phys. B* **1993**, *192*, 55–69.

Manuscript received: February 20, 2024
Revised manuscript received: April 15, 2024
Accepted manuscript online: April 23, 2024
Version of record online: June 7, 2024

4. Conclusions and perspectives

Throughout this thesis, I aimed at expanding the high-entropy concept to lithium argyrodites, understanding the effect of configurational entropy on charge transport properties and evaluated their potential as solid electrolytes for solid state batteries.

To achieve this goal, several single-phase lithium argyrodites with different compositions were designed. In general, the configurational entropy ΔS_{conf} can be deconvoluted into two contributions, including cation mixing ($\Delta S_{conf,cation}$), and anion mixing ($\Delta S_{conf,anion}$). Regarding the lithium argyrodite crystal structure, halogen anions (4*a*) form a face-centered cubic lattice, with chalcogenide ions occupying half of the tetrahedral voids (4*d*). The tetrahedral units are located at the (4*b*) sites for the central atom, while the chalcogenide ions occupy the octahedral interstices (16*e*). Thus, specifically, high-entropy lithium argyrodites with $\Delta S_{conf} > 1.5R$ can be achieved mainly through three approaches:

1) Both, anion and cation substitutions were combined (i.e. $\Delta S_{conf,cation}$ and $\Delta S_{conf,anion}$) to achieve $\Delta S_{conf} > 1.5R$ (see Publication I).

2) Introducing a complex cation substitution at the 4*b* site increasing $\Delta S_{conf,cation}$ (see Publications II and III).

3) Tailoring anion site inversion via halogen substitution at the 4*d* and 4*a* sites leading to an increase in $\Delta S_{conf,anion}$ (see Publication IV).

Starting from the possibility of applying the high-entropy concept to lithium argyrodites through modification of Li_6PS_5X (X=Cl, Br, I) through approach 1), the highest configurational entropy was achieved for $Li_{6.5}[Ge_{0.5}P_{0.5}][S_{2.5}Se_{2.5}][Cl_{0.33}Br_{0.33}I_{0.33}]$ reaching $\Delta S_{conf} = 2.98R$. However, the ionic conductivity (~ 1 mS cm^{-1} at 25 °C) did not significantly improve through increasing configurational entropy, which might be attributed to the negative effect of unknown impurities (observed by diffraction techniques), but instead a very low activation energy ($E_A = 0.22$ eV) was observed.[18] Thus, minimizing the impurities to yield phase-pure lithium argyrodites through synthesis optimization or compositional engineering is promising. However, traditional methods such as adding pre- or post-annealing steps could not address these impurity issues. For the composition $Li_{6.5}[Ge_{0.5}P_{0.5}][S_{2.5}Se_{2.5}][Cl_{0.33}Br_{0.33}I_{0.33}]$, elemental redistribution on 4*a* and 4*d* sites (38% I/ 34% Br/ 28% Se and 33% Cl/ 67% Se, respectively) was found through MAS-NMR and NPD data analysis.

Following this, in Publication II and III, compositional complex cation substituted lithium argyrodites (referring to approach 2) have been synthesized adopting the general formula $Li_{6+x}[M1_aM2_bM3_cM4_d]S_5I$, with M being P, Si, Ge, and Sb, achieving high ionic conductivities (≥ 10 mS cm^{-1}) in $Li_{6.5}[P_{0.25}Si_{0.25}Ge_{0.25}Sb_{0.25}]S_5I$ (EQ), $Li_{6.66}[P_{0.167}Si_{0.5}Ge_{0.167}Sb_{0.167}]S_5I$ ($Si_{0.5}$) and $Li_{6.66}[P_{0.167}Si_{0.167}Ge_{0.5}Sb_{0.167}]S_5I$ ($Ge_{0.5}$).[19,21] In general, an increase in Li content led to a significant increase in ionic conductivity. Specifically, the conductivity increased from below 1 mS cm^{-1} (for $P_{0.75}$ and $Sb_{0.75}$) to above 10 mS cm^{-1} (for $Si_{0.5}$ and $Ge_{0.5}$) when the Li content varied from 6.17 (for $P_{0.75}$ and $Sb_{0.75}$) to 6.66 (for $Si_{0.5}$ and $Ge_{0.5}$) per formula unit. The high ionic conductivity observed for cation substituted lithium argyrodites could be attributed to the presence of two additional Li inter-cage sites induced by

increasing the total Li content. This resulted in a shortened inter-cage jump distance, further facilitating long-term lithium diffusion. Despite, no direct correlation between configurational entropy and ionic conductivity, interestingly, again the direct correlation was observed between configurational entropy and activation energy. The samples with similar ΔS_{conf} showed similar very low activation energy (around 0.21 eV), yet significant differences in ionic conductivity (1.91 mS cm^{-1} for $P_{0.5}$ and 14.6 mS cm^{-1} for $Ge_{0.5}$), suggesting that configurational entropy plays a non-negligible role in lowering the activation energy. Delving deeper into the effect of configurational entropy on Li-ion transport, in general, the complex substitution strategy significantly improved Li-ion mobility, achieving $\mu > 10^{-6}$ cm^2 V^{-1} s^{-1}, one order of magnitude higher compared to common highly conducting lithium argyrodites. To rationalize this, one can assume an increased configurational entropy ΔS_{conf} leads to an increased vibrational entropy ΔS_{vib}. This might lower the energy barrier for diffusion and fasten Li-ion mobility through phonon-ion interactions. Turning back to the initial question of how configurational entropy affects ionic conductivity, ionic conductivity is the product of ion mobility, charge of the mobile ions and charge-carrier density. Thus, increasing ion mobility or charge carrier density can allow to reach high ionic conductivity. Increasing configurational entropy via compositional design could achieve both, and unlock compositional limitations for the design of advanced solid electrolytes.

In addition to $\Delta S_{conf,cation}$ engineering, alternatively, high-entropy lithium argyrodites ($\Delta S_{conf} > 1.5R$) can also be achieved through tuning $\Delta S_{conf,anion}$. In Publication IV, isovalent substituted halogen-rich high-entropy argyrodites with a fixed Li content $Li_{5.5}PS_{4.5}Cl_xBr_{1.5-x}$ (x = 0-1.5) have been investigated.[20] These materials demonstrate very high ionic conductivity by adjusting the anion disorder between sulfur, chlorine, and bromine, distributed across two crystallographic sites (4*a* and 4*d*). No differences in Li distribution and jump distances among these materials, characterized via NPD, challenge conventional structure-property explanations. Interestingly, $Li_{5.5}PS_{4.5}Cl_{0.8}Br_{0.7}$ demonstrated both the highest ionic conductivity (~9 mS cm^{-1} from EIS and ~22 mS cm^{-1} from PFG-NMR) and a maximum ΔS_{conf} (1.98*R*), hinting at a possible direct correlation between ΔS_{conf} and lithium transport again possibly attributed to the beneficial phonon-ion interactions.

After achieving high ionic conductivities of σ_{ion} ~ 10 mS cm^{-1} at room temperature, via varying anion and cation compositions, including $Li_{6.5}[P_{0.25}Si_{0.25}Ge_{0.25}Sb_{0.25}]S_5I$ (EQ), $Li_{6.67}[P_{0.16}Si_{0.5}Ge_{0.16}Sb_{0.16}]S_5I$ ($Si_{0.5}$), $Li_{6.67}[P_{0.16}Si_{0.16}Ge_{0.5}Sb_{0.16}]S_5I$ ($Ge_{0.5}$) and $Li_{5.5}PS_{4.5}Cl_{0.8}Br_{0.7}$ (I-free), this renders these materials promising as solid electrolytes for bulk-type SSB applications.[22] Also, the possibility of improving the (electro)chemical stability via compositional design was investigated. Hence, in Publication V, the electrochemical stability, lithium metal anode compatibility, and electrochemical performance of these complex-substituted lithium argyrodites have been systematically investigated using CV, time-resolved EIS and galvanostatic charge-discharge cycling and compared to the commercially available SE LPSCl.[22] Overall, anion substitution prevails over cation substitution, including broader electrochemical stability window (ESW) and more stable evolution of interfacial resistance with the Li metal electrode. Typically, oxidative stability of solid electrolytes depends on the anion composition. The higher ionization potentials and stronger bonding strengths of Br^- and Cl^- compared to I^- suggest enhanced oxidation stability in iodine-free and LPSCl SE.[24] Li metal compatibility was characterized by using

symmetrical Li|SE|Li cell configurations. The total resistance difference (ΔR_{total}) from interphase and interface contributions after 24 hours indicates that both LPSCl and the I-free SE demonstrate superior stability against lithium metal, forming a stable SEI over time, with the I-free SE showing particularly low resistance (ΔR_{total} = 34.5 Ω). In contrast, complex cation substituted SEs formed kinetically unstable mixed ionic/electronic conducting interfaces/interphases, attributed to the potential formation of electronically conductive Li-metal alloy (*e.g.* Li_xGe, Li_ySi and Li_zSb) at the SE/Li interface, which could lead to continuous degradation and pronounced impedance growth.[24] Finally, applied as SEs in pellet-type SSB cells, the compositionally complex solid electrolytes outperformed the reference Li_6PS_5Cl at room temperature. High currents were achieved due to their higher ionic conductivity, while the lower stability of the cation substituted materials led to accelerated capacity fading upon cycling. However, utilizing these materials only as the separator layer positively affected the cell cyclability. The overall best performance was still achieved with $Li_{5.5}PS_{4.5}Cl_{0.8}Br_{0.7}$ (I-free), a superionic high-entropy solid electrolyte. In particular, long-term cycling over 700 cycles at room temperature also performed for I-free electrolytes, showing no virtual capacity decay. Even though the initial electrochemical evaluation suggests that the $Li_{5.5}PS_{4.5}Cl_{0.8}Br_{0.7}$ is relatively stable against Li metal, the performance at high-current densities and high areal capacity Li stripping/ plating needs to be further verified. Moreover, for large-scale manufacturing, developing solution-based synthesis for this material and understanding the influence on ion transport is important for future research.

In summary, high-entropy lithium argyrodites with high ionic conductivity can be achieved through either cation or anion substitution, attributed to increased Li content per formula or Li vacancies enabled via entropy engineering, respectively.[18,20,21] However, the underlying mechanism of the configurational entropy effect on Li transport remains to be further investigated, particularly with regard to the very low activation energy (E_A) and high Li^+ mobility. Considering the large disorder of the cation and anion sublattice, phonon effects cannot be ignored.[54,57] Therefore, remaining open questions relate to how lattice dynamics affect ion transport in such materials. Note that increased structural complexity (increased ΔS_{conf}) likely affects the vibrational entropy (ΔS_{vib}), associated to phonon broadening, which is known to impact ion diffusion. For lithium argyrodite Li_6PS_5Cl, Ding *et al.* investigated the strong softening of the anharmonic Li-associated low-energy phonons as a function of temperature. The low-energy phonon modes (<10 meV) are important for fast ion conduction.[58] Thus, to gain detailed insights into the lattice vibration weighed by phonon density of states, inelastic neutron scattering is essential for the future research (aiming to fully determine the lattice dynamics and deepen the understanding on how configurational entropy affects ion transport).

Entropy stabilization as such has not been discussed in this thesis. High-entropy materials are traditionally believed to require high-temperature synthesis during solid-state reactions to lower Gibbs free energy.[17] In addition to thermodynamic factors, slower kinetics were preliminarily assumed for high-entropy materials, due to potentially complex intermediate phase formations that may hinder the inter-diffusion process.[114] However, in contrast, it has been reported for high-entropy lithium garnets that compositional complexity could lower the phase formation temperature during annealing.[131] Similarly, we observed that

multication substitution could accelerate the kinetics, as evidenced by *ex situ* XRD experiments. Although the phase evolution during annealing indicates a favorable trend, the underlying thermodynamic driving force remains elusive and warrants deeper investigation in the high-entropy materials field.

Referring back to the definition of ΔS_{conf} in equation (19), ΔS_{conf} should include the contribution of every individual element at each occupied crystallographic site, ignoring dynamic effects.[16] In the context of superionic conductors, this raises an issue for mobile ions, such as Li^+ (note that $\Delta S_{conf,\,Li}$ was not included in the calculation of ΔS_{conf} in this thesis). From a crystallographic perspective, the crystallographic sites are partially occupied by Li^+. $\Delta S_{conf,\,Li}$ could be derived using equation (19), meaning that materials with more lithium positions would present higher $\Delta S_{conf,\,Li}$. Most lithium superionic conductors (LGPS, Li_3InCl_6, LLZO, and LPSCl) could thus be defined as high-entropy materials, as their $\Delta S_{conf,\,Li}$ values range between 1.0 and $2R$. However, Li^+ diffuses so rapidly in superionic conductors that unoccupied potential Li positions may not necessarily mean that Li^+ does not occupy them—it could simply be that Li^+ diffuses so quickly that neutron diffraction cannot detect it. Therefore, using a static descriptor like $\Delta S_{conf,\,Li}$ may not be appropriate for describing such a dynamic behavior. As such, we have not included the $\Delta S_{conf,\,Li}$ contribution in this thesis. On the other hand, for superionic conductors, $\Delta S_{conf,\,Li}$ is strongly linked to changes in free energy due to defect formation, and $\Delta S_{conf,\,vacancy}$ should similarly be considered, as it affects the concentration of charge carriers and activation energy.[26] Simply excluding $\Delta S_{conf,\,Li}$ may not provide a complete theoretical model to explain the entropy effect on ion diffusion. This raises important questions about how to incorporate both $\Delta S_{conf,\,Li}$ and $\Delta S_{conf,\,vacancy}$ in such models, potentially leading to a new definition and theoretical framework for high-entropy superionic conductors.

Ultimately, the high-entropy concept has proven effective in improving material properties. However, to fully understand the mechanisms behind these improvements, advanced computational algorithms and characterization techniques need to be developed and applied, as many areas in the field of high-entropy materials remain unexplored.

5. Bibliography

[1] J. Janek, W. G. Zeier, *Nat. Energy* **2016**, *1*, 16141.

[2] J. Janek, W. G. Zeier, *Nat. Energy* **2023**, *8*, 230–240.

[3] R. Pacios, A. Villaverde, M. Martínez-Ibañez, M. Casas-Cabanas, F. Aguesse, A. Kvasha, *Adv. Energy Mater.* **2023**, *13*, 1–16.

[4] A. Aizat Razali, S. N. Norazli, W. S. Sum, S. Y. Yeo, A. Dolfi, G. Srinivasan, *ACS Sustain. Chem. Eng.* **2023**, *11*, 7927–7964.

[5] T. Schmaltz, F. Hartmann, T. Wicke, L. Weymann, C. Neef, J. Janek, *Adv. Energy Mater.* **2023**, *13*, 2301886.

[6] P. Minnmann, F. Strauss, A. Bielefeld, R. Ruess, P. Adelhelm, S. Burkhardt, S. L. Dreyer, E. Trevisanello, H. Ehrenberg, T. Brezesinski, F. H. Richter, J. Janek, *Adv. Energy Mater.* **2022**, *12*, 2201425.

[7] Q. Zhao, S. Stalin, C. Z. Zhao, L. A. Archer, *Nat. Rev. Mater.* **2020**, *5*, 229–252.

[8] N. Kamaya, K. Homma, Y. Yamakawa, M. Hirayama, R. Kanno, M. Yonemura, T. Kamiyama, Y. Kato, S. Hama, K. Kawamoto, A. Mitsui, *Nat. Mater.* **2011**, *10*, 682–686.

[9] Y. Kato, S. Hori, T. Saito, K. Suzuki, M. Hirayama, A. Mitsui, M. Yonemura, H. Iba, R. Kanno, *Nat. Energy* **2016**, *1*, 1–7.

[10] Y. Li, S. Song, H. Kim, K. Nomoto, H. Kim, X. Sun, S. Hori, K. Suzuki, N. Matsui, M. Hirayama, T. Mizoguchi, T. Saito, T. Kamiyama, R. Kanno, *Science **2023**, 381*, 50-53**.**

[11] L. Zhou, A. Assoud, Q. Zhang, X. Wu, L. F. Nazar, *J. Am. Chem. Soc.* **2019**, *141*, 19002–19013.

[12] M. A. Kraft, S. Ohno, T. Zinkevich, R. Koerver, S. P. Culver, T. Fuchs, A. Senyshyn, S. Indris, B. J. Morgan, W. G. Zeier, *J. Am. Chem. Soc.* **2018**, *140*, 16330–16339.

[13] P. Minnmann, L. Quillman, S. Burkhardt, F. H. Richter, J. Janek, *J. Electrochem. Soc.* **2021**, *168*, 040537.

[14] A. Bielefeld, D. A. Weber, J. Janek, *J. Phys. Chem. C* **2019**, *123*, 1626–1634.

[15] C. Oses, C. Toher, S. Curtarolo, *Nat. Rev. Mater.* **2020**, *5*, 295–309.

[16] S. Schweidler, M. Botros, F. Strauss, Q. Wang, Y. Ma, L. Velasco, G. Cadilha Marques, A. Sarkar, C. Kübel, H. Hahn, J. Aghassi-Hagmann, T. Brezesinski, B. Breitung, *Nat. Rev. Mater.* **2024**, *9*, 266–281.

[17] Y. Ma, Y. Ma, Q. Wang, S. Schweidler, M. Botros, T. Fu, H. Hahn, T. Brezesinski, B. Breitung, *Energy Environ. Sci.* **2021**, *14*, 2883–2905.

[18] F. Strauss, J. Lin, M. Duffiet, K. Wang, T. Zinkevich, A. L. Hansen, S. Indris, T. Brezesinski, *ACS Mater. Lett.* **2022**, *4*, 418–423.

[19] J. Lin, G. Cherkashinin, M. Schäfer, G. Melinte, S. Indris, A. Kondrakov, J. Janek, T. Brezesinski, F. Strauss, *ACS Mater. Lett.* **2022**, *4*, 2187–2194.

[20] S. Li, J. Lin, M. Schaller, S. Indris, X. Zhang, T. Brezesinski, C. W. Nan, S. Wang, F. Strauss, *Angew. Chemie - Int. Ed.* **2023**, *62*, e202314155.

[21] J. Lin, M. Schaller, S. Indris, V. Baran, A. Gautam, J. Janek, A. Kondrakov, T. Brezesinski, F. Strauss, *Angew. Chemie - Int. Ed.* **2024**, *63*, e202404874.

[22] J. Du, J. Lin, R. Zhang, S. Wang, S. Indris, H. Ehrenberg, A. Kondrakov, T. Brezesinski, F. Strauss, *Batter. Supercaps* **2024**, *7*, 1–11.

[23] J. Lin, M. Schaller, G. Cherkashinin, S. Indris, J. Du, C. Ritter, A. Kondrakov, J. Janek, T. Brezesinski, F. Strauss, *Small* **2024**, *20*, 202306832.

[24] T. Famprikis, P. Canepa, J. A. Dawson, M. S. Islam, C. Masquelier, *Nat. Mater.* **2019**, *18*, 1278–1291.

[25] V. J. Frenkel, *Zeitschrift fiir Phys.* **1925**, *XXXV*, 652–669.

[26] H. Mehrer, *Diffusion in Solids,* Springer Berlin, Heidelberg, **2007**.

[27] J. Maier, *Physical Chemistry of Ionic Materials: Ions and Electrons in Solids, 2nd Edition*, John Wiley & Sons, **2023**.

[28] M. Sotoudeh, S. Baumgart, M. Dillenz, J. Döhn, K. Forster-Tonigold, K. Helmbrecht, D. Stottmeister, A. Groß, *Adv. Energy Mater.* **2023**, 2302550.

[29] P. Debye, *Ann. Phys.* **1912**, *344*, 789–839.

[30] C. Richard A. Catlow, *J. Chem. Soc. Faraday Trans.* **1990**, *86*, 1167–1176.

[31] A. Einstein, *Ann. Phys.* **1905**, *322*, 549–560.

[32] M. von Smoluchowski, *Ann. Phys.* **1906**, *326*, 756–780.

[33] G. H. Vineyard, *J. Phys. Chem. Solids* **1957**, *3*, 121–127.

[34] G. E. Murch, *Solid State Ionics* **1982**, *7*, 177–198.

[35] K. Funke, *Zeitschrift fur Phys. Chemie* **1987**, *154*, 251–295.

[36] K. Funke, D. Wilmer, *Solid State Ionics* **2000**, *136–137*, 1329–1333.

[37] K. Funke, R. D. Banhatti, *Solid State Ionics* **2006**, *177*, 1551–1557.

[38] K. Funke, R. D. Banhatti, S. Brückner, C. Cramer, C. Krieger, A. Mandanici, C. Martiny, I. Ross, *Phys. Chem. Chem. Phys.* **2002**, *4*, 3155–3167.

[39] K. Funke, *Solid State Ionics* **1988**, *28–30*, 100–107.

[40] X. He, Y. Zhu, Y. Mo, *Nat. Commun.* **2017**, *8*, 1–7.

[41] Z. Zhang, L. F. Nazar, *Nat. Rev. Mater.* **2022**, *7*, 389-405.

[42] B. M. Jansen, *Angew. Cheni. lnt. Ed. Engl.* **1991,** 30, 1547-1558.

[43] L. Holmes, L. Peng, I. Heinmaa, L. A. O'Dell, M. E. Smith, R. N. Vannier, C. P. Grey, *Chem. Mater.* **2008**, *20*, 3638–3648.

[44] Z. Zhang, H. Li, K. Kaup, L. Zhou, P. N. Roy, L. F. Nazar, *Matter* **2020**, *2*, 1667–1684.

[45] H. Fang, P. Jena, *Nat. Commun.* **2022**, *13*, 1–11.

[46] P. C. Tsai, S. Mair, J. Smith, D. M. Halat, P. H. Chien, K. Kim, D. Zhang, Y. Li, L. Yin, J. Liu, S. H. Lapidus, J. A. Reimer, N. P. Balsara, D. J. Siegel, Y. M. Chiang, *Adv. Energy Mater.* **2023**, *13*, 202203284.

[47] Y. Sun, B. Ouyang, Y. Wang, Y. Zhang, S. Sun, Z. Cai, V. Lacivita, Y. Guo, G. Ceder, *Matter* **2022**, *5*, 4379–4395.

[48] A. Lundén, *Solid State Commun.* **1988**, *65*, 1237–1240.

[49] L. Karlsson, R. L. McGreevy, *Solid State Ionics* **1995**, *76*, 301–308.

[50] R. L. K. and G. C. KyuJung Jun, Byungju Lee, *Proc. Natl. Acad. Sci.* **2024**, *121*, e2316493121.

[51] P. V. Rysselberghe, *J. Phys. Chem.* **1931,** 36, 1152-1155.

[52] K. Wakamura, *J. Phys. Chem. Solids* **1998**, *59*, 591–598.

[53] J. C. Bachman, S. Muy, A. Grimaud, H. H. Chang, N. Pour, S. F. Lux, O. Paschos, F. Maglia, S. Lupart, P. Lamp, L. Giordano, Y. Shao-Horn, *Chem. Rev.* **2016**, *116*, 140–162.

[54] S. Muy, R. Schlem, Y. Shao-Horn, W. G. Zeier, *Adv. Energy Mater.* **2021**, *11*, 202002787.

[55] K. Gordiz, S. Muy, W. G. Zeier, Y. Shao-Horn, A. Henry, *Cell Reports Phys. Sci.* **2021**, *2*, 100431.

[56] S. Muy, J. C. Bachman, L. Giordano, H. H. Chang, D. L. Abernathy, D. Bansal, O. Delaire, S. Hori, R. Kanno, F. Maglia, S. Lupart, P. Lamp, Y. Shao-Horn, *Energy Environ. Sci.* **2018**, *11*, 850–859.

[57] T. Song, Y. Lin, D. Wang, Q. Chen, C. Ling, S. Shi, *Adv. Energy Mater.* **2024**, 2302440.

[58] J. Ding, PhD thesis, Duke University **2022,** 1–227.

[59] K. J. Jun, Y. Sun, Y. Xiao, Y. Zeng, R. Kim, H. Kim, L. J. Miara, D. Im, Y. Wang, G. Ceder, *Nat. Mater.* **2022**, *21*, 924–931.

[60] G. Han, A. Vasylenko, L. M. Daniels, C. M. Collins, L. Corti, R. Chen, H. Niu, T. D. Manning, D. Antypov, M. S. Dyer, J. Lim, M. Zanella, M. Sonni, M. Bahri, H. Jo, Y. Dang, C. M. Robertson, F. Blanc, L. J. Hardwick, N. D. Browning, J. B. Claridge, M. J. Rosseinsky, *Science* **2024**, *383*, 739–745.

[61] Y. Wang, W. D. Richards, S. P. Ong, L. J. Miara, J. C. Kim, Y. Mo, G. Ceder, *Nat. Mater.* **2015**, *14*, 1026–1031.

[62] C. Herzig, T. Surholt, *MRS Proc.* **1998**, *527*, 241–253.

[63] Y. Mishin, C. Herzig, *Mater. Sci. Eng. A* **1999**, *260*, 55–71.

[64] A. Suzuki, Y. Mishin, *Interface Sci.* **2003**, *11*, 131–148.

[65] E. Milan, M. Pasta, *Mater. Futur.* **2023**, *2*, 013501.

[66] L. Schweiger, K. Hogrefe, B. Gadermaier, J. L. M. Rupp, H. M. R. Wilkening, *J. Am. Chem. Soc.* **2022**, *144*, 9597–9609.

[67] J. A. Quirk, J. A. Dawson, *Adv. Energy Mater.* **2023**, *13*, 202301114.

[68] J. A. Dawson, P. Canepa, T. Famprikis, C. Masquelier, M. S. Islam, *J. Am. Chem. Soc.* **2018**, *140*, 362–368.

[69] M. Brinek, C. Hiebl, H. M. R. Wilkening, *Chem. Mater.* **2020**, *32*, 4754–4766.

[70] M. Gombotz, H. M. R. Wilkening, *ACS Sustain. Chem. Eng.* **2021**, *9*, 743–755.

[71] M. Brinek, C. Hiebl, K. Hogrefe, I. Hanghofer, H. M. R. Wilkening, *J. Phys. Chem. C* **2020**, *124*, 22934–22940.

[72] H. Brandstätter, D. Wohlmuth, P. Bottke, V. Pregartner, M. Wilkening, *Zeitschrift fur Phys. Chemie* **2015**, *229*, 1363–1374.

[73] P. Heitjans, M. Masoud, A. Feldhoff, M. Wilkening, *Faraday Discuss.* **2007**, *134*, 67–82.

[74] Z. Liu, W. Fu, E. A. Payzant, X. Yu, Z. Wu, N. J. Dudney, J. Kiggans, K. Hong, A. J. Rondinone, C. Liang, *J. Am. Chem. Soc.* **2013**, *135*, 975–978.

[75] D. Di Stefano, A. Miglio, K. Robeyns, Y. Filinchuk, M. Lechartier, A. Senyshyn, H. Ishida, S. Spannenberger, D. Prutsch, S. Lunghammer, D. Rettenwander, M. Wilkening, B. Roling, Y. Kato, G. Hautier, *Chem* **2019**, *5*, 2450–2460.

[76] A. Jodlbauer, J. Spychala, K. Hogrefe, B. Gadermaier, H. M. R. Wilkening, *Chem. Mater.* **2024**, *36*, 1648–1664.

[77] M. Winter, R. J. Brodd, *Chem. Rev.* **2004**, *104*, 4245–4269.

[78] M. Winter, B. Barnett, K. Xu, *Chem. Rev.* **2018**, *118*, 11433–11456.

[79] J. B. Goodenough, K. S. Park, *J. Am. Chem. Soc.* **2013**, *135*, 1167–1176.

[80] A. Manthiram, X. Yu, S. Wang, *Nat. Rev. Mater.* **2017**, *2*, 1–16.

[81] J. Wang, T. He, X. Yang, Z. Cai, Y. Wang, V. Lacivita, H. Kim, B. Ouyang, G. Ceder, *Nat. Commun.* **2023**, *14*, 5210.

[82] J. Lu, Y. Li, *J. Mater. Sci. Mater. Electron.* **2021**, *32*, 9736–9754.

[83] Y. Inaguma, L. Chen, M. Itoh, T. Nakamura, *Solid State Commun.* **1993**, *86*, 689–693.

[84] R. Murugan, V. Thangadurai, W. Weppner, *Angew. Chemie - Int. Ed.* **2007**, *46*, 7778–7781.

[85] V. Thangadurai, S. Narayanan, D. Pinzaru, *Chem. Soc. Rev.* **2014**, *43*, 4714–4727.

[86] C. Wang, K. Fu, S. P. Kammampata, D. W. McOwen, A. J. Samson, L. Zhang, G. T. Hitz, A. M. Nolan, E. D. Wachsman, Y. Mo, V. Thangadurai, L. Hu, *Chem. Rev.* **2020**, *120*, 4257–4300.

[87] R. Mercier, J.-P. Malugani, B. Fahys, G. Robert, *Solid State Ionics* **1981**, *5*, 663–666.

[88] R. Kanno, T. Hata, Y. Kawamoto, M. Irie, *Solid State Ionics* **2000**, *130*, 97–104.

[89] H. J. Deiseroth, S. T. Kong, H. Eckert, J. Vannahme, C. Reiner, T. Zaiß, M. Schlosser, *Angew. Chemie - Int. Ed.* **2008**, *47*, 755–758.

[90] P. Adeli, J. D. Bazak, K. H. Park, I. Kochetkov, A. Huq, G. R. Goward, L. F. Nazar, *Angew. Chemie* **2019**, *131*, 8773–8778.

[91] L. Zhou, N. Minafra, W. G. Zeier, L. F. Nazar, *Acc. Chem. Res.* **2021**, *54*, 2717–2728.

[92] X. Li, J. Liang, X. Yang, K. R. Adair, C. Wang, F. Zhao, X. Sun, *Energy Environ. Sci.*

2020, *13*, 1429–1461.

[93] D. C. Ginnings, T. E. Phipps, *J. Am. Chem. Soc.* **1930**, *52*, 1340–1345.

[94] W. Weppner, R. A. Huggins, *Phys. Lett. A* **1976**, *58*, 245–248.

[95] T. Asano, A. Sakai, S. Ouchi, M. Sakaida, A. Miyazaki, S. Hasegawa, *Adv. Mater.* **2018**, *30*, 1–7.

[96] Z. Liu, S. Ma, J. Liu, S. Xiong, Y. Ma, H. Chen, *ACS Energy Lett.* **2021**, *6*, 298–304.

[97] Z. Liu, P. Chien, S. Wang, S. Song, M. Lu, S. Chen, S. Xia, J. Liu, Y. Mo, H. Chen, *Nat. Chem.* **2024**, *16*, 1584–1591.

[98] L. Zhou, T. T. Zuo, C. Y. Kwok, S. Y. Kim, A. Assoud, Q. Zhang, J. Janek, L. F. Nazar, *Nat. Energy* **2022**, *7*, 83–93.

[99] F. Jin, L. Fadillah, H. Q. Nguyen, T. M. Sandvik, Y. Liu, A. García-Martín, E. Salagre, E. G. Michel, D. Stoian, K. Marshall, W. Van Beek, G. Redhammer, M. Mehraj Ud Din, D. Rettenwander, *Chem. Mater.* **2024**, *36*, 6017-6026.

[100] K. H. Park, K. Kaup, A. Assoud, Q. Zhang, X. Wu, L. F. Nazar, *ACS Energy Lett.* **2020**, 533–539.

[101] L. M. Riegger, R. Schlem, J. Sann, W. G. Zeier, J. Janek, *Angew. Chemie* **2021**, *133*, 6792–6797.

[102] Y. Wang, X. Li, *Adv. Mater.* **2024**, *36*, 1–9.

[103] L. Ye, X. Li, *Nature* **2021**, *593*, 218–222.

[104] H. Huo, J. Janek, *National Science Review* **2023**, *10(6)*.

[105] J. W. Yeh, S. K. Chen, S. J. Lin, J. Y. Gan, T. S. Chin, T. T. Shun, C. H. Tsau, S. Y. Chang, *Adv. Eng. Mater.* **2004**, *6*, 299–303.

[106] R. Z. Zhang, M. J. Reece, *J. Mater. Chem. A* **2019**, *7*, 22148–22162.

[107] E. P. George, D. Raabe, R. O. Ritchie, *Nat. Rev. Mater.* **2019**, *4*, 515–534.

[108] S. V. Krivovichev, *Acta Crystallogr. Sect. B Struct. Sci. Cryst. Eng. Mater.* **2016**, *72*, 274–276.

[109] R. K. Patel, S. K. Ojha, S. Kumar, A. Saha, P. Mandal, J. W. Freeland, S. Middey, *Appl. Phys. Lett.* **2020**, *116*, 1601–1604.

[110] S. T. Bramwell, M. J. P. Gingras, *Science* **2001**, *294*, 1495–1501.

[111] A. Navrotsky, O. J. Kleppa, *J. Inorg. Nucl. Chem.* **1968**, *30*, 479–498.

[112] B. Fultz, *Prog. Mater. Sci.* **2010**, *55*, 247–352.

[113] R. J. Spurling, E. A. Lass, X. Wang, K. Page, *Phys. Rev. Materials* **2022**, 090301.

[114] S. J. Mccormack, A. Navrotsky, *Acta Mater.* **2021**, *202*, 1–21.

[115] D. Brown, *The Chemical Bond in Inorganic Chemistry*, Oxford University Press, **2002**.

[116] F. Strauss, M. Botros, B. Breitung, T. Brezesinski, *J. Appl. Phys.* **2024**, *135*, 120901.

[117] D. Berardan, S. Franger, A. K. Meena, N. Dragoe, *J. Mater. Chem. A* **2016**, *4*, 9536–

9541.

[118] B. L. Musicó, D. Gilbert, T. Z. Ward, K. Page, E. George, J. Yan, D. Mandrus, V. Keppens, *APL Mater.* **2020**, *8*, 040912.

[119] V. S. Urusov, T. N. Nadezhina, *J. Struct. Chem.* **2009**, *50*, 22–37.

[120] L. Pauling, *J. Am. Chem. Soc.* **1929**, *51*, 1010–1026.

[121] Z. Wang, C. T. Liu, P. Dou, *Phys. Rev. Mater.* **2017**, *1*, 1–5.

[122] S. Chae, L. Williams, J. Lee, J. T. Heron, E. Kioupakis, *npj Comput. Mater.* **2022**, *8*, 95.

[123] Y. Chen, T. Wang, H. Chen, W. H. Kan, W. Yin, Z. Song, C. Wang, J. Ma, W. Luo, Y. Huang, *Matter* **2023**, *6*, 1530–1541.

[124] Z. Song, T. Wang, H. Yang, W. H. Kan, Y. Chen, Q. Yu, L. Wang, Y. Zhang, Y. Dai, H. Chen, W. Yin, T. Honda, M. Avdeev, H. Xu, J. Ma, Y. Huang, W. Luo, *Nat. Commun.* **2024**, *15*, 1481.

[125] Y. Deng, C. Eames, B. Fleutot, R. David, J. N. Chotard, E. Suard, C. Masquelier, M. S. Islam, *ACS Appl. Mater. Interfaces* **2017**, *9*, 7050–7058.

[126] G. Zhao, K. Suzuki, T. Seki, X. Sun, M. Hirayama, R. Kanno, *J. Solid State Chem.* **2020**, *292*, 121651.

[127] G. Zhao, K. Suzuki, T. Okumura, T. Takeuchi, M. Hirayama, R. Kanno, *Chem. Mater.* **2022**, *34*, 3948–3959.

[128] G. Zhao, K. Suzuki, M. Yonemura, M. Hirayama, R. Kanno, *ACS Appl. Energy Mater.* **2019**, *2*, 6608–6615.

[129] K. Suzuki, M. Kamiya, N. Matsui, S. Hori, M. Hirayama, R. Kanno, *J. Phys. Chem. C* **2023**, *127*, 10947–10952.

[130] Y. Zeng, B. Ouyang, J. Liu, Y. W. Byeon, Z. Cai, L. J. Miara, Y. Wang, G. Ceder, *Science* **2022**, *378*, 1320–1324.

[131] S. K. Jung, H. Gwon, H. Kim, G. Yoon, D. Shin, J. Hong, C. Jung, J. S. Kim, *Nat. Commun.* **2022**, *13*, 7638.

[132] Q. Wang, Y. Zhou, X. Wang, H. Guo, S. Gong, Z. Yao, F. Wu, J. Wang, S. Ganapathy, X. Bai, B. Li, C. Zhao, J. Janek, *Nat. Commun.* **2024**, *15*, 1050.

[133] S. T. Ko, T. Lee, J. Qi, D. Zhang, W. T. Peng, X. Wang, W. C. Tsai, S. Sun, Z. Wang, W. J. Bowman, S. P. Ong, X. Pan, J. Luo, *Matter* **2023**, *6*, 2395–2418.

[134] S. T. Kong, H. J. Deiseroth, C. Reiner, Ö. Gün, E. Neumann, C. Ritter, D. Zahn, *Chem. - A Eur. J.* **2010**, *16*, 2198–2206.

[135] S. T. Kong, Ö. Gün, B. Koch, H. J. Deiseroth, H. Eckert, C. Reiner, *Chem. - A Eur. J.* **2010**, *16*, 5138–5147.

[136] M. A. Kraft, S. P. Culver, M. Calderon, F. Böcher, T. Krauskopf, A. Senyshyn, C. Dietrich, A. Zevalkink, J. Janek, W. G. Zeier, *J. Am. Chem. Soc.* **2017**, *139*, 10909–10918.

[137] N. Minafra, M. A. Kraft, T. Bernges, C. Li, R. Schlem, B. J. Morgan, W. G. Zeier, *Inorg. Chem.* **2020**, *59*, 11009–11019.

[138] R. Schlenker, A. L. Hansen, A. Senyshyn, T. Zinkevich, M. Knapp, T. Hupfer, H. Ehrenberg, S. Indris, *Chem. Mater.* **2020**, *32*, 8420–8430.

[139] A. Morscher, B. B. Duff, G. Han, L. M. Daniels, Y. Dang, M. Zanella, M. Sonni, A. Malik, M. S. Dyer, R. Chen, J. B. Claridge, M. J. Rosseinsky, *J. Am. Chem. Soc.* **2022**, *144*, 22178–22192.

[140] N. J. J. De Klerk, I. Rosłoń, M. Wagemaker, *Chem. Mater.* **2016**, *28*, 7955–7963.

[141] K. Hogrefe, I. Hanghofer, H. M. R. Wilkening, *J. Phys. Chem. C* **2021**, *125*, 22457–22463.

[142] A. Gautam, M. Sadowski, N. Prinz, H. Eickhoff, N. Minafra, M. Ghidiu, S. P. Culver, K. Albe, T. F. Fässler, M. Zobel, W. G. Zeier, *Chem. Mater.* **2019**, *31*, 10178–10185.

[143] P.-H. Chien, B. Ouyang, X. Feng, L. Dong, D. Mitlin, J. Nanda, J. Liu, *Chem. Mater.* **2024**, *36*, 382–393.

[144] L. Zhou, Q. Zhang, L. F. Nazar, *Chem. Mater.* **2022**, *34*, 9634–9643.

[145] K. Hogrefe, N. Minafra, I. Hanghofer, A. Banik, W. G. Zeier, H. M. R. Wilkening, *J. Am. Chem. Soc.* **2022**, *144*, 1795–1812.

[146] A. Gautam, M. Sadowski, M. Ghidiu, N. Minafra, A. Senyshyn, K. Albe, W. G. Zeier, *Adv. Energy Mater.* **2021**, *11*, 2003369.

[147] S. Park, J. W. Lee, *J. Korean Inst. Met. Mater.* **2021**, *59*, 247–255.

[148] V. Faka, M. T. Agne, M. A. Lange, D. Daisenberger, B. Wankmiller, S. Schwarzmüller, H. Huppertz, O. Maus, B. Helm, T. Böger, J. Hartel, J. M. Gerdes, J. J. Molaison, G. Kieslich, M. R. Hansen, W. G. Zeier, *J. Am. Chem. Soc.* **2024**, *146*, 1710–1721.

[149] M. Cronau, M. Szabo, C. König, T. B. Wassermann, B. Roling, *ACS Energy Lett.* **2021**, *6*, 3072–3077.

[150] S. Wang, W. Zhang, X. Chen, D. Das, R. Ruess, A. Gautam, F. Walther, S. Ohno, R. Koerver, Q. Zhang, W. G. Zeier, F. H. Richter, C. W. Nan, J. Janek, *Adv. Energy Mater.* **2021**, *11*, 202100654.

[151] M. Sadowski, K. Albe, *Adv. Mater. Interfaces* **2024**, *2400423*, 1–10.

[152] J. H. Teo, F. Strauss, F. Walther, Y. Ma, S. Payandeh, T. Scherer, M. Bianchini, J. Janek, T. Brezesinski, *Mater. Futur.* **2022**, *1*, 015102.

[153] Y. Wang, H. Hao, K. G. Naik, B. S. Vishnugopi, C. D. Fincher, Q. Yan, V. Raj, H. Celio, G. Yang, H. Fang, Y. Chiang, F. A. Perras, P. Jena, J. Watt, P. P. Mukherjee, D. Mitlin, *Adv. Energy Mater.* **2024**, *14*, 2304530.

[154] D. K. Singh, A. Henss, B. Mogwitz, A. Gautam, J. Horn, T. Krauskopf, S. Burkhardt, J. Sann, F. H. Richter, J. Janek, *Cell Reports Phys. Sci.* **2022**, *3*, 101043.

[155] R. Schlem, T. Bernges, C. Li, M. A. Kraft, N. Minafra, W. G. Zeier, *ACS Appl. Energy Mater.* **2020**, *3*, 3684–3691.

[156] D. H. S. Tan, E. A. Wu, H. Nguyen, Z. Chen, M. A. T. Marple, J. M. Doux, X. Wang, H. Yang, A. Banerjee, Y. S. Meng, *ACS Energy Lett.* **2019**, 2418–2427.

[157] S. W. Park, G. Oh, J. W. Park, Y. C. Ha, S. M. Lee, S. Y. Yoon, B. G. Kim, *Small*

2019, *15*, 1–11.

[158] F. Walther, S. Randau, Y. Schneider, J. Sann, M. Rohnke, F. H. Richter, W. G. Zeier, J. Janek, *Chem. Mater.* **2020**, *32*, 6123–6136.

[159] J. Auvergniot, A. Cassel, J. B. Ledeuil, V. Viallet, V. Seznec, R. Dedryvère, *Chem. Mater.* **2017**, *29*, 3883–3890.

[160] S. K. Jung, H. Gwon, S. S. Lee, H. Kim, J. C. Lee, J. G. Chung, S. Y. Park, Y. Aihara, D. Im, *J. Mater. Chem. A* **2019**, *7*, 22967–22976.

[161] Y. Ma, R. Zhang, Y. Tang, Y. Ma, J. H. Teo, T. Diemant, D. Goonetilleke, J. Janek, M. Bianchini, A. Kondrakov, T. Brezesinski, *ACS Nano* **2022**, *16*, 18682–18694.

[162] D. Weber, Đ. Tripković, K. Kretschmer, M. Bianchini, T. Brezesinski, *Eur. J. Inorg. Chem.* **2020**, 3117–3130.

[163] S. Wenzel, S. J. Sedlmaier, C. Dietrich, W. G. Zeier, J. Janek, *Solid State Ionics* **2018**, *318*, 102–112.

[164] T. K. Schwietert, V. A. Arszelewska, C. Wang, C. Yu, A. Vasileiadis, N. J. J. de Klerk, J. Hageman, T. Hupfer, I. Kerkamm, Y. Xu, E. van der Maas, E. M. Kelder, S. Ganapathy, M. Wagemaker, *Nat. Mater.* **2020**, *19*, 428–435.

[165] A. O. Kondrakov, A. Schmidt, J. Xu, H. Geßwein, R. Mönig, P. Hartmann, H. Sommer, T. Brezesinski, J. Janek, *J. Phys. Chem. C* **2017**, *121*, 3286–3294.

[166] Z. Fu, **2022**, 6175–6183.

[167] C. H. Kuo, A. Y. Wang, H. Y. Liu, S. C. Huang, X. R. Chen, C. C. Chi, Y. C. Chang, M. Y. Lu, H. Y. Chen, *APL Mater.* **2022**, *10*, 121104.

[168] J. Fan, T. Wang, C. A. Bridges, A. Y. Borisevich, C. A. Steren, P. Li, B. P. Thapaliya, C. L. Do-Thanh, Z. Yang, Y. Yuan, S. Dai, *RSC Adv.* **2023**, *13*, 19856–19861.

[169] M. P. Stockham, B. Dong, P. R. Slater, *J. Solid State Chem.* **2022**, *308*, 122944.

[170] Q. Zhao, Z. Cao, X. Wang, H. Chen, Y. Shi, Z. Cheng, Y. Guo, B. Li, Y. Gong, Z. Du, S. Yang, *J. Am. Chem. Soc.* **2023**, *145*, 21242–21252.

[171] X. Li, Y. Xu, C. Zhao, D. Wu, L. Wang, M. Zheng, X. Han, S. Zhang, J. Yue, B. Xiao, W. Xiao, L. Wang, T. Mei, M. Gu, J. Liang, X. Sue, *Angew. Chemie - Int. Ed.* **2023,** *62,* e202306433.

[172] A. Gautam, M. Ghidiu, E. Suard, M. A. Kraft, W. G. Zeier, *ACS Appl. Energy Mater.* **2021**, *4*, 7309–7315.

[173] H. J. Deiseroth, J. Maier, K. Weichert, V. Nickel, S. T. Kong, C. Reiner, *Zeitschrift fur Anorg. und Allg. Chemie* **2011**, *637*, 1287–1294.

[174] W. Arnold, V. Shreyas, S. Akter, Y. Li, S. Halacoglu, M. B. Kalutara Koralalage, X. Guo, D. Vithanage, W. Wei, G. Sumanasekera, J. B. Jasinski, B. Narayanan, H. Wang, *J. Phys. Chem. C* **2023**, *127*, 11801–11809.

[175] W. Arnold, V. Shreyas, Y. Li, M. K. Koralalage, J. B. Jasinski, A. Thapa, G. Sumanasekera, A. T. Ngo, B. Narayanan, H. Wang, *ACS Appl. Mater. Interfaces* **2022**, *14*, 11483–11492.

[176] P. Adeli, J. David Bazak, A. Huq, G. R. Goward, L. F. Nazar, *Chem. Mater.* **2021**,

33, 146–157.

[177] P. Wang, H. Liu, S. Patel, X. Feng, P. H. Chien, Y. Wang, Y. Y. Hu, *Chem. Mater.* **2020**, *32*, 3833–3840.

[178] S. V. Patel, S. Banerjee, H. Liu, P. Wang, P. H. Chien, X. Feng, J. Liu, S. P. Ong, Y. Y. Hu, *Chem. Mater.* **2021**, *33*, 1435–1443.

[179] P. Wang, S. Patel, H. Liu, P. H. Chien, X. Feng, L. Gao, B. Chen, J. Liu, Y. Y. Hu, *Adv. Funct. Mater.* **2023**, *33*, 1–11.

[180] H. Schneider, S. J. Sedlmaier, H. Du, T. Kelley, K. Leitner, J. ter Maat, C. Scordilis-Kelley, A. Mudalige, J. Kulisch, L. Schneider, *ChemistrySelect* **2019**, *4*, 3351–3354.

[181] Z. Zhang, J. Zhang, H. Jia, L. Peng, T. An, J. Xie, *J. Power Sources* **2020**, *450*, 227601.

[182] B. W. Taklu, W. N. Su, Y. Nikodimos, K. Lakshmanan, N. T. Temesgen, P. X. Lin, S. K. Jiang, C. J. Huang, D. Y. Wang, H. S. Sheu, S. H. Wu, B. J. Hwang, *Nano Energy* **2021**, *90*, 106542.

[183] Z. Jiang, Y. Liu, H. Peng, J. Li, X. Xu, H. Su, Y. Zhong, X. Wang, C. Gu, J. Tu, *Energy Storage Mater.* **2023**, *56*, 300–309.

[184] Z. Zhang, Y. Sun, X. Duan, L. Peng, H. Jia, Y. Zhang, B. Shan, J. Xie, *J. Mater. Chem. A* **2019**, *7*, 2717–2722.

[185] R. Argyrodite, L. Zn, B. T. Leube, C. M. Collins, L. M. Daniels, B. B. Du, Y. Dang, R. Chen, M. W. Gaultois, T. D. Manning, M. S. Dyer, J. B. Claridge, M. J. Rosseinsky, *Chem. Mater.* **2022**, *34*, 4073-4087.

[186] N. Minafra, S. P. Culver, T. Krauskopf, A. Senyshyn, W. G. Zeier, *J. Mater. Chem. A* **2018**, *6*, 645–651.

[187] S. Ohno, B. Helm, T. Fuchs, G. Dewald, M. A. Kraft, S. P. Culver, A. Senyshyn, W. G. Zeier, *Chem. Mater.* **2019**, *31*, 4936–4944.

[188] A. Gautam, M. Ghidiu, A. L. Hansen, S. Ohno, W. G. Zeier, *Inorg. Chem.* **2021**, *60*, 18975–18980.

[189] M. Wu, G. Liu, X. Yao, *Appl. Phys. Lett.* **2022**, *121*, 203904.

[190] S. Kong, H. Deiseroth, J. Maier, V. Nickel, K. Weichert, C. Reiner, *Z. Anorg. Allg. Chem.* **2010**, *636*, 1920–1924.

[191] A. Morscher, M. S. Dyer, B. B. Du, G. Han, J. Gamon, L. M. Daniels, Y. Dang, T. W. Surta, C. M. Robertson, J. B. Claridge, M. J. Rosseinsky, *Chem. Mater.* **2021**, *33*, 2206–2217.

6. Appendix

6.1. Summary tables

Table S1 Overview about reported room temperature ionic conductivities for different oxide-, sulfide- and halide-based high-entropy (or multicomponent substituted) SEs highlighted in blue, green and yellow, respectively.

Materials	Compositions	σ_{ion} / mS cm^{-1}	E_A (EIS) / eV	Ref.
Rocksalt	$(Mg_{0.2}Co_{0.2}Ni_{0.2}Cu_{0.2}Zn_{0.2})_{0.66}Li_{0.33}O$	~1.0 (20°C)	0.20	[117]
LIPON	$(Li_{0.375}Sr_{0.4375})(Ta_{0.375}Nb_{0.375}Zr_{0.125}Hf_{0.125})O_{3-d}$	0.256	-	[133]
	$(Li_{0.375}Sr_{0.4375})(Ta_{0.45}Nb_{0.3}Zr_{0.125}Hf_{0.125})O_{3-\delta}$	0.204	-	[133]
Garnet	$Li_6La_3Zr_{0.5}Hf_{0.5}Ta_{0.5}Nb_{0.5}O_{12}$	0.33	0.44	[123]
	$Li_6La_3Zr_{0.5}Nb_{0.5}Ta_{0.5}Hf_{0.5}O_{12}$	0.467 (23°C)	0.25	[166]
	$Li_{6.4}La_3Zr_{0.4}Ta_{0.4}Nb_{0.4}Y_{0.6}W_{0.2}O_{12}$	0.16	0.23	[167]
	$Li_7La_3Zr_{0.5}Hf_{0.5}Sc_{0.5}Nb_{0.5}O_{12}$	0.27	-	[131]
	$Li_7La_3Zr_{0.4}Hf_{0.4}Sn_{0.4}Sc_{0.4}Ta_{0.4}O_{12}$	0.17	0.406	[131]
	$Li_{6.6}La_3Zr_{0.4}Hf_{0.4}Sn_{0.4}Sc_{0.2}Ta_{0.6}O_{12}$	0.32	0.403	[131]
	$Li_{5.4}La_3Zr_{0.4}Hf_{0.4}Nb_{0.4}Ta_{0.4}W_{0.4}O_{12}$	0.017	-	[168]
	$Ga_{0.2}Li_{5.75}La_{2.5}Nd_{0.5}Nb_{0.65}Ce_{0.1}Zr_1Ti_{0.25}O_{12}$	0.1	-	[169]
	$Ga_{0.2}Li_{5.75}La_{2.5}Nd_{0.5}Nb_{0.35}Ta_{0.3}Ce_{0.1}Zr_{0.75}Hf_{0.25}Ti_{0.25}O_{12}$	0.2	0.33	[169]
Sulfide	$Li_{9.54}[Si_{0.6}Ge_{0.4}]_{1.74}P_{1.44}S_{11.1}Br_{0.3}O_{0.6}$	32	0.24	[10]
	$Li_x(Fe_{0.2}Co_{0.2}Ni_{0.2}Mn_{0.2}Zn_{0.2})PS_3$	0.4	0.38	[170]
Halide	$LiCl-(LaCl_3 \cdot CeCl_3 \cdot ZrCl_4 \cdot AlCl_3 \cdot TaCl_5)_{0.2}$	1	0.336	[171]
	$1.5LiCl-(LaCl_3 \cdot CeCl_3 \cdot ZrCl_4 \cdot HfCl_4 \cdot AlCl_3 \cdot TaCl_5)_{1/6}$	1.1	0.383	[171]
	$1.5LiCl-(LaCl_3 \cdot CeCl_3 \cdot ZrCl_4 \cdot HfCl_4 \cdot TaCl_5)_{0.2}$	1.8	0.318	[171]
	$1.5LiCl-(LaCl_3 \cdot CeCl_3 \cdot HfCl_4 \cdot AlCl_3 \cdot TaCl_5)_{0.2}$	1.3	0.364	[171]
	$Li_{2.8}In_{0.2}Sc_{0.2}Yb_{0.2}Lu_{0.2}Zr_{0.2}Cl_6$	2.13	0.286	[132]
	$Li_{2.75}Y_{0.16}Er_{0.16}Yb_{0.16}In_{0.25}Zr_{0.25}Cl_6$	0.849	0.338	[124]

Table S2 Li-ion conductivity (σ_{ion}) at T = 298 K (unless otherwise noted) and activation energies (E_A) of various lithium argyrodites determined by temperature-dependent EIS and ^{7}Li PFG-NMR spectroscopy. Without specific notation, the lithium argyrodites crystalized in cubic symmetry ($F\bar{4}3m$)

Material	σ_{ion} / mS cm^{-1}	E_A (EIS) / eV	E_A (^{7}Li PFG-NMR) / eV	Site-inversion at 4*d* $X_1^-/Ch^{2-}/X_2^-$	Li positions	Ref.
$Li_{7-a-b-c}PS_{6-a-b}X_{1a}X_{2b}$ (X_1=F, Cl, Br, I; X_2=F, Cl, Br, I)						
Li_7PS_6	0.55 - 1	0.475	-			[172,173]
Li_6PS_5Cl	1.3 - 3.4	0.34 - 0.38	0.29 - 0.35	0.538(Cl^-)/0.462(S^{2-})	T5(48*h*), T2(48*h*), T4(16*e*)*	[90,137,138,143, 173]
$Li_6PS_5Cl_{0.5}Br_{0.5}$	~3	0.37	-	0.211(Cl^-)/0.492(S^{2-})/0.297(Br^-)	T5(48*h*)	[136,137]
Li_6PS_5Br	1.09	0.30	-	0.221(Br^-)/0.779(S^{2-})	T5(48*h*), T5a(24*g*), T2(48*h*)	[136,137]
$Li_6PS_5Br_{0.5}I_{0.5}$	10^{-2}	0.32		0.035(Br^-)/0.965(S^{2-})	T5(48*h*), T5a(24*g*)	[136,137]
Li_6PS_5I	10^{-3}	0.38	-	0.0 (I^-)/1.0(S^{2-})	T5(48*h*), T5a(24*g*)	[136,137]
$Li_6PS_5I_{0.25}F_{0.75}$	0.15	0.34	-	-	-	[174]
Li_6PS_5F	0.23	0.45	-	-	-	[175]
$Li_6PS_5F_{0.5}Cl_{0.5}$	0.35	0.32	-	-	-	[175]
$Li_6PS_5F_{0.5}Br_{0.5}$	0.32	0.37	-	-	-	[175]
$Li_{6.75}PS_{6.75}Cl_{0.25}$	0.7	0.447	-	0.108(Cl^-)/0.892(S^{2-})	T5(48*h*), T2(48*h*)	[172]
$Li_{6.25}PS_{6.25}Cl_{0.75}$	1.2	0.45	-	0.426(Cl^-)/0.574(S^{2-})	T5(48*h*), T2(48*h*)	[172]
$Li_{5.75}PS_{4.75}Cl_{1.25}$	~4.0	0.33 - 0.40	0.35	0.67(Cl^-)/0.35(S^{2-})	T5(48*h*), T2(48*h*)	[90,172]

$Li_{5.5}PS_{4.5}Cl_{1.5}$	9.4	0.29	0.29	0.9(Cl^-)/0.1(S^{2-})	T5(48*h*), T2(48*h*)	[20,90,172,176]
$Li_{5.5}PS_{4.5}Br_{1.3}$	6	0.183	-	-	T5(48*h*), T5a (24*g*)	[177]
$Li_{5.5}PS_{4.5}Br_{1.5}$	10	0.188	0.24	-	T5(48*h*), T5a(24*g*)	[20,177]
$Li_{5.3}PS_{4.3}Br_{1.7}$	10	0.178	-	-	T5(48*h*), T5a(24*g*)	[177]
$Li_{5.7}PS_{4.5}ClBr_{0.3}$	12	0.194	-	0.57(Cl^-)/0.11(S^{2-})/0.32(Br^-)	T5(48*h*), T5a(24*g*)	[178]
$Li_{5.5}PS_{4.5}ClBr_{0.5}$	17	0.157	-	0.5(Cl^-)/0.28(S^{2-})/0.22(Br^-)	T5(48*h*), T5a(24*g*)	[178]
$Li_{5.3}PS_{4.3}ClBr_{0.7}$	24	0.155	-	0.5(Cl^-)/0.36(S^{2-})/0.15(Br^-)	T5(48*h*), T5a(24*g*)	[178]
$Li_{5.3}PS_{4.3}Cl_{0.3}Br_{1.4}$	17	0.197	-	-	T5(48*h*), T5a(24*g*)	[179]
$Li_{5.3}PS_{4.3}Cl_{0.7}Br$	24	0.155	-	-	T5(48*h*), T5a(24*g*)	[179]
$Li_{5.3}PS_{4.3}ClBr_{0.7}$	26	0.16	-	-	T5(48*h*), T5a(24*g*)	[179]
$Li_{5.3}PS_{4.3}Cl_{0.3}Br_{1.4}$	10	0.17	-	-	T5(48*h*), T5a(24*g*)	[179]
$Li_{5.5}PS_{4.5}Cl_{0.4}Br_{1.1}$	7.15	0.31	0.27	0.341(Cl^-)/0.390(S^{2-})/0.277(Br^-)	T5(48*h*), T5a(24*g*)	[20]
$Li_{5.5}PS_{4.5}Cl_{0.8}Br_{0.7}$	9.56	0.30	0.28	0.555(Cl^-)/0.289(S^{2-})/0.147(Br^-)	T5(48*h*), T5a(24*g*)	[20]
$Li_{5.5}PS_{4.5}Cl_{1.2}Br_{0.3}$	8.08	0.32	0.32	0.716(Cl^-)/0.136(S^{2-})/0.145(Br^-)	T5(48*h*)	[20]
$Li_{7-a-c}Y_cPS_{6-a}X_a$ (X=Cl, Br, I; Y=Al, Ca, Ga, Ag, Cu, Fe, B)						
$Li_6Fe_{0.5}PS_6$	0.14	-	-	-	-	[180]
$Li_{5.7}Al_{0.1}PS_5Cl$	3.7	-	-	-	-	[176]
$Li_{5.4}Al_{0.2}PS_5Cl$	3.6	-	-	-	-	[176]
$Li_{5.7}Ga_{0.1}PS_5Cl$	3.9	-	-	-	-	[176]
$Li_{5.4}Ga_{0.2}PS_5Cl$	4	-	-	-	-	[176]

$Li_{5.8}Ca_{0.1}PS_5Cl$	4.3	0.35	0.33	0.83(Cl^-)/0.17(S^{2-})	-	[176]
$Li_{5.6}Ca_{0.2}PS_5Cl$	3.4	0.325	0.305		-	[176]
$Li_{5.4}Al_{0.2}PS_5Br$	2.4	0.254	-	0.2(Br^-)/0.8(S^{2-})	-	[181]
$Li_{5.4}B_{0.2}PS_5Br$	1.3	-	-	-	-	[181]
$Li_{5.45}Al_{0.1}PS_{4.75}Cl_{1.25}$	5.7	-	-	-	-	[176]
$Li_{5.15}Al_{0.2}PS_{4.75}Cl_{1.25}$	3.6	-	-	-	-	[176]
$Li_{5.45}Ga_{0.1}PS_{4.75}Cl_{1.25}$	4.8	-	-	-	-	[176]
$Li_{5.35}Ca_{0.1}PS_{4.5}Cl_{1.55}$	10.2	0.30	0.257-0.383	0.867(Cl^-)/0.133(S^{2-})	T5(48*h*)	[176]
$Li_{6.3}P_{0.9}Cu_{0.1}S_{4.9}Cl_{1.1}$	4.2	0.27	-	-	-	[182]
$Li_{5.6}Cu_{0.2}PS_{4.8}Br_{1.2}$	3.5	0.24	-	-	-	[183]
$Li_{7-a}M_1M_2S_{6-a}X_a$ (X=Cl, Br, I; M_1=P, Si, Ge, Sb; M_2=P, Si, Ge, Sb)						
$Li_{7.3}P_{0.7}Si_{0.3}S_6$	1.27	-	-	-	-	[184]
$Li_{7.3}P_{0.7}Ge_{0.3}S_6$	1.96	-	-	-	-	[184]
$Li_7Zn_{0.5}SiS_6$ $I\bar{4}$	10^{-4}	0.66	-	-	T5(48*h*), T4(16*e*), T2(48*h*), T1, T2a	[185]
$Li_{6.125}P_{0.875}Si_{0.125}S_5Br$	0.8	0.19	-	0.18(Br^-)/0.82(S^{2-})	T5(48*h*), T5a(24*g*)	[186]
$Li_{6.5}P_{0.5}Si_{0.5}S_5Br$	2.2	0.26	-	-	-	[186]
$Li_{6.5}P_{0.5}Si_{0.5}S_5I$	2.0	0.24	-	0.10(I^-)/0.90(S^{2-})	T5(48*h*), T5a(24*g*)	[187]
$Li_{6.7}P_{0.3}Si_{0.7}S_5I$	2.0	0.22	-	0.12(I^-)/0.88(S^{2-})	T5(48*h*), T5a(24*g*)	[187]
$Li_{6.3}P_{0.7}Sn_{0.3}S_5I$	0.1	0.33	-	-	-	[187,188]

$Li_{6.6}P_{0.4}Ge_{0.6}S_5I$	5.4	0.24	-	0.063(I^-)/0.937(S^{2-})	T5(48*h*), T5a(24*g*), T4(16*e*), T2(48*h*)	[187]
$Li_{6.7}Sb_{0.3}Si_{0.7}S_5I$	14.8 (302 K)	0.25	-	0.0(I^-)/1.0(S^{2-})	T5(48*h*), T5a(24*g*), T4(16*e*), T3(4*c*)	[11]
$Li_{6.4}Sb_{0.6}Ge_{0.4}S_5I$	6.3 (302 K)	0.23	-	0.0(I^-)/1.0(S^{2-})	T5(48*h*)	[11]
$Li_{7-a}M_1M_2Ch_{6-a}X_a$ (X=Cl, Br, I; M_1=P, Si, Ge, Sb; M_2=P, Si, Ge, Sb, Ch=O, S, Se)						
Li_7PSe_6 (*Pna*2_1 at RT)	-	-	-	-	7 Li positions	[135]
Li_6PSe_5I	0.28	0.285	-	0.0(I^-)/1.0(Se^{2-})	T5(48*h*), T5a(24*g*)	[155]
$Li_{6.3}Sn_{0.3}P_{0.7}Se_5I$	2.4	0.26	-	0.04(I^-)/0.96(Se^{2-})	T5(48*h*), T5a(24*g*)	[188]
$Li_{6.05}PS_{4.9}O_{0.1}Cl_{1.05}$	7.49	-	-	-	-	[189]
Li_6PO_5Br	-	-	-	-	T5a(24*g*)	[190]
Li_6PO_5Cl	-	-	-	-	T5a(24*g*)	[190]
$Li_6SiO_4Cl_2$ (*Pna*2_1)	~10^{-7}	0.560	-	-	6 Li positions	[191]
$Li_{6.5}P_{0.25}Si_{0.75}O_5Cl$ (*P*$2_1$3)	1.82×10^{-6}	0.52	-	-	T5(48*h*), T5a(24*g*), T4(16*e*), T3(4*c*)	[139]

6.2. Publication VI: Synthetic Tailoring of Ionic Conductivity in Multicationic- Substituted, High-Entropy Lithium Argyrodites Solid Electrolytes

Publication VI is a follow-up to publication II (3.2). It illustrates the effect of cooling rate (fast, moderate and slow cooling) during solid state synthesis on the bulk structure, surface compositions as well as charge transport. It reveals that moderate cooling rates are favorable in achieving the highest conductivity compared to fast and slow cooling. No significant differences in the bulk structure were observed through NPD and ^{31}P as well as ^{6}Li MAS-NMR, while surface compositions (e.g. SiO_x and Sb^{3+}) were found to vary with cooling rates, as determined by XPS analysis. Moreover, based on electrochemical methods (EIS and PFG-NMR), it was found that higher concentrations of SiO_x and Sb^{3+}on the particle surface, are associated with increased ionic conductivity and reduced electronic conductivity. Finally, moderate cooled $Li_{6.5}[P_{0.25}Si_{0.25}Ge_{0.25}Sb_{0.25}]S_5I$ was electrochemically tested in pellet-type SSBs with a layered Ni-rich oxide cathode at 25 °C, and compared with the commercial available SE Li_6PS_5Cl. Although the high-entropy Li-ion conductor delivers larger specific capacities than Li_6PS_5Cl-based cells at high current rates, its lower electrochemical stability results in continuous capacity fading.

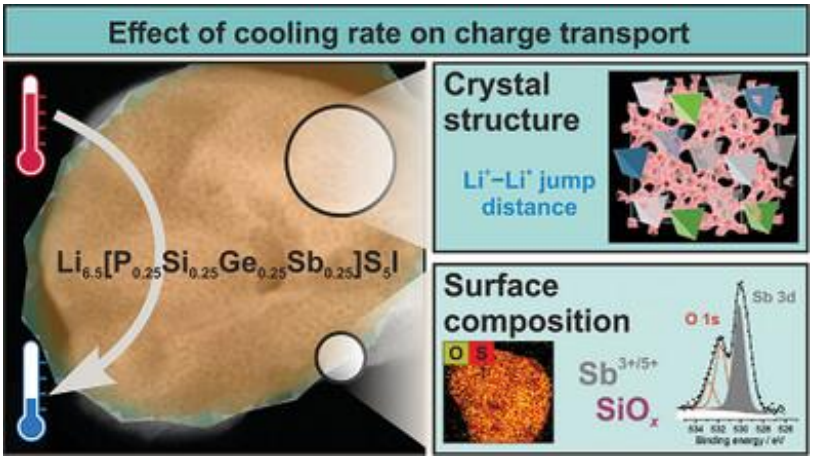

Figure 20 Table of Contents (TOC) of Publication V. Adapted from reference [23].

The experiments were planned and designed by the first author, J. Lin. under the supervision of J. Janek, T. Brezesinski and F. Strauss. The first author designed the conception and optimized the synthesis method. The NPD measurements were carried out at Institute Laue-Langevin (ILL D2B) (D2B) under proposal number (5-21-1164) with assistance from C. Ritter and J. Lin analyzed the results. J. Lin carried out the electrochemical experiments (EIS, CV and GCPL) and data analysis. J. D supported part of SSB assembling. M. Schäfer carried out the ^{7}Li PFG-NMR measurements and analyzed the date together with J. Lin. G. Cherkashinin conducted the XPS experiments and analyzed the data and assisted in the interpretation. G. Melinte performed the (S)TEM investigation. S. Indris carried out the MAS NMR spectroscopy experiments. The XAS experiments were carried out by Y. Hu and J. Lin analyzed the data. The main part of first draft was written by F. Strauss, while the experiment and data analysis were mainly performed by J. Lin. J. Lin supported writing of the publication. The final paper was then edited by all co-authors.

RESEARCH ARTICLE

NANO · MICRO small
www.small-journal.com

Synthetic Tailoring of Ionic Conductivity in Multicationic Substituted, High-Entropy Lithium Argyrodite Solid Electrolytes

Jing Lin, Mareen Schaller, Gennady Cherkashinin, Sylvio Indris, Jianxuan Du, Clemens Ritter, Aleksandr Kondrakov, Jürgen Janek, Torsten Brezesinski, and Florian Strauss**

Superionic conductors are key components of solid-state batteries (SSBs). Multicomponent or high-entropy materials, offering a vast compositional space for tailoring properties, have recently attracted attention as novel solid electrolytes (SEs). However, the influence of synthetic parameters on ionic conductivity in compositionally complex SEs has not yet been investigated. Herein, the effect of cooling rate after high-temperature annealing on charge transport in the multicationic substituted lithium argyrodite $Li_{6.5}[P_{0.25}Si_{0.25}Ge_{0.25}Sb_{0.25}]S_5I$ is reported. It is demonstrated that a room-temperature ionic conductivity of ~12 mS cm^{-1} can be achieved upon cooling at a moderate rate, superior to that of fast- and slow-cooled samples. To rationalize the findings, the material is probed using powder diffraction, nuclear magnetic resonance and X-ray photoelectron spectroscopy combined with electrochemical methods. In the case of moderate cooling rate, favorable structural (bulk) and compositional (surface) characteristics for lithium diffusion evolve. $Li_{6.5}[P_{0.25}Si_{0.25}Ge_{0.25}Sb_{0.25}]S_5I$ is also electrochemically tested in pellet-type SSBs with a layered Ni-rich oxide cathode. Although delivering larger specific capacities than Li_6PS_5Cl-based cells at high current rates, the lower (electro)chemical stability of the high-entropy Li-ion conductor led to pronounced capacity fading. The research data indicate that subtle changes in bulk structure and surface composition strongly affect the electrical conductivity of high-entropy lithium argyrodites.

1. Introduction

Increasing demands for fast charging, high-energy-density rechargeable batteries have pushed academic and industrial research towards solid-state battery (SSB) design.[1,2] From a materials perspective, this is pursued through the development of improved cathode, anode and solid electrolyte (SE) materials.[3,4] Apart from the challenge of utilizing lithium-metal anodes and designing a stable interface between the cathode active material (CAM) and the superionic SE, a key requirement for achieving advanced SSBs is the use of (electro)chemically stable and mechanically soft ion conductors. In this regard, lithium thiophosphates represent a major class of promising SEs, as they offer high ionic conductivities and are mechanically soft. The latter allows for intimate contact with the active electrode material(s), which in turn helps reducing detrimental (chemo)mechanical effects during cell cycling.[5–7]

Particularly lithium argyrodites with the general formula Li_6PS_5X (with X = Cl, Br or

J. Lin, J. Du, A. Kondrakov, J. Janek, T. Brezesinski, F. Strauss
Battery and Electrochemistry Laboratory (BELLA)
Institute of Nanotechnology (INT)
Karlsruhe Institute of Technology (KIT)
Hermann-von-Helmholtz-Platz 1
76344 Eggenstein-Leopoldshafen, Germany
E-mail: torsten.brezesinski@kit.edu; florian.strauss@kit.edu

M. Schaller, S. Indris
Institute for Applied Materials–Energy Storage Systems (IAM-ESS)
Karlsruhe Institute of Technology (KIT)
Hermann-von-Helmholtz-Platz 1
76344 Eggenstein-Leopoldshafen, Germany

G. Cherkashinin
Advanced Thin Film Technology
Institute of Materials Science
Technical University of Darmstadt
Alarich-Weiss Str. 2, 64287 Darmstadt, Germany

C. Ritter
Institut Laue-Langevin
Grenoble Cedex 9 38042, France

A. Kondrakov
BASF SE
Carl-Bosch-Str. 38, 67056 Ludwigshafen, Germany

The ORCID identification number(s) for the author(s) of this article can be found under https://doi.org/10.1002/smll.202306832

DOI: 10.1002/smll.202306832

ADVANCED SCIENCE NEWS
www.advancedsciencenews.com

NANO · MICRO small
www.small-journal.com

I) were subject of intense SE development. Over the years, their ionic conductivity could be increased beyond 10 mS cm^{-1} through substitution on the P and/or X site.[8–13] Substitutions typically increase the S^{2-}/X^{-} site inversion and/or modify the lithium sublattice, which can lead to high ion mobility.[10,12,14,15] Apart from improving ionic conductivity in crystalline solids by iso- or aliovalent substitutions in the host lattice,[14–17] the temperature profile used in the solid-state synthesis, i.e., the annealing temperature and especially the cooling rate, can also have a profound effect on the resulting charge-transport properties. For instance, fast cooling via immersing the sample in liquid nitrogen immediately after annealing can stabilize high-temperature polymorphs or point defects at room temperature[18–24] or freeze the S^{2-}/X^{-} site inversion in the case of Li_6PS_5Br and $Li_{5.5}PS_{4.5}Cl_{1.5}$ (possibly leading to enhanced conductivity).[25–27] When it comes to high-entropy (compositionally complex) lithium-ion conductors, the effect of annealing temperature and cooling rate in general has not yet been thoroughly investigated.

For high-entropy materials (HEMs), which are characterized by a $\Delta S_{conf} > 1.5R$ (with ΔS_{conf} representing the configurational entropy), the emergence of new and/or improved properties has been reported.[28–30] Various HEMs including oxides, sulfides and carbides have been synthesized and employed, among others, as battery materials, catalysts or thermoelectrics.[31,32] Recently, this concept has been transferred to ceramic ion conductors, and some promising materials crystallizing in garnet, rock salt or Na SuperIonic CONDuctor (NASICON)-type structures have been reported.[33–37] However, their (electro)chemical assessment is sparse, and very high ionic conductivities could so far only be achieved for multicationic and -anionic substituted sulfide-based SEs.[36,38,39] Depending on the elemental composition, the entropy contribution may compete with (destabilizing) positive mixing enthalpies ΔH_{mix}. This is particularly critical at low temperatures. While a uniform solid solution may be achieved at elevated temperatures during synthesis, the entropy term may become too small during cooling, leading to demixing depending on the cooling conditions. Whether demixing has a negative effect on ionic conductivity is unclear, and it surely depends on the type of demixing, i.e., if spinodal decomposition occurs or nucleation is required during the demixing process.

In view of these considerations, herein we report on the investigation into how the temperature profile, in particular the cooling rate after high-temperature annealing, affects the ionic conductivity in a multicationic substituted (high-entropy) lithium argyrodite. We demonstrate that altering the cooling rate in the synthesis of $Li_{6.5}[P_{0.25}Si_{0.25}Ge_{0.25}Sb_{0.25}]S_5I$ has indeed a profound effect on conductivity. We find that the maximum ionic conductivity is achieved when the sample is cooled at a moderate rate. Using a combination of structure and charge-transport characterization techniques, the crystalline lattice is found to be relatively robust against different cooling rates, however it exhibits unique characteristics that enable high ionic conductivity. In addition, X-ray photoelectron spectroscopy (XPS) revealed a surface composition that deviates from the original stoichiometry but appears to be beneficial for charge transport. Finally, the as-synthesized SE was tested in pelletized SSBs and compared to the commonly used argyrodite Li_6PS_5Cl. Because of the much higher ionic conductivity of the high-entropy material, larger cell capacities were obtained, especially at high C-rates. Yet, the lower (electro)chemical stability of $Li_{6.5}[P_{0.25}Si_{0.25}Ge_{0.25}Sb_{0.25}]S_5I$ than Li_6PS_5Cl led to a stronger capacity decay during cycling.

2. Results and Discussion

Inorganic superionic conductors consisting of a compositionally complex rigid host structure and a defective lithium sublattice (with mobile ions) may be highly sensitive to the synthesis procedure, i.e., annealing temperature and cooling rate. Regarding the synthesis of lithium argyrodites, temperatures ranging from ≈300 to 550 °C with dwell times ranging from a few hours to days are usually applied in the annealing step. However, incorporating a high-energy milling step prior to heating can strongly reduce the required annealing time and induce crystallization, and is even more crucial in the case of compositionally complex materials for ensuring uniform mixing of precursors/elements. Here, stoichiometric amounts of precursors were mixed by ball milling at a relatively low speed, and differential scanning calorimetry (DSC) measurements were performed to reveal potential crystallization and decomposition temperatures (Figure S1a, Supporting Information). Based on the DSC results, three different annealing temperatures, namely 400, 500 and 550 °C, were tested. The corresponding X-ray diffraction (XRD) patterns indicated that 500 °C leads to negligible Li_2S and LiI impurity phase formation (Figure S1b,c, Supporting Information). Moreover, the material obtained at 500 °C exhibited the highest room-temperature ionic conductivity (in cold-pressed state) among the different samples (10.7 mS cm^{-1}, see Table S1, Supporting Information). Therefore, an annealing temperature of 500 °C was selected for any further experiments.

A schematic presentation of the synthesis protocol used and the respective temperature profile are depicted in **Figure 1**a. After the first precursor mixing step (1 h at 250 rpm), the milling speed was increased to 450 rpm, and milling was continued for another 10 h. Subsequently, the recovered powder was pelletized, annealed for 10 h and thereafter cooled at three different rates, namely fast cooling via quenching in liquid nitrogen, moderate (medium) cooling over a time of ≈1.5 h (5 °C min^{-1}) and slow cooling over ≈48 h (10 °C h^{-1}), which is referred to as Q, MC and SC, respectively, hereafter. As can be seen from the XRD patterns in Figure 1b, the high-energy milling step already induced crystallization of the argyrodite phase. This is commonly observed in the literature for non-high-entropy lithium argyrodites.[40–42] A small crystallite size can be expected considering the broad reflections. To improve crystallinity of the material, pelletized samples were annealed in vacuum-sealed quartz ampules for 10 h at 500 °C. At first glance, no major differences in the patterns were noticed (Figure 1b). To probe the crystal structure, the samples were subjected to high-resolution neutron powder diffraction (NPD) at 298 and 10 K (to minimize atomic displacement), followed by Rietveld refinement analysis.

J. Janek
Institute of Physical Chemistry & Center for Materials Research (ZfM/LaMa)
Justus-Liebig-University Giessen
Heinrich-Buff-Ring 17, 35392 Giessen, Germany

ADVANCED SCIENCE NEWS
www.advancedsciencenews.com

NANO · MICRO small
www.small-journal.com

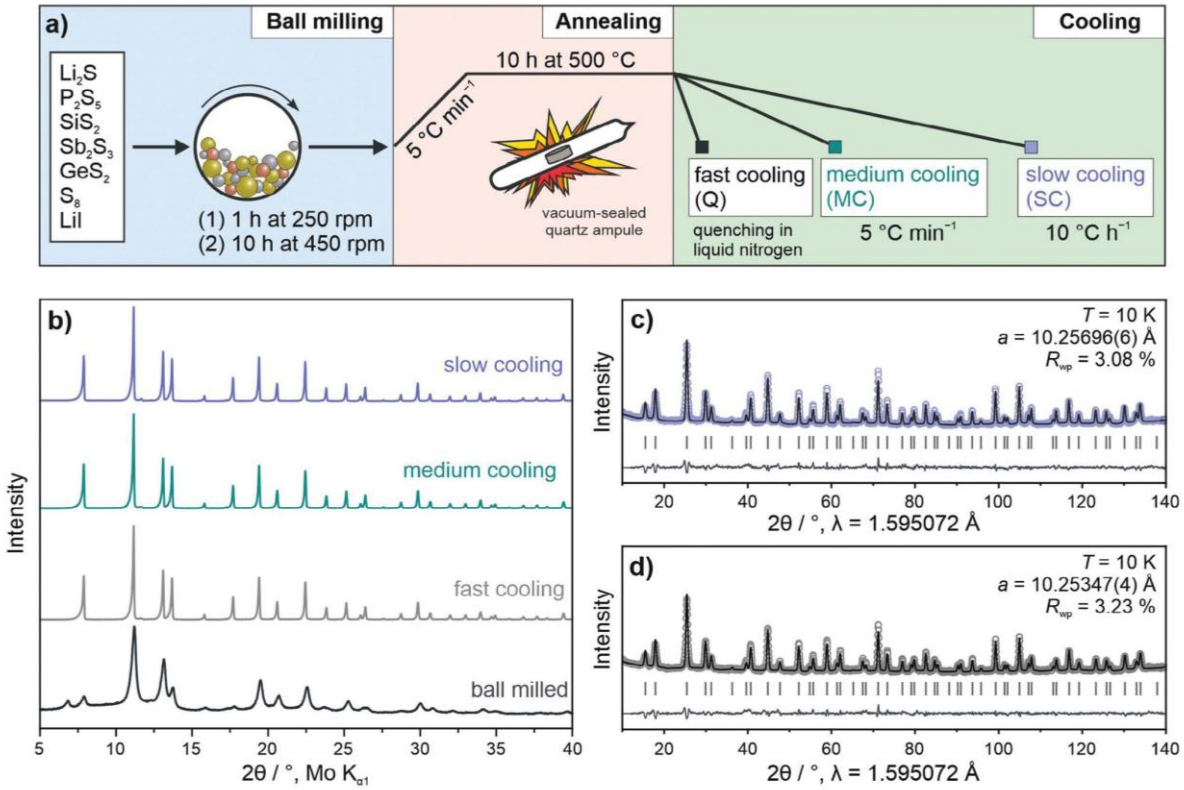

Figure 1. Synthesis and structural characterization of $Li_{6.5}[P_{0.25}Si_{0.25}Ge_{0.25}Sb_{0.25}]S_5I$. a) Schematic illustration of the synthesis pathway including milling and annealing, followed by one of the three chosen cooling rates. b) XRD patterns for the ball-milled precursor mixture and samples prepared with different cooling rates. c,d) NPD patterns and corresponding Rietveld plots at $T = 10$ K for slow- and fast-cooled samples. The open circles and black and gray lines represent the observed, calculated and difference profiles, respectively. Expected Bragg reflections are indicated by vertical ticks.

The Rietveld profiles for the Q and SC samples measured at $T = 10$ K are exemplarily shown in Figure 1c,d. The patterns could be indexed in the $F\bar{4}3m$ space group with very similar lattice parameter of $a = 10.25696(6)$ Å (SC) and 10.25347(4) Å (Q) ($a = 10.24932(5)$ Å for the MC sample, see Table S2, Supporting Information). The structural parameters from Rietveld analysis are given in Table S3–S6 (Supporting Information) and ref. [36].

The calculated crystal structure of $Li_{6.5}[P_{0.25}Si_{0.25}Ge_{0.25}Sb_{0.25}]S_5I$ is depicted in **Figure 2**a. The S^{2-} and I^- ions form a face-centered cubic anion sublattice (Wyckoff positions 4*a* and 4*d*), and in addition, S^{2-} ions are located in half of the tetrahedral voids (16*e*) around the multicationic substituted octahedral sites (4*b*), forming $[P_{0.25}Si_{0.25}Ge_{0.25}Sb_{0.25}]S_4^{3.5-}$ polyanions. In fact, such mixed polyanions constitute a combination of individual $[PS_4]^{3-}$, $[SiS_4]^{4-}$, $[GeS_4]^{4-}$ and $[SbS_4]^{3-}$ species, which are evenly

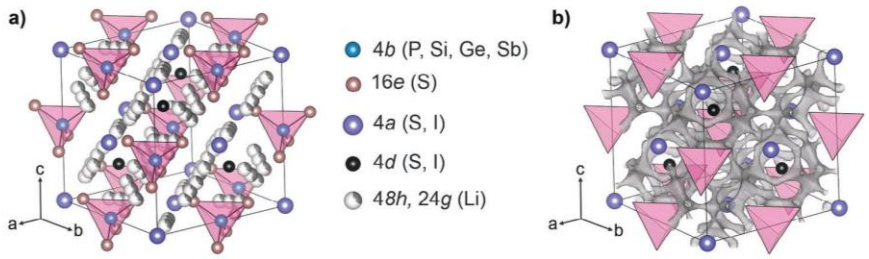

Figure 2. Crystal structure of $Li_{6.5}[P_{0.25}Si_{0.25}Ge_{0.25}Sb_{0.25}]S_5I$. a) Schematic view with the different Wyckoff positions and their elemental constituents indicated in the legend on the right. b) Bond-valence energy landscape revealing the 3D lithium diffusion pathways (gray trajectories). For clarity, only atoms on the 4*a* and 4*d* sites are shown. $[P_{0.25}Si_{0.25}Ge_{0.25}Sb_{0.25}]S_4^{3.5-}$ polyanions are depicted as pink tetrahedra.

ADVANCED SCIENCE NEWS
www.advancedsciencenews.com

NANO · MICRO small
www.small-journal.com

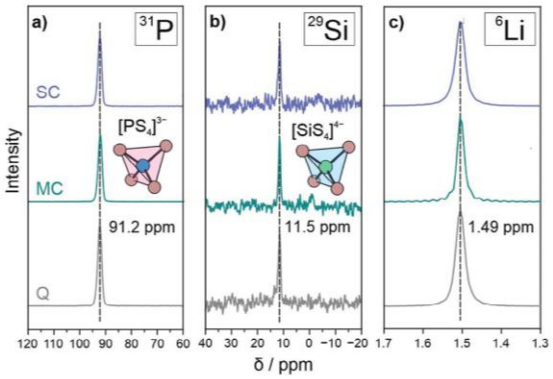

Figure 3. Sulfide-based tetrahedral polyanions revealed by MAS NMR spectroscopy. a) ^{31}P, b) ^{29}Si and c) ^{6}Li spectra collected from the $Li_{6.5}[P_{0.25}Si_{0.25}Ge_{0.25}Sb_{0.25}]S_5I$ samples prepared with different cooling rates (Q, MC and SC refer to fast, medium and slow cooling, respectively).

distributed throughout the lattice. Moreover, in the argyrodite structure, S^{2-} (4*d*) and I^- (4*a*) anions are known to mix over the respective Wyckoff positions (S^{2-}/X^- site inversion). We found a site inversion of ≈13% for the Q and SC samples, compared to 12% for the MC sample, among the highest values reported in the literature for S^{2-}/I^- mixing. Analysis of the NPD data also provided detailed structural information on the lithium sublattice. The Li atoms usually form Frank-Kasper polyhedra around the 4*d* site, expressed in two Wyckoff positions, namely 48*h* and 24*g*,[8] thereby producing 3D lithium diffusion pathways (Figure 2b). For the Q sample, it was found that 70 and 30% of Li is located on 48*h* and 24*g*, respectively, at room temperature. Upon reducing the cooling rate, the Li occupancy on the 48*h* site is lowered to 62 and 60% for MC and SC, respectively (Figure S2a, Supporting Information). We note that the occupancies remained virtually unaltered at 10 K. Surprisingly, a slight increase in Li situated on the 24*g* site was observed with decreasing cooling rate, which can be regarded as an intermediate/transition site. Therefore, the opposite trend might be expected, meaning quenching the sample should lead to increased Li occupancy on 24*g*. This counterintuitive finding seems to be a result of the large lattice distortions prevailing in high-entropy lithium argyrodites. The slightly varying Li occupancies also led to somewhat different Li-Li jump distances, with the intercage jump distance being an important structural parameter in determining the long-range lithium-diffusion characteristics (Figure S2b, Supporting Information). At room temperature, this distance was smallest for the MC sample [3.24(2) Å, compared to 3.28(3) and 3.25(3) Å for Q and SC, respectively, see Table S7, Supporting Information). Naturally, all Li-Li distances were lower upon cooling to 10 K.

To further corroborate the presence of $[PS_4]^{3-}$ and $[SiS_4]^{4-}$ tetrahedra within the $Li_{6.5}[P_{0.25}Si_{0.25}Ge_{0.25}Sb_{0.25}]S_5I$ structure and reveal the presence of potential amorphous impurities (invisible from diffraction data), ^{31}P, ^{29}Si and ^{6}Li magic-angle spinning (MAS) nuclear magnetic resonance (NMR) spectroscopy measurements were carried out. The respective spectra are shown in **Figure 3**. A distinct peaks at 91.2 ppm was observed for ^{31}P for all samples (Figure 3a), indicative of phosphorus being in a $[PS_4]^{3-}$ (tetrahedral) environment and consistent with the chemical shift found for other lithium thiophosphates.[35,36,43–45] It should be noted that, compared to Li_6PS_5I, the ^{31}P signal was shifted by ≈5 ppm, which is probably due to the unique chemical environment around the $[P_{0.25}Si_{0.25}Ge_{0.25}Sb_{0.25}]S_4^{3.5-}$ tetrahedra.[8] Regarding the ^{29}Si signal, a distinct peak located at 11.5 ppm was observed in all cases (Figure 3b), evidencing the presence of $[SiS_4]^{4-}$ species, in agreement with literature results.[36,43] In the ^{6}Li MAS NMR data (Figure 3c), a peak at 1.49 ppm appeared, similar to other lithium argyrodites.[9,45,46] Overall, comparable spectra with no signs of impurity contributions were obtained for the samples prepared with different cooling rates. This again demonstrates the minor effect that cooling rate has on the average/local crystal structure and further verifies the robustness of the high-entropy argyrodite lattice.

The local structure of the $[GeS_4]^{4-}$ tetrahedra was studied by Ge K-edge transmission X-ray absorption spectroscopy (XAS) measurements conducted on the MC sample and a GeS_2 reference material. Extended X-ray absorption fine structure (EXAFS) spectra [k^2-weighted $\chi(k)$] and the corresponding magnitudes of the Fourier transform are shown in Figure S3a–c (Supporting Information). The $|\chi(R)|$ peak for both the $Li_{6.5}[P_{0.25}Si_{0.25}Ge_{0.25}Sb_{0.25}]S_5I$ and GeS_2 is located at $R \approx$ 1.65 Å, indicating the presence of $[GeS_4]^{4-}$ tetrahedra.[47]

To gain information on the oxidation state of the elements and possible differences in near-surface composition, XPS measurements were carried out. The respective binding energies from curve fitting are given in Table S8 (Supporting Information). For the Sb 3d core-level region, only the $3d_{5/2}$ components are shown (**Figure 4**a–c) due to the large spin-orbit splitting (≈9.3 eV). For all samples, the Sb $3d_{5/2}$ spectrum is superimposed by the O 1s signal at a binding energy of ≈532 eV. The asymmetry of the Sb $3d_{5/2}$ line indicates two different oxidation states, with peaks centered at 530.3 and 529.4 eV. They can be assigned to Sb^{5+} and Sb^{3+}, respectively, in a Sb-S chemical environment, originating from the presence of $[SbS_4]^{3-}$ structural motifs and Sb^{3+} surface impurities.[36,48–50] The asymmetric O 1s line also points toward at least two chemical states, which can most likely be attributed to oxygenated Si, Sb, P and/or Ge. However, clear assignment is challenging. The S 2p detail spectra are depicted in Figure 4d–f, with the main contribution at 161.4 eV evidencing the presence of sulfide species, in agreement with literature data.[36,51–53] In addition, a minor S 2p component is evident at 163.5 eV, which is usually ascribed to polysulfide impurities.[54] Figure 4g–i shows the P 2p core-level region, revealing a doublet peak at 132.2 eV for all samples characteristic of the $[PS_4]^{3-}$ units.[36,51,55,56] The Si 2p data are centered at ≈101 eV, and again, they are virtually identical for the different samples (Figure 4j–l). The major component can be assigned to $[SiS_4]^{4-}$, in agreement with reports available in the literature,[57,58] while the minor component at 102.6 eV lies in between the binding energies usually detected for $[SiS_4]^{4-}$ and SiO_2. It can thus be correlated with partially oxygenated SiO_x surface impurities.[36,57–60] The I 4d region (≈2.0 eV spin-orbit splitting) is depicted in Figure 4m–o. The presence of I^- is apparent from the characteristic contributions, with the major one at ≈49 eV and the minor one centered ≈0.5 eV higher in binding energy. It has been hypothesized that these contributions stem from two different crystallographic environments in the structure (4*a* and 4*d* sites).[36] The Ge 3d and

ADVANCED SCIENCE NEWS
www.advancedsciencenews.com

NANO · MICRO small
www.small-journal.com

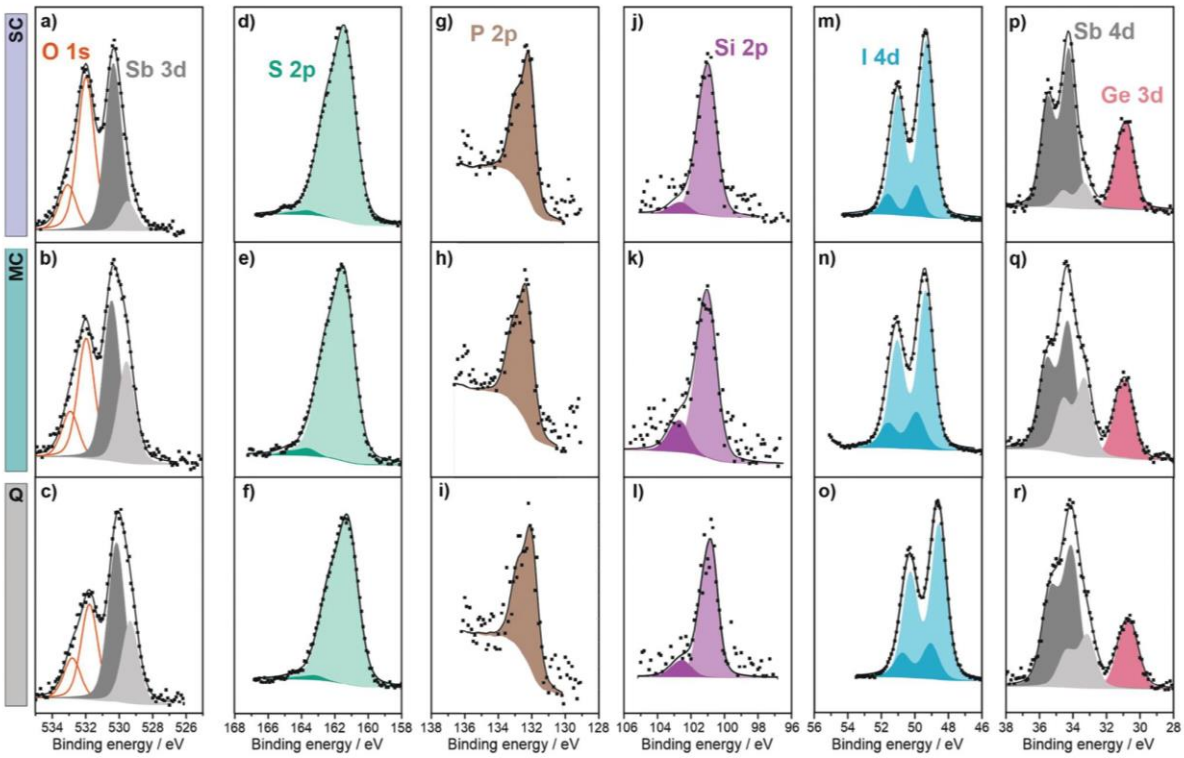

Figure 4. Effect of cooling rate on surface composition of $Li_{6.5}[P_{0.25}Si_{0.25}Ge_{0.25}Sb_{0.25}]S_5I$ probed using XPS. High-resolution a–c) Sb $3d_{5/2}$ and O 1s, d–f) S 2p, g–i) P 2p, j–l) Si 2p, m–o) I 4d and p–r) Sb 4d and Ge 3d photoelectron spectra collected from samples prepared with different cooling rates (Q, MC and SC refer to fast, medium and slow cooling, respectively). Black dots and solid lines represent the experimental data and curve-fitting results, respectively.

Sb 4d regions are shown in Figure 4p–r. The Sb 4d peaks comprise two contributions, at ≈34.3 and 33.2 eV, confirming the presence of Sb^{5+} and Sb^{3+}, respectively, at the near-surface regions of the samples. In addition, the Ge 3d spectra (≈30.8 eV) seem to indicate the presence of a single component (corresponding to $[GeS_4]^{4-}$).[48,61] Taken together, the spectra collected from the samples prepared with different cooling rates were found to be very similar for the S 2p, P 2p, I 4d and Ge 3d core levels. However, the data also revealed increased Sb^{3+} (contribution at 529.4 eV) and SiO_x (contribution at 102.6 eV) contents for the MC sample.

To visualize the complex surface composition of $Li_{6.5}[P_{0.25}Si_{0.25}Ge_{0.25}Sb_{0.25}]S_5I$, scanning transmission electron microscopy (STEM) imaging combined with energy-dispersive X-ray spectroscopy (EDX) was used. As shown in **Figure 5**, particles in the micrometer size range were observed. The corresponding elemental maps revealed uniform distributions on the nanoscale. As expected, oxygen was also found on the particle surface, in agreement with the oxygenated species detected by XPS (see Figure 4a–c,j–l). According to quantitative XPS analysis, the concentration of surface oxygen was much lower than that of sulfur (Table S9, Supporting Information). However,

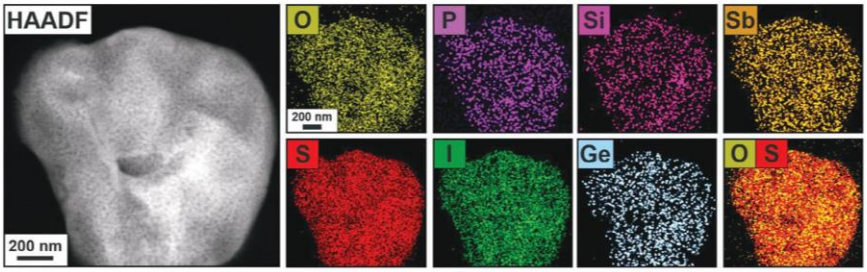

Figure 5. Results from STEM-EDX imaging/mapping. A representative high-angle annular dark field (HAADF) image and corresponding elemental maps from EDX are shown.

ADVANCED SCIENCE NEWS
www.advancedsciencenews.com

NANO · MICRO small
www.small-journal.com

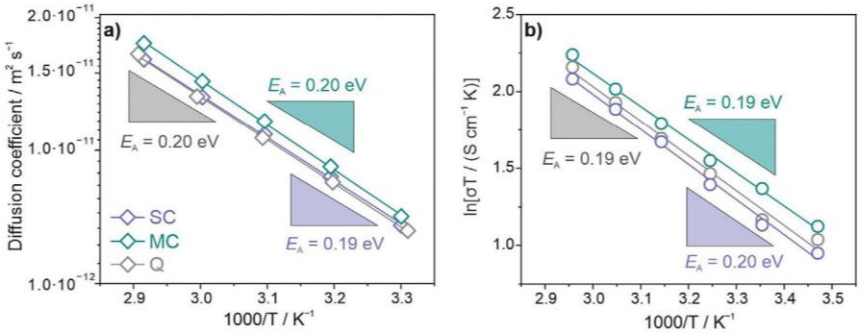

Figure 6. Charge-transport properties of $Li_{6.5}[P_{0.25}Si_{0.25}Ge_{0.25}Sb_{0.25}]S_5I$ determined by a) ^{7}Li PFG NMR spectroscopy and b) EIS. a) Arrhenius plot of the diffusion coefficient and b) conductivity versus reciprocal temperature for the samples prepared with different cooling rates. The activation energies are indicated. If error bars are not visible, the standard deviation is smaller than the symbol.

when the cooling rate was very low, a slight increase in oxygen content was noticed (for the SC sample). Overall, the oxygen signals from XPS and STEM-EDX can be clearly assigned to surface impurity formation, despite the fact that the materials were strictly handled under inert atmosphere.

After having revealed similar bulk and surface structural characteristics for the $Li_{6.5}[P_{0.25}Si_{0.25}Ge_{0.25}Sb_{0.25}]S_5I$ prepared with different cooling rates, the Li-ion dynamics were probed in the temperature range of 30–70 °C using ^{7}Li pulsed field gradient (PFG) NMR spectroscopy (Figure S4, Supporting Information). In so doing, diffusion coefficients of $D_{Li} = 6.58{\cdot}10^{-12}$ m^2 s^{-1} (Q), $7.09{\cdot}10^{-12}$ m^2 s^{-1} (MC) and $6.77{\cdot}10^{-12}$ m^2 s^{-1} (SC) were determined at 30 °C, which are on the same order of magnitude to that of other highly conducting lithium thiophosphates.[9,36,45,46,62,63] Arrhenius plots of diffusivity against reciprocal temperature are shown in **Figure 6**a. Virtually identical activation energies of E_A = 0.20, 0.20 and 0.19 eV were determined from the slopes (assuming Arrhenius-type temperature dependence) for Q, MC and SC, respectively.

The electrical conductivities were determined by electrochemical impedance spectroscopy (EIS) measurements conducted on sintered pellets with ion-blocking electrodes between 15 and 65 °C. The corresponding Nyquist plots of the electrochemical impedance only revealed a capacitive tail, indicating high ionic conductivity (Figure S5, Supporting Information). Room-temperature conductivities of 11.9 (±0.39), 12.3 (±0.70) and 11.0 (±0.57) mS cm^{-1} were calculated for Q, MC and SC, respectively, and very similar activation energies of E_A = 0.19 (Q), 0.19 (MC) and 0.20 eV (SC) were determined from the corresponding Arrhenius plots (Figure 6b). As can be seen, they agree well with the ^{7}Li PFG NMR results.

Using the Nernst-Einstein equation, the ionic conductivities were also estimated from the diffusion coefficients. A summary of the EIS and ^{7}Li PFG NMR results is given in **Table 1** and further depicted in **Figure 7**a. From the data, it is evident that the ionic conductivities determined by ^{7}Li PFG NMR are lower by ≈2 mS cm^{-1}. This difference between EIS and ^{7}Li PFG NMR is presumably rooted in the contribution of (favorable) grain-boundary conduction, as EIS probes the overall specimen conductivity unlike ^{7}Li PFG NMR (only bulk transport properties are probed). However, a similar trend in conductivity with cooling rate is apparent from both techniques. This means that the conductivity of $Li_{6.5}[P_{0.25}Si_{0.25}Ge_{0.25}Sb_{0.25}]S_5I$ (MC) is indeed higher than that of the Q and SC samples. No significant influence of the cooling rate on activation energy was found.

Table 1. Summary of the Li-ion conductivities (σ_{ion}) at T = 298 K and corresponding activation energies (E_A) from temperature-dependent EIS and ^{7}Li PFG NMR spectroscopy measurements..

Sample	σ_{ion} / mS cm^{-1} [EIS]	E_A / eV [EIS]	σ_{ion} / mS cm^{-1} [PFG NMR]	E_A / eV [PFG NMR]
Quenching (Q)	11.9 ± 0.39	0.19 ± 0.01	9.12 ± 0.05	0.20 ± 0.01
Medium cooling (MC)	12.3 ± 0.70	0.19 ± 0.01	10.9 ± 0.04	0.20 ± 0.01
Slow cooling (SC)	11.0 ± 0.57	0.20 ± 0.01	9.12 ± 0.05	0.19 ± 0.01

To further assess the transport properties of the $Li_{6.5}[P_{0.25}Si_{0.25}Ge_{0.25}Sb_{0.25}]S_5I$ samples, their electronic conductivity was determined by DC polarization measurements to be $3.83{\cdot}10^{-5}$, $3.18{\cdot}10^{-7}$ and $1.23{\cdot}10^{-5}$ S cm^{-1} for Q, MC and SC, respectively. Interestingly, MC was found to exhibit two orders of magnitude lower electronic conductivity than the Q and SC samples (Figure 7b). We assume that this is related to the surface composition and presence of impurities. The fact that the electronic conductivity is orders of magnitude higher than that of other Li-ion conductors seems to be due, in part, to the intrinsic properties of high-entropy lithium argyrodites.[9,46,64]

SSBs with lithium thiophosphate SEs typically make use of cold-pressed materials. For that reason, the conductivity of the different samples was also determined in a cold-pressed state. As expected, the resulting ionic conductivities were somewhat lower than those of sintered pellets. Nevertheless, high room-temperature conductivities of 7.4 (±0.4), 10.9 (±0.25) and 5.5 (±0.15) mS cm^{-1} were found by EIS for Q, MC and SC, respectively, following a similar trend to the sintered pellets (Figure 7b). As mentioned above, this means that the MC sample indeed shows superior ionic conductivity over Q and SC and sintering helps to achieve better grain contact, thereby minimizing grain-boundary contributions.

ADVANCED SCIENCE NEWS
www.advancedsciencenews.com

NANO · MICRO small
www.small-journal.com

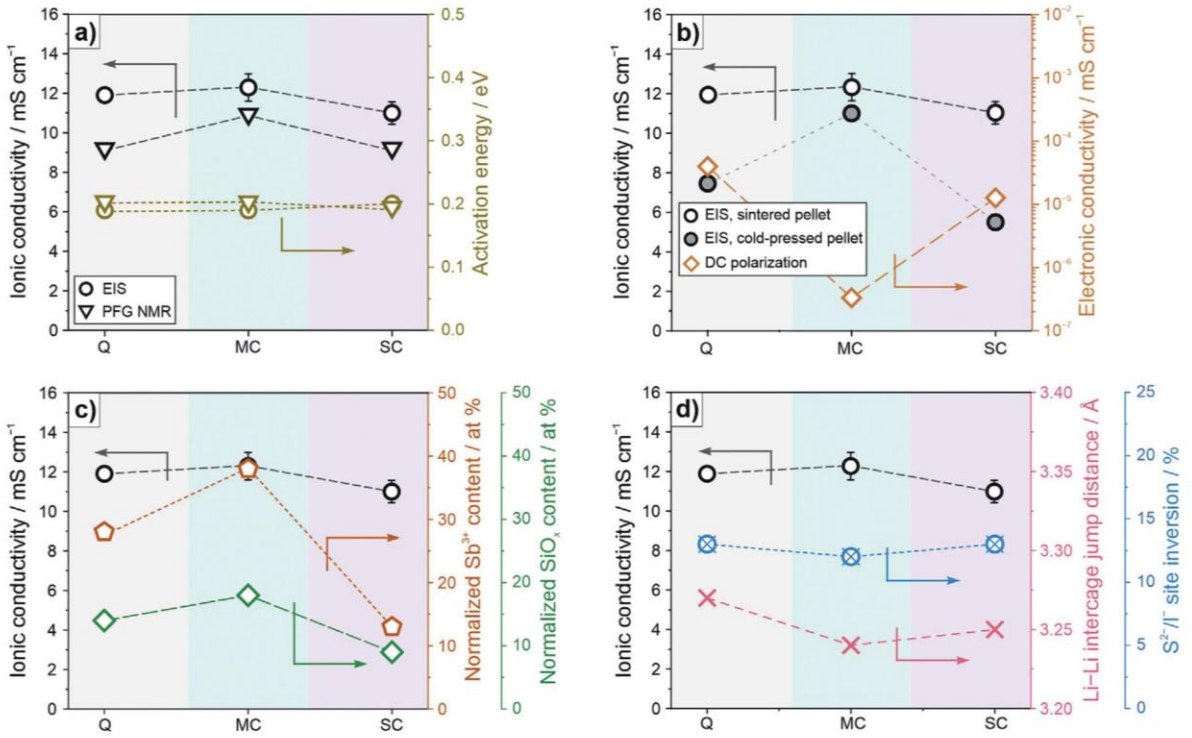

Figure 7. Bulk structure/surface composition-charge transport property relationships. a) Ionic conductivities and activation energies determined by EIS and ^{7}Li PFG NMR spectroscopy. b) Comparison of ionic conductivities measured on sintered and cold-pressed pellets and electronic conductivities determined from DC polarization measurements (on sintered pellets) for the $Li_{6.5}[P_{0.25}Si_{0.25}Ge_{0.25}Sb_{0.25}]S_5I$ samples prepared with different cooling rates. c) Normalized Sb^{3+} and SiO_x contents from XPS and d) Li-Li intercage jump distances and S^{2-}/I^{-} site inversions shown together with the ionic conductivities. If error bars are not visible, the standard deviation is smaller than the symbol. Dashed lines are for eye guidance only.

From a surface composition point of view, it is found that increasing amounts of Sb^{3+} and SiO_x species correlate with increasing ionic conductivity and decreasing electronic conductivity (Figure 7c). Hence, slight changes in surface composition apparently can exert a substantial impact on the conductivity of polycrystalline materials. In this regard, it is important to note that enhanced interfacial ion transport is a well-known phenomenon[65,66] and might play a role here as well. For example, Sb_2S_3 (with Sb^{3+}) is a poor electronic conductor,[67,68] which agrees with our finding that an increasing Sb^{3+} (surface) fraction leads a strong decrease in electronic conductivity. From a structural perspective, the short Li-Li intercage jump distances (Figure 7d), together with favorable surface/grain-boundary composition, are likely responsible for fast lithium transport in the MC sample. These results collectively show that, in addition to favorable bulk structural features, the surface composition strongly affects the overall ionic conductivity. However, little attention has been paid to this in the context of sulfide-based SEs up until now.

Finally, the electrochemical behavior of the best-conducting SE sample (MC) was tested in pellet-type SSBs with a $LiNbO_3$-coated $LiNi_{0.85}Co_{0.1}Mn_{0.05}O_2$ (NCM851005) cathode and an indium-lithium anode and compared to that of commercially available argyrodite Li_6PS_5Cl. Initially, the cells were cycled at a C/10 rate and 25 °C, followed by ex situ EIS measurements. For the $Li_{6.5}[P_{0.25}Si_{0.25}Ge_{0.25}Sb_{0.25}]S_5I$, first-cycle specific charge and discharge capacities of 237 and 182 mAh g^{-1} were achieved, which translates to 77% Coulomb efficiency (referred to as CE in the following, see **Figure 8**a). In the case of Li_6PS_5Cl, the cells delivered a lower charge but higher discharge capacity, with q_{ch} = 221 mAh g^{-1} and q_{dis} = 190 mAh g^{-1}, corresponding to a CE of 86%. The ≈10% difference in CE upon using the multi-component SE suggests a lower (electro)chemical stability compared to the Li_6PS_5Cl. However, the impedance spectra revealed a larger charge-transfer resistance for Li_6PS_5Cl (Figure 8b). Fitting of the data allowed determining the different contributions to the overall impedance (Figure S6, Supporting Information), namely bulk SE (R_{bulk}), SE grain boundary (R_{GB}), CAM/SE ($R_{CAM/SE}$) and anode/SE ($R_{anode/SE}$). The R_{GB} was found to be 15.5 Ω (12.2 Ω cm^2) for Li_6PS_5Cl and only 3.4 Ω (2.7 Ω cm^2) for $Li_{6.5}[P_{0.25}Si_{0.25}Ge_{0.25}Sb_{0.25}]S_5I$, presumably due to favorable grain-boundary conduction as discussed above. For the $R_{CAM/SE}$ and $R_{anode/SE}$, values of 78.9 Ω (61.9 Ω cm^2)/6.6 Ω (5.2 Ω cm^2) and 4.7 Ω (3.7 Ω cm^2)/27.1 Ω (21.3 Ω cm^2) were obtained for Li_6PS_5Cl and the high-entropy SE, respectively. Interestingly, the $R_{CAM/SE}$ showed the opposite trend to the first-cycle CE, which was significantly lower for $Li_{6.5}[P_{0.25}Si_{0.25}Ge_{0.25}Sb_{0.25}]S_5I$. We assume that, despite more severe degradation, the charge transport through

ADVANCED SCIENCE NEWS
www.advancedsciencenews.com

NANO · MICRO small
www.small-journal.com

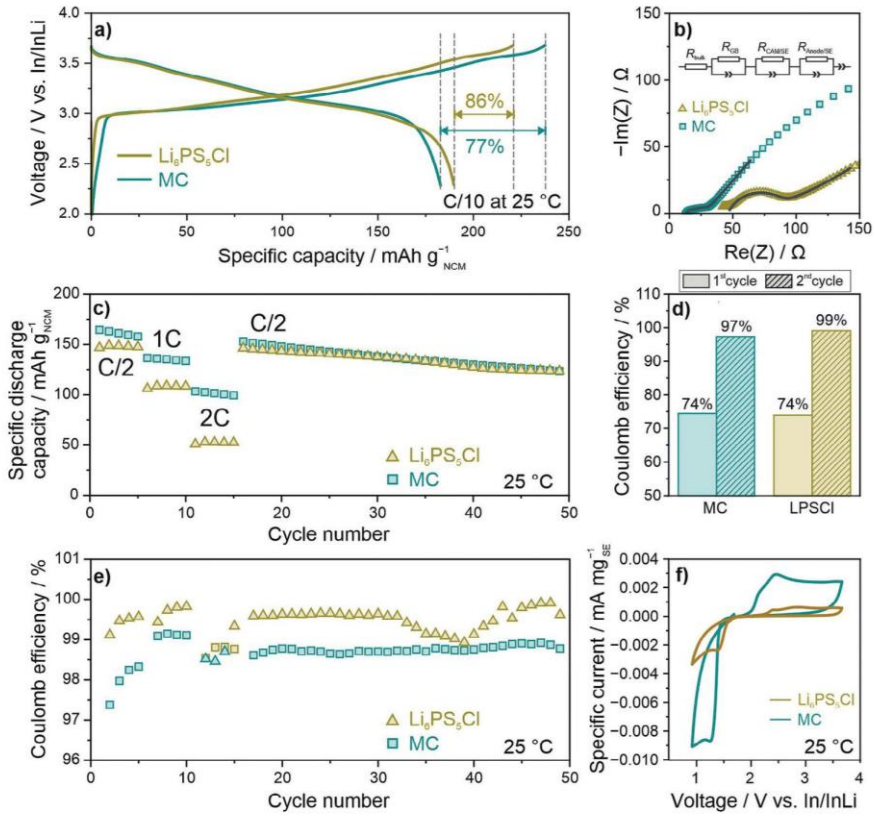

Figure 8. (Electro)chemical testing of bulk-type SSBs. a) Initial voltage profiles of cells containing either the $Li_{6.5}[P_{0.25}Si_{0.25}Ge_{0.25}Sb_{0.25}]S_5I$ (MC) or commercial argyrodite Li_6PS_5Cl SE at C/10 rate and 25 °C. b) Impedance spectra collected after the first cycle shown in a). c) Rate capability and long-term cycling performance. d) Coulomb efficiencies for the first two and e) following cycles. f) First-cycle CV curves for mixtures of SE and carbon black as working electrode. Data are averaged from two identical cells.

the cathode interface(s) is facilitated, which is directly reflected in the impedance spectra.

Next, the SSB cells were subjected to rate capability and long-term performance testing. To this end, the galvanostatic cycling was conducted at 25 °C and C-rates ranging from C/2 to 2C (Figure 8c; Figure S7a, Supporting Information). For $Li_{6.5}[P_{0.25}Si_{0.25}Ge_{0.25}Sb_{0.25}]S_5I$, first-cycle specific charge and discharge capacities of 226 and 168 mAh g^{-1} were achieved at C/2, corresponding to an initial CE of 74% (Figure 8d). In contrast, the Li_6PS_5Cl-based cells delivered lower capacities of $q_{ch} = 198$ mAh g^{-1} and $q_{dis} = 147$ mAh g^{-1}, leading to a similar CE of 74%. Notable is the large overpotential of the Li_6PS_5Cl-based cells (increased by ≈250 mV compared to the high-entropy SE, see differential capacity plots in Figure S7b, Supporting Information). This increase in overpotential is probably due to the lower room-temperature ionic conductivity of Li_6PS_5Cl (≈2 mS cm^{-1} versus 11–12 mS cm^{-1}). After five cycles, the C-rate was first increased to 1C and then to 2C. As can be seen from the data for the high-entropy SE, specific discharge capacities of ≈135 and 101 mAh g^{-1} were achieved at 1C and 2C, respectively. For Li_6PS_5Cl, the drop in discharge capacity with increasing current rate was much more pronounced, with q_{dis} ≈ 109 mAh g^{-1} at 1C and 53 mAh g^{-1} at 2C. This result can be explained by the significantly higher ionic conductivity of the high-entropy SE, which is capable of better accommodating high current densities (2C ≈ 4.4 mA cm^{-2}). Subsequently, the cells were cycled at C/2 and found to undergo virtually linear capacity decay, with q_{dis} ≈ 123 mAh g^{-1} in the 49th cycle, corresponding to an overall capacity loss of 27% and 16% (relative to the initial discharge capacity) for $Li_{6.5}[P_{0.25}Si_{0.25}Ge_{0.25}Sb_{0.25}]S_5I$ and Li_6PS_5Cl, respectively. This difference in capacity retention provides evidence for the lower electrochemical stability of the multicomponent SE, for which possible decomposition phases (interfacial degradation products) have recently been identified by XPS.[36] Although the initial CE (C/2 rate) was similar for both SEs tested, it was lower for the high-entropy material during subsequent cycling (Figure 8e). After an increase over the first five cycles, the CE stabilized below 99% for $Li_{6.5}[P_{0.25}Si_{0.25}Ge_{0.25}Sb_{0.25}]S_5I$ but above 99.5% for Li_6PS_5Cl, corroborating the above conclusions. This further implies that the as-formed decomposition interphase is kinetically unstable, leading to continuous SE degradation, which might be associated with the increased electronic conductivity. Interestingly, a bump in the CE data between cycles 30 and 40 was noticed for Li_6PS_5Cl, which is

ADVANCED SCIENCE NEWS
www.advancedsciencenews.com

NANO · MICRO small
www.small-journal.com

not mirrored in the specific discharge capacities in Figure 8c. This has repeatedly been reported in the literature and assigned to (chemo)mechanically-driven cell degradation.[51,69,70] However, in the case of the $Li_{6.5}[P_{0.25}Si_{0.25}Ge_{0.25}Sb_{0.25}]S_5I$, it did not occur, and we assume that this is because of the different softness of the SEs (Young's modulus). Note that increasing compositional complexity typically causes a lowering of the Young's modulus.[71]

To determine the (electro)chemical stability window of both materials and deconvolute anodic and cathodic stability issues, cyclic voltammetry (CV) measurements were conducted on mixtures of SE and carbon black as working electrode. Figure 8f shows the first-cycle CV curves, which reveal larger currents in the anodic and cathodic scans for $Li_{6.5}[P_{0.25}Si_{0.25}Ge_{0.25}Sb_{0.25}]S_5I$. This again confirms the lower stability of the high-entropy SE (exhibiting a relatively narrow electrochemical stability window). With further cycling (Figure S8, Supporting Information), a strong decrease in the absolute reductive (cathodic) current was noticed for both SEs, while the oxidative (anodic) current only changed marginally in the case of the high-entropy SE.

Overall, the CV data agree with the results from galvanostatic cycling, indicating the formation of a kinetically unstable decomposition interphase that does not effectively prevent SE degradation during battery operation.

3. Conclusion

In summary, we have examined the impact of the synthesis procedure, especially annealing temperature and cooling rate, on structure-charge transport property relationships in the multicationic substituted $Li_{6.5}[P_{0.25}Si_{0.25}Ge_{0.25}Sb_{0.25}]S_5I$ SE. As reported in the past for ceramic Li-ion conductors, the synthesis procedure/conditions may have a profound effect on ionic conductivity, however clear trends have yet to be established. In the case of Li_6PS_5Br, this has been attributed to increased S^{2-}/Br^- site inversion with fast sample cooling via quenching in liquid nitrogen, i.e., site-disorder freezing.[25–27] For the material studied in this work, we found that the cooling rate after a given high-temperature anneal indeed affects the ionic conductivity. For medium cooling, an increase in conductivity over fast- and slow-cooled samples was observed. To understand the origin of this result, the bulk crystal structure was probed using XRD and NPD in combination with MAS NMR spectroscopy. For the medium-cooled sample, the shortest Li-Li intercage jump distances and a high degree of S^{2-}/I^- site inversion (12-13%) were found. Apart from these for ion mobility favorable bulk structural characteristics, the surface composition was also investigated via XPS and STEM-EDX. Small differences among the samples were noticed, in particular the presence of increased amounts of Sb^{3+} and SiO_x surface impurities for the medium-cooled material. It can be assumed that the unique surface composition also affects, at least to some degree, the conductivity. Overall, it seems that the high ionic conductivity of the $Li_{6.5}[P_{0.25}Si_{0.25}Ge_{0.25}Sb_{0.25}]S_5I$ SE is mainly due to a combination of advantageous bulk and surface structural/compositional features. However, the bulk crystal structure was found to be less susceptible to temperature effects than the surface (composition). The findings further emphasize that classical synthetic approaches to optimize ionic conductivity in ceramic ion conductors may not be transferable to compositionally complex SEs.

Because of the high room-temperature ionic conductivity, the MC sample was also tested in pellet-type SSBs and the performance compared to that achieved with Li_6PS_5Cl. The high-entropy SE cells were capable of delivering larger specific discharge capacities at high current rates but suffered from more pronounced (electro)chemically-driven degradation, leading to faster performance decay. The data clearly demonstrate that the conductivity in lithium argyrodite SEs can be synthetically tailored, however their stability seems to be lower than that of Li_6PS_5Cl. This indicates that achieving high ionic conductivity is not the only challenge but other metrics, such as (electro)chemical stability and mechanical behavior, need to be considered too. Taken together, high-entropy SEs provide a vast compositional space that is not limited to sulfide-based materials, thereby maximizing the opportunity to improve several key performance indicators of SSBs by compositional design.

4. Experimental Section

General: If not stated otherwise, all work steps were performed under inert atmosphere, and the precursors were used as received.

Synthesis: A stoichiometric mixture of Li_2S (99.99%, Sigma-Aldrich), P_2S_5 (99%, Sigma-Aldrich), GeS_2 (99.9%, Goodfellow), SiS_2 (99.99%, Goodfellow), Sb_2S_3 (99.99%, Alfa Aesar) and LiI (99.999%, Sigma-Aldrich) plus 10 wt.% excess sulfur (99.99%, Sigma-Aldrich) was weighed into a 70 mL zirconia milling jar. Next, 20 zirconia milling balls with a diameter of 10 mm were added, and the mixture was milled for 1 h at 250 rpm, followed by 10 h at 450 rpm. The resulting powder was pressed into pellets (≈300 mg, 10 mm diameter) at 3 t and vacuum sealed in quartz ampules (10^{-3} bar). To avoid trace water, the ampules were dried at 500 °C using a heat gun under dynamic vacuum (10^{-3} bar) prior to use. The samples were then annealed at 500 °C for 10 h at a heating rate of 5 °C min^{-1} and cooled down at different rates: (1) Quenching in liquid N_2, (2) 5 °C min^{-1} or (3) 10 °C h^{-1}. During the initial survey of the optimal temperature, the samples were prepared as described above and annealed at 450, 500 or 550 °C for 10 h with heating and cooling rates set to 5 °C min^{-1}.

Differential Scanning Calorimetry: Measurements were performed at a heating rate of 5 °C min^{-1} using a NETZSCH DSC 204 F1 Phoenix. To this end, the samples were sealed in alumina crucibles under Ar atmosphere.

Laboratory X-ray Diffraction: The samples were sealed in borosilicate capillaries (0.68 mm inner diameter and 0.01 mm wall thickness, Hilgenberg) under Ar atmosphere and subjected to XRD analysis using a STOE Stadi-P diffractometer with a DECTRIS MYTHEN 1K strip detector in Debye-Scherrer geometry. The instrument utilizes a Mo anode to generate X-rays of wavelength $\lambda = 0.70926$ Å.

Neutron Powder Diffraction: For NPD, cylindrical vanadium containers of diameter 6 mm were filled with ≈2 g of sample. The measurements were performed at the D2B high-resolution powder diffractometer located at the Institut Laue-Langevin (ILL) using a wavelength of $\lambda = 1.595072$ Å at both $T = 10$ and 298 K. The diffraction data were analyzed via Rietveld refinement using the FullProf Suite software.[72] The peak shape was modeled using the Thompson-Cox-Hastings pseudo-Voigt function, and a point-by-point background was subtracted. The following parameters were refined one by one: Scale factor, peak shape parameters, lattice parameters, atomic coordinates, individual anisotropic atomic displacement parameters and lithium occupancies. The zero-shift parameter was refined last, and any occupancies that resulted in unreasonable values were disregarded. Finally, all parameters were refined simultaneously to ensure stability of the calculated crystal structure.

Magic-Angle Spinning Nuclear Magnetic Resonance Spectroscopy: A Bruker Avance 500 MHz spectrometer was used for MAS NMR spectroscopy measurements with a magnetic field strength of 11.7 T, corresponding to resonance frequencies of 73.6, 99.4 and 202.5 MHz for ^6Li, ^{29}Si and ^{31}P, respectively. The samples were inserted into 2.5 mm rotors

ADVANCED SCIENCE NEWS
www.advancedsciencenews.com

NANO · MICRO small
www.small-journal.com

under Ar atmosphere and subjected to spinning at a frequency of 30 kHz. The $\pi/2$ pulse length was 2.8 µs for ^{6}Li, 1.8 µs for ^{29}Si and 2.1 µs for ^{31}P, while the recycle delay was set to 30 s for ^{6}Li and 60 s for ^{29}Si/^{31}P. The chemical shifts are referenced to 1 M ^{6}LiCl for ^{6}Li, tetramethyl silane for ^{29}Si and H_3PO_4 (85%) for ^{31}P.

Transmission X-ray Absorption Spectroscopy: Measurements were performed on a laboratory device (easyXAFS300+, easy XAFS LLC, Renton, WA, USA) based on Rowland-circle geometries. Pelletized samples were prepared inside an Ar-filled glovebox. Appropriate amounts of the $Li_{6.5}[P_{0.25}Si_{0.25}Ge_{0.25}Sb_{0.25}]S_5I$ (MC) and reference GeS_2 were diluted with cellulose and then pressed into 10 mm diameter pellets, which were further sealed by Kapton tape before being taken out from the glovebox. The Ge K-edge absorption spectra were measured using a Ge(555) spherically bent crystal analyzer (SBCA) and an Ag X-ray tube. An energy step of 0.25 eV was used for the X-ray absorption near edge structure (XANES) region and a step of 0.05 Å^{-1} for the post-edge region (extended X-ray absorption fine structure, EXAFS). Multiple scans for each sample were performed to improve the signal-to-noise ratio and monitor the energy drift. The absorption spectra were calculated according to the transmission relation $\mu(E) \approx \ln(I_0/I_t)$ through a python-based software (easy XAFS LLC, Renton, WA, USA), which was also used for dead time correction. The reduced data were further processed and analyzed via the Demeter system.

X-ray Photoelectron Spectroscopy: XPS was applied to examine the differences in (surface) chemical composition of the different samples. The SE materials were transferred from the glovebox to the spectrometer (PHI 5000 VersaProbe equipped with a monochromatic Al K_α source, $h\nu$ = 1486.7 eV) without exposure to air. The diameter of the illuminated area was 200 µm. Photoelectrons were collected with a pass energy of E_{pass} = 23.5 eV at three different electron escape angles, namely 20, 45 and 90° with respect to the surface normal. Because the SEs are poor electronic conductors, a neutralizer equipped with both a low-voltage electron gun and a floating ion gun generating a low-energy ion beam was used to compensate for sample charging. The binding energies are referenced to the C 1s photoelectron line of the C—C bond (E_{bin} = 284.8 eV). Fitting of the spectra was done as detailed in the literature.[36]

Electrochemical Impedance Spectroscopy: To measure the conductivity, pellets made from ≈200 mg of ball-milled precursor mixture were compressed at 3 t for 3 min in a 10 mm pellet die. They were then vacuum-sealed in quartz ampules (10^{-3} mbar) and annealed for 10 h at 500 °C using the same synthetic procedure mentioned earlier. In electrodes (10 mm diameter) were attached on both sides of the pellets, and EIS was measured using a SP-200 potentiostat (BioLogic) with a 20 mV voltage amplitude from 0.1 Hz to 7 MHz. Spectra were collected in the temperature range from 15 to 65 °C after at least 1 h rest for equilibration. The conductivity was determined from the intercept with the *x*-axis, and the activation energy was calculated by linear fitting of the temperature-dependent conductivity using the Arrhenius equation. Residual porosity was not considered. For EIS on cold-pressed samples, ≈200 mg of powder was compressed in a customized setup with stainless steel dies and a PEEK sleeve (10 mm diameter) at 437 MPa for 3 min. A pressure of 250 MPa was maintained during the measurements.

DC Polarization: To determine the partial electronic conductivity, DC polarization measurements were performed at 25 °C by applying different voltages of 0.3, 0.4 and 0.5 V. Note that a similar setup as for EIS was used, and the measurements were conducted on sintered pellets. The resistance and the respective electronic conductivity were calculated from the steady-state current.

Temperature-Dependent Pulsed Field Gradient Nuclear Magnetic Resonance Spectroscopy: Temperature-dependent ^{7}Li PFG NMR measurements were performed on a Bruker Avance 300 MHz spectrometer. The samples were enclosed in an evacuated 5 mm borosilicate glass tube, and a PFG probe with maximum gradient field strength of 30 T m^{-1} was utilized. To suppress the effect of eddy currents, a stimulated-echo pulse sequence with bipolar gradients was employed.[73,74] Data were collected in the temperature range from 302 to 345 K. The $\pi/2$ pulse length was between 5.35 and 5.9 µs, and the recycle delay was 0.4–0.6 s. For all samples and temperatures, gradient duration and diffusion time was 3 and 30 ms, respectively.

Scanning Transmission Electron Microscopy: Specimen preparation was done under Ar atmosphere in a glovebox (using a direct dispersion of the dry powders), and transfer to the microscope was accomplished using a Gatan inert transfer holder. The measurements were performed at 300 kV on a Themis 300 electron microscope with a DCOR probe corrector and Super X EDX detector.

Electrode Preparation and Cell Assembly and Testing: For SSB cells, the cathode composite was prepared by mixing $LiNbO_3$-coated NCM851005 (85% Ni, BASF SE) with the $Li_{6.5}[P_{0.25}Si_{0.25}Ge_{0.25}Sb_{0.25}]S_5I$ (MC) or Li_6PS_5Cl SE (NEI Corp.) and Super C65 carbon black additive in a 69.3:29.7:1.0 weight ratio at 140 rpm for 30 min under Ar atmosphere using a 70 mL zirconia milling jar with 10 zirconia balls (10 mm diameter). The NCM851005 was heated for 2 h at 730 °C in O_2 flow to remove surface impurities, and the $LiNbO_3$ coating was prepared as reported in the literature.[75,76] The Super C65 carbon black was also dried at 300 °C in a dynamic vacuum overnight prior to use. For cell assembly, a customized setup with stainless steel dies and a PEEK sleeve (10 mm diameter) was used. First, ≈100 mg of SE was compacted at 62 MPa to form the SE separator layer. The cathode (≈13 mg) was then distributed onto the SE layer, and the stack was compressed at 437 MPa. Finally, an In anode (8 mm diameter, 125 µm thickness, Goodfellow) combined with a Li disc (3 mm diameter, 50 µm thickness, Albemarle) was attached to the other side of the separator layer. Galvanostatic testing was done at 25°C and under an external pressure of 81 MPa in the potential window of 2.28-3.68 V versus In/InLi (≈2.9-4.3 V versus Li^+/Li) after a resting period at open-circuit voltage (OCV) for 1 h using a MACCOR battery cycler. The C-rate was varied from 0.5 to 2.0C, with 1C = 190 mA $g_{NCM851005}^{-1}$.

Cyclic Voltammetry: SE and Super C65 carbon black were mixed at 140 rpm for 30 min under Ar atmosphere using a 70 mL zirconia milling jar with 10 zirconia balls (10 mm diameter). Cell assembly was done as described above, except that ≈13 mg of SE/Super C65 blend was used as working electrode (cathode). Scanning was done between 0.92 and 3.68 V versus In/InLi (≈1.54-4.3 V versus Li^+/Li) at 0.1 mV s^{-1} and 25 °C after a resting period at OCV for 1 h using a SP-200 potentiostat (BioLogic).

Statistical Analysis: If not stated otherwise, all quantitative results reported in this paper are expressed as mean ± standard deviation.

Supporting Information

Supporting Information is available from the Wiley Online Library or from the author.

Acknowledgements

J.L. acknowledges the Fonds der Chemischen Industrie (FCI) for financial support. F.S. is grateful to the Federal Ministry of Education and Research (BMBF) for funding within the project MELLi (03XP0447). This work was partially supported by BASF SE. The authors thank Institut Laue-Langevin (ILL) for beamtime allocation under proposal number 5-21-1164 (https://doi.org/10.5291/ILL-DATA.5-21-1164). Georgian Melinte is acknowledged for electron microscopy support. The authors also thank Yang Hu and Maximilian Fichtner from Helmholtz Institute Ulm (HIU) for support during XAS measurements.

Open access funding enabled and organized by Projekt DEAL.

Conflict of Interest

The authors declare no conflict of interest.

Data Availability Statement

The data that support the findings of this study are available from the corresponding author upon reasonable request.

ADVANCED SCIENCE NEWS
www.advancedsciencenews.com

NANO · MICRO small
www.small-journal.com

Keywords

configurational entropy, solid electrolyte, superionic conductor, solid-state batteries

Received: August 9, 2023
Revised: November 7, 2023
Published online:

[1] J. Janek, W. G. Zeier, *Nat. Energy* **2016**, *1*, 16141.
[2] J. T. Frith, M. J. Lacey, U. Ulissi, *Nat. Commun.* **2023**, *14*, 420.
[3] Y. Kato, S. Hori, T. Saito, K. Suzuki, M. Hirayama, A. Mitsui, M. Yonemura, H. Iba, R. Kanno, *Nat. Energy* **2016**, *1*, 16030.
[4] J. Janek, W. G. Zeier, *Nat. Energy* **2023**, *8*, 230.
[5] J. C. Bachman, S. Muy, A. Grimaud, H.-H. Chang, N. Pour, S. F. Lux, O. Paschos, F. Maglia, S. Lupart, P. Lamp, L. Giordano, Y. Shao-Horn, *Chem. Rev.* **2016**, *116*, 140.
[6] R. Chen, Q. Li, X. Yu, L. Chen, H. Li, *Chem. Rev.* **2020**, *120*, 6820.
[7] Z. Zhang, Y. Shao, B. Lotsch, Y.-S. Hu, H. Li, J. Janek, L. F. Nazar, C.-W. Nan, J. Maier, M. Armand, L. Chent, *Energy Environ. Sci.* **2018**, *11*, 1945.
[8] H.-J. Deiseroth, S.-T. Kong, H. Eckert, J. Vannahme, C. Reiner, T. Zaiß, M. Schlosser, *Angew. Chem., Int. Ed.* **2008**, *47*, 755.
[9] P. Adeli, J. D. Bazak, K. H. Park, I. Kochetkov, A. Huq, G. R. Goward, L. F. Nazar, *Angew. Chem., Int. Ed.* **2019**, *58*, 8681.
[10] X. Bai, Y. Duan, W. Zhuang, R. Yang, J. Wang, *J. Mater. Chem. A* **2020**, *8*, 25663.
[11] M. A. Kraft, S. Ohno, T. Zinkevich, R. Koerver, S. P. Culver, T. Fuchs, A. Senyshyn, S. Indris, B. J. Morgan, W. G. Zeier, *J. Am. Chem. Soc.* **2018**, *140*, 16330.
[12] L. Zhou, A. Assoud, Q. Zhang, X. Wu, L. F. Nazar, *J. Am. Chem. Soc.* **2019**, *141*, 19002.
[13] C. Yu, F. Zhao, J. Luo, L. Zhang, X. Sun, *Nano Energy* **2021**, *83*, 105858.
[14] S. Ohno, B. Helm, T. Fuchs, G. Dewald, M. A. Kraft, S. P. Culver, A. Senyshyn, W. G. Zeier, *Chem. Mater.* **2019**, *31*, 4936.
[15] L. Zhou, N. Minafra, W. G. Zeier, L. F. Nazar, *Acc. Chem. Res.* **2021**, *54*, 2717.
[16] S. Saha, G. Rousse, I. B. Alcover, M. Courty, D. A. Dalla Corte, J.-M. Tarascon, *Chem. Mater.* **2018**, *30*, 1379.
[17] C. A. Geiger, E. Alekseev, B. Lazic, M. Fisch, T. Armbruster, R. Langner, M. Fechtelkord, N. Kim, T. Pettke, W. Weppner, *Inorg. Chem.* **2011**, *50*, 1089.
[18] Y. Harada, T. Ishigaki, H. Kawai, J. Kuwano, *Solid State Ionics* **1998**, *108*, 407.
[19] A. Robertson, A. R. West, *Solid State Ionics* **1992**, *58*, 351.
[20] T. M. F. Restle, S. Strangmüller, V. Baran, A. Senyshyn, H. Kirchhain, W. Klein, S. Merk, D. Müller, T. Kutsch, L. van Wüllen, T. F. Fässler, *Adv. Funct. Mater.* **2022**, *32*, 2112377.
[21] F. Strauss, G. Rousse, D. Alves Dalla Corte, C. Giacobbe, R. Dominko, J.-M. Tarascon, *Inorg. Chem.* **2018**, *57*, 11646.
[22] H. Layer, M. G. Miller, L. Slifkin, *J. Appl. Phys.* **1962**, *33*, 478.
[23] L. K. Venkataraman, *Materials* **2021**, *14*, 2149.
[24] J. Hong, S. Kobayashi, A. Kuwabara, Y. H. Ikuhara, Y. Fujiwara, Y. Ikuhara, *Molecules* **2021**, *26*, 3559.
[25] A. Gautam, M. Sadowski, M. Ghidiu, N. Minafra, A. Senyshyn, K. Albe, W. G. Zeier, *Adv. Energy Mater.* **2021**, *11*, 2003369.
[26] S. Park, J.-W. Lee, *Korean J. Met. Mater.* **2021**, *59*, 247.
[27] A. Gautam, M. Sadowski, N. Prinz, H. Eickhoff, N. Minafra, M. Ghidiu, S. P. Culver, K. Albe, T. F. Fässler, M. Zobel, W. G. Zeier, *Chem. Mater.* **2019**, *31*, 10178.
[28] A. Behera, *In Advanced Materials: An Introduction to Modern Materials Science*, (Ed.: A. Behera), Springer International Publishing, Cham, **2022**, 291.
[29] C. Oses, C. Toher, S. Curtarolo, *Nat. Rev. Mater.* **2020**, *5*, 295.
[30] R.-Z. Zhang, M. J. Reece, *J. Mater. Chem. A* **2019**, *7*, 22148.
[31] Y. Ma, Y. Ma, Q. Wang, S. Schweidler, M. Botros, T. Fu, H. Hahn, T. Brezesinski, B. Breitung, *Energy Environ. Sci.* **2021**, *14*, 2883.
[32] A. Sarkar, Q. Wang, A. Schiele, M. R. Chellali, S. S. Bhattacharya, D. Wang, T. Brezesinski, H. Hahn, L. Velasco, B. Breitung, *Adv. Mater.* **2019**, *31*, 1806236.
[33] S.-K. Jung, H. Gwon, H. Kim, G. Yoon, D. Shin, J. Hong, C. Jung, J.-S. Kim, *Nat. Commun.* **2022**, *13*, 7638.
[34] Y. Zeng, B. Ouyang, J. Liu, Y.-W. Byeon, Z. Cai, L. J. Miara, Y. Wang, G. Ceder, *Science* **2022**, *378*, 1320.
[35] F. Strauss, J. Lin, M. Duffiet, K. Wang, T. Zinkevich, A.-L. Hansen, S. Indris, T. Brezesinski, *ACS Materials Lett.* **2022**, *4*, 418.
[36] J. Lin, G. Cherkashinin, M. Schäfer, G. Melinte, S. Indris, A. Kondrakov, J. Janek, T. Brezesinski, F. Strauss, *ACS Materials Lett.* **2022**, *4*, 2187.
[37] D. Bérardan, S. Franger, A. K. Meena, N. Dragoe, *J. Mater. Chem. A* **2016**, *4*, 9536.
[38] F. Strauss, J. Lin, A. Kondrakov, T. Brezesinski, *Matter* **2023**, *6*, 1068.
[39] Y. Li, S. Song, H. Kim, K. Nomoto, H. Kim, X. Sun, S. Hori, K. Suzuki, N. Matsui, M. Hirayama, T. Mizoguchi, T. Saito, T. Kamiyama, R. Kanno, *Science* **2023**, *381*, 50.
[40] S. Boulineau, M. Courty, J.-M. Tarascon, V. Viallet, *Solid State Ionics* **2012**, *221*, 1.
[41] C. Yu, L. van Eijck, S. Ganapathy, M. Wagemaker, *Electrochim. Acta* **2016**, *215*, 93.
[42] C. Yu, S. Ganapathy, E. R. H. van Eck, L. van Eijck, S. Basak, Y. Liu, L. Zhang, H. W. Zandbergen, M. Wagemaker, *J. Mater. Chem. A* **2017**, *5*, 21178.
[43] S. Harm, A.-K. Hatz, I. Moudrakovski, R. Eger, A. Kuhn, C. Hoch, B. V. Lotsch, *Chem. Mater.* **2019**, *31*, 1280.
[44] C. Dietrich, M. Sadowski, S. Sicolo, D. A. Weber, S. J. Sedlmaier, K. S. Weldert, S. Indris, K. Albe, J. Janek, W. G. Zeier, *Chem. Mater.* **2016**, *28*, 8764.
[45] R. Schlenker, A.-L. Hansen, A. Senyshyn, T. Zinkevich, M. Knapp, T. Hupfer, H. Ehrenberg, S. Indris, *Chem. Mater.* **2020**, *32*, 8420.
[46] F. Strauss, T. Zinkevich, S. Indris, T. Brezesinski, *Inorg. Chem.* **2020**, *59*, 12954.
[47] J. H. Song, Y. G. Choi, J. Heo, *J. Non-Cryst. Solids* **2006**, *352*, 423.
[48] Y. Lee, J. Jeong, H. J. Lee, M. Kim, D. Han, H. Kim, J. M. Yuk, K.-W. Nam, K. Y. Chung, H.-G. Jung, S. Yu, *ACS Energy Lett.* **2022**, *7*, 171.
[49] V. P. Zakaznova-Herzog, S. L. Harmer, H. W. Nesbitt, G. M. Bancroft, R. Flemming, A. R. Pratt, *Surf. Sci.* **2006**, *600*, 348.
[50] R. G. Avilez Garcia, C. A. Meza Avendaño, M. Pal, F. Paraguay Delgado, N. R. Mathews, *Mater. Sci. Semicond. Process.* **2016**, *44*, 91.
[51] J. H. Teo, F. Strauss, F. Walther, Y. Ma, S. Payandeh, T. Scherer, M. Bianchini, J. Janek, T. Brezesinski, *Mater. Futures* **2021**, *1*, 015102.
[52] Y. Ma, J. H. Teo, D. Kitsche, T. Diemant, F. Strauss, Y. Ma, D. Goonetilleke, J. Janek, M. Bianchini, T. Brezesinski, *ACS Energy Lett.* **2021**, *6*, 3020.
[53] J. Auvergniot, A. Cassel, J.-B. Ledeuil, V. Viallet, V. Seznec, R. Dedryvère, *Chem. Mater.* **2017**, *29*, 3883.
[54] F. Walther, R. Koerver, T. Fuchs, S. Ohno, J. Sann, M. Rohnke, W. G. Zeier, J. Janek, *Chem. Mater.* **2019**, *31*, 3745.
[55] R. Koerver, F. Walther, I. Aygün, J. Sann, C. Dietrich, W. G. Zeier, J. Janek, *J. Mater. Chem. A* **2017**, *5*, 22750.
[56] F. Walther, F. Strauss, X. Wu, B. Mogwitz, J. Hertle, J. Sann, M. Rohnke, T. Brezesinski, J. Janek, *Chem. Mater.* **2021**, *33*, 2110.
[57] J. Liang, X. Li, Y. Zhao, L. V. Goncharova, W. Li, K. R. Adair, M. N. Banis, Y. Hu, T.-K. Sham, H. Huang, L. Zhang, S. Zhao, S. Lu, R. Li, X. Sun, *Adv. Energy Mater.* **2019**, *9*, 1902125.
[58] D. Foix, D. Gonbeau, G. Taillades, A. Pradel, M. Ribes, *Solid State Sci.* **2001**, *3*, 235.

[59] D. A. Zatsepin, A. F. Zatsepin, D. W. Boukhvalov, E. Z. Kurmaev, N. V. Gavrilov, N. A. Skorikov, A. von Czarnowski, H.-J. Fitting, *Phys. Status Solidi B* **2015**, *252*, 2185.
[60] Y. Xu, K. Han, J. Xiang, X. Wang, *IEEE Access* **2020**, *8*, 159162.
[61] W. Zhang, T. Leichtweiß, S. P. Culver, R. Koerver, D. Das, D. A. Weber, W. G. Zeier, J. Janek, *ACS Appl. Mater. Interfaces* **2017**, *9*, 35888.
[62] A. Kuhn, V. Duppel, B. V. Lotsch, *Energy Environ. Sci.* **2013**, *6*, 3548.
[63] A. Kuhn, O. Gerbig, C. Zhu, F. Falkenberg, J. Maier, B. V. Lotsch, *Phys. Chem. Chem. Phys.* **2014**, *16*, 14669.
[64] S. J. Sedlmaier, S. Indris, C. Dietrich, M. Yavuz, C. Dräger, F. von Seggern, H. Sommer, J. Janek, *Chem. Mater.* **2017**, *29*, 1830.
[65] J. Maier, *Prog. Solid State Chem.* **1995**, *23*, 171.
[66] Y. Wang, H. Qu, B. Liu, X. Li, J. Ju, J. Li, S. Zhang, J. Ma, C. Li, Z. Hu, C.-K. Chang, H.-S. Sheu, L. Cui, F. Jiang, E. R. H. van Eck, A. P. M. Kentgens, G. Cui, L. Chen, *Nat. Commun.* **2023**, *14*, 669.
[67] P. Myagmarsereejid, M. Ingram, M. Batmunkh, Y. L. Zhong, *Small* **2021**, *17*, 2100241.
[68] B. Roy, B. R. Chakraborty, R. Bhattacharya, A. K. Dutta, *Solid State Commun.* **1978**, *25*, 937.
[69] F. Strauss, J. H. Teo, J. Janek, T. Brezesinski, *Inorg. Chem. Front.* **2020**, *7*, 3953.
[70] T. Shi, Y.-Q. Zhang, Q. Tu, Y. Wang, M. C. Scott, G. Ceder, *J. Mater. Chem. A* **2020**, *8*, 17399.
[71] F. Körmann, Y. Ikeda, B. Grabowski, M. H. F. Sluiter, *npj Comp. Mater.* **2017**, *3*, 36.
[72] J. Rodríguez-Carvajal, *Phys. B: Condens. Matter* **1993**, *192*, 55.
[73] K. S. Han, J. D. Bazak, Y. Chen, T. R. Graham, N. M. Washton, J. Z. Hu, V. Murugesan, K. T. Mueller, *Chem. Mater.* **2021**, *33*, 8562.
[74] W. S. Price, *Concepts Magn. Reson.* **1997**, *9*, 299.
[75] A.-Y. Kim, F. Strauss, T. Bartsch, J. H. Teo, T. Hatsukade, A. Mazilkin, J. Janek, P. Hartmann, T. Brezesinski, *Chem. Mater.* **2019**, *31*, 9664.
[76] S. Payandeh, F. Strauss, A. Mazilkin, A. Kondrakov, T. Brezesinski, *Nano Res. Energy* **2022**, *1*, e9120016.

6.3. Supporting Information

6.3.1. Publication I

Supporting Information

High-Entropy Polyanionic Lithium Superionic Conductors

Florian Strauss,[1,2]* Jing Lin,[1,2] Marie Duffiet,[1,2] Kai Wang,[2] Tatiana Zinkevich,[3,4] Anna-Lena Hansen,[3] Sylvio Indris,[3,4] Torsten Brezesinski[1,2]*

[1]Battery and Electrochemistry Laboratory, [2]Institute of Nanotechnology, Karlsruhe Institute of Technology (KIT), Hermann-von-Helmholtz-Platz 1, 76344 Eggenstein-Leopoldshafen, Germany.

[3]Institute for Applied Materials-Energy Storage Systems (IAM-ESS), Karlsruhe Institute of Technology (KIT), Hermann-von-Helmholtz-Platz 1, 76344 Eggenstein-Leopoldshafen, Germany.

[4]Helmholtz Institute Ulm (HIU) Electrochemical Energy Storage, 89081 Ulm, Germany.

*Corresponding authors: florian.strauss@kit.edu, torsten.brezesinski@kit.edu

Materials

General

If not stated otherwise, the work was conducted under inert argon atmosphere in a glovebox (MBraun, with [O_2] and [H_2O] < 0.1 ppm) or using Schlenk line techniques. Chemicals were used as received.

Lithium Selenide (Li_2Se)

Li_2Se was synthesized according to a procedure reported in literature.[1] 3.52 g Se powder (44.5 mmol, >99.5%, Sigma Aldrich) was slowly added to a solution of 48 mL 1.0 M lithium triethylborohydride ($Li(C_2H_5)_3BH$, 48 mmol, Super-Hydride® solution, Sigma Aldrich) in 48 mL tetrahydrofurane (THF, anhydrous, ≥99.9%, Sigma Aldrich) under vigorous stirring. After the exothermic reaction slowed down, additional $Li(C_2H_5)_3BH$ (48 mL, 48 mmol) was added gently, and the resulting white suspension was stirred at room temperature for 72 h. Afterwards, the white precipitate was washed three times with 30 mL THF and dried in a vacuum (10^{-3} mbar) at room temperature for 12 h. The obtained powder was ground using a mortar and pestle and subsequently heated at 140 °C in a dynamic vacuum for 12 h. The XRD pattern and corresponding LeBail fit are shown in Figure S7.

HEAR1 - $Li_6PS_5[Cl_{0.33}Br_{0.33}I_{0.33}]$

Stoichiometric amounts of Li_2S (99.99%, Sigma Aldrich), P_2S_5 (99%, Sigma Aldrich), LiCl (99.9%, Alfa Aesar), LiBr (99.999%, Sigma Aldrich), and LiI (99.999%, Sigma Aldrich) were mixed using a zirconia milling jar with zirconia balls (10 mm diameter) for 1 h at 250 rpm, and subsequently for 20 h at 450 rpm to ensure uniform distribution of the precursors. The recovered powder was pressed into pellets (10 mm diameter, ~200 mg) at 3 t, vacuum sealed in quartz ampoules (10^{-3} mbar), and annealed at 500 °C for 24 h with heating and cooling rates set to 5 °C min^{-1} using a Nabertherm box furnace.

HEAR2 - $Li_6P[S_{2.5}Se_{2.5}][Cl_{0.33}Br_{0.33}I_{0.33}]$, HEAR3 - $Li_{6.5}[Ge_{0.5}P_{0.5}][S_{2.5}Se_{2.5}][Cl_{0.33}Br_{0.33}I_{0.33}]$

Both materials were prepared according to the procedure described above for HEAR1. However, as-synthesized Li_2Se and/or GeS_2 (99.9%, GoodFellow) was/were additionally added in stoichiometric amounts, and the final annealing temperature was 400 °C.

Characterization

Laboratory X-ray Diffraction (XRD)

Samples were flame sealed in borosilicate capillaries (0.48 mm inner diameter and 0.01 mm wall thickness, Hilgenberg) under argon atmosphere and XRD pattern were collected using a STADI P diffractometer (STOE) equipped with a Cu-$K_{\alpha1}$ radiation source.

Synchrotron X-ray Diffraction (SXRD)

SXRD measurements were conducted at PETRA III (P02.1 beamline) at the Deutsches Elektronen-Synchrotron (DESY) using a wavelength of λ = 0.207400 Å in transmission geometry. To this end, powder samples were flame sealed in borosilicate glass capillaries (0.68 mm inner diameter and 0.01 mm wall thickness, Hilgenberg) under argon atmosphere.

Synchrotron Pair Distribution Function (PDF) Analysis

Measurements were conducted on powder samples sealed in glass capillaries as used for SXRD at the same beamline (λ = 0.207400 Å). An empty capillary sealed under identical conditions was used to measure the background contribution. The PDFgetX3 software was applied to calculate G(r) from the raw total scattering data.[2] The data were first corrected for sample container contribution and Compton scattering, and then the normalized structure functions, S(Q), were obtained. Finally, S(Q) was Fourier-transformed to yield G(r) with Q_{max} = 17 Å^{-1} and r_{poly} = 1.17 Å.

Time-of-Flight (ToF) Neutron Powder Diffraction (NPD)

~2 g of powder samples were filled into cylindrical (8 mm diameter) vanadium containers. NPD data were collected at the Oak Ridge National Laboratory (ORNL) POWGEN beamline using a wavelength of λ = 1.5 Å.

Structural Refinement

Structural analysis was done using the FullProf software.[3] The approximate halide/chalcogenide site occupancies (Wyckoff sites 4*a* and 4*d*) were determined first via pattern simulation with different occupation numbers (note that it was not possible to freely refine these without causing divergence of the refinement). The pattern simulations were performed to match the intensity (and intensity ratio) of the 111, 200, 220, and 311 reflections. During the course of this study, we observed that in particular the intensity of these reflections is strongly affected by the halide/chalcogenide site disorder and occupation on the respective Wyckoff sites. Once a reasonable pattern match was achieved, Rietveld refinements were carried out. To this end, a Thompson-Cox-Hastings pseudo-Voigt function was used to describe the profile shape. Scale factor, reflection shape parameters, lattice parameters, atomic positions isotropic displacement factors, and atomic occupations were refined (except for Li). Li positions and occupancies were refined for the respective crystallographic positions (24*g* and 48*h*) using the NPD data. However, if unreasonable values for a single position were obtained, its occupancy was disregarded. Structural parameters can be found in Tables S2-4.

Scanning Transmission Electron Microscopy (STEM)

STEM measurements were performed on a double corrected Thermo Fisher Themis Z, equipped with a Super-X EDX detector. The microscope was operated at an accelerating voltage of 300 kV. The powder samples were dispersed on holey carbon-coated gold grids and loaded onto a Gatan 648 vacuum transfer holder to avoid sample degradation in air.

Raman Spectroscopy

Powder samples were flame sealed in borosilicate glass capillaries (0.48 mm inner diameter and 0.01 mm wall thickness, Hilgenberg) under argon atmosphere. Measurements were done with an excitation wavelength of λ = 532 nm using an inVia confocal Raman microscope (Renishaw).

^{31}P Magic-Angle Spinning (MAS) Nuclear Magnetic Resonance (NMR) Spectroscopy

^{31}P MAS NMR spectroscopy was performed on a Bruker Avance 500 MHz spectrometer at 11.7 T, corresponding to a resonance frequency of 202.5 MHz. Spinning was done in 2.5 mm rotors at 30 kHz. Spectra were acquired with a rotor-synchronized Hahn-echo pulse sequence,

a π/2 pulse duration of 6 μs, and a recycle delay of 60 s. Chemical shifts are given relative to that of H_3PO_4 (85%).

^{7}Li Pulsed Field Gradient (PFG) NMR Spectroscopy

^{7}Li PFG NMR spectroscopy was performed on a Bruker Avance 300 MHz spectrometer, equipped with a PFG NMR probe providing pulsed field gradients up to 30 T m^{-1}. A stimulated-echo pulse sequence was applied with bipolar gradients, a gradient duration of 3.0 ms, and a diffusion time of 100 ms. The activation energy was determined by linear fitting of the temperature-dependent diffusion data using the Arrhenius equation. The ionic conductivity was calculated from the diffusion coefficient using the Nernst-Einstein equation.

Electrochemical Impedance Spectroscopy (EIS)

To prepare specimens for conductivity measurements, ~200 mg powder was compressed at 3 t for 3 min in a 10 mm pellet die. The pellet was then sealed under vacuum (10^{-3} mbar) in a quartz ampoule and annealed for 6 h at the synthesis temperature using 5 °C min^{-1} heating and cooling rates. Next, both top and bottom of the pellet were covered with 200 nm of gold, evaporated using an EVAP System (MBraun). The pellets were placed inside a Swagelok cell setup, and EIS was measured from 0.1 Hz to 7 MHz with a 20 mV voltage amplitude using a SP-200 potentiostat (BioLogic). Spectra were taken from 15 to 65 °C, with at least 1 h of equilibration prior to data collection.

Calculation of Configurational Entropy

Configurational entropy values were calculated based on the following equations. As the argyrodite structure has different sublattices possibly accommodating different elements, each configurational entropy part (anionic and cationic) was further deconvoluted into two contributions:

$$\Delta S_{\text{config}} = \Delta S_{\text{cation}} + \Delta S_{\text{cation}}$$

$$\Delta S_{\text{config}} = (\Delta S_{\text{cation,1}} + \Delta S_{\text{cation,2}}) + (\Delta S_{\text{anion,1}} + \Delta S_{\text{anion,2}})$$

$$\Delta S_{\text{config}} = -R\left\{\left[\left(\sum_{i=1}^{N} x_i \ln x_i\right) + \left(\sum_{j=1}^{N} x_j \ln x_j\right)\right] + \left[\left(\sum_{k=1}^{N} x_k \ln x_k\right) + \left(\sum_{l=1}^{N} x_l \ln x_l\right)\right]\right\}.$$

Here, x_i and x_j represent the mole fractions of elements on the cation sublattices, x_k and x_l are the mole fractions of elements on the anion sublattices (occupied by the elements indicated in Figure S8). R and N are the universal gas constant and number of cation or anion species on each sublattice, respectively. Note that in the case of HEAR1 and HEAR2, configurational entropy is solely introduced via anion mixing, and the $\Delta S_{\text{cation,1}}$ term equals to zero (as it is only partially occupied by Li).

Table S1. Configurational entropy for the HEAR materials calculated based on the assumption that the elements are equally distributed over the respective crystallographic sites. Note that for $\Delta S_{config} \geq 1.5R$, samples are considered as high-entropy materials.

Sample	Composition	ΔS_{config}
HEAR1	$Li_6PS_5[Cl_{0.33}Br_{0.33}I_{0.33}]$	1.24R
HEAR2	$Li_6P[S_{2.5}Se_{2.5}][Cl_{0.33}Br_{0.33}I_{0.33}]$	2.28R
HEAR3	$Li_{6.5}[Ge_{0.5}P_{0.5}][S_{2.5}Se_{2.5}][Cl_{0.33}Br_{0.33}I_{0.33}]$	2.98R

Table S2. Structural parameters for HEAR1 from Rietveld refinement of NPD data.

Atom	Wyckoff site	*x*	*y*	*z*	B_{iso} / Å^2	Occ
I1	4*a*	0	0	1	1.34(2)	0.33(1)
S1	4*a*	0	0	1	1.34(2)	0.24(8)
Cl1	4*a*	0	0	1	1.34(2)	0.20(9)
Br1	4*a*	0	0	1	1.34(2)	0.20(9)
P1	4*b*	0	0	0.5	0.94(1)	1
Cl2	4*d*	0.25	0.25	0.75	1.34(2)	0.13(2)
S2	4*d*	0.25	0.25	0.75	1.34(2)	0.73(9)
Br2	4*d*	0.25	0.25	0.75	1.34(2)	0.13(1)
S3	16*e*	0.1169(1)	−0.1169(1)	0.1169(1)	1.61(5)	1
Li1	24*g*	0.25	0.0213(9)	0.75	1.89(5)	0.07(4)
Li2	48*h*	0.2998(7)	0.0224(3)	0.7011(3)	1.89(5)	0.46(3)

Table S3. Structural parameters for HEAR2 from Rietveld refinement of NPD data.

Atom	Wyckoff site	*x*	*y*	*z*	B_{iso} / Å^2	Occ
I1	4*a*	0	0	1	2.07(7)	0.34(6)
Se1	4*a*	0	0	1	2.07(7)	0.32(1)
Br1	4*a*	0	0	1	2.07(7)	0.33(3)
P1	4*b*	0	0	0.5	1.02(1)	1
Cl1	4*d*	0.25	0.25	0.75	1.29(4)	0.28(1)
Se2	4*d*	0.25	0.25	0.75	1.29(4)	0.58(2)
S1	4*d*	0.25	0.25	0.75	1.29(4)	0.12(9)
S2	16*e*	0.1190(6)	−0.1190(6)	0.6190(6)	1.85(7)	0.60
Se3	16*e*	0.1190(6)	−0.1190(6)	0.6190(6)	1.85(7)	0.40
Li1	24*g*	0.25	0.0180(2)	0.75	1.21(8)	0.05(1)
Li2	48*h*	0.2956(1)	0.0266(1)	0.7044(2)	1.21(8)	0.47(3)

Table S4. Structural parameters for HEAR3 from Rietveld refinement of NPD data.

Atom	Wyckoff site	*x*	*y*	*z*	B_{iso} / Å^2	Occ
I1	4*a*	0	0	1	2.08(7)	0.37(7)
Se1	4*a*	0	0	1	2.08(7)	0.26(9)
Br1	4*a*	0	0	1	2.08(7)	0.33(3)
P1	4*b*	0	0	0.5	1.77(9)	0.5
Ge1	4*b*	0	0	0.5	1.77(9)	0.5
Cl1	4*d*	0.25	0.25	0.75	1.10(5)	0.32(5)
Se2	4*d*	0.25	0.25	0.75	1.10(5)	0.67(6)
S1	16*e*	0.1217(2)	−0.1217(2)	0.6217(2)	2.73(5)	0.30
Se3	16*e*	0.1217(2)	−0.1217(2)	0.6217(2)	2.73(5)	0.70
Li1	48*h*	0.2988(2)	0.0205(2)	0.7040(3)	3.13(1)	0.54(2)

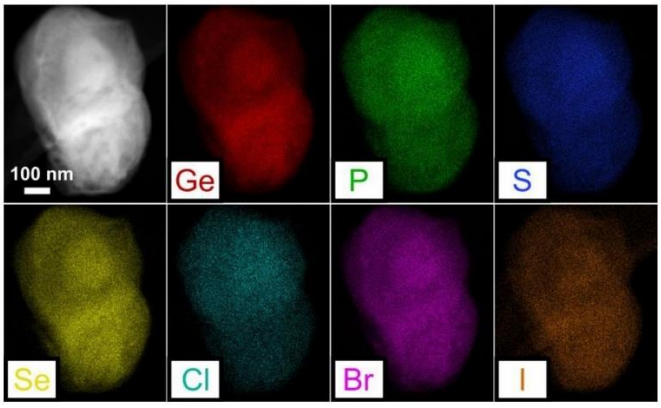

Figure S1. STEM-EDS for HEAR3 showing uniform elemental distribution on the nanometer level.

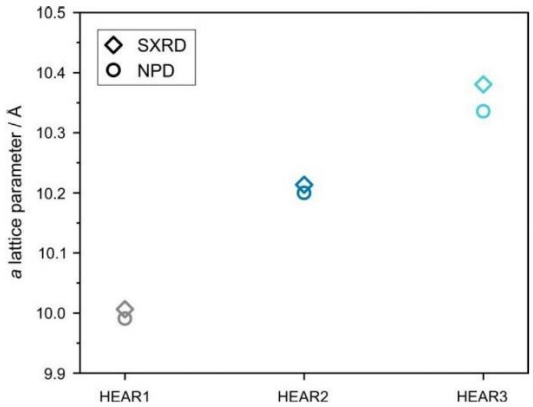

Figure S2. Calculated *a* lattice parameters from SXRD and NPD measurements.

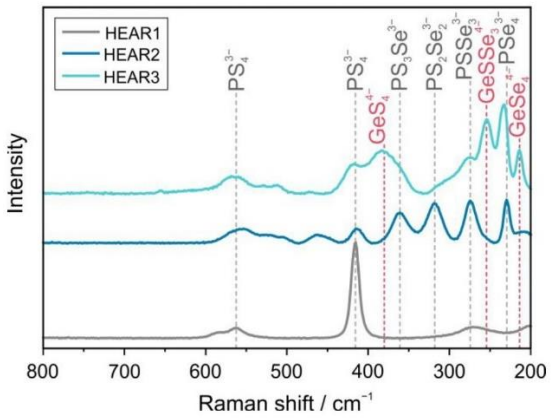

Figure S3. Raman spectra and corresponding shift of the $[PS_{4-x}Se_x]^{3-}$ tetrahedra indicated by the gray dashed lines. Red dashed lines denote the additional bands arising from the $[GeS_{4-x}Se_x]^{4-}$ vibrations.

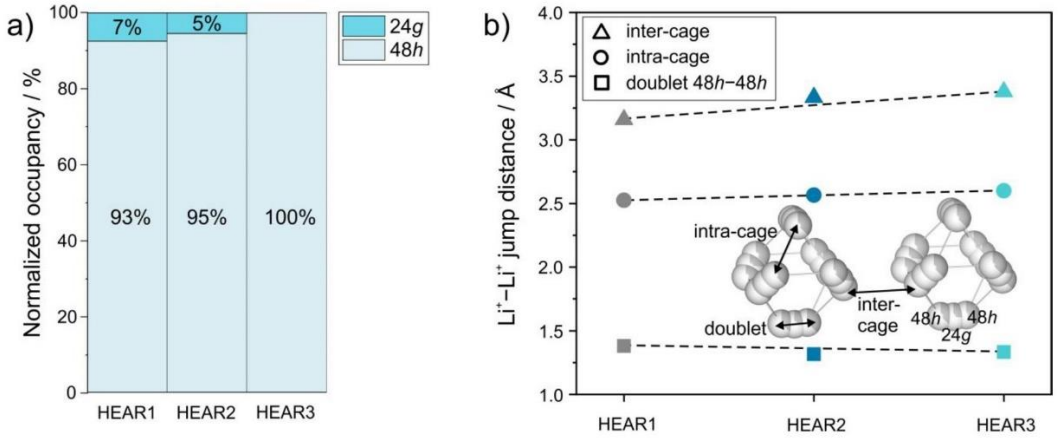

Figure S4. (a) Normalized Li occupancies over the two different crystallographic sites and (b) possible Li^+-Li^+ jump distances. The inset shows two neighboring cages of the Li-sublattice.

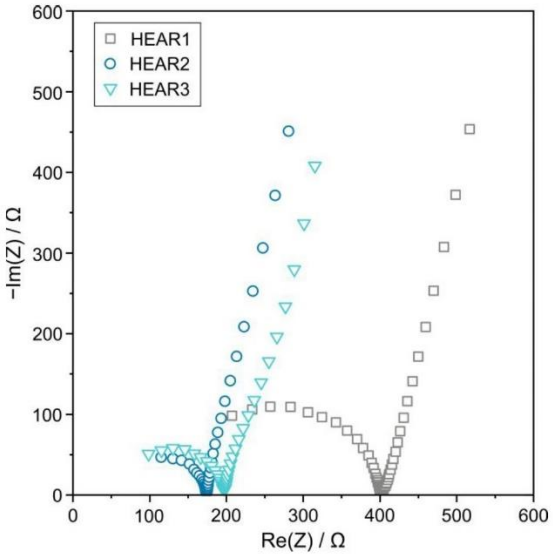

Figure S5. Nyquist plots of the electrochemical impedance at 25 °C.

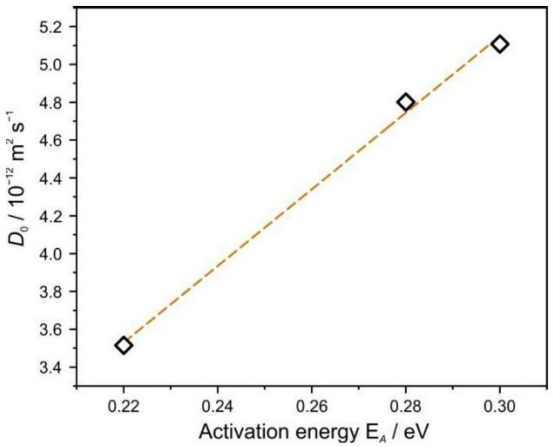

Figure S6. Pre-exponential factor of the diffusivity, D_0, as a function of the activation energy from ^{7}Li PFG NMR spectroscopy measurements.

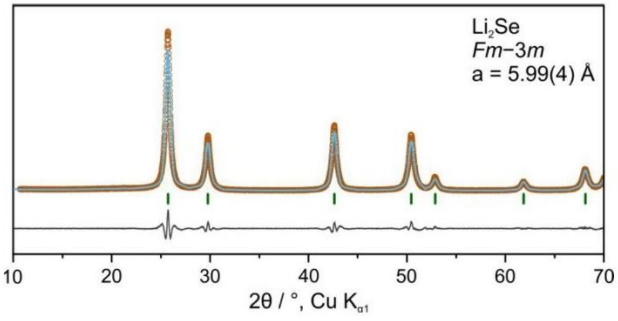

Figure S7. LeBail fit of the XRD data for as-synthesized Li_2Se. The observed, calculated, and difference profiles are shown in orange, blue, and gray, respectively. The vertical tick marks denote the expected Bragg positions.

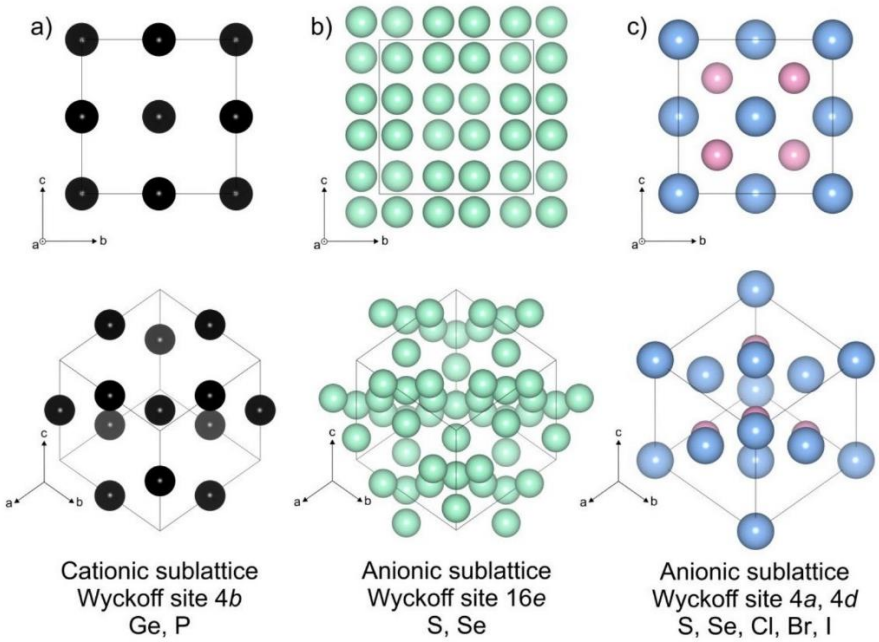

Figure S8. Sublattices of the argyrodite structure. Note that Li is omitted for clarity. The different crystallographic sites and possible constituents are denoted.

References

[1] Gladysz, J. A.; Hornby, J. L.; Garbe, J. E. A Convenient One-Flask Synthesis of Dialkyl Selenides and Diselenides via Lithium Tiethylborohydride Reduction of Se_x. *J. Org. Chem.* **1978**, *43*, 1204.

[2] Juhás P.; Davis, T.; Farrow, C. L.; Billinge, S. J. L. PDFgetX3: A Rapid and Highly Automatable Program for Processing Powder Diffraction Data into Total Scattering Pair Distribution Functions. *J. Appl. Cryst.* **2013**, *46*, 560.

[3] Rodríguez-Carvajal, J. Recent Advances in Magnetic Structure Determination by Neutron Powder Diffraction, *Physica B* **1993**, *192*, 55.

6.3.2. Publication II

Supporting Information

A High Entropy Multicationic Substituted Lithium Argyrodite Superionic Solid Electrolyte

Jing Lin,[a] Gennady Cherkashinin,[b] Mareen Schäfer,[c] Georgian Melinte,[d] Sylvio Indris,[c,e] Aleksandr Kondrakov,[a,f] Jürgen Janek,[a,g] Torsten Brezesinski,[a*] and Florian Strauss[a*]

[a] Battery and Electrochemistry Laboratory (BELLA), Institute of Nanotechnology, Karlsruhe Institute of Technology (KIT), Hermann-von-Helmholtz-Platz 1, 76344 Eggenstein-Leopoldshafen, Germany.

[b] Institute for Materials Science, Technical University Darmstadt, Alarich-Weiss Str. 2, 64287 Darmstadt, Germany.

[c] Institute for Applied Materials–Energy Storage Systems, Karlsruhe Institute of Technology (KIT), Hermann-von-Helmholtz-Platz 1, 76344 Eggenstein-Leopoldshafen, Germany.

[d] Institute of Nanotechnology, Karlsruhe Institute of Technology (KIT), Hermann-von-Helmholtz-Platz 1, 76344 Eggenstein-Leopoldshafen, Germany.

[e] Helmholtz Institute Ulm (HIU) Electrochemical Energy Storage, Helmholtzstr. 11, 89081 Ulm, Germany.

[f] BASF SE, Carl-Bosch-Str. 38, 67056 Ludwigshafen, Germany.

[g] Institute of Physical Chemistry & Center for Materials Science (ZfM/LaMa), Justus-Liebig-University Giessen, Heinrich-Buff-Ring 17, 35392 Giessen, Germany.

*Corresponding authors: torsten.brezesinski@kit.edu, florian.strauss@kit.edu

Experimental Section

General

All preparation steps were conducted under Ar atmosphere in a glovebox (MBraun, [O_2] and [H_2O] < 0.1 ppm), and all precursors were used as received.

Synthesis

A stoichiometric mixture of Li_2S (99.99 %, Sigma Aldrich), P_2S_5 (99 %, Sigma Aldrich), GeS_2 (99.9 %, GoodFellow), SiS_2 (99.99 %, GoodFellow), Sb_2S_3 (99.99 %, Alfa Aesar), and LiI (99.999 %, Sigma Aldrich) plus 10 wt % excess sulfur (99.99 %, Sigma Aldrich) was loaded into a 70 mL zirconia milling jar with 20 zirconia balls (10 mm diameter, ~1.5 g total amount of precursor mixture). After milling for 1 h at 250 rpm, the speed was increased to 450 rpm and milling was continued for another 10 h. The recovered powder was pressed into pellets (~300 mg, 10 mm diameter) at 3 t and vacuum-sealed (10^{-3} bar) in a quartz ampule, followed by annealing at 500 °C for 24 h with heating and cooling rates set to 5 °C min^{-1}. The ampule was pre-dried at 500 °C for 10 min using a heat gun (in a dynamic vacuum) to avoid the presence of trace water.

Characterization

Inductively Coupled Plasma-Optical Emission Spectroscopy (ICE-OES)

The Li, P, Si, Ge, Sb, and I contents were determined by ICP-OES from three independent measurements using a Thermo Fisher Scientific iCAP 7600 Duo.

Scanning Transmission Electron Microscopy (STEM)

In order to protect the sample from air exposure, the specimen preparation was done under Ar atmosphere in a glovebox (using a direct dispersion of the dry powder), and the transfer to the microscope was achieved via a Gatan inert transfer holder. The measurements were performed at 300 kV using a Themis 300 electron microscope with DCOR probe corrector and Super X EDX detector.

Laboratory X-ray Diffraction (XRD)

The samples were flame-sealed in borosilicate capillaries (0.68 mm inner diameter and 0.01 mm wall thickness; Hilgenberg) under Ar atmosphere, and XRD patterns were collected on a STOE Stadi-P diffractometer with DECTRIS MYTHEN 1K strip detector. The instrument uses a Mo anode (λ = 0.70926 Å).

Neutron Powder Diffraction (NPD)

For NPD, ~2 g powder sample was filled into cylindrical vanadium containers of 6 mm diameter. Data were collected at T = 10 K and 298 K using the D2B high-resolution powder diffractometer (λ = 1.595072 Å) at the Institute Laue-Langevin (ILL). Rietveld analysis of diffraction data was done with the help of FullProf Suite. The Thompson-Cox-Hastings pseudo-Voigt function was used to describe the peak shape. A point-by-point background was applied. Scale factor, peak shape parameters, lattice parameters, atomic coordinates, individual anisotropic atomic displacement

parameters, S^{2-}/I^- site inversion, and Li occupancies were refined. The zero-shift parameter was treated last.

^{29}Si and ^{31}P Magic-angle Spinning (MAS) Nuclear Magnetic Resonance (NMR) Spectroscopy

MAS NMR spectroscopy was performed on a Bruker Advance 500 MHz spectrometer at 11.7 T, corresponding to resonance frequencies of 73.6, 99.4, and 202.5 MHz. The samples were packed into 2.5 mm rotors in an Ar-filled glovebox, and spinning was done at 30 kHz. The π/2 pulse length was 1.8 µs for ^{29}Si and 2.1 µs for ^{31}P. The recycle delay was 60 s for ^{29}Si/^{31}P. The chemical shifts are referenced to tetramethylsilane and H_3PO_4 (85 %) for ^{29}Si and ^{31}P, respectively.

X-ray Photoelectron Spectroscopy (XPS)

Quasi *in situ* XPS was applied to study the changes in chemical composition at the cathodelelectrolyte interface after 200 cycles of the SSB cell. The cathode was carefully separated from the anode and the SE separator layer was removed. The pristine SE and cycled cathode were transferred under Ar atmosphere from the glovebox to the XPS spectrometer (PHI 5000 VersaProbe equipped with a monochromatic Al Kα source, $h\nu$ =1486.7 eV) without exposure to air. The diameter of the illuminated area was 200 µm. Photoelectrons were collected with the pass energy of E_{pass} = 23.5 eV at three different electron escape angles, namely 20, 45, and 90° with respect to the surface normal. Because the solid electrolyte is a poor electronic conductor, a neutralizer equipped with both low-voltage electron gun and floating ion gun generating a low-energy ion beam was used to compensate for sample charging. Additionally, the binding energies were referenced to the C 1s line of the C-C bond (E_{bin} = 284.8 eV). The background was subtracted by a Shirley-type function. The photoelectron peak positions and areas were obtained by weighted least-square fitting of model curves to the experimental data.

The XPS fitting results were used for quantitative analysis of the elemental composition. Note that a typical error in the quantitative XPS analysis is 15-20 %. The composition was estimated considering a semi-infinite sample and assuming uniform distribution of elements over the depth:

$$X_A = \frac{\frac{X_A}{X_B}}{\sum_{all\_elements}\frac{X_A}{X_B}} \times 100\%\text{, where } X_A = \frac{I_A}{\sigma(h\nu)\times D(E_{kin}^A)\times \lambda(E_{kin}^A)\times\cos(\theta)}.$$

Here, I_A is the intensity of photoelectrons emitted from the core-level A, $\sigma(h\nu)$ is the photoionization cross-section, $D(E_{kin}^A)$ is the detection efficiency, which depends on the kinetic energy E_{kin}, θ is the angle of the emitted photoelectrons with respect to the surface normal, and $\lambda(E_{kin}^A)$ represents the inelastic mean free path of photoelectrons emitted from the core-level A. Generally, $\lambda(E_{kin}^A)$ depends upon the materials properties. In the present work, only the dependence on E_{kin} was taken account with: $\lambda(E_{kin}^A) = \sqrt{E_{kin}}$ according to the universal curve.[1] The values for $\sigma(h\nu)$ were taken from

reference.[2] In the analysis, the areas under the I 4d, Ge 3d, Sb 4d, Li 1s, Si 2p, and P 2p spectra were used, allowing to estimate the chemical composition approximately to the same depth, as well as to minimize the error due to differences in kinetic energies associated with the λ and the instrumental factor. For the oxygen content, the area under the O 1s spectrum was used. Results are provided in Table S6.

Electrochemical Impedance Spectroscopy (EIS)

For ionic conductivity measurements, ~200 mg ball-milled precursor mixture was compressed at 2.5 t for 3 min in a 10 mm pellet die. The pellet was then sealed under vacuum in a quartz ampule (10^{-3} mbar) and heated at 500 °C for 24 h with 5 °C min^{-1} heating and cooling rates. Indium foil (10 mm diameter) was attached on both sides to ensure good contact between sample and current collector. The pellet was then placed into a customized cell setup with stainless steel dies and a PEEK sleeve (10 mm diameter). EIS was measured from 0.1 Hz to 7 MHz with a 20 mV voltage amplitude using a SP-200 potentiostat (BioLogic). Impedance spectra were collected from 15 to 65 °C with at least 1 h of temperature equilibration prior to data acquisition. The conductivity was calculated from the value of R_1 (intercept with the *x*-axis). The point of intersection was determined via linear fitting of the capacitive tail. The activation energy was determined from linear fitting of the temperature-dependent conductivity using the Arrhenius equation. In the calculations, residual porosity was not taken into account.

DC polarization measurements

DC polarization measurements were performed at 25 °C, applying different voltages of 0.3, 0.4, and 0.5 V, to determine the partial electronic conductivity (note that a similar setup as for the EIS measurements was used). The resistance and electronic conductivity were calculated from the steady-state current.

Temperature-Dependent ^{7}Li Pulsed Field Gradient (PFG) Nuclear Magnetic Resonance (NMR) Spectroscopy

Temperature-dependent ^{7}Li PFG NMR experiments were performed on a Bruker Advance 300 MHz spectrometer. The samples where sealed in evacuated 5 mm borosilicate glass tubes. A PFG probe with a maximum gradient field strength of 30 T m^{-1} was used. Data were acquired in the temperature range 302-345 K using a stimulated-echo pulse sequence with bipolar gradients to suppress the effect of eddy currents. The π/2 pulse length was between 5.35 and 5.9 µs, and the recycle delay was 0.4-0.6 s. For all samples and temperatures, the gradient duration was 3 ms, and the diffusion time was 30 ms.

Electrode Preparation, Cell Assembly, and Electrochemical Measurements

For the SSB cells, the cathode composite was prepared by mixing $LiNbO_3$-coated NCM851005 (85 % Ni, BASF SE) with the $Li_{6.5}[P_{0.25}Si_{0.25}Ge_{0.25}Sb_{0.25}]S_5I$ SE and Super C65 carbon black additive in a 69.3:29.7:1.0 weight ratio at 140 rpm for 30 min under Ar atmosphere using a 70 mL zirconia milling jar with 10 zirconia balls of diameter 10 mm. The $LiNbO_3$ coating was prepared as reported elsewhere.[3] The anode composite

was produced in a similar fashion, but the weight ratio of carbon-coated LTO (NEI Corp.), Super C65, and SE was 30:10:60.

For cell assembly, a customized setup with stainless steel dies and a PEEK sleeve (10 mm diameter) was used. First, ~100 mg SE was compacted at 62 MPa to form the SE separator layer. Next, the cathode (~13 mg) and anode composites (~65 mg) were separately distributed on both sides of the SE layer, and then the whole stack was compressed at 437 MPa. Galvanostatic testing was done at 25 °C and under an external pressure of 81 MPa in the voltage range between 1.35 and 2.75 V vs $Li_4Ti_5O_{12}/Li_7Ti_5O_{12}$ (~2.9-4.3 V vs Li^+/Li) after a resting period at open-circuit voltage for 1 h using a MACCOR battery cycler. The C-rate was varied from 0.5 to 2.0C, with 1C = 190 mA $g_{NCM851005}^{-1}$.

Calculation of Configurational Entropy

Configurational entropy values were calculated based on the equations below. The argyrodite structure consists of different sublattices, possibly accommodating different elements. Each configurational entropy fraction (anionic and cationic) was thus further deconvoluted into two contributions:[4]

$$\Delta S_{\mathrm{config}} = \Delta S_{\mathrm{cation}} + \Delta S_{\mathrm{cation}},$$

$$\Delta S_{\mathrm{config}} = (\Delta S_{\mathrm{cation,1}} + \Delta S_{\mathrm{cation,2}}) + (\Delta S_{\mathrm{anion,1}} + \Delta S_{\mathrm{anion,2}}),$$

$$\Delta S_{\mathrm{config}} = -R\left\{\left[\left(\sum_{\mathrm{i}=1}^{\mathrm{N}} x_{\mathrm{i}} \ln x_{\mathrm{i}}\right) + \left(\sum_{\mathrm{j}=1}^{\mathrm{N}} x_{\mathrm{j}} \ln x_{\mathrm{j}}\right)\right] + \left[\left(\sum_{\mathrm{k}=1}^{\mathrm{N}} x_{\mathrm{k}} \ln x_{\mathrm{k}}\right) + \left(\sum_{\mathrm{l}=1}^{\mathrm{N}} x_{\mathrm{l}} \ln x_{\mathrm{l}}\right)\right]\right\}.$$

Here, x_i and x_j represent the mole fractions of elements on the cation sublattices and x_k and x_l the mole fractions of elements on the anion sublattices. *R* and *N* are the universal gas constant and number of cation or anion species on each sublattice, respectively. Note that the $\Delta S_{\mathrm{cation,1}}$ and $\Delta S_{\mathrm{anion,1}}$ terms equal to zero, as the crystallographic sites are only partially or fully occupied by Li or S.

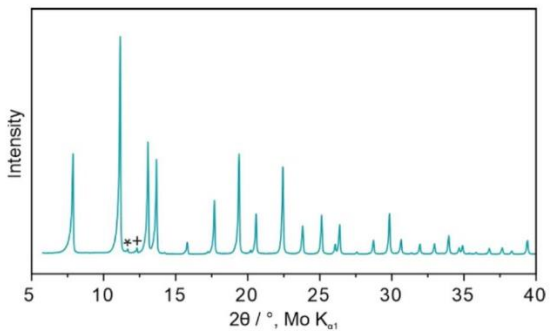

Figure S1. Laboratory XRD pattern collected from the $Li_{6.5}[P_{0.25}Si_{0.25}Ge_{0.25}Sb_{0.25}]S_5I$. The minor reflections denoted by symbols indicate the presence of LiI and Li_2S impurities.

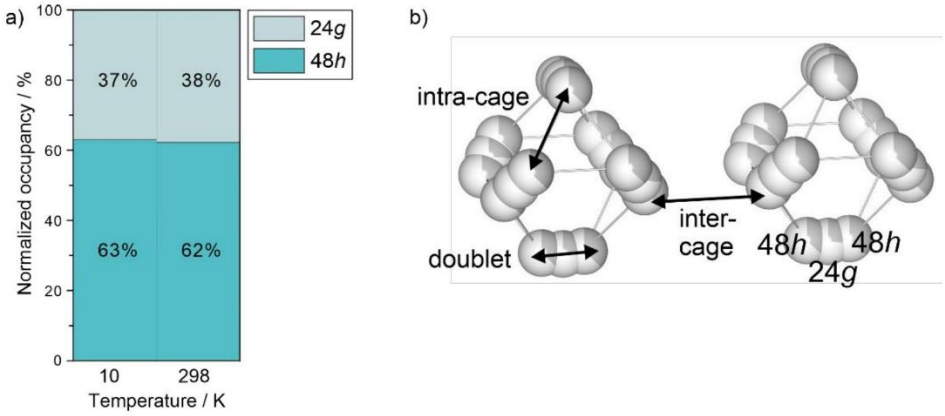

Figure S2. (a) Normalized Li occupancies over the two crystallographic sites. (b) Two neighboring Li cages, where the different Li-Li jumps and Wyckoff sites are denoted.

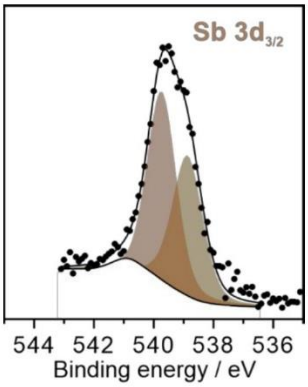

Figure S3. The Sb $3d_{3/2}$ photoelectron spectrum for the pristine SE.

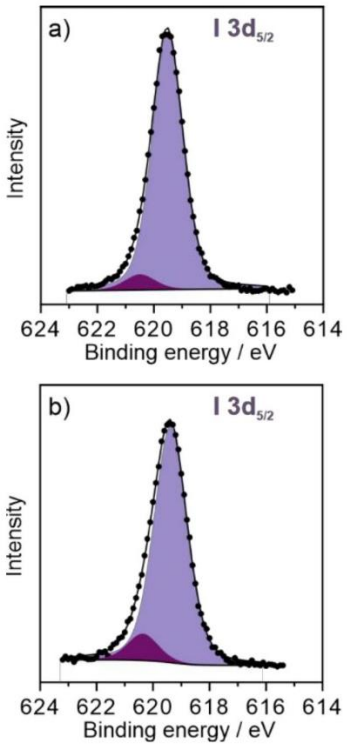

Figure S4. The I $3d_{5/2}$ photoelectron spectrum for (a) the pristine and (b) cycled SE. Line asymmetry of a "non-metallic" compound to high E_{bin} indicates the presence of an additional chemical state, resolved at E_{bin} = (620.5 ± 0.2) eV and (620.3 ± 0.2) eV, respectively.

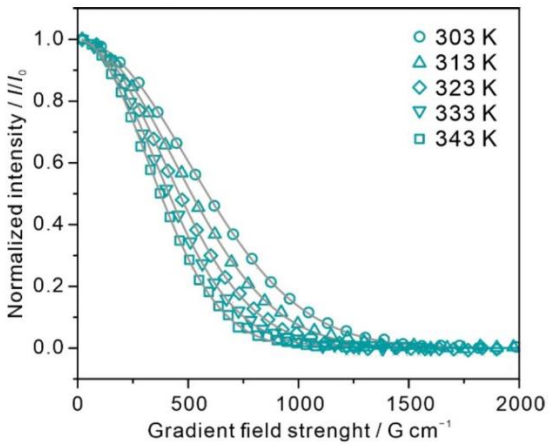

Figure S5. Results from temperature-dependent ^{7}Li PFG NMR spectroscopy, with symbols and lines representing the measured and calculated data, respectively.

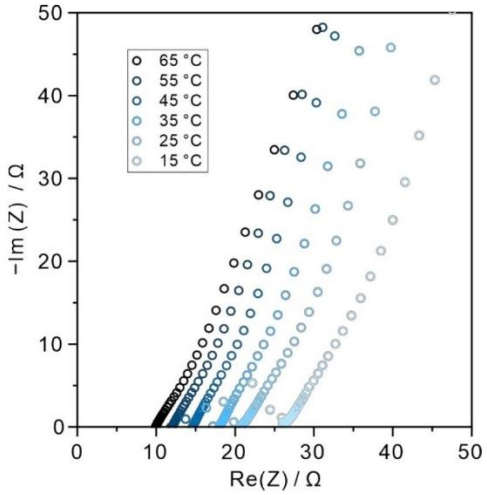

Figure S6. Nyquist plots of the electrochemical impedance in the temperature range 15-65 °C.

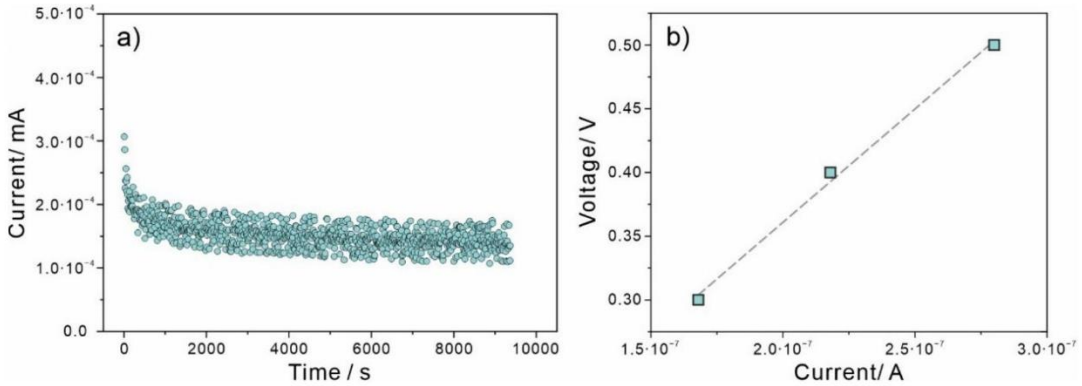

Figure S7. (a) Current response after applying a DC voltage of 300 mV and (b) linear relationship between applied voltage and measured current.

Table S1. Other targeted compositions not yielding single-phase argyrodite materials. Note that a similar synthesis procedure as for $Li_{6.5}[P_{0.25}Si_{0.25}Ge_{0.25}Sb_{0.25}]S_5I$ was used (with the respective sulfide precursors).

Composition
$Li_7[P_{0.25}Si_{0.25}Ge_{0.25}Ga_{0.25}]S_5I$
$Li_{6.75}[P_{0.25}Si_{0.25}Ge_{0.25}W_{0.25}]S_5I$
$Li_{6.75}[P_{0.25}Si_{0.25}Ge_{0.25}Sn_{0.25}]S_5I$
$Li_{6.75}[Si_{0.25}Ge_{0.25}Sb_{0.25}Sn_{0.25}]S_5I$
$Li_{6.6}[P_{0.2}Si_{0.2}Ge_{0.2}Sb_{0.2}Sn_{0.2}]S_5I$
$Li_{6.6}[P_{0.2}Si_{0.2}Ge_{0.2}Sb_{0.2}W_{0.2}]S_5I$

$Li_{6.8}[P_{0.2}Si_{0.2}Ge_{0.2}Sb_{0.2}Ga_{0.2}]S_5I$
$Li_7[P_{0.2}Si_{0.2}Ge_{0.2}Sb_{0.2}Zn_{0.2}]S_5I$
$Li_7[P_{0.2}Si_{0.2}Ge_{0.2}Sn_{0.2}Ga_{0.2}]S_5I$

Table S2. Chemical composition of the pristine SE from ICP-OES analysis.

Element	**Li**	**P**	**Si**	**Ge**	**Sb**	**I**
Stoichiometry	6.37 ±0.32	0.25 ±0.01	0.26 ±0.01	0.24 ±0.01	0.25 ±0.01	1.00 ±0.09

Table S3. Structural parameters for $Li_{6.5}[P_{0.25}Si_{0.25}Ge_{0.25}Sb_{0.25}]S_5I$ from Rietveld analysis of NPD data collected at T = 298 K.[a]

Atom	Wyckoff site	*x*	*y*	*z*	B_{iso} / Å^2	Occ
I1	4*d*	0.25	0.25	0.75	1.35(9)	0.11(6)
I2	4*a*	0	0	0	2.56(5)	0.88(4)
S1	4*d*	0.25	0.25	0.75	1.35(9)	0.88(4)
S2	4*a*	0	0	0	2.56(5)	0.11(6)
S3	16*e*	0.1237(6)	−0.1237(6)	0.6237(6)	1.09(8)	1
Si1	4*b*	0	0	0.5	1.06(2)	0.25
Ge1	4*b*	0	0	0.5	1.06(2)	0.25
P1	4*b*	0	0	0.5	1.06(2)	0.25
Sb1	4*b*	0	0	0.5	1.06(2)	0.25
Li1	48*h*	0.2979(4)	0.0205(1)	0.7020(6)	3.50(4)	0.33(8)
Li2	24*g*	0.25	0.0147(6)	0.75	1.61(9)	0.40(7)

[a] *F*−43*m* space group, a = 10.29714(9) Å, V = 1091.816(2) Å^3, ρ = 2.407 g cm^{-3}, R_{wp} = 3.03 %, X^2 = 3.38.

Table S4. Structural parameters for $Li_{6.5}[P_{0.25}Si_{0.25}Ge_{0.25}Sb_{0.25}]S_5I$ from Rietveld analysis of NPD data collected at T = 10 K.[a]

Atom	Wyckoff site	*x*	*y*	*z*	B_{iso} / Å^2	Occ
I1	4*d*	0.25	0.25	0.75	0.70(8)	0.11(5)
I2	4*a*	0	0	0	1.07(4)	0.88(5)
S1	4*d*	0.25	0.25	0.75	0.70(8)	0.88(5)
S2	4*a*	0	0	0	1.07(4)	0.11(5)
S3	16*e*	0.1251(2)	−0.1251(2)	0.6251(2)	0.47(1)	1
Si1	4*b*	0	0	0.5	0.13(7)	0.25
Ge1	4*b*	0	0	0.5	0.13(7)	0.25
P1	4*b*	0	0	0.5	0.13(7)	0.25

Sb1	4*b*	0	0	0.5	0.13(7)	0.25
Li1	48*h*	0.2979(4)	0.0204(6)	0.7020(6)	1.60(3)	0.33(9)
Li2	24*g*	0.25	0.0221(6)	0.75	0.70(8)	0.41(1)

[a]*F*−43*m* space group, a = 10.24932(5) Å, V = 1076.677(10) Å^3, ρ = 2.441 g cm^{-3}, R_{wp} = 3.64 %, X^2 = 4.52.

Table S5. Li-Li jump distances for $Li_{6.5}[P_{0.25}Si_{0.25}Ge_{0.25}Sb_{0.25}]S_5I$ at T = 298 K and 10 K. Corresponding jump distances for Li_6PS_5I (T = 300 K) from the literature are also shown for comparison.[5]

***T* / K**	**48h—48h / Å**	**Intracage / Å**	**Intercage / Å**
298	1.39	2.64	3.24
10	1.39	2.63	3.23
300 (Li_6PS_5I)	1.25	2.57	3.35

Table S6. Surface composition of the SE prior to and after cycling in units of at % from XPS. The theoretical values are also shown for comparison.

Sample	**Li**	**P**	**Si**	**Ge**	**Sb**	**S**	**I**	**O**
Pristine	37.9	1.6	3.1	1.8	2.9	32.1	12.0	8.7
Cycled	30.9	2.8	4.5	2.3	2.6	31.5	4.5	20.9
Theoretical	48.1	1.85	1.85	1.85	1.85	37	7.41	0

Table S7. Li-ion conductivity σ_{ion} at T = 298 K (if not stated otherwise) and activation energy E_A for different lithium argyrodites determined by EIS and/or ^{7}Li PFG NMR spectroscopy.

Material	**σ_{ion} / mS cm^{-1}**	**E_A (EIS) / eV**	**E_A (^{7}Li PFG NMR) / eV**	**Ref.**
Li_6PS_5Cl	3.1	0.34	0.35	[6]
Li_6PS_5Cl	3.4	0.35	0.28	[7]
$Li_{5.5}PS_{4.5}Cl_{1.5}$	9.4	0.29	0.29	[8]
$Li_{5.35}Ca_{0.1}PS_{4.5}Cl_{1.55}$	10.2	0.30	0.287	[6]
Li_6PS_5I	10^{-3}	0.38	-	[9]
$Li_{6.7}P_{0.3}Si_{0.7}S_5I$	2.0	0.24	-	[10]
$Li_{6.3}P_{0.7}Sn_{0.2}S_5I$	0.1	0.34	-	[10]
$Li_{6.6}P_{0.4}Ge_{0.6}S_5I$	5.4	0.24	-	[11]
$Li_{6.6}Sb_{0.4}Si_{0.6}S_5I$	14.8 (302 K)	0.25	-	[12]
$Li_{6.4}Sb_{0.6}Ge_{0.4}S_5I$	6.3 (302 K)	0.23	-	[12]
$Li_{6.75}Sb_{0.25}Si_{0.75}S_5I$	12.1 (301 K)	0.16		[13]
$Li_{6.5}Sb_{0.5}Ge_{0.5}S_5I$	16.1 (301 K)	0.18	-	[14]
$Li_6PS_5[Cl_{0.33}Br_{0.33}I_{0.33}]$	0.7	0.29	0.28	[4]
$Li_6P[S_{2.5}Se_{2.5}][Cl_{0.33}Br_{0.33}I_{0.33}]$	1.3	0.31	0.30	[4]
$Li_{6.5}[Ge_{0.5}P_{0.5}][S_{2.5}Se_{2.5}][Cl_{0.33}Br_{0.33}I_{0.33}]$	1.1	0.31	0.22	[4]

$Li_{6.5}[P_{0.25}Si_{0.25}Ge_{0.25}Sb_{0.25}]S_5I$	13.2	0.19	0.20	this work

References

(1) Bubert, H. Practical Surface Analysis A2, Vol. 1. Auger and X-Ray Photoelectron Spectroscopy. 2. Auflage. Herausgegeben von D. Briggs Und M. P. Seah. Wiley, Chichester, Salle + Sauerländer, Aarau, 1994. 649 S. *Angew. Chem.* **1995**, *107*, 1367–1367.

(2) Scofield, J. H. Hartree-Slater Subshell Photoionization Cross-Sections at 1254 and 1487 eV. *J. Electron Spectrosc. Relat. Phenom.* **1976**, *8*, 129–137.

(3) Kim, A.-Y.; Strauss, F.; Bartsch, T.; Teo, J. H.; Hatsukade, T.; Mazilkin, A.; Janek, J.; Hartmann, P.; Brezesinski, T. Stabilizing Effect of a Hybrid Surface Coating on a Ni-Rich NCM Cathode Material in All-Solid-State Batteries. *Chem. Mater.* **2019**.

(4) Strauss, F.; Lin, J.; Duffiet, M.; Wang, K.; Zinkevich, T.; Hansen, A.-L.; Indris, S.; Brezesinski, T. High-Entropy Polyanionic Lithium Superionic Conductors. *ACS Mater. Lett.* **2022**, *4*, 418–423.

(5) Minafra, N.; Kraft, M. A.; Bernges, T.; Li, C.; Schlem, R.; Morgan, B. J.; Zeier, W. G. Local Charge Inhomogeneity and Lithium Distribution in the Superionic Argyrodites Li_6PS_5X (X = Cl, Br, I). *Inorg. Chem.* **2020**, *59*, 11009–11019.

(6) Adeli, P.; Bazak, J. D.; Huq, A.; Goward, G. R.; Nazar, L. F. Influence of Aliovalent Cation Substitution and Mechanical Compression on Li-Ion Conductivity and Diffusivity in Argyrodite Solid Electrolytes. *Chem. Mater.* **2021**, *33*, 146–157.

(7) Schlenker, R.; Hansen, A. L.; Senyshyn, A.; Zinkevich, T.; Knapp, M.; Hupfer, T.; Ehrenberg, H.; Indris, S. Structure and Diffusion Pathways in Li_6PS_5Cl Argyrodite from Neutron Diffraction, Pair-Distribution Function Analysis, and NMR. *Chem. Mater.* **2020**, *32*, 8420–8430.

(8) Adeli, P.; Bazak, J. D.; Park, K. H.; Kochetkov, I.; Huq, A.; Goward, G. R.; Nazar, L. F. Boosting Solid-State Diffusivity and Conductivity in Lithium Superionic Argyrodites by Halide Substitution. *Angew. Chem. Int. Ed.* **2019**, *58*, 8681–8686.

(9) Kraft, M. A.; Culver, S. P.; Calderon, M.; Böcher, F.; Krauskopf, T.; Senyshyn, A.; Dietrich, C.; Zevalkink, A.; Janek, J.; Zeier, W. G. Influence of Lattice Polarizability on the Ionic Conductivity in the Lithium Superionic Argyrodites Li_6PS_5X (X = Cl, Br, I). *J. Am. Chem. Soc.* **2017**, *139*, 10909–10918.

(10) Ohno, S.; Helm, B.; Fuchs, T.; Dewald, G.; Kraft, M. A.; Culver, S. P.; Senyshyn, A.; Zeier, W. G. Further Evidence for Energy Landscape Flattening in the Superionic Argyrodites $Li_{6+x}P_{1-x}M_xS_5I$ (M = Si, Ge, Sn). *Chem. Mater.* **2019**, *31*, 4936–4944.

(11) Kraft, M. A.; Ohno, S.; Zinkevich, T.; Koerver, R.; Culver, S. P.; Fuchs, T.; Senyshyn, A.; Indris, S.; Morgan, B. J.; Zeier, W. G. Inducing High Ionic Conductivity in the Lithium Superionic Argyrodites $Li_{6+x}P_{1-x}Ge_xS_5I$ for All-Solid-State Batteries. *J. Am. Chem. Soc.* **2018**, *140*, 16330–16339.

(12) Zhou, L.; Assoud, A.; Zhang, Q.; Wu, X.; Nazar, L. F. New Family of Argyrodite Thioantimonate Lithium Superionic Conductors. *J. Am. Chem. Soc.* **2019**, *141*, 19002–19013.

(13) Lee, Y.; Jeong, J.; Lim, H. D.; Kim, S. O.; Jung, H. G.; Chung, K. Y.; Yu, S. Superionic Si-Substituted Lithium Argyrodite Sulfide Electrolyte $Li_{6+x}Sb_{1-x}Si_xS_5I$ for All-Solid-State Batteries. *ACS Sustain. Chem. Eng.* **2021**, *9*, 120–128.

(14) Lee, Y.; Jeong, J.; Lee, H. J.; Kim, M.; Han, D.; Kim, H.; Yuk, J. M.; Nam, K. W.; Chung, K. Y.; Jung, H. G.; Yu, S. Lithium Argyrodite Sulfide Electrolytes with High Ionic Conductivity and Air Stability for All-Solid-State Li-Ion Batteries. *ACS Energy Lett.* **2022**, *7*, 171–179.

6.3.3. Publication III

Supporting Information

Tuning Ion Mobility in Lithium Argyrodite Solid Electrolytes via Entropy Engineering

Jing Lin,[a] Mareen Schaller,[b] Sylvio Indris,[b] Volodymyr Baran,[c] Ajay Gautam,[d] Jürgen Janek,[a,e] Aleksandr Kondrakov,[a,f] Torsten Brezesinski,[a*] and Florian Strauss[a*]

[a] Battery and Electrochemistry Laboratory (BELLA), Institute of Nanotechnology (INT), Karlsruhe Institute of Technology (KIT), Hermann-von-Helmholtz-Platz 1, 76344 Eggenstein-Leopoldshafen, Germany.

[b] Institute for Applied Materials–Energy Storage Systems (IAM-ESS), Karlsruhe Institute of Technology (KIT), Hermann-von-Helmholtz-Platz 1, 76344 Eggenstein-Leopoldshafen, Germany.

[c] Deutsches Elektronen-Synchrotron DESY, Notkestr. 85, 22607 Hamburg, Germany.

[d] Section Storage of Electrochemical Energy, Radiation Science and Technology, Faculty of Applied Sciences, Delft University of Technology, Delft 2629 JB, The Netherlands.

[e] Institute of Physical Chemistry & Center for Materials Research (ZfM/LaMa), Justus-Liebig-University Giessen, Heinrich-Buff-Ring 17, 35392 Giessen, Germany.

[f] BASF SE, Carl-Bosch-Str. 38, 67056 Ludwigshafen, Germany.

*Corresponding authors: torsten.brezesinski@kit.edu, florian.strauss@kit.edu

Experimental Section

General

All preparation steps were done under an Ar atmosphere in a glovebox (MBraun, [O_2] and [H_2O] < 0.1 ppm), and all precursors were used as received.

Synthesis

The synthesis of the cationic substituted lithium argyrodites involved high-energy ball-milling, followed by calcination. In short, Li_2S (99.99%, Sigma-Aldrich), P_2S_5 (99%, Sigma-Aldrich), GeS_2 (99.9%, Goodfellow), SiS_2 (99.99%, Goodfellow), Sb_2S_3 (99.99%, Alfa Aesar), LiI (99.999%, Sigma-Aldrich), and 10 wt.% excess sulfur (99.99%, Sigma-Aldrich) were combined in a stoichiometric ratio in a 70 mL zirconia milling jar (total amount of ~1.5 g). 20 zirconia milling balls with a diameter of 10 mm were added to the jar, and the mixture was milled for 1 h at 250 rpm, followed by 40 h at 450 rpm. The recovered powder was pressed into pellets (~300 mg, 10 mm diameter) at 3 t and vacuum-sealed in quartz ampules (10^{-3} bar). Subsequently, the samples were calcined for 10 h at 500 °C with heating and cooling rates of 5 °C min^{-1}. This synthetic procedure has been optimized; more detailed information is available in the literature.[1] To avoid trace water, the ampules were pre-dried at 500 °C for 10 min using a heat gun under dynamic vacuum (10^{-3} bar).

Characterization

Inductively Coupled Plasma-Optical Emission Spectroscopy (ICE-OES). The Li, P, Si, Ge, Sb, and I contents were determined by ICP-OES using a Thermo Fisher Scientific iCAP 7600 DUO. To this end, the samples were dissolved in an acid digester in a graphite furnace, and the resulting mass fraction values were obtained from three independent measurements.

Laboratory X-ray Diffraction (XRD). The sample were sealed in borosilicate capillaries (Hilgenberg, 0.68 mm inner diameter and 0.01 mm wall thickness) and subjected to XRD measurements using a STOE STADI P diffractometer with a DECTRIS MYTHEN 1K strip detector in Debye-Scherrer geometry. The instrument utilizes a Mo anode to generate X-rays of wavelength λ = 0.70926 Å.

Synchrotron X-ray Diffraction (SXRD). Measurements were performed with a photon energy of 60 keV (λ = 0.2072 Å) at the beamline P02.1, PETRA III at Deutsches Elektronen-Synchrotron DESY in Hamburg, Germany.[2] The diffraction patterns were acquired using a VAREX XRD 4343CT (150 × 150 μm^2 pixel size, 2880 × 2880 pixel area) 2D position-sensitive detector at a sample-to-detector distance of 2200 mm. The

exposure time for each pattern was 60 s. Data integration was done using the pyFAI software.[3] The data obtained was subjected to Rietveld analysis using FullProf Suite.[4,5] LaB_6 was refined first, including scale factor, peak shape parameters, overall anisotropic atomic displacement parameters, and lattice parameters. The peak shape refined from LaB_6 was included as instrument resolution file for the refinement process of newly synthesized lithium argyrodites.

Neutron Powder Diffraction (NPD). For NPD, cylindrical vanadium containers with a diameter of 6 mm were filled with ~2 g of material. Measurements were performed at room temperature using the HRPT at Paul Scherrer Institute (PSI) with a wavelength of λ = 1.494 Å[6] or PEARL at Delft University of Technology with a wavelength of λ = 1.67 Å. The diffraction data was analyzed via Rietveld refinement using FullProf Suite.[4,5] The instrumental contribution to the peak shape broadening was determined via the Thompson-Cox-Hastings pseudo-Voigt function using $Na_2Ca_3Al_2F_{14}$. An absorption correction was included during the refinement process. The background was determined using a linear interpolation between selected data points in non-overlapping regions. The zero shift, lattice parameters, and peak shape parameters were determined first via Le Bail fitting. Afterwards, Rietveld refinement was performed to calculate individual atomic coordinates, occupancies, and thermal displacement factors. The total Li content was constrained to the nominal values. To determine the Li positions and occupancies, a two position model (24*g* and 48*h,* referring to T5 and T5a*,* respectively*)* was initially examined. If unreasonable physical parameters were obtained, other Li positions were taken into account (16*e* and 48*h,* referring to T4 and T2, respectively). Anisotropic atomic displacement parameters (ADP) were considered when B_{iso} exceeded 5 Å^2. Finally, simultaneous refinement of all structural parameters was done to ensure the stability of the calculated structure. The standard deviation depicted in figures is calculated through score times.

^{6}Li, ^{29}Si, and ^{31}P Magic-Angle Spinning (MAS) Nuclear Magnetic Resonance (NMR) Spectroscopy. ^{6}Li, ^{29}Si, and ^{31}P MAS NMR spectroscopy measurements were performed at a magnetic field of 11.7 T, corresponding to resonance frequencies of 73.6, 99.4, and 202.5 MHz, respectively. Spinning was performed in 2.5 mm rotors at 20 kHz. Spectra were acquired with a single-pulse sequence for ^{6}Li and ^{29}Si, and with a Hahn-echo sequence for ^{31}P. The recycle delay was 60 s for ^{6}Li, ^{29}Si, and ^{31}P. The π/2 pulse length was 2.9 µs for ^{6}Li, 3.3 µs for ^{29}Si, and 2.7 µs for ^{31}P. The spectra are

referenced to an aqueous 1 M ^{6}LiCl solution for ^{6}Li, tetramethylsilane for ^{29}Si, and H_3PO_4 (85%) for ^{31}P.

Electrochemical Impedance Spectroscopy (EIS). A 200 mg pellet was prepared by compacting the ball-milled precursor mixture at 3.5 t for 3 min in a 10 mm die. The pellet was then vacuum-sealed in a quartz ampule (10^{-3} mbar) and subjected to 10 h calcination at 500 °C with heating and cooling rates of 5 °C min^{-1}. Indium foil (10 mm diameter) was attached on both sides to ensure optimal contact between the sample and current collector. The prepared pellet was inserted into a customized cell equipped with stainless steel dies and a PEEK sleeve (10 mm diameter). EIS measurements were performed in a frequency range from 0.1 Hz to 7 MHz with a 20 mV voltage amplitude utilizing a SP-200 potentiostat (BioLogic). Impedance spectra were recorded in the temperature range of 15–65 °C after equilibration for at least 1 h prior to data acquisition. Conductivity values were derived from the intercept with the *x*-axis (R_1) for EQ, $Si_{0.5}$, and $Ge_{0.5}$. The intersection point was determined through linear fitting of the capacitive tail. The spectra collected from the other samples were fitted using an equivalent circuit model (R_1/Q_1)–Q_2, with Q being a constant phase element. The activation energy was obtained by linear fitting of the temperature-dependent conductivity employing the Arrhenius equation. Residual porosity was not considered in the calculations.

DC polarization measurements were conducted to determine the partial electronic conductivity at room temperature, utilizing voltages of 0.3, 0.4, and 0.5 V on the same setup employed for EIS. The resistance and corresponding electronic conductivity were calculated from the steady-state current.

Temperature-Dependent ^{7}Li Pulsed Field Gradient (PFG) NMR Spectroscopy. ^{7}Li PFG NMR measurements were performed on a Bruker Avance spectrometer at a magnetic field of 7.05 T in the temperature range of 30–70 °C. The maximal gradient strength of the diffusion probe head is 30 T/m. A stimulated-echo pulse sequence with bipolar gradients was used to suppress the effects of eddy currents.[7,8] The gradient duration and diffusion time were set to 3 ms and 30 ms, respectively. The recycle delay was always well above five times the spin-lattice relaxation time. All samples were measured under an Ar atmosphere in 5 mm borosilicate glass tubes.

Explanation for two-component fitting for PFG NMR results: PFG NMR allows to investigate the long-range transport (several 100 nm) of Li^+ ions by varying the applied

gradient field strength *g*. In the case of uniform diffusion coefficient *D*, the recorded echo intensities *I* can be described by the Stejskal and Tanner equation:

$$I = I_0 \cdot \exp\left(-D\gamma^2\delta^2 g^2\left(\Delta - \frac{\delta}{3}\right)\right) \quad (1)$$

with the gradient pulse duration δ, the diffusion time Δ, and the magnetogyric ratio γ.[9] When it presents results like in **Figure S7d**, the slope of ln(I) changes with increasing g^2, thus indicating the presence of a second diffusion coefficient. In the case of two independent diffusion coefficients (e.g., for amorphous and crystalline phases), the damping of the echo intensity can be analyzed by the Kärger equations.[10] Thereby, one distinguishes between fast and slow exchange relative to the measurement timescale, given by the diffusion time Δ between the two phase fractions. Fast exchange occurs if the lifetime of the state (here, the residence time of an ion in one phase) τ is much smaller than Δ ($\tau \ll \Delta$). In the case of $\tau \gg \Delta$, one speaks of slow exchange. Ramos *et al.* used an intermediate-time approximation to the Kärger equations to fit the multicomponent diffusion described by the PFG attenuation curve of a solid electrolyte.[11] In this case, special requirements for the occupation fractions and diffusion rates have to be fulfilled. For slow exchange, a signal-fraction weighted two-component fit can be used to describe the decay of the echo intensity, yielding the diffusion coefficients D_i as well as the signal fractions of both phases. These fractions can be differently affected by the spin-spin and spin-lattice relaxation times, and therefore provide only an estimate of the real phase fractions that are characterized by D_i.

Calculation of Li-ion mobility: The mobility μ was derived based on the Einstein-Smoluchowski equation:

$$D_\mathrm{Li} = \frac{\mu k_\mathrm{B} T}{q} \quad (2)$$

where D, μ, k_B, T, and q represent the diffusion coefficient, mobility, Boltzmann constant, absolute temperature, and particle charge, respectively.

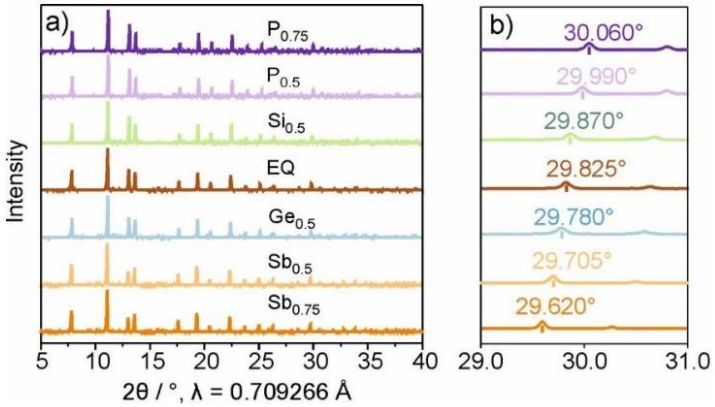

Figure S1. (a) Laboratory XRD patterns for all samples and (b) magnified view of the 2*θ* range from 29° to 31°.

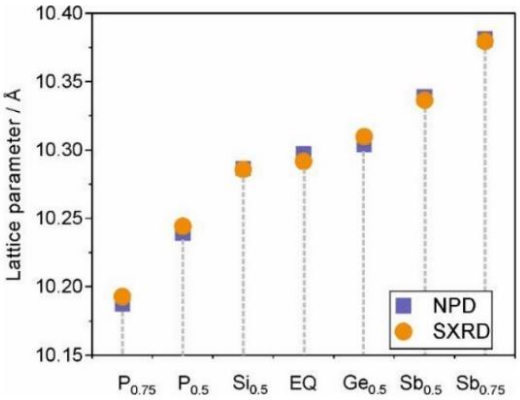

Figure S2. Calculated lattice parameter *a* from SXRD (orange) and NPD (blue) experiments. The NPD data for $Li_{6.5}[P_{0.25}Si_{0.25}Ge_{0.25}Sb_{0.25}]S_5I$ (EQ) was taken from the literature.[1,12]

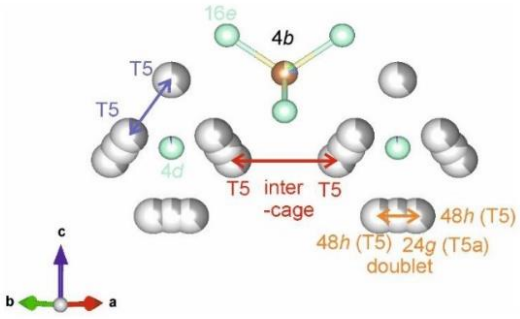

Figure S3. Li sublattice for $Li_{6.17}[P_{0.083}Si_{0.083}Ge_{0.083}Sb_{0.75}]S_5I$ ($Sb_{0.75}$), where Li only occupies the 48*h* (T5) and 24*g* (T5*a*) positions.

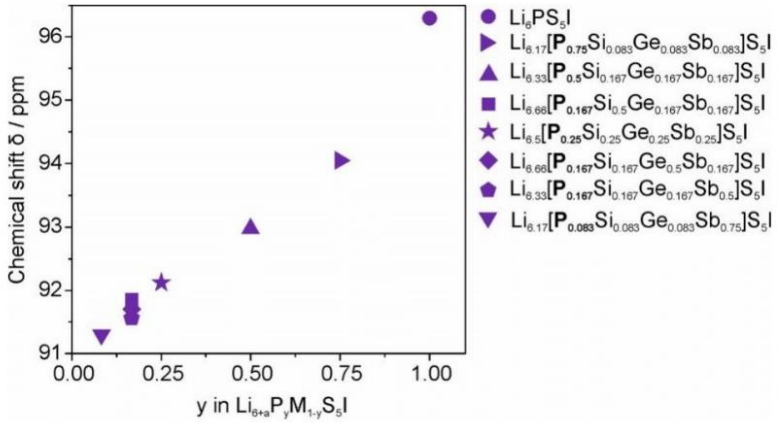

Figure S4. Correlation between phosphorus content and chemical peak shift of the ^{31}P signal from MAS NMR spectroscopy. The data for $Li_{6.5}[P_{0.25}Si_{0.25}Ge_{0.25}Sb_{0.25}]S_5I$ (EQ) and Li_6PS_5I was taken from the literature.[1,12,13]

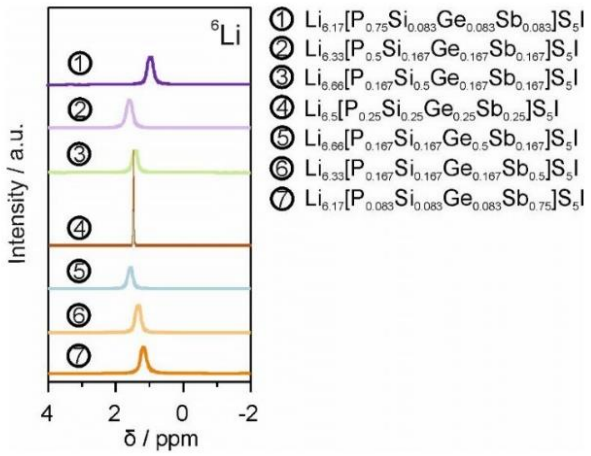

Figure S5. ^6Li MAS NMR spectra for the substituted lithium argyrodite samples. The data for $Li_{6.5}[P_{0.25}Si_{0.25}Ge_{0.25}Sb_{0.25}]S_5I$ (EQ) was taken from the literature.[1,12] The more narrow peak shape of EQ is due to higher homogeneity of the applied magnetic field during the measurement.

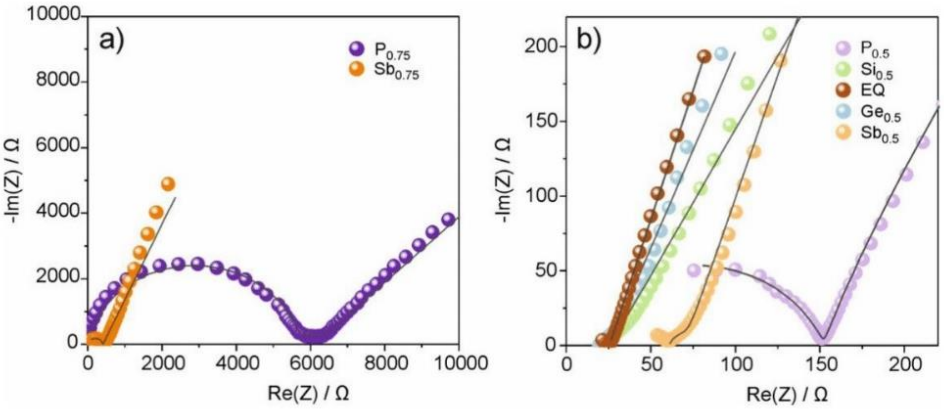

Figure S6. Nyquist plots and corresponding calculated data of the electrochemical impedance measured at 25 °C for the substituted lithium argyrodite samples.

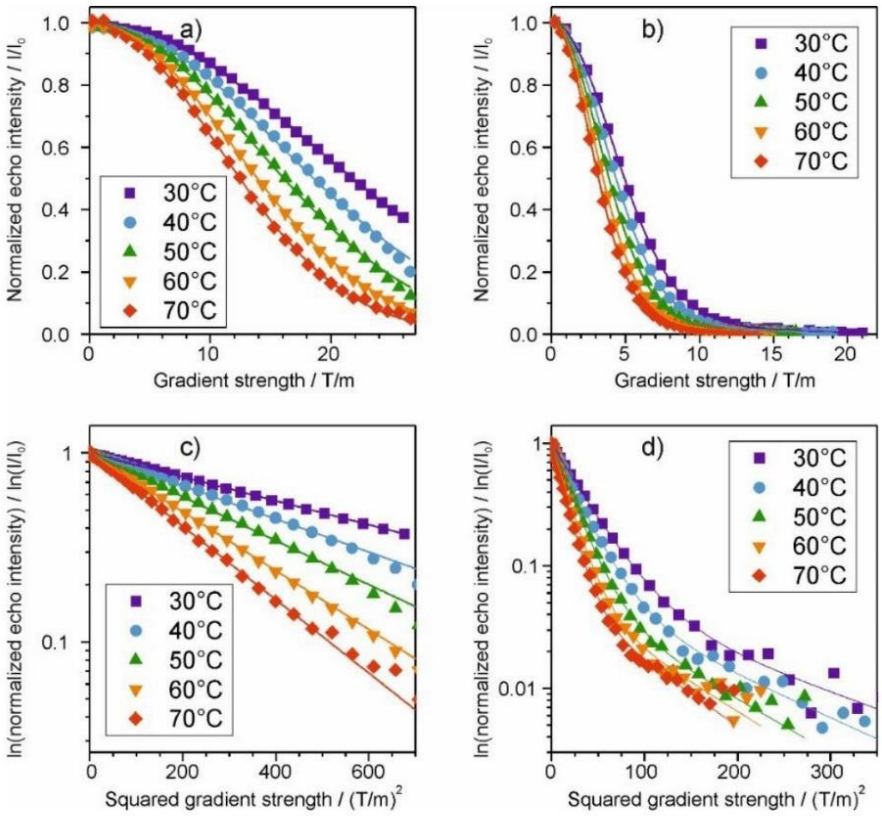

Figure S7. Temperature-dependent echo intensity of $Sb_{0.75}$ (a, c) and $Si_{0.5}$ (b, d) plotted as echo intensity vs. gradient strength (top) and ln(echo intensity) vs. squared gradient strength (bottom). $Sb_{0.75}$ can be analyzed with a one-component fit, whereas for $Si_{0.5}$ a two-component fit is necessary.

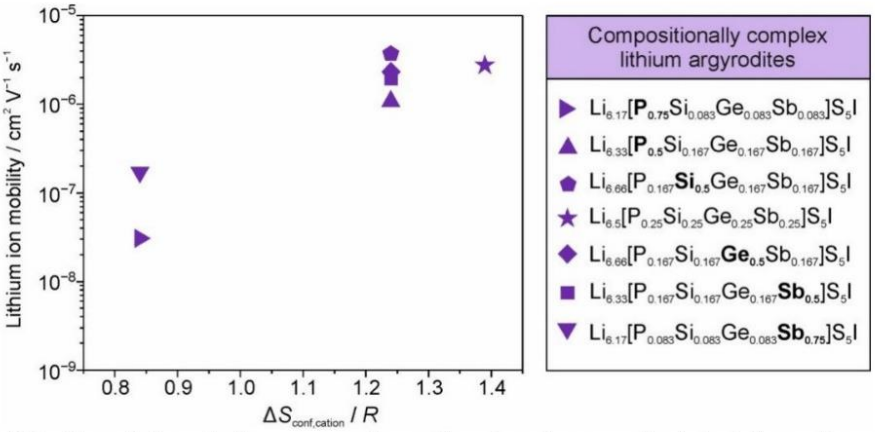

Figure S8. Correlation between configurational entropy calculated from the cation disorder and Li-ion mobility for the substituted lithium argyrodite samples.

Table S1. Nominal and calculated chemical composition based on ICP-OES measurements.

Nominal Stoichiometry	Measured Stoichiometry					
	Li	P	Si	Ge	Sb	I
$Li_{6.17}[P_{0.75}Si_{0.083}Ge_{0.083}Sb_{0.083}]S_5I$	6.14 ±0.14	0.75 ±0.005	0.080 ±0.008	0.082 ±0.005	0.080 ±0.010	0.942 ±0.09
$Li_{6.33}[P_{0.5}Si_{0.167}Ge_{0.167}Sb_{0.167}]S_5I$	6.30 ±0.09	0.49 ±0.003	0.168 ±0.04	0.170 ±0.06	0.156 ±0.04	1.01 ±0.03
$Li_{6.66}[P_{0.167}Si_{0.5}Ge_{0.167}Sb_{0.167}]S_5I$	6.59 ±0.23	0.173 ±0.01	0.53 ±0.03	0.160 ±0.07	0.164 ±0.09	1.01 ±0.09
$Li_{6.66}[P_{0.167}Si_{0.167}Ge_{0.5}Sb_{0.167}]S_5I$	6.62 ±0.13	0.165 ±0.05	0.172 ±0.02	0.47 ±0.50	0.160 ±0.04	0.992 ±0.06
$Li_{6.33}[P_{0.167}Si_{0.167}Ge_{0.167}Sb_{0.5}]S_5I$	6.29 ±0.09	0.163 ±0.02	0.171 ±0.07	0.164 ±0.06	0.45 ±0.50	1.03 ±0.03
$Li_{6.17}[P_{0.083}Si_{0.083}Ge_{0.083}Sb_{0.75}]S_5I$	6.13 ±0.20	0.087 ±0.005	0.081 ±0.008	0.082 ±0.005	0.73 ±0.04	0.987 ±0.06

Table S2. Structural parameters for $Li_{6.17}[P_{0.75}Si_{0.083}Ge_{0.083}Sb_{0.083}]S_5I$ ($P_{0.75}$) from Rietveld analysis of SXPD data collected at T = 298 K.[a]

Atom	Wyckoff site	*x*	*y*	*z*	B_{iso} / Å²	Occ
I1	4*a*	0	0	0	1.90(1)	0.984(1)
S2	4*a*	0	0	0	1.90(1)	0.016(1)
S1	4*d*	0.25	0.25	0.75	1.40(2)	0.984(1)
I2	4*d*	0.25	0.25	0.75	1.40(2)	0.016(1)
S3	16*e*	0.1190(6)	−0.1190(6)	0.6190(6)	1.33(4)	1
Si1	4*b*	0	0	0.5	0.81(2)	0.083
Ge1	4*b*	0	0	0.5	0.81(2)	0.083

P1	4*b*	0	0	0.5	0.81(2)	0.75
Sb1	4*b*	0	0	0.5	0.81(2)	0.083

[a] *F*−43*m* space group, a = 10.19283(1) Å, V = 1058.971(1) Å^3, ρ = 2.331 g cm^{-3}, R_{wp} = 6.47%; Li_2S: wt.% 0.88(4), LiI: wt.% 2.29(2).

Table S3. Structural parameters for $Li_{6.33}[P_{0.5}Si_{0.167}Ge_{0.167}Sb_{0.167}]S_5I$ ($P_{0.5}$) from Rietveld analysis of SXPD data collected at T = 298 K.[a]

Atom	Wyckoff site	*x*	*y*	*z*	B_{iso} / Å^2	Occ
I1	4*a*	0	0	0	1.98(6)	0.997(7)
S2	4*a*	0	0	0	1.98(6)	0.003(2)
S1	4*d*	0.25	0.25	0.75	1.30(2)	0.997(7)
I2	4*d*	0.25	0.25	0.75	0.81(9)	0.003(2)
S3	16*e*	0.1202(6)	−0.1202(6)	0.6202(6)	0.81(9)	1
Si1	4*b*	0	0	0.5	0.53(6)	0.167
Ge1	4*b*	0	0	0.5	0.53(6)	0.167
P1	4*b*	0	0	0.5	0.53(6)	0.5
Sb1	4*b*	0	0	0.5	0.53(6)	0.167

[a] *F*−43*m* space group, a = 10.24428(1) Å, V = 1075.088(1) Å^3, ρ = 2.376 g cm^{-3}, R_{wp} = 8.72%; Li_2S: wt.% 1.36(4), LiI wt.% 2.59(2).

Table S4. Structural parameters for $Li_{6.66}[P_{0.167}Si_{0.5}Ge_{0.167}Sb_{0.167}]S_5I$ ($Si_{0.5}$) from Rietveld analysis of SXPD data collected at T = 298 K.[a]

Atom	Wyckoff site	*x*	*y*	*z*	B_{iso} / Å^2	Occ
I1	4*a*	0	0	0	2.80(2)	0.979(1)
S2	4*a*	0	0	0	2.80(2)	0.021(1)
S1	4*d*	0.25	0.25	0.75	1.80(1)	0.979(1)
I2	4*d*	0.25	0.25	0.75	1.80(1)	0.021(1)
S3	16*e*	0.1213(2)	0.1213(2)	0.6213(2)	1.90(2)	1
Si1	4*b*	0	0	0.5	0.95(6)	0.5
Ge1	4*b*	0	0	0.5	0.95(6)	0.167
P1	4*b*	0	0	0.5	0.95(6)	0.167
Sb1	4*b*	0	0	0.5	0.95(6)	0.167

[a] *F*−43*m* space group, a = 10.28599(1) Å, V = 1088.274(2) Å^3, ρ = 2.351 g cm^{-3}, R_{wp} = 2.76%; Li_2S: wt.% 1.52(6), LiI: wt.% 2.44(2).

Table S5. Structural parameters for $Li_{6.5}[P_{0.25}Si_{0.25}Ge_{0.25}Sb_{0.25}]S_5I$ (EQ) from Rietveld analysis of SXPD data collected at T = 298 K.[a]

Atom	Wyckoff site	*x*	*y*	*z*	B_{iso} / Å^2	Occ
I1	4*a*	0	0	0	2.05(4)	0.966(1)
S2	4*a*	0	0	0	2.05(4)	0.034(1)
S1	4*d*	0.25	0.25	0.75	1.12(5)	0.966(1)
I2	4*d*	0.25	0.25	0.75	1.12(5)	0.034(1)
S3	16*e*	0.1224(8)	−0.1224(8)	0.6224(8)	1.06(2)	1
Si1	4*b*	0	0	0.5	0.41(2)	0.25
Ge1	4*b*	0	0	0.5	0.41(2)	0.25
P1	4*b*	0	0	0.5	0.41(2)	0.25
Sb1	4*b*	0	0	0.5	0.41(2)	0.25

[a] *F*−43*m* space group, a = 10.29171(1) Å, V = 1090.092(1) Å^3, ρ = 2.411 g cm^{-3}, R_{wp} = 6.28%; Li_2S: wt.% 0.85(4), LiI: wt.% 1.36(2).

Table S6. Structural parameters for $Li_{6.66}[P_{0.167}Si_{0.167}Ge_{0.5}Sb_{0.167}]S_5I$ ($Ge_{0.5}$) from Rietveld analysis of SXPD data collected at T = 298 K.[a]

Atom	Wyckoff site	*x*	*y*	*z*	B_{iso} / Å^2	Occ
I1	4*a*	0	0	0	3.2(1)	0.974(6)
S2	4*a*	0	0	0	3.2(1)	0.026(6)
S1	4*d*	0.25	0.25	0.75	1.7(2)	0.974(6)
I2	4*d*	0.25	0.25	0.75	1.7(2)	0.026(6)
S3	16*e*	0.1218(4)	−0.1218(4)	0.6218(4)	1.6(1)	1
Si1	4*b*	0	0	0.5	0.9(1)	0.167
Ge1	4*b*	0	0	0.5	0.9(1)	0.5
P1	4*b*	0	0	0.5	0.9(1)	0.167
Sb1	4*b*	0	0	0.5	0.9(1)	0.167

[a] *F*−43*m* space group, a = 10.3099(2) Å, V = 1095.88(4) Å^3, ρ = 2.424 g cm^{-3}, R_{wp} = 6.89%; Li_2S: wt.% 0.14(6), LiI: wt.% 0.74(3).

Table S7. Structural parameters for $Li_{6.33}[P_{0.167}Si_{0.167}Ge_{0.167}Sb_{0.5}]S_5I$ ($Sb_{0.5}$) from Rietveld analysis of SXPD data collected at T = 298 K.[a]

Atom	Wyckoff site	*x*	*y*	*z*	B_{iso} / Å^2	Occ
I1	4*a*	0	0	0	2.89(6)	0.991(1)
S2	4*a*	0	0	0	2.89(6)	0.009(1)
S1	4*d*	0.25	0.25	0.75	1.59(7)	0.991(1)
I2	4*d*	0.25	0.25	0.75	1.59(7)	0.009(1)
S3	16*e*	0.1244(4)	−0.1244(4)	0.6244(4)	2.02(7)	1
Si1	4*b*	0	0	0.5	0.98(3)	0.167

Ge1	4*b*	0	0	0.5	0.98(3)	0.167
P1	4*b*	0	0	0.5	0.98(3)	0.167
Sb1	4*b*	0	0	0.5	0.98(3)	0.5

[a] *F*−43*m* space group, a = 10.33644(1) Å, V = 1104.365(1) Å^3, ρ = 2.490 g cm^{-3}, R_{wp} = 1.93%, Li_2S wt.% 0.74(4); LiI wt.% 1.17(2).

Table S8. Structural parameters for $Li_{6.17}[Sb_{0.75}Si_{0.083}Ge_{0.083}P_{0.083}]S_5I$ ($Sb_{0.75}$) from Rietveld analysis of SXPD data collected at T = 298 K.[a]

Atom	Wyckoff site	*x*	*y*	*z*	B_{iso} / Å^2	Occ
I1	4*a*	0	0	0	2.84(6)	0.9999
S2	4*a*	0	0	0	2.84(6)	0.0001
S1	4*d*	0.25	0.25	0.75	1.53(2)	0.9999
I2	4*d*	0.25	0.25	0.75	1.53(2)	0.0001
S3	16*e*	0.1266(0)	−0.1266(0)	0.6266(0)	2.05(3)	1
Si1	4*b*	0	0	0.5	0.81(2)	0.083
Ge1	4*b*	0	0	0.5	0.81(2)	0.083
P1	4*b*	0	0	0.5	0.81(2)	0.083
Sb1	4*b*	0	0	0.5	0.81(2)	0.75

[a] *F*−43*m* space group, a = 10.37950(1) Å, V = 1118.225(3) Å^3, ρ = 2.567 g cm^{-3}, R_{wp} = 2.37%; Li_2S: wt.% 0.90(5), Li_2I: wt.% 1.75(2).

Table S9. Structural parameters for $Li_{6.17}[P_{0.75}Si_{0.083}Ge_{0.083}Sb_{0.083}]S_5I$ ($P_{0.75}$) from Rietveld analysis of NPD data collected at T = 298 K.[a]

Atom	Wyckoff site	*x*	*y*	*z*	B_{iso} / Å^2	Occ
I1	4*a*	0	0	0	1.5(9)	0.995(1)
S2	4*a*	0	0	0	1.5(9)	0.005(1)
S1	4*d*	0.25	0.25	0.75	2.51(0)	0.995(1)
I2	4*d*	0.25	0.25	0.75	2.51(0)	0.005(1)
S3	16*e*	0.119(6)	−0.119(6)	0.619(6)	1.8(3)	1
Si1	4*b*	0	0	0.5	1.0(8)	0.083
Ge1	4*b*	0	0	0.5	1.0(8)	0.083
P1	4*b*	0	0	0.5	1.0(8)	0.75
Sb1	4*b*	0	0	0.5	1.0(8)	0.083
Li1	48h	0.29(1)	0.026(6)	0.71(1)	2.1(8)	0.36(4)
Li2	24g	0.25000	0.02160(3)	0.75000	-	0.21(9)
		$\beta_{11} = \beta_{33}$ = 0.002(8); β_{22} = 0.0007(8); $\beta_{12} = \beta_{13} = \beta_{23}$ = 0.000				
Li3	48h	0.2158(3)	0.4229(3)	0.9229(3)	-	0.03(8)
		β_{11} = 0.011(8); $\beta_{22} = \beta_{33}$ = 0.0002(2); $\beta_{12} = \beta_{13}$ = 0.003(1); β_{23} = 0.002(6)				

[a] *F*−43*m* space group, a = 10.1875(7) Å, V = 1057.33(4) Å^3, ρ = 2.325 g cm^{-3}, R_{wp} = 4.94%.

Table S10. Structural parameters for $Li_{6.33}[P_{0.5}Si_{0.167}Ge_{0.167}Sb_{0.167}]S_5I$ ($P_{0.5}$) from Rietveld analysis of NPD data collected at T = 298 K.[a]

Atom	Wyckoff site	*x*	*y*	*z*	B_{iso} / Å^2	Occ
I1	4*a*	0	0	0	1.7(8)	0.94(4)
S2	4*a*	0	0	0	1.7(8)	0.05(4)
S1	4*d*	0.25	0.25	0.75	2.52(6)	0.94(4)
I2	4*d*	0.25	0.25	0.75	2.52(6)	0.05(4)
S3	16*e*	0.1204(9)	−0.1204(9)	0.6204(9)	1.6(5)	1
Si1	4*b*	0	0	0.5	0.9(5)	0.167
Ge1	4*b*	0	0	0.5	0.9(5)	0.167
P1	4*b*	0	0	0.5	0.9(5)	0.5
Sb1	4*b*	0	0	0.5	0.9(5)	0.167
Li1	48*h*	0.299(0)	0.025(8)	0.701(9)	1.5(1)	0.28(2)
Li2	24*g*	0.25	0.021(9)	0.75	2.3(5)	0.41(8)
Li3	48*h*	0.231(8)	0.425(7)	0.925(7)	-	0.04(5)
		β_{11} = 0.007(2); β_{22} = β_{33} = 0.007(1); β_{12} = β_{13} = −0.006(0); β_{23} = −0.008(6)				

[a] *F*−43*m* space group, a = 10.2393(5) Å, V = 1073.53(9) Å^3, ρ = 2.379 g cm^{-3}, R_{wp} = 3.35%.

Table S11. Structural parameters for $Li_{6.66}[P_{0.167}Si_{0.5}Ge_{0.167}Sb_{0.167}]S_5I$ ($Si_{0.5}$) from Rietveld analysis of NPD data collected at T = 298 K.[a]

Atom	Wyckoff site	*x*	*y*	*z*	B_{iso} / Å^2	Occ
I1	4*a*	0	0	0	1.5(3)	0.987(3)
S2	4*a*	0	0	0	1.5(3)	0.013(3)
S1	4*d*	0.25	0.25	0.75	3.1(1)	0.987(3)
I2	4*d*	0.25	0.25	0.75	3.1(1)	0.013(3)
S3	16*e*	0.1214(2)	−0.1214(2)	0.6214(2)	2.4(0)	1
Si1	4*b*	0	0	0.5	1.00(7)	0.167
Ge1	4*b*	0	0	0.5	1.00(7)	0.5
P1	4*b*	0	0	0.5	1.00(7)	0.167
Sb1	4*b*	0	0	0.5	1.00(7)	0.167
Li1	48*h*	0.294(8)	0.014(8)	0.706(1)	3.2(4)	0.28(9)
Li2	24*g*	0.25	0.0275(1)	0.75	-	0.40(6)
		β_{11} = β_{33} = 0.009(3); β_{22} = 0.004(4); β_{12} = β_{13} = β_{23} = 0.000				
Li3	48*h*	0.277(1)	0.444(9)	0.944(9)	2.1(4)	0.04(8)
Li4	16*e*	0.150(9)	0.150(9)	0.150(9)	-	0.04(0)
		β_{11} = β_{22} = β_{33} = 0.03(7); β_{12} = β_{13} = β_{23} = 0.04(9)				

[a] *F*−43*m* space group, a = 10.2867(3) Å, V = 1088.51(9) Å^3, ρ = 2.349 g cm^{-3}, R_{wp} = 4.85%; LiI: wt.% 2.6(7).

Table S12. Structural parameters for $Li_{6.66}[P_{0.167}Si_{0.167}Ge_{0.5}Sb_{0.167}]S_5I$ ($Ge_{0.5}$) from Rietveld analysis of NPD data collected at T = 298 K.[a]

Atom	Wyckoff site	*x*	*y*	*z*	B_{iso} / Å^2	Occ
I1	4*a*	0	0	0	1.3(8)	0.997(3)
S2	4*a*	0	0	0	1.3(8)	0.003(3)
S1	4*d*	0.25	0.25	0.75	3.3(6)	0.997(3)
I2	4*d*	0.25	0.25	0.75	3.3(6)	0.003(3)
S3	16*e*	0.1236(9)	−0.1236(9)	0.6236(9)	2.3(5)	1
Si1	4*b*	0	0	0.5	0.98(9)	0.167
Ge1	4*b*	0	0	0.5	0.98(9)	0.5
P1	4*b*	0	0	0.5	0.98(9)	0.167
Sb1	4*b*	0	0	0.5	0.98(9)	0.167
Li1	48*h*	0.296(3)	0.012(9)	0.704(6)	3.0(3)	0.26(9)
Li2	24*g*	0.25	0.029(0)	0.75	-	0.45(1)
		$\beta_{11} = \beta_{33} = 0.007(3)$; $\beta_{22} = 0.001(7)$; $\beta_{12} = \beta_{13} = \beta_{23} = 0.000$				
Li3	48*h*	0.28(1)	0.43(7)	0.93(7)	2.1(4)	0.04(7)
		$\beta_{11} = 0.01(0)$; $\beta_{22} = \beta_{33} = 0.01(3)$; $\beta_{12} = \beta_{13} = -0.002(7)$; $\beta_{23} = -0.01(1)$				
Li4	16*e*	0.12(7)	0.12(7)	0.12(7)	-	0.03(2)
		$\beta_{11} = \beta_{22} = \beta_{33} = 0.03(0)$; $\beta_{12} = \beta_{13} = \beta_{23} = 0.04(6)$				

[a] *F*−43*m* space group, a = 10.3039(1) Å, V = 1093.970(2) Å^3, ρ = 2.426 g cm^{-3}, R_{wp} = 4.98%; LiI: wt.% 3.8(3).

Table S13. Structural parameters for $Li_{6.33}[P_{0.167}Si_{0.167}Ge_{0.167}Sb_{0.5}]S_5I$ ($Sb_{0.5}$) from Rietveld analysis of NPD data collected at T = 298 K.[a]

Atom	Wyckoff site	*x*	*y*	*z*	B_{iso} / Å^2	Occ
I1	4*a*	0	0	0	1.6(3)	0.999
S2	4*a*	0	0	0	1.6(3)	0.001
S1	4*d*	0.25	0.25	0.75	2.7(8)	0.999
I2	4*d*	0.25	0.25	0.75	2.7(8)	0.001
S3	16*e*	0.1252(0)	−0.1252(0)	0.6252(0)	2.0(6)	1
Si1	4*b*	0	0	0.5	1.16(6)	0.167
Ge1	4*b*	0	0	0.5	1.16(6)	0.167
P1	4*b*	0	0	0.5	1.16(6)	0.167
Sb1	4*b*	0	0	0.5	1.16(6)	0.5
Li1	48*h*	0.28(9)	0.025(3)	0.71(1)	4.1(8)	0.30(1)
Li2	24*g*	0.25	0.022(1)	0.75	-	0.31(6)

		$\beta_{11} = \beta_{33} = 0.01(6)$; $\beta_{22} = 0.006(7)$; $\beta_{12} = \beta_{13} = \beta_{23} = 0.000$				
Li3	48*h*	0.20(7)	0.43(4)	0.93(4)	0.6(2)	0.06(7)
		$\beta_{11} = 0.009(5)$; $\beta_{22} = \beta_{33} = 0.01(2)$; $\beta_{12} = \beta_{13} = 0.005(9)$; $\beta_{23} = -0.08(4)$				

[a] *F*−43*m* space group, a = 10.3390(3) Å, V = 1105.19(5) Å^3, ρ = 2.488 g cm^{-3}, R_{wp} = 4.96%.

Table S14. Structural parameters for $Li_{6.17}[P_{0.083}Si_{0.083}Ge_{0.083}Sb_{0.75}]S_5I$ ($Sb_{0.75}$) from Rietveld analysis of NPD data collected at T = 298 K.[a]

Atom	Wyckoff site	*x*	*y*	*z*	B_{iso} / Å^2	Occ
I1	4*a*	0	0	0	1.4(2)	0.979(1)
S2	4*a*	0	0	0	1.4(2)	0.021(1)
S1	4*d*	0.25	0.25	0.75	2.6(1)	0.979(1)
I2	4*d*	0.25	0.25	0.75	2.6(1)	0.021(1)
S3	16*e*	0.1274(3)	−0.1274(3)	0.6274(3)	1.62(0)	1
Si1	4*b*	0	0	0.5	1.10(5)	0.083
Ge1	4*b*	0	0	0.5	1.10(5)	0.083
P1	4*b*	0	0	0.5	1.10(5)	0.083
Sb1	4*b*	0	0	0.5	1.10(5)	0.75
Li1	48*h*	0.290(2)	0.021(5)	0.710(8)	2.8(8)	0.39(1)
Li2	24*g*	0.25	0.023(1)	0.75	-	0.24(3)
		$\beta_{11} = \beta_{33} = 0.004(3)$; $\beta_{22} = 0.003(5)$; $\beta_{12} = \beta_{13} = \beta_{23} = 0.000$				

[a] *F*−43*m* space group, a = 10.3810(2) Å, V = 1118.71(8) Å^3, ρ = 2.557 g cm^{-3}, R_{wp} = 4.90%; LiI: wt.% 1.8(4).

Table S15. Li–Li jump distances and possible diffusion pathways at T = 298 K for all samples. The data for $Li_{6.5}[Si_{0.25}Ge_{0.25}P_{0.25}Sb_{0.25}]S_5I$ was taken from the literature.[12] For comparison, the corresponding jump distances in Li_6PS_5I are also given (T = 300 K) from reference.[14]

Sample	Doublet / Å	Intracage / Å		Intercage / Å	
$Li_{6.17}[\mathbf{P_{0.75}}Si_{0.083}Ge_{0.083}Sb_{0.083}]S_5I$	1.20(4)	1	T5 $\underline{1.63(5)}$ T2 $\underline{1.63(5)}$ T5	1	T5 $\underline{1.63(5)}$ T2 $\underline{2.22(9)}$ T2 $\underline{1.63(5)}$ T5
		2	T5 $\underline{2.62(3)}$ T5	2	T5 $\underline{3.39(3)}$ T5
$Li_{6.33}[\mathbf{P_{0.5}}Si_{0.16}Ge_{0.16}Sb_{0.16}]S_5I$	1.42(0)	1	T5 $\underline{1.55(1)}$ T2 $\underline{1.55(1)}$ T5	1	T5 $\underline{1.55(1)}$ T2 $\underline{2.15(0)}$ T2 $\underline{1.55(1)}$ T5
		2	T5 $\underline{2.53(7)}$ T5	2	T5 $\underline{3.28(5)}$ T5
$Li_{6.67}[P_{0.16}\mathbf{Si_{0.5}}Ge_{0.16}Sb_{0.16}]S_5I$	1.30(3)	1	T5 $\underline{1.61(7)}$ T2 $\underline{1.61(7)}$ T5	1	T5 $\underline{1.61(7)}$ T2 $\underline{1.60(1)}$ T2 $\underline{1.61(7)}$ T5

		2	T5 2.77(4) T5	2	T5 1.88 T4 1.88 T5
				3	T5 3.20(4) T5
$Li_{6.5}[P_{0.25}Sb_{0.25}Si_{0.25}Ge_{0.25}]S_5I$	1.39(6)	1	T5 2.64(2) T5	1	T5 3.24(2) T5
$Li_{6.67}[P_{0.16}Si_{0.16}\mathbf{Ge_{0.5}}Sb_{0.16}]S_5I$	1.35(3)	1	T5 1.55(8) T2 1.55(8) T5	1	T5 1.55(8) T2 1.84(1) T2 1.55(8) T5
		2	T5 2.78(5) T5	2	T5 1.80(3) T4 1.80(3) T5
				3	T5 3.16(5) T5
$Li_{6.33}[P_{0.16}Si_{0.16}Ge_{0.16}\mathbf{Sb_{0.5}}]S_5I$	1.16(4)	1	T5 1.77(1) T2 1.77(1) T5	1	T5 1.77(1) T2 1.90(3) T2 1.77(1) T5
		2	T5 2.71(7) T5	2	T5 3.44 T5
$Li_{6.17}[P_{0.083}Si_{0.083}Ge_{0.083}\mathbf{Sb_{0.75}}]S_5I$	1.18(3)	1	T5 2.76(3) T5	1	T5 3.39(3) T5
Li_6PS_5I (300K)	1.25	1	T5 2.57 T5	1	T5 3.35 T5

Table S16. Overview of ionic conductivities at 25 °C, activation energies determined by EIS and ^{7}Li PFG NMR spectroscopy, and configurational entropy.

Sample	^{7}Li PFG NMR						EIS		ΔS_{conf} / R
	E_A / eV (maj. com.)	$D_{Li,\ 30°C}$ / m^2 s^{-1} (maj. com.)	$\sigma_{ion,\ 25\ °C}$ / mS cm^{-1} (maj. com.)	E_A / eV (min. com.)	$D_{Li,\ 30°C}$ / m^2 s^{-1} (min. com.)	$\sigma_{ion,\ 25\ °C}$ / mS cm^{-1} (min. com.)	E_A / eV	$\sigma_{ion,\ 25\ °C}$ / mS cm^{-1}	
$P_{0.75}$	0.37 ± 0.014	(9.80 ± 0.59)·10^{-14}	0.14	--	--	--	0.37 ± 0.002	0.043 ± 0.004	1.0
$P_{0.5}$	0.17 ± 0.002	(3.13 ± 0.19)·10^{-12}	5.06	0.08 ± 0.007	(1.59 ± 0.19)· 10^{-12}	2.87	0.22 ± 0.002	1.91 ± 0.016	1.64
$Si_{0.5}$	0.20 ± 0.002	(1.08 ± 0.01)· 10^{-11}	17.94	0.14 ± 0.013	(2.21 ± 0.30)· 10^{-12}	4.32	0.20 ± 0.006	12.00 ± 0.132	1.37
EQ	0.20 ± 0.002	(7.09 ± 0.03)·10^{-12}	11.82	--	--	--	0.19 ± 0.006	12.30 ± 0.700	2.08
$Ge_{0.5}$	0.25 ± 0.018	(7.64 ± 0.48)· 10^{-12}	11.87	0.24 ± 0.053	(2.30 ± 0.46)· 10^{-12}	4.14	0.21 ± 0.011	14.05 ± 1.019	1.29
$Sb_{0.5}$	0.16 ± 0.003	(5.59 ± 0.09) · 10^{-12}	9.00	--	--	--	0.23 ± 0.012	4.88 ± 0.673	1.25
$Sb_{0.75}$	0.26 ± 0.004	(5.16 ± 0.02)· 10^{-13}	0.76	--	--	--	0.29 ± 0.009	0.760 ± 0.071	1.04

Table S17. Electronic conductivities determined from DC measurements. The data for $Li_{6.5}[P_{0.25}Si_{0.25}Ge_{0.25}Sb_{0.25}]S_5I$ (EQ) was taken from the literature.[1,12]

Sample	σ_{el} / mS cm^{-1}
$P_{0.75}$	$5.55 \cdot 10^{-8}$
$P_{0.5}$	$1.37 \cdot 10^{-8}$
$Si_{0.5}$	$4.13 \cdot 10^{-5}$
EQ	$3.18 \cdot 10^{-7}$
$Ge_{0.5}$	$3.83 \cdot 10^{-5}$
$Sb_{0.5}$	$7.41 \cdot 10^{-6}$
$Sb_{0.75}$	$5.82 \cdot 10^{-6}$

Table S18. Li-ion mobility, charge-carrier density, and ionic conductivity at T = 298 K (if not stated otherwise), and activation energy determined by EIS for different lithium argyrodites, as well as for $Li_{10}GeP_2S_{12}$.

Material	μ_{Li+} / cm^2 V^{-1} s^{-1}	n / 10^{22} cm^{-3}	σ_{ion} / mS cm^{-1}	E_A / eV	Ref.
$Li_{10}GeP_2S_{12}$	$2.27 \cdot 10^{-6}$	2.09	6.96 ± 0.41	0.27 ± 0.003	[15][16]
Li_6PS_5Cl	$4.98 \cdot 10^{-7}$	2.47	1.93 ± 0.4	0.45 ± 0.02	[14][16]
$Li_6PS_5Cl_{0.5}Br_{0.5}$	$8.42 \cdot 10^{-7}$	2.43	3.28 ± 0.67	0.36 ± 0.02	[14][16]
Li_6PS_5Br	$2.94 \cdot 10^{-7}$	2.39	1.09 ± 0.11	0.30 ± 0.01	[14][16]
$Li_6PS_5Br_{0.5}I_{0.5}$	$6.92 \cdot 10^{-9}$	2.90	0.26 ± 0.03	0.31 ± 0.004	[14][16]
Li_6PS_5I	$3.43 \cdot 10^{-10}$	2.27	0.01 ± 0.001	0.38 ± 0.02	[14][16]
Li_6PS_5I	$3.4 \cdot 10^{-10}$	2.30	0.01 ± 0.001	0.37 ± 0.01	[17][16]
$Li_{6.25}P_{0.75}Ge_{0.25}S_5I$	$3.97 \cdot 10^{-8}$	2.36	0.32 ± 0.05	0.35 ± 0.002	[17][16]
$Li_{6.5}P_{0.5}Ge_{0.5}S_5I$	$4.75 \cdot 10^{-7}$	2.42	1.50 ± 0.23	0.23 ± 0.002	[17][16]
$Li_{6.6}P_{0.4}Ge_{0.6}S_5I$	$1.31 \cdot 10^{-6}$	2.46	5.81 ± 0.68	0.23 ± 0.002	[17][16]
$Li_{6.6}Si_{0.6}Sb_{0.4}S_5I$	$3.88 \cdot 10^{-6}$	2.38	14.8 (302 K)	0.25	[16][18]
$Li_{6.17}[\mathbf{P_{0.75}}Si_{0.083}Ge_{0.083}Sb_{0.083}]S_5I$	$3.07 \cdot 10^{-8}$	2.32	0.043 ± 0.004	0.37 ± 0.002	This work
$Li_{6.33}[\mathbf{P_{0.5}}Si_{0.16}Ge_{0.16}Sb_{0.16}]S_5I$	$1.09 \cdot 10^{-6}$	2.35	1.91 ± 0.016	0.22 ± 0.002	This work

$Li_{6.67}[P_{0.16}\mathbf{Si_{0.5}}Ge_{0.16}Sb_{0.16}]S_5I$	$3.72 \cdot 10^{-6}$	2.44	12.00 ± 0.132	0.20 ± 0.006	This work
$Li_{6.5}[P_{0.25}Sb_{0.25}Si_{0.25}Ge_{0.25}]S_5I$	$2.76 \cdot 10^{-6}$	2.38	12.30 ± 0.700	0.19 ± 0.006	[12]
$Li_{6.67}[P_{0.16}Si_{0.16}\mathbf{Ge_{0.5}}Sb_{0.16}]S_5I$	$2.33 \cdot 10^{-6}$	2.43	14.05 ± 1.019	0.21 ± 0.011	This work
$Li_{6.33}[P_{0.16}Si_{0.16}Ge_{0.16}\mathbf{Sb_{0.5}}]S_5I$	$1.97 \cdot 10^{-6}$	2.29	4.88 ± 0.673	0.23 ± 0.012	This work
$Li_{6.17}[P_{0.083}Si_{0.083}Ge_{0.083}\mathbf{Sb_{0.75}}]S_5I$	$1.71 \cdot 10^{-7}$	2.20	0.760 ± 0.071	0.29 ± 0.009	This work

References

[1] J. Lin, M. Schaller, G. Cherkashinin, S. Indris, J. Du, C. Ritter, A. Kondrakov, J. Janek, T. Brezesinski, F. Strauss, *Small* **2024**, *20*, 2306832.

[2] A. C. Dippel, H. P. Liermann, J. T. Delitz, P. Walter, H. Schulte-Schrepping, O. H. Seeck, H. Franz, *J. Synchrotron Radiat.* **2015**, *22*, 675.

[3] G. Ashiotis, A. Deschildre, Z. Nawaz, J. P. Wright, D. Karkoulis, F. E. Picca, J. Kieffer, *J. Appl. Crystallogr.* **2015**, *48*, 510.

[4] H. M. Rietveld, *J. Appl. Cryst.* **1969**, 2, 65.

[5] J. Rodríguez-Carvajal, *Phys. B* **1993**, *192*, 55.

[6] P. Fischer, G. Frey, M. Koch, M. Ko, V. Pomjakushin, J. Schefer, R. Thut, N. Schlumpf, R. Bu, U. Greuter, S. Bondt, E. Berruyer, **2000**, *278*, 146.

[7] W. S. Price, *Concepts Magn. Reson.* **1998**, *10*, 197.

[8] K. S. Han, J. D. Bazak, Y. Chen, T. R. Graham, N. M. Washton, J. Z. Hu, V. Murugesan, K. T. Mueller, *Chem. Mater.* **2021**, *33*, 8562.

[9] E. O. Stejskal, J. E. Tanner, *J. Chem. Phys.* **1965**, *42*, 288.

[10] D. Wijesekera, T. Stait-Gardner, A. Gupta, J. Chen, G. Zheng, A. M. Torres, W. S. Price, *Concepts Magn. Reson. Part A.* **2019**, *47A*, e21468.

[11] E. P. Ramos, J. D. Bazak, A. Assoud, A. Huq, G. Goward, L. F. Nazar, *ACS Appl. Mater. Interfaces* **2022**, *14*, 56767.

[12] J. Lin, G. Cherkashinin, M. Schäfer, G. Melinte, S. Indris, A. Kondrakov, J. Janek, T. Brezesinski, F. Strauss, *ACS Mater. Lett.* **2022**, *4*, 2187.

[13] H. J. Deiseroth, S. T. Kong, H. Eckert, J. Vannahme, C. Reiner, T. Zaiß, M. Schlosser, *Angew. Chem., Int. Ed.* **2008**, *47*, 755.

[14] M. A. Kraft, S. P. Culver, M. Calderon, F. Böcher, T. Krauskopf, A. Senyshyn, C. Dietrich, A. Zevalkink, J. Janek, W. G. Zeier, *J. Am. Chem. Soc.* **2017**, *139*, 10909.

[15] T. Krauskopf, S. P. Culver, W. G. Zeier, *Chem. Mater.* **2018**, *30*, 1791.

[16] J. Janek, W. G. Zeier, *Nat. Energy* **2023**, *8*, 230.

[17] M. A. Kraft, S. Ohno, T. Zinkevich, R. Koerver, S. P. Culver, T. Fuchs, A. Senyshyn, S. Indris, B. J. Morgan, W. G. Zeier, *J. Am. Chem. Soc.* **2018**, *140*, 16330.

[18] L. Zhou, A. Assoud, Q. Zhang, X. Wu, L. F. Nazar, *J. Am. Chem. Soc.* **2019**, *141*, 19002.

6.3.4. Publication IV

Angewandte Chemie
Eine Zeitschrift der Gesellschaft Deutscher Chemiker

Supporting Information

High-Entropy Lithium Argyrodite Solid Electrolytes Enabling Stable All-Solid-State Batteries

S. Li, J. Lin, M. Schaller, S. Indris, X. Zhang, T. Brezesinski, C.-W. Nan, S. Wang, F. Strauss**

Experimental

Synthesis. The $Li_{5.5}PS_{4.5}Cl_xBr_{1.5-x}$ (with x = 0, 0.2, 0.4, 0.6, 0.8, 1.0, 1.2 and 1.5) solid electrolytes were prepared via solid-state reaction. The starting materials Li_2S (Alfa Aesar, 99.9%), P_2S_5 (Sigma-Aldrich, 99%), LiCl (Aladdin, 99%) and LiBr (Alfa Aesar, 99.9%) were weighed in an appropriate ratio and then blended using a planetary ball mill (FRITSCH PULVERISETTE 7 premium line) for 2 h at 110 rpm. Then, the mixtures were pressed into pellets and sealed in quartz ampules using a vacuum sealing machine (VS-Q2, Guangzhou SunJune technology Co. Ltd.). Next, the ampules were put into a furnace and annealed at 430-450 °C for 6 h using a heating rate of 90 °C h^{-1}. Finally, they were cooled down to r.t. naturally inside the furnace.

Laboratory X-ray diffraction (XRD). The samples were sealed in borosilicate capillaries (Hilgenberg, 0.68 mm inner diameter and 0.01 mm wall thickness) under Ar atmosphere and subjected to XRD analysis using a STOE Stadi-P diffractometer with a DECTRIS MYTHEN 1K strip detector in Debye-Scherrer geometry. The instrument utilizes a Mo anode to generate X-rays of wavelength λ = 0.70926 Å.

Neutron powder diffraction (NPD). For NPD measurements, cylindrical vanadium containers of diameter 6 mm were filled with around 2 g of sample. The measurements were conducted either at the Oak Ridge National Laboratory (ORNL) POWGEN beamline using a wavelength of λ = 1.5 Å or at the HRPT instrument at the Paul Scherrer Institute (PSI) using a wavelength of λ = 1.494 Å at r.t..[1] The diffraction data were analyzed via Rietveld refinement using FullProf Suite software.[2] The peak shape was described using the Thompson-Cox-Hastings pseudo-Voigt function and a point-by-point background was subtracted. The following parameters were refined one by another: scale factor, peak shape parameters, lattice parameters, shared $S^{2-}/Cl^-/Br^-$ occupancies on the 4*a*/4*d* site, atomic coordinates, individual anisotropic atomic displacement parameters and lithium occupancies. The zero-shift parameter was refined last and any positions for which occupancy or displacement factors resulted in unreasonable values were disregarded. Finally, all parameters were refined simultaneously to ensure stability of the calculated structure.

^{6}Li and ^{31}P magic-angle spinning (MAS) nuclear magnetic resonance (NMR) spectroscopy. A Bruker Avance 500 MHz spectrometer was used for MAS NMR measurements with a magnetic field strength of 11.7 T, corresponding to resonance frequencies of 73.6 and 202.5 MHz for ^{6}Li and ^{31}P, respectively. The samples were inserted into 2.5 mm rotors under Ar atmosphere and subjected to spinning at a frequency of 30 kHz. The π/2 pulse length was 2.8 µs for ^{6}Li and 2.1 µs for ^{31}P, while the recycle delay was set to 30 s for ^{6}Li and 60 s for ^{31}P. The chemical shifts are referenced to 1 M ^{6}LiCl for ^{6}Li and 85% H_3PO_4 for ^{31}P. Fitting of the spectra was done using DMFIT.[3]

Temperature-dependent ^{7}Li pulsed field gradient (PFG) NMR spectroscopy. Temperature-dependent ^{7}Li PFG NMR experiments were conducted using a Bruker Advance 300 MHz spectrometer. The samples were enclosed in an evacuated 5 mm borosilicate glass tube and a PFG probe with a maximum gradient field strength of 30

T m^{-1} was utilized. To suppress the effect of eddy currents, a stimulated echo pulse sequence with bipolar gradients was used.[4,5] Experimental data were collected in the temperature range of 302-345 K. The π/2 pulse length was between 5.35 and 5.9 µs and the recycle delay was 0.4-0.6 s. For all samples and temperatures, the gradient duration and diffusion time were 3 and 30 ms, respectively.

Electrochemical impedance spectroscopy (EIS). To determine the ionic conductivity and activation energy for lithium diffusion, 120 mg of $Li_{5.5}PS_{4.5}Cl_xBr_{1.5-x}$ was pressed into pellets of diameter 10 mm at 150 MPa. Two stainless steel rods were attached to the pellets as current collectors. AC impedance measurements were performed at r.t. in the frequency range between 8 MHz and 1 Hz with an amplitude of 10 mV using an impedance analyzer (ZAHNER, ZENNIUM PRO). The impedance data were collected in the temperature range of 10-60 °C.

To prepare a sintered 10 mm diameter pellet, 400 mg of annealed $Li_{5.5}PS_{4.5}Cl_{0.8}Br_{0.7}$ was hot pressed at 2 t and 400 °C for 5 h. After that, two pieces of indium foil were attached to both sides to ensure good contact. EIS measurements were performed at r.t. and an external pressure of 150 MPa, as described above.

Scanning electron microscopy (SEM) with energy dispersive X-ray spectroscopy (EDS). The morphology and chemical composition of the $Li_{5.5}PS_{4.5}Cl_{0.8}Br_{0.7}$ powder were examined by SEM (Zeiss Merlin) at an acceleration voltage of 15 kV and EDS.

Electrode preparation, cell assembly and electrochemical measurements. The composite cathode was prepared by hand mixing single-crystal $LiNi_{0.9}Co_{0.06}Mn_{0.04}O_2$ (Li_3BO_3@s-NCM90, provided by BASF Shanshan Battery Materials Co., Ltd.), $Li_{5.5}PS_{4.5}Cl_{0.8}Br_{0.7}$ and Super C65 carbon black in a weight ratio of 70:30:1 for 1 h. SSB cells were assembled as follows: Firstly, 80 mg of $Li_{5.5}PS_{4.5}Cl_{0.8}Br_{0.7}$ was pressed at 100 MPa in a PEEK housing of diameter 10 mm. Then, 10 µm-thick Li foil of diameter 4 mm (China Energy Lithium Co., Ltd.) was put onto the solid electrolyte pellet followed by 30 µm-thick In foil of diameter 9 mm (Zhejiang Haosheng New Material Co., Ltd.) and pressing at 100 MPa. Afterwards, the cathode composite was spread onto the other side of the pellet and the stack was pressed at 50 MPa. Finally, a pressure of 150 MPa was applied for 3 min. The SSBs were tested in a customized Swagelok cell at a constant pressure of 120 MPa using a LANHE battery testing system (CT3001A) in the potential window of 2.4-3.7 V vs. In/InLi, corresponding to ~3.0-4.3 V vs. Li^+/Li. All cell cycling was carried out in a glovebox at r.t. The C-rate was either set to 0.1C or 2C, with 1C = 200 mA g^{-1}.

Calculation of configurational entropy. The ΔS_{conf} was calculated based on the following equation: $\Delta S_{\mathrm{config}} = -R\left(\sum_{\mathrm{i}=1}^{\mathrm{N}} x_{\mathrm{i}} \ln x_{\mathrm{i}}\right)$. Here, x_i and x_j represent the mole fraction of elements on the specific Wyckoff positions. *R* and *N* are the universal gas constant and number of anion species. Note that in the presented materials, configurational entropy is solely introduced via anion mixing [S^{2-}, Cl^- and Br^- are distributed over two crystallographic sites, namely 4*a* and 4*d*, in the argyrodite structure, see **Figure 3e**). Calculated ΔS_{conf} values are given in **Table S10**.

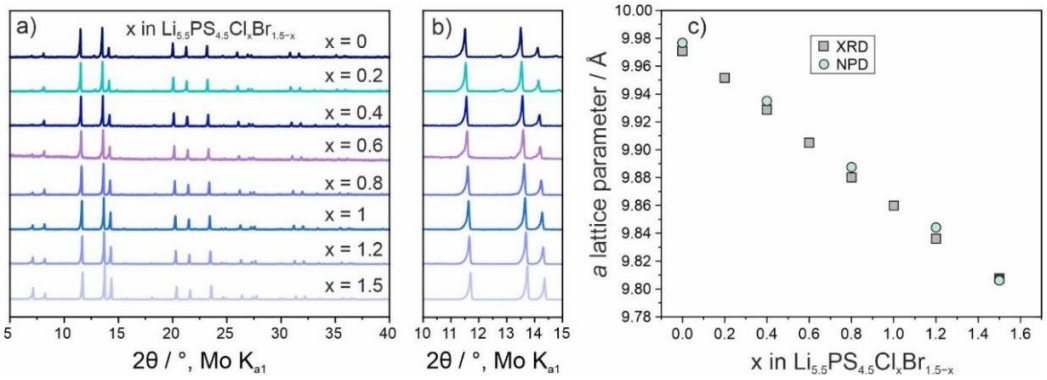

Figure S1. (a) Laboratory XRD patterns of the $Li_{5.5}PS_{4.5}Cl_xBr_{1.5-x}$ samples and (b) magnified view on the main reflections. (c) Calculated lattice parameters from XRD and NPD experiments.

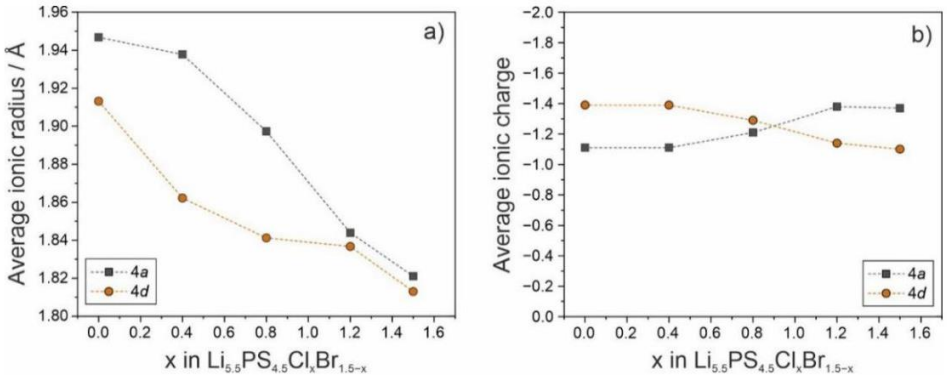

Figure S2. (a) Average ionic radius on the 4*a* and 4*d* Wyckoff positions calculated from the refined occupancies and (b) corresponding average ionic charge.

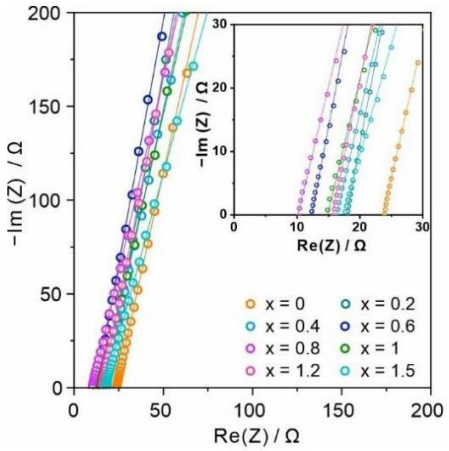

Figure S3. Nyquist plots of the electrochemical impedance measured at 25 °C for the different $Li_{5.5}PS_{4.5}Cl_xBr_{1.5-x}$ samples.

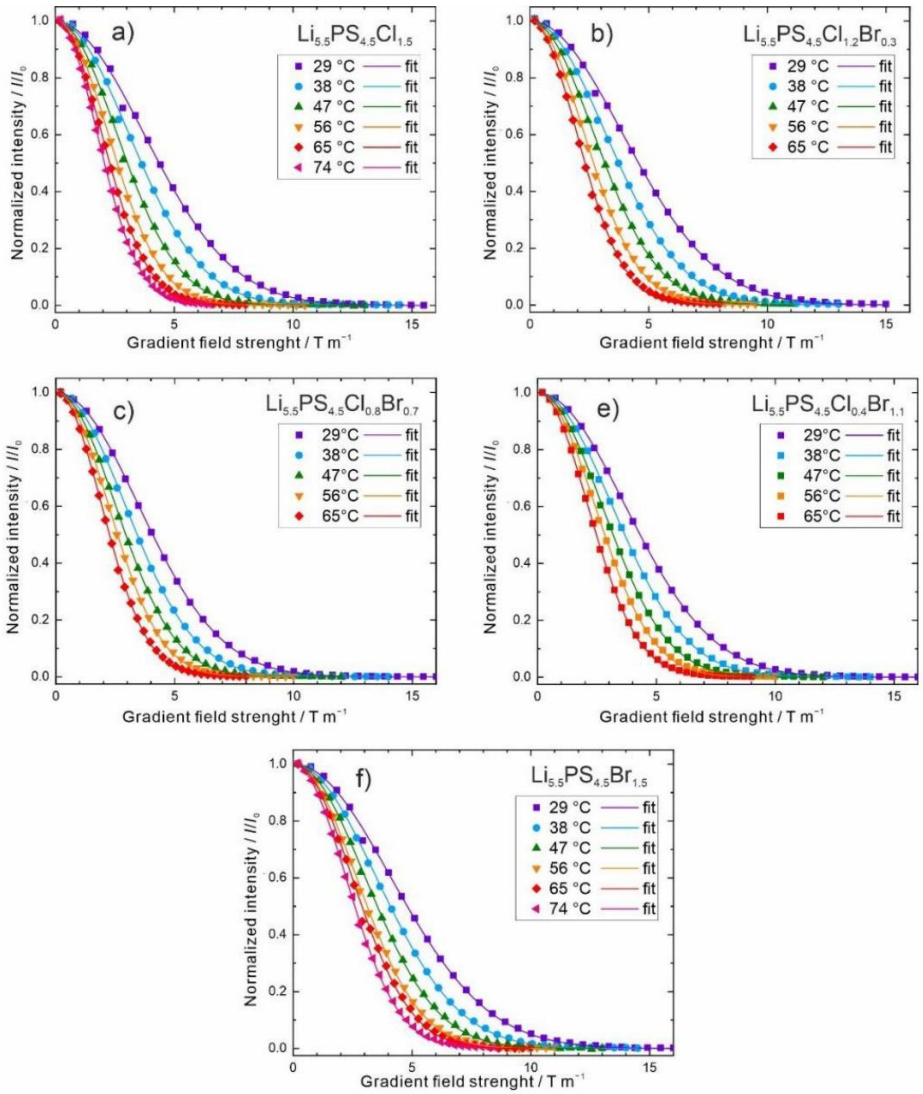

Figure S4. Results from temperature-dependent ^{7}Li PFG NMR spectroscopy measurements for selected $Li_{5.5}PS_{4.5}Cl_xBr_{1.5-x}$ samples as indicated.

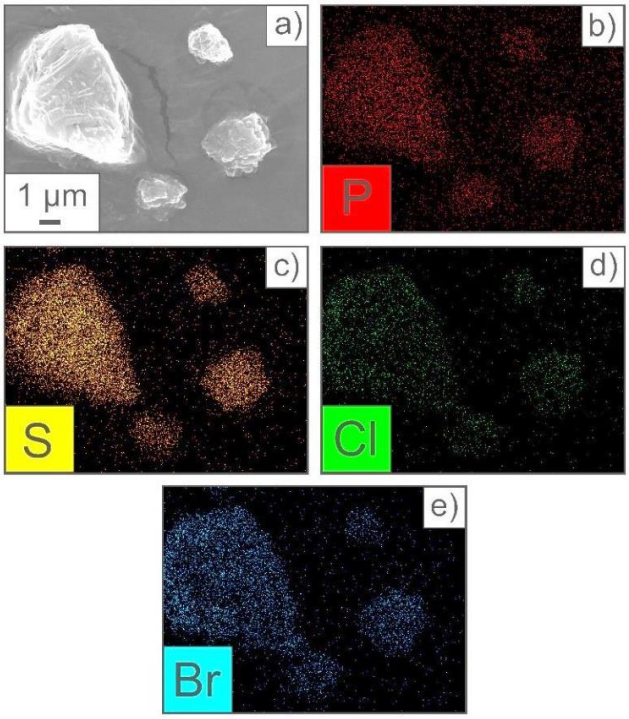

Figure S5. (a) SEM images of the $Li_{5.5}PS_{4.5}Cl_{0.8}Br_{0.7}$ sample and (b-e) corresponding elemental maps for P, S, Cl and Br.

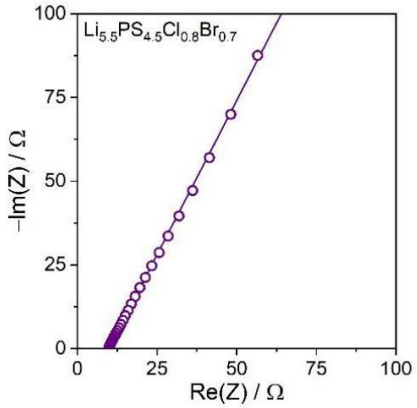

Figure S6. Nyquist plot of the electrochemical impedance measured at 25 °C on the hot-pressed $Li_{5.5}PS_{4.5}Cl_{0.8}Br_{0.7}$ sample.

Table S1. Calculated lattice parameters from laboratory XRD and NPD experiments.

x in $Li_{5.5}PS_{4.5}Cl_xBr_{1.5-x}$	a / Å (XRD)	a / Å (NPD)
0	9.97079	9.97671
0.2	9.9515	-
0.4	9.92871	9.93497
0.6	9.90504	-
0.8	9.88014	9.88741
1.0	9.85985	-
1.2	9.83612	9.84409
1.5	9.80753	9.80603

Table S2. Structural parameters for $Li_{5.5}PS_{4.5}Cl_{1.5}$ from Rietveld refinement analysis of NPD data collected at T = 297 K.[a]

Atom	Wyckoff site	x	y	z	B_{iso} / Å^2	Occ
Cl1	4*a*	0	0	0	1.199(8)	0.632(2)
S1	4*a*	0	0	0	1.199(8)	0.368(2)
Cl2	4*d*	0.25	0.25	0.75	3.380(1)	0.903(6)
S2	4*d*	0.25	0.25	0.75	3.380(1)	0.097(6)
S3	16*e*	0.1237	−0.1237	0.6237	4.340(2)	1
P1	4*b*	0	0	0.5	3.237(2)	1
Li1	48*h*	0.3175(6)	0.0226(9)	0.6824(6)	5.675(3)	0.458

[a] *F*−43*m* space group, a = 9.80603(8) Å, V = 942.930(1) Å^3, ρ = 1.879 g cm^{-3}, R_{wp} = 11.5%, χ^2 = 27.8.

Table S3. Structural parameters for $Li_{5.5}PS_{4.5}Cl_{1.2}Br_{0.3}$ from Rietveld refinement analysis of NPD data collected at T = 298 K.[a]

Atom	Wyckoff site	x	y	z	B_{iso} / Å^2	Occ
Cl1	4*a*	0	0	0	1.454(8)	0.490(9)
Br1	4*a*	0	0	0	1.454(8)	0.155(9)
S1	4*a*	0	0	0	1.454(8)	0.403(9)
Cl2	4*d*	0.25	0.25	0.75	3.246(2)	0.716(9)
Br2	4*d*	0.25	0.25	0.75	3.246(2)	0.145(9)
S2	4*d*	0.25	0.25	0.75	3.246(2)	0.136(9)
S3	16*e*	0.1237	−0.1237	0.6237	4.832(2)	1
P1	4*b*	0	0	0.5	3.264(1)	1
Li1	48*h*	0.3194(2)	0.03164(8)	0.6806(2)	7.748(4)	0.458

[a] *F*−43*m* space group, a = 9.84409(1) Å, V = 953.953(2) Å^3, ρ = 2.787 g cm^{-3}, R_{wp} = 5.20%, χ^2 = 2.58.

Table S4. Structural parameters for $Li_{5.5}PS_{4.5}Cl_{0.8}Br_{0.7}$ from Rietveld refinement analysis of NPD data collected at T = 298 K.[a]

Atom	Wyckoff site	*x*	*y*	*z*	B_{iso} / Å^2	Occ
Cl1	4*a*	0	0	0	3.125(1)	0.253(7)
Br1	4*a*	0	0	0	3.125(1)	0.553(7)
S1	4*a*	0	0	0	3.125(1)	0.210(7)
Cl2	4*d*	0.25	0.25	0.75	2.564 (2)	0.555(7)
Br2	4*d*	0.25	0.25	0.75	2.564 (2)	0.147(7)
S2	4*d*	0.25	0.25	0.75	2.564(2)	0.289(7)
S3	16*e*	0.1237	−0.1237	0.6237	3.119(2)	1
P1	4*b*	0	0	0.5	1.935(1)	1
Li1	48*h*	0.3106(9)	0.0225(1)	0.6894(9)	4.421(4)	0.375(6)
Li2	24*g*	0.25	0.02448(4)	0.75	1.389(1)	0.166(2)

[a] *F*−43*m* space group, a = 9.88741(16) Å, V = 966.602(3) Å^3, ρ = 2.563 g cm^{-3}, R_{wp} = 5.51%, χ^2 = 2.36.

Table S5. Structural parameters for $Li_{5.5}PS_{4.5}Cl_{0.4}Br_{1.1}$ from Rietveld refinement analysis of NPD data collected at T = 298 K.[a]

Atom	Wyckoff site	*x*	*y*	*z*	B_{iso} / Å^2	Occ
Cl1	4*a*	0	0	0	3.011(1)	0.059(2)
Br1	4*a*	0	0	0	3.011(1)	0.823(2)
S1	4*a*	0	0	0	3.011(1)	0.108(2)
Cl2	4*d*	0.25	0.25	0.75	2.849(2)	0.341(2)
Br2	4*d*	0.25	0.25	0.75	2.849(2)	0.277(2)
S2	4*d*	0.25	0.25	0.75	2.849(2)	0.390(2)
S3	16*e*	0.1237	−0.1237	0.6237	2.550(9)	1
P1	4*b*	0	0	0.5	1.614(1)	1
Li1	48*h*	0.3071(8)	0.0220(1)	0.6928(9)	4.656(3)	0.375(1)
Li2	24*g*	0.25	0.01587(4)	0.75	1.387(2)	0.166(1)

[a] *F*−43*m* space group, a = 9.93497(13) Å, V = 980.619(22) Å^3, ρ = 2.424 g cm^{-3}, R_{wp} = 5.12%, χ^2 = 2.00.

Table S6. Structural parameters for $Li_{5.5}PS_{4.5}Br_{1.5}$ from Rietveld refinement analysis of NPD data collected at T = 297 K.[a]

Atom	Wyckoff site	*x*	*y*	*z*	B_{iso} / Å^2	Occ
Br1	4*a*	0	0	0	3.580(1)	0.893(2)
S1	4*a*	0	0	0	3.580(1)	0.107(2)
Br2	4*d*	0.25	0.25	0.75	2.087(2)	0.607(2)
S2	4*d*	0.25	0.25	0.75	2.087(2)	0.393(2)
S3	16*e*	0.1237	−0.1237	0.6237	2.144(9)	1

P1	4*b*	0	0	0.5	1.045(6)	1
Li1	48*h*	0.3076(9)	0.0185(9)	0.6923(6)	5.018(2)	0.374(2)
Li2	24*g*	0.25	0.01508(4)	0.75	1.385(6)	0.168(2)

[a] *F*−43*m* space group, a = 9.97671(6) Å, V = 993.029(11) Å^3, ρ = 2.264 g cm^{-3}, R_{wp} = 13.5%, χ^2 = 10.3.

Table S7. Li^+-Li^+ jump distances for the different $Li_{5.5}PS_{4.5}Cl_xBr_{1.5-x}$ samples.

Material	48*h*-48*h* / Å	Intracage / Å	Intercage / Å
$Li_{5.5}PS_{4.5}Cl_{1.5}$	1.87(3)	2.21(3)	2.84(3)
$Li_{5.5}PS_{4.5}Cl_{1.2}Br_{0.3}$	1.92(3)	2.15(3)	2.90(3)
$Li_{5.5}PS_{4.5}Cl_{0.8}Br_{0.7}$	1.89(3)	2.07(19)	2.88(19)
$Li_{5.5}PS_{4.5}Cl_{0.4}Br_{1.1}$	1.78(2)	2.21(3)	2.96(3)
$Li_{5.5}PS_{4.5}Br_{1.5}$	1.82(4)	2.31(6)	2.92(6)

Table S8. Nominal and calculated compositions for the different $Li_{5.5}PS_{4.5}Cl_xBr_{1.5-x}$ samples.

Nominal composition	Refined composition
$Li_{5.5}PS_{4.5}Cl_{1.5}$	$Li_{5.496}PS_{4.46(5)}Cl_{1.53(5)}$
$Li_{5.5}PS_{4.5}Cl_{1.2}Br_{0.3}$	$Li_{5.496}PS_{4.53(9)}Cl_{1.20(6)}Br_{0.30(0)}$
$Li_{5.5}PS_{4.5}Cl_{0.8}Br_{0.7}$	$Li_{5.49(6)}PS_{4.49(9)}Cl_{0.80(8)}Br_{0.7(0)}$
$Li_{5.5}PS_{4.5}Cl_{0.4}Br_{1.1}$	$Li_{5.49(6)}PS_{4.49(8)}Cl_{0.40(0)}Br_{1.10(0)}$
$Li_{5.5}PS_{4.5}Br_{1.5}$	$Li_{5.49(6)}PS_{4.50(0)}Br_{1.5(0)}$

Table S9. Ionic conductivities and corresponding activation energies calculated from EIS or ^{7}Li PFG NMR spectroscopy data collected at 25 °C.

x in $Li_{5.5}PS_{4.5}Cl_xBr_{1.5-x}$	σ_{ion} / mS cm^{-1} (EIS)	σ_{ion} / mS cm^{-1} (PFG NMR)	E_A / eV (EIS)	E_A / eV (PFG NMR)
0	4.16 ± 0.60	16.4	0.34 ± 0.02	0.24 ± 0.02
0.2	6.32 ± 0.56	-	0.32 ± 0.01	-
0.4	7.15 ± 0.7	20.03	0.31 ± 0.01	0.27 ± 0.01
0.6	8.65 ± 0.57	-	0.31 ± 0.01	-
0.8	9.56 ± 0.87	22.71	0.30 ± 0.01	0.28 ± 0.01
1.0	8.54 ± 0.81	-	0.31 ± 0.02	-
1.2	8.08 ± 0.54	18.03	0.32 ± 0.02	0.32 ± 0.01
1.5	7.11 ± 0.48	19.85	0.33 ± 0.01	0.29 ± 0.02

Table S10. Calculated configurational entropy for the different $Li_{5.5}PS_{4.5}Cl_xBr_{1.5-x}$ samples.

Material	ΔS_{conf} / R
$Li_{5.5}PS_{4.5}Cl_{1.5}$	0.98
$Li_{5.5}PS_{4.5}Cl_{1.2}Br_{0.3}$	1.67
$Li_{5.5}PS_{4.5}Cl_{0.8}Br_{0.7}$	1.98
$Li_{5.5}PS_{4.5}Cl_{0.4}Br_{1.1}$	1.66
$Li_{5.5}PS_{4.5}Br_{1.5}$	1.02

References

[1] P. Fischer, G. Frey, M. Koch, M. Könnecke, V. Ponjakushin, J. Schefer, R. Thut, N. Schlumpf, R. Bürge, U. Greuter, S. Bondt, E. Berruyer, *Physica B Condens. Matter* **2000**, 276 ,146–147.

[2] J. Rodríguez-Carvajal, *Physica B Condens. Matter* **1993**, *192*, 55–69.

[3] D. Massiot, F. Fayon, M. Capron, I. King, S. Le Calvé, B. Alonso, J.-O. Durand, B. Bujoli, Z. Gan, G. Hoatson, *Magn. Reson. Chem.* **2002**, *40*, 70–76.

[4] K. S. Han, J. D. Bazak, Y. Chen, T. R. Graham, N. M. Washton, J. Z. Hu, V. Murugesan, K. T. Mueller, *Chem. Mater.* **2021**, *33*, 8562–8590.

[5] W. S. Price, *Concepts in Magn. Reson.* **1997**, *9*, 299–336.

6.3.5. Publication V

Supporting Information

Electrochemical Testing and Benchmarking of Compositionally Complex Lithium Argyrodite Electrolytes for All-Solid-State Battery Application

Jianxuan Du,[#[a]] Jing Lin,[#[a]] Ruizhuo Zhang,[[a]] Shuo Wang,[[b,c]] Sylvio Indris,[[d]] Helmut Ehrenberg,[[d]] Aleksandr Kondrakov,[[a,e]] Torsten Brezesinski*[[a]] and Florian Strauss*[[a]]

[a] J. Du, J. Lin, R. Zhang, Dr. A. Kondrakov, Dr. T. Brezesinski, Dr. F. Strauss

Battery and Electrochemistry Laboratory (BELLA), Institute of Nanotechnology, Karlsruhe Institute of Technology (KIT), Kaiserstr. 12, 76131 Karlsruhe, Germany

[b] Prof. S. Wang

Center of Smart Materials and Devices, State Key Laboratory of Advanced Technology for Materials Synthesis and Processing, School of Material Science and Engineering, Wuhan University of Technology, Wuhan 430070, China

[c] Prof. S. Wang

Foshan (Southern China) Institute for New Materials, Foshan 528200, China

[d] Dr. S. Indris, Prof. H. Ehrenberg

Institute for Applied Materials–Energy Storage Systems (IAM-ESS), Karlsruhe Institute of Technology (KIT), Kaiserstr. 12, 76131 Karlsruhe, Germany

[e] Dr. A. Kondrakov

BASF SE, Carl-Bosch-Str. 38, 67056 Ludwigshafen, Germany

[#] Contributed equally to this work.

Email: torsten.brezesinski@kit.edu, florian.strauss@kit.edu

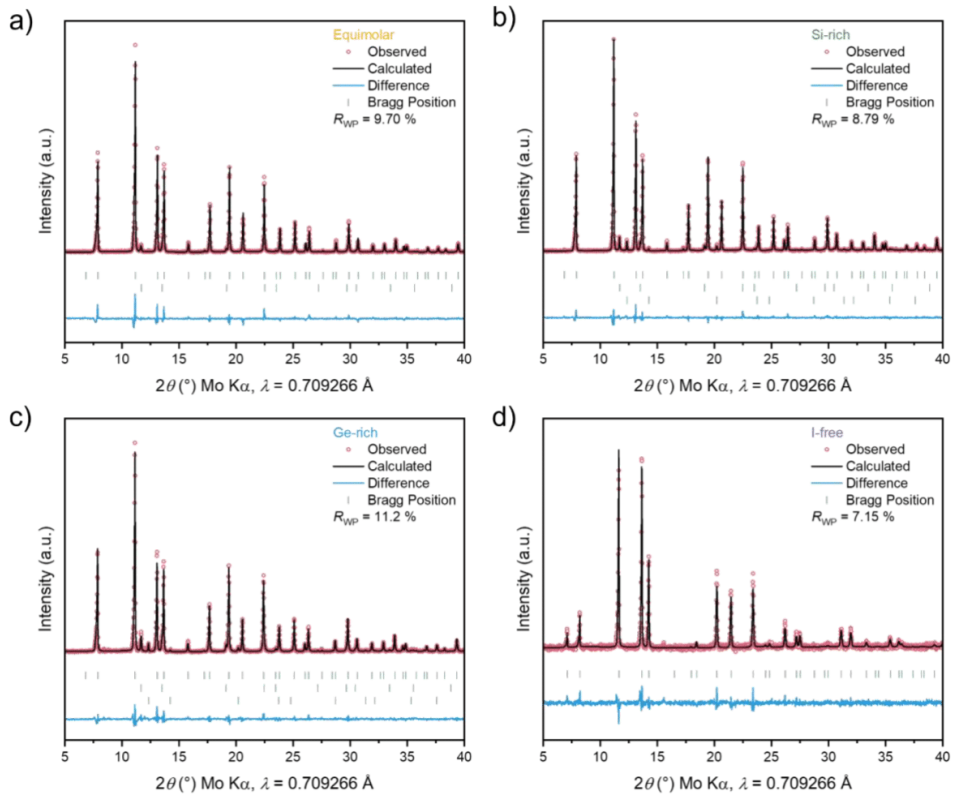

Figure S1. (a-d) XRD patterns and corresponding Rietveld plots [Le Bail analysis in (d)] for the different solid electrolytes. The observed, calculated, and difference profiles are shown in red, black, and blue, respectively. Vertical tick marks denote the expected Bragg reflections for the majority (argyrodite) phase and minor impurities.

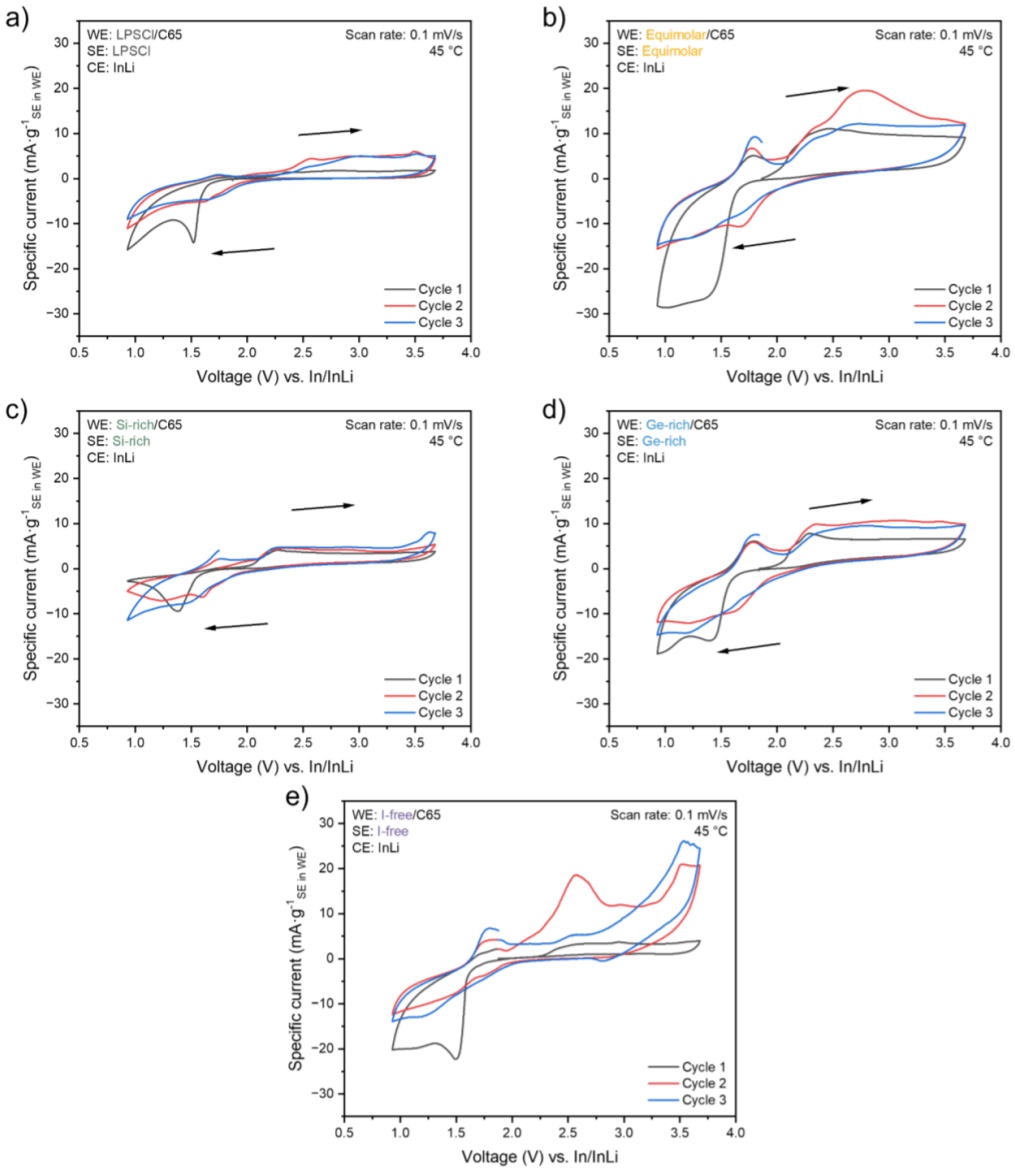

Figure S2. (a-e) CV curves of the first three cycles at 0.1 mV s^{-1} and 45 °C for the different solid electrolytes.

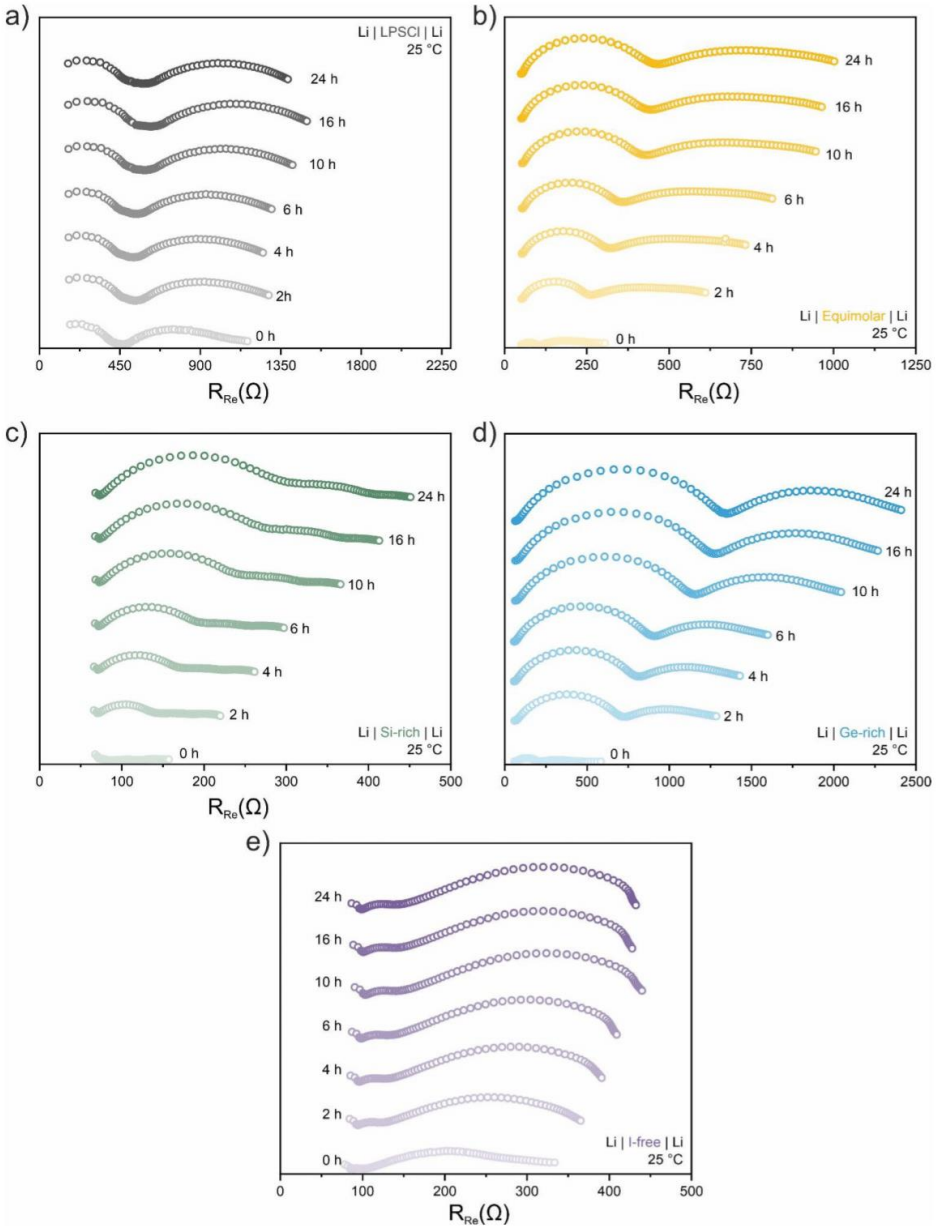

Figure S3. (a-e) EIS spectra obtained on symmetrical Li cells using the different solid electrolytes after 0, 2, 4, 6, 10, 16, and 24 h.

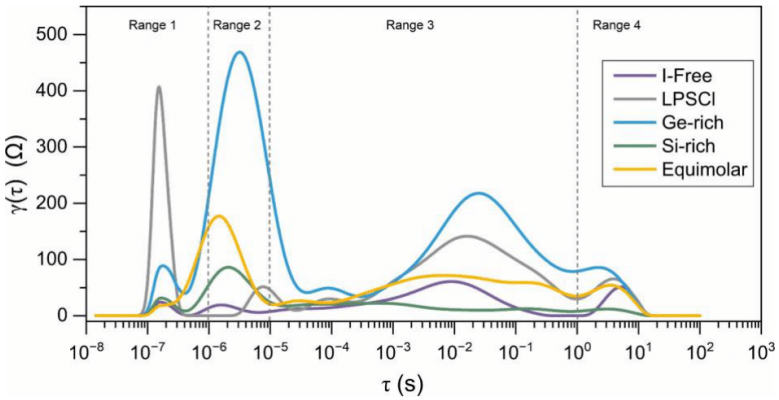

Figure S4. DRT transformation of the impedance data collected from the symmetrical Li cells after 24 h. In range no. 1, with $\tau < 10^{-6}$ s, the signal can be attributed to the response of the bulk SE. Range no. 2, with 10^{-6} s $< \tau < 10^{-5}$ s refers to particle-particle contact within the electrode or the contact resistance between electrode and current collector. Range no. 3, with 10^{-5} s $< \tau < 10^{0}$ s can be correlated to a wide range of processes, including interphase formation and charge transfer over the as-formed interfaces. However, due to severe time response overlap, it is virtually impossible to deconvolute each single process. Therefore, the calculated τ within this range has been assigned to the contribution of the interface without further distinguishing between multiple processes. Range no. 4 (with $\tau > 10^{0}$ s) can be attributed to diffusion processes.[1,2]

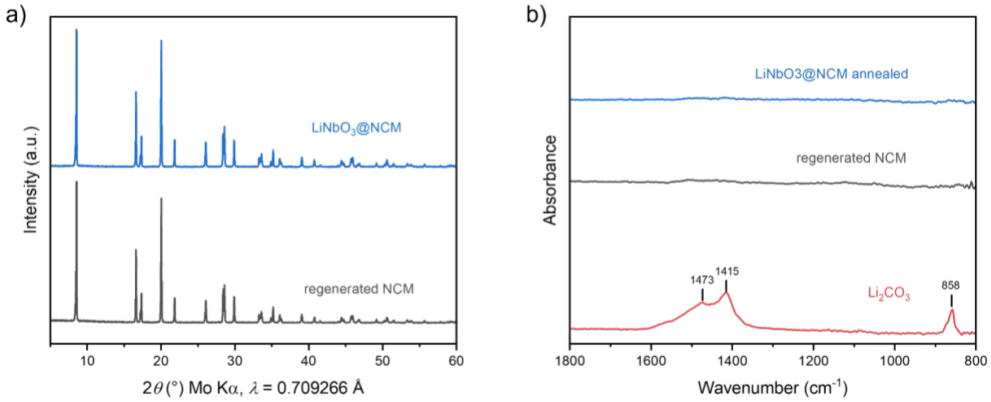

Figure S5. (a) XRD patterns and (b) ATR-IR spectra collected from the regenerated and $LiNbO_3$-coated NCM851005. Li_2CO_3 served as a reference in (b). The ATR-IR data confirm that the surface-protected NCM851005 used in the battery testing was largely free of carbonate surface impurities.

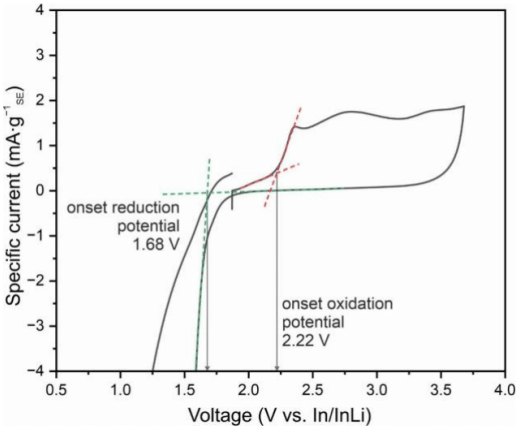

Figure S6. First cycle CV curve at 0.1 mV s^{-1} and 45 °C for the LPSCl solid electrolyte. The determination of the onset potentials for interfacial degradation is indicated.

Table S1. Structural parameters for the equimolar solid electrolyte from Rietveld refinement of XRD data.[a]

Atom	Wyckoff site	*x*	*y*	*z*	B_{iso} / Å^2	Occ
I1	4*a*	0	0	0	2.34(2)	0.97(8)
I2	4*d*	0.25	0.25	0.25	2.22(2)	0.02(2)
S1	16*e*	0.1235(8)	−0.1237(6)	0.6235(8)	1.88(7)	4
S2	4*a*	0	0	0	2.34(2)	0.02(2)
S3	4*d*	0.25	0.25	0.25	2.22(2)	0.97(8)
P1	4*b*	0	0	0.5	2.36(2)	0.25
Si1	4*b*	0	0	0.5	2.36(2)	0.25
Ge1	4*b*	0	0	0.5	2.36(2)	0.25
Sb1	4*b*	0	0	0.5	2.36(2)	0.25

[a] *F*−43*m* space group, a = 10.29224(12) Å, ρ = 2.411 g cm^{-3}, R_{wp} = 9.70%, χ^2 = 1.97. The sample contains LiI impurities (1.18%).

Table S2. Structural parameters for the Si-rich solid electrolyte from Rietveld refinement of XRD data.[a]

Atom	Wyckoff site	*x*	*y*	*z*	B_{iso} / Å^2	Occ
I1	4*a*	0	0	0	3.17(1)	0.97(4)
I2	4*d*	0.25	0.25	0.25	1.57(5)	0.02(6)
S1	16*e*	0.1235(8)	−0.1237(6)	0.6235(8)	1.18(7)	4
S2	4*a*	0	0	0	3.17(1)	0.02(6)
S3	4*d*	0.25	0.25	0.25	1.57(5)	0.97(4)
P1	4*b*	0	0	0.5	0.41(3)	0.167
Si1	4*b*	0	0	0.5	0.41(3)	0.5
Ge1	4*b*	0	0	0.5	0.41(3)	0.167
Sb1	4*b*	0	0	0.5	0.41(3)	0.167

[a]*F*−43*m* space group, a = 10.28330(9) Å, ρ = 2.345 g cm^{-3}, R_{wp} = 8.79%, χ^2 = 1.35. The sample contains LiI (2.11%) and Li_2S impurities (4.47%).

Table S3. Structural parameters for the Ge-rich solid electrolyte from Rietveld refinement of XRD data.[a]

Atom	Wyckoff site	*x*	*y*	*z*	B_{iso} / Å^2	Occ
I1	4*a*	0	0	0	2.70(1)	0.97(9)
I2	4*d*	0.25	0.25	0.25	0.64(6)	0.02(1)
S1	16*e*	0.1235(8)	−0.1237(6)	0.6235(8)	0.58(3)	4
S2	4*a*	0	0	0	2.70(1)	0.02(1)
S3	4*d*	0.25	0.25	0.25	0.64(6)	0.97(9)
P1	4*b*	0	0	0.5	0.33(6)	0.167
Si1	4*b*	0	0	0.5	0.33(6)	0.167
Ge1	4*b*	0	0	0.5	0.33(6)	0.5
Sb1	4*b*	0	0	0.5	0.33(6)	0.167

[a]*F*−43*m* space group, a = 10.32186(13) Å, ρ = 2.409 g cm^{-3}, R_{wp} = 11.2%, χ^2 = 1.98. The sample contains LiI (2.76%) and Li_2S (4.72%) impurities.

Table S4. Parameters derived from fitting the EIS data for the LPSCl solid electrolyte.

Calculated parameters	0 h	24 h
R_1 / Ω	346	380
CPE_1 / F s$^{\alpha-1}$	$1.9\cdot10^{-10}$	$1.9\cdot10^{-10}$
α_1	0.95	0.96

τ_1 / s	$2.9 \cdot 10^{-8}$	$3.3 \cdot 10^{-8}$
R_2 / Ω	174	260
CPE_2 / F $s^{\alpha-1}$	$1.9 \cdot 10^{-5}$	$1.9 \cdot 10^{-5}$
α_2	0.39	0.39
τ_2 / s	$4.4 \cdot 10^{-7}$	$1.1 \cdot 10^{-6}$
R_3 / Ω	622	702
CPE_3 / F $s^{\alpha-1}$	$1.2 \cdot 10^{-4}$	$1.2 \cdot 10^{-4}$
α_3	0.55	0.58
τ_3 / s	$8.8 \cdot 10^{-3}$	$1.4 \cdot 10^{-2}$
R_4 / Ω	97	138
CPE_4 / F $s^{\alpha-1}$	$6.2 \cdot 10^{-3}$	$5.5 \cdot 10^{-3}$
α_4	0.86	0.64
τ_4 / s	$5.6 \cdot 10^{-1}$	$6.5 \cdot 10^{-1}$

Table S5. Parameters derived from fitting the EIS data for the equimolar solid electrolyte.

Calculated parameters	0 h	24 h
R_1 / Ω	45	44
R_2 / Ω	42	359
CPE_2 / F $s^{\alpha-1}$	$3.4 \cdot 10^{-8}$	$3.1 \cdot 10^{-8}$
α_2	0.87	0.85
τ_2 / s	$1.8 \cdot 10^{-7}$	$1.5 \cdot 10^{-6}$
R_3 / Ω	42	111
CPE_3 / F $s^{\alpha-1}$	$5.3 \cdot 10^{-4}$	$2.2 \cdot 10^{-4}$
α_3	0.51	0.61
τ_3 / s	$5.7 \cdot 10^{-4}$	$2.4 \cdot 10^{-3}$
R_4 / Ω	229	632
CPE_4 / F $s^{\alpha-1}$	$2.4 \cdot 10^{-3}$	$5.6 \cdot 10^{-4}$
α_4	0.26	0.33
τ_4 / s	$8.9 \cdot 10^{-2}$	$4.5 \cdot 10^{-2}$

Table S6. Parameters derived from fitting the EIS data for the Si-rich solid electrolyte.

Calculated parameters	0 h	24 h
R_1 / Ω	66	72
CPE_1 / F $s^{\alpha-1}$	$2.8 \cdot 10^{-10}$	$6.1 \cdot 10^{-10}$
α_1	0.92	0.87
τ_1 / s	$3.7 \cdot 10^{-9}$	$3.6 \cdot 10^{-9}$
R_2 / Ω	8	201
CPE_2 / F $s^{\alpha-1}$	$7.0 \cdot 10^{-8}$	$2.0 \cdot 10^{-7}$

α_2	0.94	0.77
τ_2 / s	$2.3 \cdot 10^{-7}$	$2.1 \cdot 10^{-6}$
R_3 / Ω	95	132
CPE_3 / F $s^{\alpha-1}$	$2.4 \cdot 10^{-3}$	$1.3 \cdot 10^{-4}$
α_3	0.22	0.51
τ_3 / s	$1.2 \cdot 10^{-3}$	$3.5 \cdot 10^{-4}$
R_4 / Ω	13	73
CPE_4 / F $s^{\alpha-1}$	$3.6 \cdot 10^{-2}$	$9.3 \cdot 10^{-3}$
α_4	0.75	0.45
τ_4 / s	$3.6 \cdot 10^{-1}$	$4.1 \cdot 10^{-1}$

Table S7. Parameters derived from fitting the EIS data for the Ge-rich solid electrolyte.

Calculated parameters	0 h	24 h
R_1 / Ω	56	61
R_2 / Ω	259	1267
CPE_2 / F $s^{\alpha-1}$	$1.5 \cdot 10^{-7}$	$6.0 \cdot 10^{-8}$
α_2	0.72	0.75
τ_2 / s	$8.3 \cdot 10^{-7}$	$3.3 \cdot 10^{-6}$
R_3 / Ω	172	837
CPE_3 / F $s^{\alpha-1}$	$1.2 \cdot 10^{-4}$	$1.0 \cdot 10^{-4}$
α_3	0.57	0.62
τ_3 / s	$1.1 \cdot 10^{-3}$	$1.9 \cdot 10^{-2}$
R_4 / Ω	207	446
CPE_4 / F $s^{\alpha-1}$	$1.9 \cdot 10^{-3}$	$1.8 \cdot 10^{-3}$
α_4	0.51	0.45
τ_4 / s	$1.6 \cdot 10^{-1}$	$5.9 \cdot 10^{-1}$

Table S8. Parameters derived from fitting the EIS data for the I-free solid electrolyte.

Calculated parameters	0 h	24 h
R_1 / Ω	87	96
CPE_1 / F $s^{\alpha-1}$	$4.9 \cdot 10^{-10}$	$5.0 \cdot 10^{-10}$
α_1	0.86	0.85
τ_1 / s	$2.7 \cdot 10^{-9}$	$2.7 \cdot 10^{-9}$
R_2 / Ω	14	34
CPE_2 / F $s^{\alpha-1}$	$7.0 \cdot 10^{-7}$	$5.3 \cdot 10^{-7}$
α_2	0.80	0.79
τ_2 / s	$5.1 \cdot 10^{-7}$	$1.1 \cdot 10^{-6}$
R_3 / Ω	64	287
CPE_3 / F $s^{\alpha-1}$	$5.4 \cdot 10^{-4}$	$4.2 \cdot 10^{-4}$

SE-9

α_3	0.59	0.40
τ_3 / s	$3.3 \cdot 10^{-3}$	$5.2 \cdot 10^{-3}$
R_4 / Ω	225	71
CPE_4 / F $s^{\alpha-1}$	$1.3 \cdot 10^{-3}$	$2.5 \cdot 10^{-4}$
α_4	0.30	0.84
τ_4 / s	$1.8 \cdot 10^{-2}$	$8.4 \cdot 10^{-3}$

References

[1] Y. Zhao, W. E. Tenhaeff, *ACS Appl. Polym. Mater.* **2020**, *2*, 80-90.

[2] P. Bron, B. Roling, S. Dehnen, *J. Power Sources* **2017**, *352*, 127-134.

6.3.6. Publication VI

NANO · MICRO small

Supporting Information

for *Small*, DOI 10.1002/smll.202306832

Synthetic Tailoring of Ionic Conductivity in Multicationic Substituted, High-Entropy Lithium Argyrodite Solid Electrolytes

Jing Lin, Mareen Schaller, Gennady Cherkashinin, Sylvio Indris, Jianxuan Du, Clemens Ritter, Aleksandr Kondrakov, Jürgen Janek, Torsten Brezesinski and Florian Strauss**

Supporting Information

Synthetic Tailoring of Ionic Conductivity in Multicationic Substituted, High-Entropy Lithium Argyrodite Solid Electrolytes

Jing Lin,[a] Mareen Schaller,[b] Gennady Cherkashinin,[c] Sylvio Indris,[b] Jianxuan Du,[a] Clemens Ritter,[d] Aleksandr Kondrakov,[a,e] Jürgen Janek,[a,f] Torsten Brezesinski,[a*] and Florian Strauss[a*]

[a] Battery and Electrochemistry Laboratory (BELLA), Institute of Nanotechnology (INT), Karlsruhe Institute of Technology (KIT), Hermann-von-Helmholtz-Platz 1, 76344 Eggenstein-Leopoldshafen, Germany.

[b] Institute for Applied Materials–Energy Storage Systems (IAM-ESS), Karlsruhe Institute of Technology (KIT), Hermann-von-Helmholtz-Platz 1, 76344 Eggenstein-Leopoldshafen, Germany.

[c] Advanced Thin Film Technology, Institute of Materials Science, Technical University of Darmstadt, Alarich-Weiss Str. 2, 64287 Darmstadt, Germany.

[d] Institut Laue-Langevin, 38042 Grenoble Cedex 9, France.

[e] BASF SE, Carl-Bosch-Str. 38, 67056 Ludwigshafen, Germany.

[f] Institute of Physical Chemistry & Center for Materials Research (ZfM/LaMa), Justus-Liebig-University Giessen, Heinrich-Buff-Ring 17, 35392 Giessen, Germany.

*Corresponding authors: torsten.brezesinski@kit.edu, florian.strauss@kit.edu

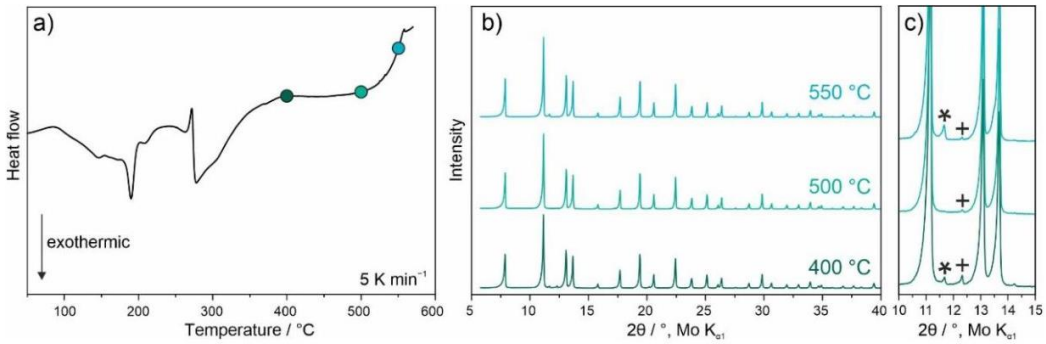

Figure S1. a) DSC trace of the precursor mixture. b) XRD patterns after annealing at different temperatures as indicated in a). c) Magnified view to visualize the additional reflections arising from Li_2S (asterisk) and LiI (cross) impurities. Ionic conductivities of the same samples from cold-pressed pellets are given in **Table S1**.

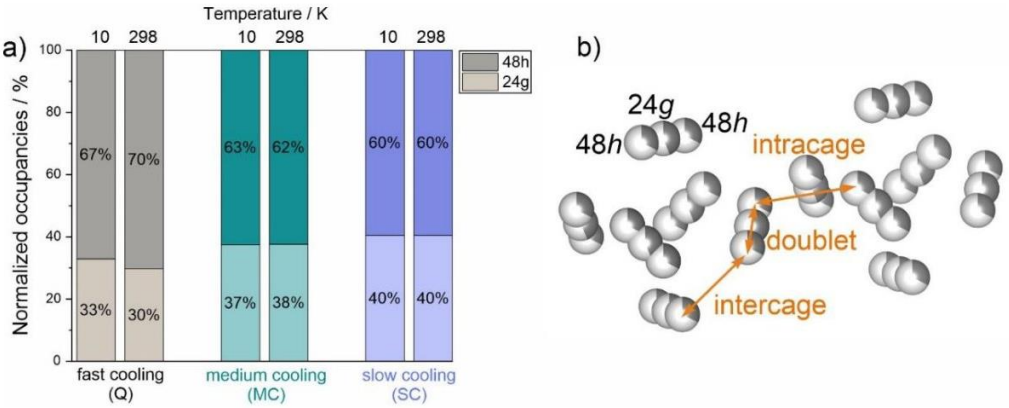

Figure S2. a) Normalized Li occupancies over the Wyckoff positions 48*h* and 24*g*. b) Two neighboring Li cages. The different transport (jump) pathways and sites are indicated.

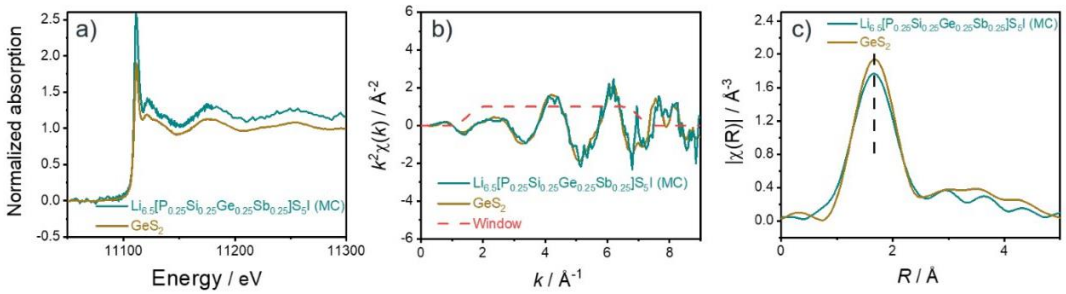

Figure S3. a) Ge K-edge XANES and b) k^2-weighted EXAFS [χ(k)] spectra. c) Corresponding magnitudes of the Fourier transform for $Li_{6.5}[P_{0.25}Si_{0.25}Ge_{0.25}Sb_{0.25}]S_5I$ (MC) (cyan) and the GeS_2 reference material (brown).

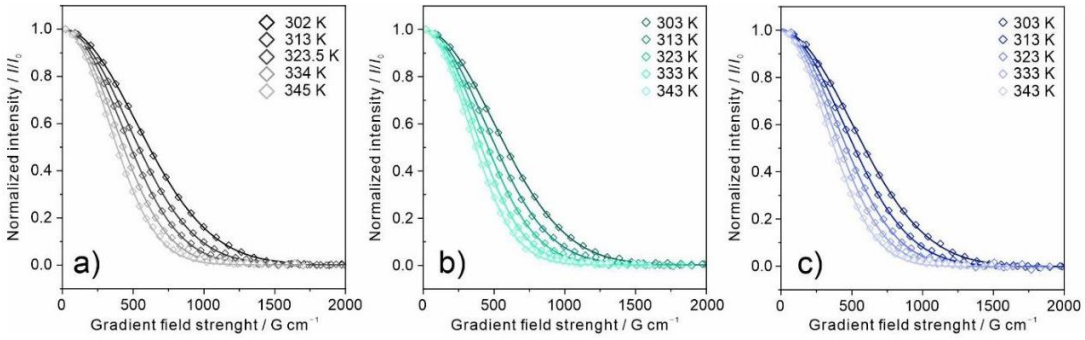

Figure S4. Results from temperature-dependent ^{7}Li PFG NMR spectroscopy measurements for a) fast- (Q), b) medium- (MC) and c) slow-cooled (SC) samples, with symbols and lines representing experimental and calculated data, respectively.

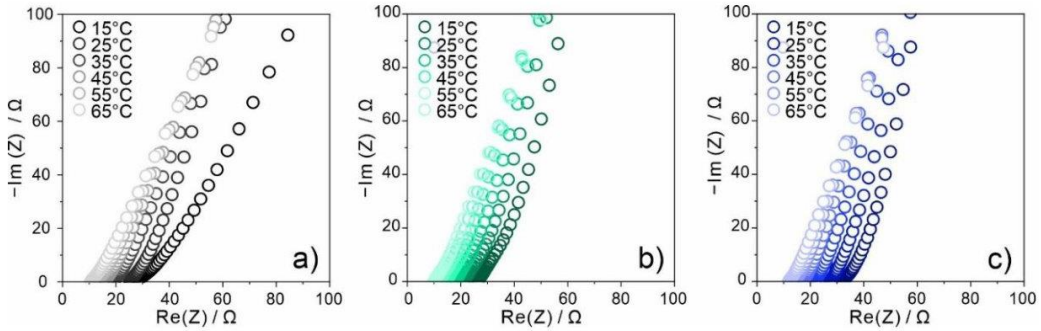

Figure S5. Nyquist plots of the electrochemical impedance measured between 15 and 65 °C for a) fast- (Q), b) medium- (MC) and c) slow-cooled (SC) samples.

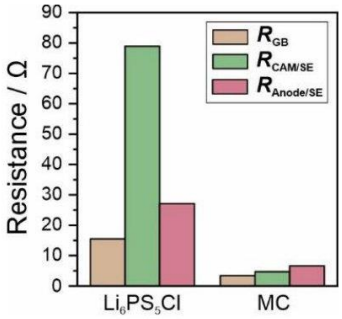

Figure S6. Calculated resistances from the impedance spectra in **Figure 8b** for the $Li_{6.5}[P_{0.25}Si_{0.25}Ge_{0.25}Sb_{0.25}]S_5I$- (MC) and Li_6PS_5Cl-based cells after the first cycle.

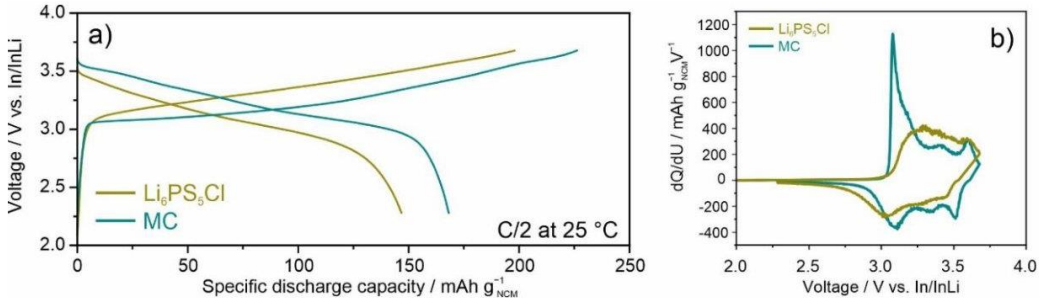

Figure S7. a) First- and second-cycle voltage profiles at 25 °C and C/2 rate and b) corresponding differential capacity plots for the $Li_{6.5}[P_{0.25}Si_{0.25}Ge_{0.25}Sb_{0.25}]S_5I$- (MC) and Li_6PS_5Cl-based cells.

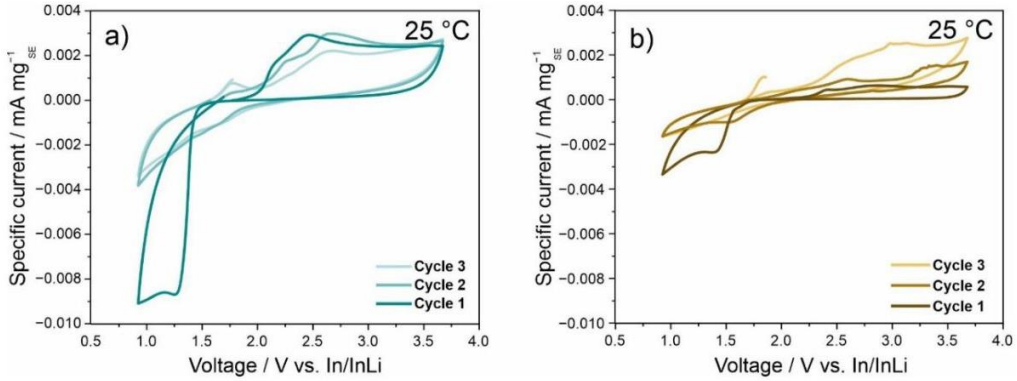

Figure S8. CV curves at 0.1 mV s^{-1} and 25 °C for a) $Li_{6.5}[P_{0.25}Si_{0.25}Ge_{0.25}Sb_{0.25}]S_5I$ (MC) and b) Li_6PS_5Cl. Note that mixtures of SE and carbon black were used as working electrode.

Table S1. Ionic conductivities determined from cold-pressed pellets annealed at different temperatures (see **Figure S1**).

Annealing temperature / °C	**σ_{ion} / mS cm^{-1}**
400	7.6
500	10.7
550	8.7

Table S2. Lattice parameters for the samples prepared with different cooling rates, with MC data taken from the literature.[1]

Sample	***a* / Å (*T* = 298 K)**	***a* / Å (*T* = 10 K)**
Quenched (Q)	10.29903(7)	10.25347(4)
Medium cooled (MC)	10.29714(9)	10.24932(5)
Slow cooled (SC)	10.30141(7)	10.25696(6)

Table S3. Structural parameters for $Li_{6.5}[Si_{0.25}Ge_{0.25}P_{0.25}Sb_{0.25}]S_5I$ (Q) from Rietveld analysis of NPD data collected at T = 298 K.[a]

Atom	**Wyckoff site**	***x***	***y***	***z***	**B_{iso} / Å^2**	**Occ**
I1	4*d*	0.25	0.25	0.75	1.64(4)	0.11(2)
I2	4*a*	0	0	0	2.19(3)	0.88(7)
S1	4*d*	0.25	0.25	0.75	1.64(4)	0.88(7)
S2	4*a*	0	0	0	2.19(3)	0.11(2)
S3	16*e*	0.1237(6)	−0.1237(6)	0.6237(6)	1.26(4)	1
Si1	4*b*	0	0	0.5	0.96(0)	0.25
Ge1	4*b*	0	0	0.5	0.96(0)	0.25
P1	4*b*	0	0	0.5	0.96(0)	0.25

Sb1	4*b*	0	0	0.5	0.96(0)	0.25
Li1	48*h*	0.2948(9)	0.0202(8)	0.7051(3)	3.67(4)	0.38(0)
Li2	24*g*	0.25	0.0205(4)	0.75	1.57(7)	0.32(0)

[a] *F*−43*m* space group, a = 10.29903(7) Å, V = 1092.421(17) Å^3, ρ = 2.406 g cm^{-3}, R_{wp} = 7.58%, χ^2 = 4.060.

Table S4. Structural parameters for $Li_{6.5}[Si_{0.25}Ge_{0.25}P_{0.25}Sb_{0.25}]S_5I$ (Q) from Rietveld analysis of NPD data collected at T = 10 K.[a]

Atom	Wyckoff site	*x*	*y*	*z*	B_{iso} / Å^2	Occ
I1	4*d*	0.25	0.25	0.75	0.93(9)	0.14(1)
I2	4*a*	0	0	0	1.04(6)	0.85(9)
S1	4*d*	0.25	0.25	0.75	0.93(9)	0.85(9)
S2	4*a*	0	0	0	1.04(6)	0.14(1)
S3	16*e*	0.1261(2)	−0.1261(2)	0.6261(2)	0.57(6)	1
Si1	4*b*	0	0	0.5	0.10(4)	0.25
Ge1	4*b*	0	0	0.5	0.10(4)	0.25
P1	4*b*	0	0	0.5	0.10(4)	0.25
Sb1	4*b*	0	0	0.5	0.10(4)	0.25
Li1	48*h*	0.2958(2)	0.0210(2)	0.7041(8)	1.93(2)	0.36(0)
Li2	24*g*	0.25	0.0242(0)	0.75	0.71(6)	0.36(0)

[a] *F*−43*m* space group, a = 10.25347(4) Å, V = 1078.984(10) Å^3, ρ = 2.439 g cm^{-3}, R_{wp} = 3.23%, χ^2 = 3.329.

Table S5. Structural parameters for $Li_{6.5}[Si_{0.25}Ge_{0.25}P_{0.25}Sb_{0.25}]S_5I$ (SC) from Rietveld analysis of NPD data collected at T = 298 K.[a]

Atom	Wyckoff site	*x*	*y*	*z*	B_{iso} / Å^2	Occ
I1	4*d*	0.25	0.25	0.75	1.56(9)	0.12(7)
I2	4*a*	0	0	0	2.09(6)	0.87(2)
S1	4*d*	0.25	0.25	0.75	1.56(9)	0.87(2)
S2	4*a*	0	0	0	2.09(6)	0.12(7)
S3	16*e*	0.1234(9)	−0.1234(9)	0.6234(9)	1.16(1)	1
Si1	4*b*	0	0	0.5	0.87(8)	0.25
Ge1	4*b*	0	0	0.5	0.87(8)	0.25
P1	4*b*	0	0	0.5	0.87(8)	0.25
Sb1	4*b*	0	0	0.5	0.87(8)	0.25

Li1	48*h*	0.2967(5)	0.0200(2)	0.7032(5)	3.09(5)	0.32(2)
Li2	24*g*	0.25	0.0184(9)	0.75	1.57(9)	0.43(8)

[a] *F*–43*m* space group, a = 10.30141(7) Å, V = 1093.178(17) Å^3, ρ = 2.407 g cm^{-3}, R_{wp} = 3.92%, χ^2 = 2.807.

Table S6. Structural parameters for $Li_{6.5}[Si_{0.25}Ge_{0.25}P_{0.25}Sb_{0.25}]S_5I$ (SC) from Rietveld analysis of NPD data collected at T = 10 K.[a]

Atom	Wyckoff site	*x*	*y*	*z*	B_{iso} / Å^2	Occ
I1	4*d*	0.25	0.25	0.75	0.92(9)	0.13(5)
I2	4*a*	0	0	0	1.07(7)	0.86(5)
S1	4*d*	0.25	0.25	0.75	0.92(9)	0.86(5)
S2	4*a*	0	0	0	1.07(7)	0.13(5)
S3	16*e*	0.1254(3)	–0.1254(3)	0.6254(3)	0.49(8)	1
Si1	4*b*	0	0	0.5	0.15(8)	0.25
Ge1	4*b*	0	0	0.5	0.15(8)	0.25
P1	4*b*	0	0	0.5	0.15(8)	0.25
Sb1	4*b*	0	0	0.5	0.15(8)	0.25
Li1	48*h*	0.2973(9)	0.0199(5)	0.7026(1)	1.85(8)	0.32(2)
Li2	24*g*	0.25	0.0211(3)	0.75	1.54(4)	0.43(8)

[a] *F*–43*m* space group, a = 10.25696(6) Å, V = 1079.088(15) Å^3, ρ = 2.436 g cm^{-3}, R_{wp} = 3.08%, χ^2 = 3.122.

Table S7. Li-Li jump distances at T = 298 and 10 K for the $Li_{6.5}[Si_{0.25}Ge_{0.25}P_{0.25}Sb_{0.25}]S_5I$ samples prepared with different cooling rates, with MC data taken from the literature.[1] For comparison, the corresponding jump distances in Li_6PS_5I are also given (T = 300 K, from ref. [2]).

T / K	48h-48h / Å	Intracage / Å	Intercage / Å
298 (Q)	1.31(4)	2.69(3)	3.28(3)
298 (MC)	1.39(6)	2.64(2)	3.24(2)
298 (SC)	1.361(2)	2.67(3)	3.25(3)
10 (Q)	1.33(3)	2.66(3)	3.27(3)
10 (MC)	1.39(2)	2.63(2)	3.23(1)
10 (SC)	1.38(1)	2.65(2)	3.22(2)
300 (Li_6PS_5I)	1.25	2.57	3.35

Table S8. Binding energies from fitting of XPS data. Major and minor indicate that two contributions were assumed in the curve fitting.

Element	BE / eV (Q)	BE / eV (MC)	BE / eV (SC)
O 1s	531.8 (major) 532.8 (minor)	532.0 (major) 533.0 (minor)	532.0 (major) 533.1 (minor)
Sb 3d	530.2 (major) 529.3 (minor)	530.4 (major) 529.5 (minor)	530.3 (major) 529.5 (minor)
S 2p	161.3 (major) 163.3 (minor)	161.5 (major) 163.7 (minor)	161.4 (major) 163.7 (minor)
P 2p	132.1	132.4	132.2
Si 2p	100.9 (major) 102.5 (minor)	101.0 (major) 102.7 (minor)	101.0 (major) 102.7 (minor)
I 4d	48.6 (major) 49.1 (minor)	49.4 (major) 49.9 (minor)	49.3 (major) 49.9 (minor)
Sb 4d	34.1 (major) 33.2 (minor)	34.3 (major) 33.3 (minor)	34.2 (major) 33.3 (minor)
Ge 3d	30.7	30.9	30.8

Table S9. Surface composition of the samples prepared with different cooling rates in units of at.% from XPS.

Sample	Li	P	Si	Ge	Sb	S	I	O
Q	39.1	1.3	1.9	1.7	2.9	32.4	12.3	8.3
MC	37.9	1.6	3.1	1.8	2.9	32.1	12.0	8.7
SC	35.5	1.4	2.0	1.6	2.0	36.6	9.4	11.6

[1] J. Lin, G. Cherkashinin, M. Schäfer, G. Melinte, S. Indris, A. Kondrakov, J. Janek, T. Brezesinski, F. Strauss, ACS Materials Lett. **2022**, *4*, 2187.

[2] N. Minafra, M. A. Kraft, T. Bernges, C. Li, R. Schlem, B. J. Morgan, W. G. Zeier, Inorg. Chem. **2020**, *59*, 11009.

6.4. Scientific contributions

6.4.1. List of publications

Publications within this thesis

06. Du, J., **Lin, J. (co-first author)**, Zhang, R., Wang, S., Indris, S., Ehrenberg, H., Brezesinski, T., & Strauss, F. (2024). Electrochemical Testing and Benchmarking of Compositionally Complex Lithium Argyrodite Electrolytes for All‐Solid‐State Battery Application. Batteries & Supercaps, e202400112.

05. **Lin, J.**, Schaller, M., Indris, S., Baran, V., Gautam, A., Janek, J., Kondrakov, A., Brezesinski, T., & Strauss, F. (2024). Tuning Ion Mobility in Lithium Argyrodite Solid Electrolytes via Entropy Engineering. Angewandte Chemie International Edition, e202404874.

04. **Lin, J.**, Schaller, M., Cherkashinin, G., Indris, S., Melinte, G., Janek, J., Brezesinski, T., & Strauss, F. (2023) Synthetic Tailoring of Ionic Conductivity in Multicationic Substituted, High-Entropy Lithium Argyrodite Solid Electrolytes. Small, 2306832.

03. Li, S., **Lin, J. (co-first author)**, Schaller, M., Indris, S., Zhang, X., Brezesinski, T., Nan, C., Wang, S., & Strauss, F. (2023) High‐Entropy Lithium Argyrodite Solid Electrolytes Enabling Stable All‐Solid‐State Batteries. Angewandte Chemie International Edition, e202314155.

02. **Lin, J.**, Cherkashinin, G., Schäfer, M., Indris, S., Melinte, G., Janek, J., Kondrakov, A., Brezesinski, T., & Strauss, F. (2022). A High-Entropy Multicationic Substituted Lithium Argyrodite Superionic Solid Electrolyte. ACS Materials Letters, 4(11), 2187–2194.

01. Strauss, F., **Lin, J.**, Duffiet, M., Wang, K., Zinkevich, T., Hansen, A. L., Indris, S., & Brezesinski, T. (2022). High-Entropy Polyanionic Lithium Superionic Conductors. ACS Materials Letters, 4(2), 418–423.

Publications beyond this thesis

22. **Lin, J. (co-first author)**, Schaller, M., Hu, Y., Zhou, L., Indris, S., Liu, J., Fichtner, M., Brezesinski, T., & Strauss, F. Underneath the General Structure – Local Structure and Local Dynamics for High-Entropy Lithium Argyrodites (*in preparation*)

21. **Lin, J.**, Schaller, M., Bergfeldt, T., Indris, S., Brezesinski, T., & Strauss, F. Boosting the mobility for Lithium Garnets via Complex Substitution (*in preparation*)

20. **Lin, J.**, Schaller, M., Zhang, R., Indris, S., Baran, V., Liu, H., Kondrakov, A., Brezesinski, T., & Strauss, F. Nanocrystalline High-Entropy Argyrodite Enhanced (Chemo-)mechanical Stability in All-Solid-State Batteries (*submitted*)

19. Liu, H., Hua, W., Li, H., Ying, B., Kleiner, K., **Lin, J.**, Xu, H., Deng, B., Wong, D., Bergfeldt, T., Mangold, S., Nagel, P., Schuppler, S., Merz, M., Baran, V., Ritter, C., Xu, H., Li, Y., Li, N., Knapp, M., Ehrenberg, H., & Indris, S. Integrating Ni-pinned honeycomb structures enables high-performance lithium-ion layered oxide cathodes (*submitted*)

18. An, S., Karger, K., Müller, P., **Lin, J.**, Vasala, S. J., Baran, V., Dreyer, S. L., Ulusoy, F., Kondrakov, A., Janek, L. & Brezesinski, T. Understanding the Impact of Ca Pillaring Ion for the O3-type $NaNi_{0.9}Ti_{0.1}O_2$ Cathode in Sodium-Ion Batteries (*submitted*)

17. Wang, S., Tang, M., Wu, X., **Lin, J.**, Gautam, A., Cheng, Z., Zhang, S., Lou, C., Li, S., Zhou, R., Mu, Y., Zhang, X., Strauss, F., Brezesinski, T., Shen, Y., Lin, Y. & Nan, C-W. Large-Scale Manufacturing Superionic Lithium Argyrodite Solid Electrolytes Enabling Stable All-Solid-State Battery (*submitted to Matter, under reviewing*)

16. Shu, Y., Zhao, W., Chen, H., **Lin, J.**, Chen, D., Huang, J., Ren, F., Lei, H., Yan, Q., Yu, H., Du, K., Hu, G., Cao, Y., Brezesinski, T., Peng, Z., Ji, X., Fan, X. & Yang, Y. Unraveling and Suppression of Multi-Directional Planar Slipping and Microcracking in Single-Crystal Co-free Ni-rich Cathodes (*submitted to Nature Communication, under reviewing*)

15. Zhao, W., Zhang, R., Ren, R., Karger, L., Dreyer, S., **Lin, J.,** Ma, Y., Cheng, Y., Pal, S.A., Velazquez-Rizo, M., Ahmadian, A., Zhang, Z., Janek, J., Yang, Y., Kondrakov, A., & Brezesinski, T. $LiNbO_3$ Protective Coating on Single-Crystalline Ni-Rich Cathodes for Advancing All-Solid-State-Batteries (*submitted to ACS Nano, under reviewing)*

14.Yang, J., **Lin, J.**, Brezesinski, T., & Strauss, F. Designing Amorphous-Nanocrystalline Sulfide- and Halide-Based Solid Electrolytes. ACS Energy Letters, 9, 5977-5990.

13. Tan, Z., Chen, X., **Lin, J.**, Chen, W., Liu, Q., Zhang, H., Huang, Y., Liu, Z., Brezesinski, T., Huang, Y., Yang, Y., & Zhao, W. Restraining Planar Gliding in Single-crystalline $LiNi_{0.9}Co_{0.05}Mn_{0.05}O_2$ Cathode through Combining Internal and External Modification Strategy. Angewandte Chemie, e202419903.

12. He, Y., Ting, Y-Y., Hu, H., Diemant, T., Dai, Y., **Lin, J.**, Marques, G., Hahn, H., Ma, Y., Brezesinski, T., Kowalski, P., Aghassi-Hagmann, J., & Breitung, B. Emerging Sodium ion-modulated Non-Volatile Printed Memory based on Multicomponent Prussian Blue Material. Advanced Materials, 2410060.

11. Liu, H., Hua, W., Kunz, S., Bianchini, M., Li, H., Peng, J., **Lin, J.**, Dolotko, O., Bergfeldt, T., Wang, K., Kübel, K., Ying, B., Kleiner, K., Nagel, P., Schuppler, S., Merz, M., Mangold, S., Wong, D., Baran, V., Knapp, M., Ehrenberg, H., & Indris, S. Tailoring Superstructure Units for Enhanced Oxygen Redox in Li-Rich Layered Oxides. Nature Communication, 15(1), 9981.

10. He, Y., Akcay, T., Dreyer, S., Diemant, T., Mönig, R., Ma, Y., Tang, Y., Wang, H., Liu, H., **Lin, J.**, Schweidler, S., Fichtner, M., Hahn, H., Aghassi-Hagmann, J., Brezesinski, T., Breitung, B., & Ma, Y. (2024) Leveraging Entropy and Crystal Structure Engineering in Prussian Blue Analogue Cathodes for Advancing Sodium-Ion Batteries. ACS Nano 18(35), 24441-24457.

09. Cui, Y., Tang, Y., **Lin, J.**, Wang, J., Hahn, H., Schweidler, S., Brezesinski, T., & Botros, M. (2024). Photonic Synthesis and Coating of High-Entropy Oxide on Layered Ni-Rich Cathode Particles. Small Structures, 2400197.

08. An, S., Karger, L., Dreyer, S., Hu, Y., Barbosa, E., Zhang, R., **Lin, J.**, Fichtner, M., Kondrakov, A., Janek, J., & Brezesinski, T. (2024). Improving Cycling Performance of the $NaNiO_2$ Cathode in Sodium-Ion Batteries by Titanium Substitution. Materials Futures, 3(3), 035103

07. Zhao, Z., Waqar, M., Jaiswal, A., Raghavan, A., Fuchs, D., **Lin, J.**, Brezesinski, T., Bhattacharya, S., Hahn, H., Pan, X., Kruk, R., & Sarkar, A. (2024). Strained single crystal high entropy oxide manganite thin films. Applied Physics Letter, 125(1).

06. Ren, F., Wu, Y., Zuo, W., Zhao, W., Pan, S., Lin, H., **Lin, J.**, Lin, M., Brezesinski, T., Gong, Z., & Yang, Y. (2024). Visualizing the SEI formation between lithium metal and solid-state electrolyte. Energy & Environmental Science, 17, 2743-2752.

05. Ma, Y., Zhang, R., Ma, Y., Diemant, T., Tang, Y., Payandeh, S., Goonetilleke, D., Kitsche, D., **Lin, J.**, Kondrakov, A., & Brezesinski, T. (2024). Interface and Electrode Microstructure Engineering for Optimizing Performance of the $LiNiO_2$ Cathode in All-Solid-State Batteries. Chemistry of Materials, 36(5), 2588–2598.

04. Strauss, F., **Lin, J**., Kondrakov, A., & Brezesinski, T. (2023). High-entropy argyrodite lithium superionic conductors. Matter, 6(4), 1068-1070.

03. Strauss, F., **Lin, J**., Karger, L., Weber, D., & Brezesinski, T. (2022). Probing the Lithium Substructure and Ionic Conductivity of the Solid Electrolyte Li_4PS_4I. Inorganic Chemistry, 61(15), 5885-5890.

02. Weber, D., **Lin, J. (co-first author)**, Pokle, A., Volz, K., Janek, J., Brezesinski, T., & Bianchini, M. (2022). Tracing Low Amounts of Mg in the Doped Cathode Active Material $LiNiO_2$. Journal of the Electrochemical Society, 169(3), 030540.

01. Strauss, F., **Lin, J.**, Janek, J., & Brezesinski, T. (2021). Influence of Synthesis Parameters on Crystallization Behavior and Ionic Conductivity of the Li_4PS_4I Solid Electrolyte. Scientific Reports, 11(1), 1–9.

6.4.2. List of patents

Lin, J., Strauss, F., Kondrakov, A., & Brezesinski, T. (2021). Lithium Ion-Conducting Solid Material. European Patent Application 2021, 21215717.6.

6.4.3. List of conference contributions

24th International Conference on Solid State Ionics (SSI 24)
London, UK, 2024
Oral: Multicationic Substituted High-Entropy Lithium Argyrodite Superionic Conductors

2023 Material Research Society Fall Meeting & Exhibit (MRS Fall 2023)
Boston, US, 2023
Oral: High-entropy Lithium Argyrodite Solid Electrolytes

Gordon Research Seminar – Neutron Scattering
Ventura, United States (US), 2023
Oral (invited): High-entropy Lithium Argyrodites Solid Electrolytes.

Gordon Research Seminar – Neutron Scattering
Ventura, United States (US), 2023
Poster: Neutron Powder Diffraction Investigations of Structure-Charge Transport Relationships in High-Entropy Lithium Argyrodite Superionic Conductors

Gordon Research Conference – Neutron Scattering

Ventura, United States (US), 2023
Poster: Neutron Powder Diffraction Investigations of Structure-Charge Transport Relationships in High-Entropy Lithium Argyrodite Superionic Conductors

2022 Material Research Society Fall Meeting & Exhibit (MRS Fall 2022)
Boston, US, 2023
Oral: Multi-Element Substituted Lithium Argyrodite Solid Electrolytes

Verband der Chemischen Industrie (VCI) Seminar
Karlsruhe, Germany, 2022
Oral: A Polycationic Substituted Lithium Argyrodite Superionic Solid Electrolytes

33rd European Crystallography Meeting (ECM33 2022)
Versailles, France, 2022
Poster: Polyanionic/-cationic Substituted Lithium Argyrodites Solid Electrolytes

7. Acknowledgements

Writing has finally reached the conclusion of this thesis, allowing me the opportunity to express my gratitude for all the support I have received.

First and foremost, I would like to extend my sincere appreciation to my supervisor, Prof. Dr. Jürgen Janek, for his insightful suggestions when I was new to this field, and for his strong support throughout the finalization of my thesis.

I am truly grateful to my advisors, Dr. Florian Strauss and Dr. Torsten Brezesinski, for their constant encouragement and unwavering support during the challenges encountered on this high-entropy journey.

I extend my thanks to my co-referee, Prof. Dr. Bernd Smarsly, and the other members of my doctoral examination committee, Prof. Dr.-Ing. Maren Lepple and Dr. Mattias Elm, for the time they dedicated to evaluating my work.

Special thanks are due to my master supervisor, Ass. Prof. Dr. Daniel Weber, and Prof. Dr. Matteo Bianchini from the University of Bayreuth, for providing me with the initial opportunity to work in BELLA during my master's studies, and for their patient guidance during the Rietveld refinement process. Thanks also go to my first advisor and mentor Dr. Dajian Li for guiding me when I knew nothing in the field of battery technology.

Furthermore, I am grateful for the strong support from the Institute of Applied Materials – Energy Storage System. I appreciate the invaluable NMR technology support from Dr. Sylvio Indris and Dr. Mareen Schaller. Their assistance has been crucial in providing evidence for the high-entropy ion conductors. I am also thankful to Dr. Michael Knapp for his helpful supervision during practical Rietveld refinement lectures, and to Dr. Anna-Lena Hansen for her insightful suggestions and assistance with PDF refinement. Similar gratitude extends to Dr. Maxwell Terban from MPI, Stuttgart.

During these three years, one of the most stressful aspects for me was securing neutron and synchrotron beamtime. I am thankful for the strong support from beamline scientists Dr. Volodymyr Baran (P02.1, DESY), Dr. Clemens Ritter (D2B, ILL), Dr. Ajay Gautam (Technische Universität Delft), Dr. Jue Liu (NOMAD, ORNL), and Dr. Stephanie Berlin (ROCK, SOLEIL), whose assistance alleviated the pressure of proposal submission. I am also grateful for TEM support from Dr. Ziming Ding, Dr. Kai Wang, and Dr. Georgian Melinte. I appreciate the help from Dr. Gennady Cherkashinin (Technische Universität Darmstadt) for XPS characterization. Thanks are due to Dr. Frank Weber and Dr. Xingchen Shen for explaining inelastic neutron scattering, and I eagerly await the acceptance of our proposal. Additionally, I appreciate Dr. Yang Hu from HIU for his patient guidance and explanations for EXAFS measurement and data analysis. Also, I am grateful for the insightful suggestions not only about the science also about the career pathway from Dr. Guiliang Xu (Argonne National Laboratory). I am expecting for the results and our future discussions.

My time at BELLA has been incredible, filled with laughter, jokes, beer, BBQ, and cakes shared with my kind colleagues. I remember fondly the camaraderie with Dr. Damian Goonetilleke, Dr. Marie Duffie, Dr. Teo Jun Hao, Dr. David Kitchen, Dr. Yuan Ma, Dr. Wengao

Zhao, Dr. Barbara Nascimento Nunes, Dr. Eduardo Barbosa, Dr. Leonhard Kager, Dr. Sören Dreyer, Ruizhuo Zhang, Siyu An, Jianxuan Du, Jingui Yang, and Nicolai Bartnick.

I am grateful for the precious friendship with my roommate, Dr. Wenwen and Shiqing Li. Life in Karlsruhe would have been much more challenging without you both, especially for delicious food. I also extend my thanks to my dearest friends, Dr. Xiaoli Shen, Dr. Xiaofei Sun, Shanshan Hu, Hongru Zhou, Xueshan Hong, Wenjun Li, Yuting Li, Yixin Yang, Lei Qi, and Dr. Wei Huang, for their unconditional support and accompany. I also appreciate my basketball buddies, Zhibo Zhao, Dr. Hongrong Hu, and Xiaohanwen Lin, for the enjoyable Saturday morning games at DT during the summer. Thanks, are also due to my table-tennis and squash buddies, Dr. Guanglang Xu, Dr. Zewei Lü, and Dongfang Yuan. To the women's basketball team members at Frankfurt, Yixin Wang, Jiao Xiao, Shi Yao, and Julia, I wish us success in the upcoming games. Thanks to Qinxuan Xu, without you, I would not been in Germany.

Hang Xu (Xianyan Bao), being with you has been the best part of my life. You are always my sunshine and summer to light my darkness.

Finally, I express my deepest appreciation to my parents and grandparents, Wei Lin, Hongyan Yao, Huarui Wen, Yongfu Yao, Zhicheng Lin and Gou Qian, for their unconditional love. I miss you all dearly.